Dissertation

Structure-Property Relation in Self-Assembled Monolayers: Electrostatic Engineering, Charge Transport Properties, and Thermal Stability

Andika Asyuda
2021

INAUGURAL-DISSERTATION

zur

Erlangung der Doktorwürde

der

Naturwissenschaflich-Mathematischen
Gesamfakultät

der

Ruprecht-Karls-Universität
Heidelberg

Vorgelegt von

M.Sc. Andika Asyuda
aus Indonesia

Tag der mündlichen Prüfung: 10.12.2021

Structure-Property Relation in Self-Assembled Monolayers: Electrostatic Engineering, Charge Transport Properties, and Thermal Stability

Gutachter:
Prof. (apl) Dr. Michael Zharnikov
Prof. (apl) Dr. Hans-Robert Volpp

To my parents, brother, and sister.

Abstract

The major goals of the thesis are design and characterization of functional self-assembled monolayers (SAMs) in context of electrostatic interfacial engineering and molecular electronics as well as a study of their thermal stability. The issue of electrostatic engineering can be addressed using custom-designed SAMs with either terminal dipolar groups or dipolar groups embedded into the molecular backbone.

As for the first task, the novel concept of embedded dipole was successfully applied to the oxide substrates, which are highly important for photovoltaic applications. A variation of the work function of indium tin oxide (ITO) by □0.5 eV as compared to the reference non-polar functionalization was achieved at the invariable character of the SAM-ambient interface, allowing, thus, to decouple electrostatic engineering from the interface chemistry. The extremely low work function value for one of the tested monolayers expands a rather limited selection of SAMs capable of significantly lowering the work function of ITO.

As a further task, electrostatic effects in charge transport across monomolecular films were studied, which is currently one of the most intensely discussed topics in molecular electronics. The tuning of the electrostatic properties was achieved by the fabrication of binary SAMs of biphenylthiolates (BPT) on Au(111), namely by mixing of BPT with fluorine-substituted-BPT (F-BPT) and 4-methyl-4′-BPT (CH$_3$-BPT) with 4-trifluoromethyl-4′-BPT (CF$_3$-BPT). The charge tunneling rate across the binary SAMs was found to vary progressively with their composition between the values for the single-component monolayers, and could, consequently, be fine-tuned and correlated with the work function. The observed behavior was tentatively explained by the appearance of an internal electrostatic field in the SAMs, leading to a change of the energy-level alignments within the junction upon contact of the SAMs to the top eutectic GaIn electrode.

The height of the respective injection barrier is, however, unaffected by such a field, corresponding to the values of the transition voltage, which do not change notably with the SAM composition. Analysis of the presented and literature data suggests that the position of a dipolar group in SAM-forming molecules has significant impact on the charge transport behavior of the respective SAMs in the context of molecular electronics.

As the next sub-project in the latter context, custom-designed SAMs of ferrocene/ruthenocene-substituted biphenylthiolates and fluorenethiolates on Au(111) were studied. The novel element of these SAMs was the fully conjugated molecular backbone, in contrast to the previous studies utilizing alkyl linkers as elements of molecular diodes. The designed SAMs exhibited a highly exceptional charge transport behavior showing conductance switching triggered by the applied bias. The extent of this switching, described by a maximum rectification ratio (RR) higher than 1000, was comparable to the best performing molecular diodes but in contrast to these "devices" was maintained at very low bias, close to zero volts. The observed behavior could be tentatively explained by a non-reversible redox process affecting the electronic structure of the molecules and their coupling to the top electrode. The above results are particularly promising to create novel molecular devices for potential applications in electronic circuits, molecular memory, or as an electrochemical sensor.

Finally, the issue of thermal stability of functional SAMs on coinage metal and oxide substrates was addressed. This issue is of a crucial importance for applications, defining the temperature range of SAM-based devices and framing the preparation routes involving high temperature steps. Several representative SAMs with thiol anchoring group on Au(111) substrates and phosphonic acid (PA) anchoring group on Al_2O_3 substrates were studied by high resolution X-ray photoelectron spectroscopy chosen as the most suitable experimental tool. The range of the thermal stability and the degradation pathways were found to depend on the chemical composition of the SAM-forming molecules and the character of the substrates, with such crucial parameters as the strength of substrate-anchoring group bond and the presence of a backbone-specific "weak links". In general, PA monolayers on oxide substrates were found to have higher robustness and better thermal stability compared to thiolates SAMs on coinage metal substrates. My results show, however, that is always advisable to test thermal stability of a specifically designed functional SAM in context of possible "weak links" as far as this stability is important for a particular application.

Zusammenfassung

Die Hauptziele der Dissertation waren das Design und die Charakterisierung von funktionellen, selbst-aggregierenden Monolagen (SAMs) im Bezug auf der elektrostatischen Grenzflächentechnik und der molekularen Elektronik sowie die Untersuchung der thermischen Stabilität der SAMs. Das Konzept der Elektrostatik in SAMs konnte durch speziell angefertigte Molecules mit entweder einer terminalen dipolaren Gruppe oder dipolaren Gruppe, die in das molekulare Gerüst eingebettet ist, studiert werden.

Als erste Aufgabe, das neuartige Konzept des eingebetteten Dipols wurde auf Oxidsubstrate erfolgreich angewandt. Oxidsubstrate sind sehr wichtig für Photovoltaikanwendungen. Eine Variation der Austrittsarbeit von Indium-Zinn-Oxid (ITO) um ±0.5 eV im Vergleich zur unpolaren Referenzfunktionalisierung wurde am unveränderlichen Charakter der SAM-Umgebungsgrenzfläche erreicht, wodurch die Elektrostatik von den einflussen der chemischen Grenzfläche entkoppelt werden konnte. Der extrem niedrige Austrittsarbeit einer getesteten Monolagen erweitert die bislang eher begrenzte Auswahl von SAMs, die Austrittsarbeit von ITO senken können.

Weiterhin wurden die elektrostatische Effekte beim Ladungstransport durch monomolekulare Filme untersucht, eines derzeit der bedeutendsten Themen der molekularen Elektronik ist. Die Abstimmung der elektrostatischen Eigenschaften wurde durch die Herstellung binärer SAMs von Biphenylthiolaten (BPT) auf Au(111) erreicht, im speziellen waren diese Mischungen von H-BPT mit F-BPT und CH$_3$-BPT mit CF$_3$-BPT. Es wurde festgestellt, dass die Ladungstunnelrate über die binären SAMs hinweg progressiv mit ihrer Zusammensetzung zwischen den Werten für die reinen SAMs variiert und folglich fein abgestimmt und mit der Austrittsarbeit korreliert werden konnte. Das beobachtete Verhalten wurde vorläufig durch das Auftreten eines internen elektrostatischen Feldes in den SAMs erklärt, dass zu einer Änderung der Energieniveau-Ausrichtungen innerhalb des Übergangs beim Kontakt der SAMs mit der oberen eutektischen GaIn-Elektrode führte. Die Höhe der jeweiligen Injektionsbarriere wird jedoch von einem solchen Feld nicht beeinflusst, dies ergibt sich aus den Werten der Übergangsspannung, die sich mit der SAM-Zusammensetzung nicht merklich ändern. Die in dieser Arbeit präsentierten Ergebnisse sowie der Literaturdaten legt nahe, dass die Position einer dipolaren Gruppe in SAM-bildenden Molekülen einen signifikanten Einfluss auf das Ladungstransportverhalten durch die jeweilige SAM im Kontext der molekularen Elektronik hat.

Weiterhin wurden speziell angefertigte SAMs von Ferrocen/Ruthenocen-substituierten Biphenylthiolaten und Fluorenthiolaten auf Au(111) untersucht. Das neuartige Element dieser SAMs war das vollständig konjugierte molekulare Gerüst, im Gegensatz zu den früheren Studien, die sich mit molekularen Dioden unter Verwendung von Alkan-Monolagen beschäftigten. Die entworfenen SAMs besaßen ein außergewöhnliches Ladungstransportverhalten und zeigten, dass die Änderung der Leitfähigkeit durch die angelegte Vorspannung ausgelöst wurde. Das Ausmaß dieses Schaltens, die durch ein maximales Gleichrichtungsverhältnis von mehr als 1000 geschrieben wurde, war vergleichbar mit den leistungsstärksten molekularen Dioden, wurde jedoch im Gegensatz

zu unseren Dioden bei sehr niedriger Vorspannung nahe Null Volt erreicht. Das beobachtete Verhalten konnte versuchsweise durch einen nicht reversiblen Redoxprozess erklärt werden, der die elektronische Struktur der Moleküle und ihre Kopplung an die obere Elektrode beeinflusst. Die Ergebnisse sind besonders vielversprechend um eine neuartige molekulare Vorrichtung für potenzielle Anwendungen in elektronischen Schaltungen, molekularen Speichern oder als elektrochemischer Sensor zu realisieren.

Schließlich wurde die Frage der thermischen Stabilität funktionaler SAMs auf Münzmetall- und Oxidsubstraten behandelt. Dieses Thema ist von entscheidender Bedeutung für Anwendungen, die den Temperaturbereich von SAM-basierten Geräten definieren und die Herstellungsverfahren mit Hochtemperaturbehandlung festlegen. Mehrere repräsentative SAMs mit Thiol-Ankergruppe auf Au-Substraten und Phosphonsäure (PA)-Ankergruppe auf Al_2O_3-Substraten wurden untersucht, wobei hochauflösende Röntgenphotoelektronenspektroskopie als experimentelles Werkzeug diente. Es wurde festgestellt, dass der Bereich der thermischen Stabilität und die Abbauwege von der chemischen Zusammensetzung der SAM-bildenden Moleküle, insbesondere der SAM-Andockgruppe und der Rückgrat-spezifischen "schwache Bindungen" abhängig sind. PA- Monolagen weisen im Vergleich zu Thiol-SAMs auf Münzmetallsubstraten eine höhere Robustheit und bessere thermische Stabilität auf. Es ist jedoch ratsam, die thermische Stabilität eines speziell entwickelten funktionalen SAM im Kontext möglicher "schwache Bindungen" zu testen, sofern dies für die entsprechende Anwendung von Bedeutung ist.

TABLE OF CONTENTS

Page

1. Introduction

As part of the advent of organic and molecular electronics, design and optimization of the involved interfaces and functional molecular films become increasingly important. Self-assembled monolayers (SAMs) of tailored organic molecules are highly relevant in this context for precise adjustment of surface and interfacial properties, as well as for performing specific functions in electronic devices.[1] SAMs are defined as two-dimensional assembles of rod-like molecules, which are chemically anchored to a substrate. In particular, SAMs have been used as charge-carrier injection layers,[2–5] as templates for the directed growth of semiconductor layers,[6,7] and as ultrathin insulating layers.[8,9] For the smallest SAM-based electronic devices, so-called SAMFETs (self-assembled monolayer field-effect transistors), the molecules even contain parts fulfilling several different roles, e.g., carrying simultaneously a semi-conducting tail-group for the formation of the charge-transport channel and aliphatic part to act as gate insulator.[10–12]

The most attractive property of SAMs is the flexibility of their design, allowing a combination of different functional moieties within a SAM precursor, consisting usually of a suitable anchoring group providing bonding to the specific substrate, rod-like molecular backbone (spacer) mediating the self-assembly, and a terminal tail group redefining the identity of a particular substrate or an interface. The chemical, physical, and biological properties of surfaces and interfaces can thus be controlled and readjusted in a desired way by SAM assembly.[1,13–15]. One of these tasks is tuning of the work function of the substrate, described also as its electrostatic engineering.

Tuning of substrate work function is a crucial task in organic electronics and photovoltaics, particularly to adjust injection barriers and to improve energy-level alignments between the adjacent layers.[16,17] SAMs can be used for this purpose, viz. suitable dipolar SAMs, specifically adjusted to a particular substrate or an interface.[18–22] The adjustment is achieved by selecting a proper anchoring group, providing the bonding to the substrate in a predefined orientation.[23]An example would be thiolates in the case of gold, which is a popular electrode material especially for transistors. The backbones of the SAM constituents have then a nearly upright orientation, exposing their terminal groups to the SAM-ambient interface. The molecular alignment resulting from such an architecture leads to an upright orientation of polar functional groups incorporated into the molecules. Depending on the exact orientation of these polar groups, their density, and dipole moment, the work function of the resulting interface can be adjusted to specific requirements.

In most cases, polar moieties are introduced as terminal tail groups, changing simultaneously the electronic and chemical character of the SAM-ambient interface. Frequently used moieties are −F, −CF3, −CN, −NH2, −NO2, and −CH3 groups.[19,24–26] This strategy has, however, several potential drawbacks, such as strong influence of the nature of SAMs polar tail group on organic semiconductor (OSC) film growth on the SAMs-covered substrate and the risk of modification of the chemical structure of SAMs tail groups due to interaction with the deposited OSC.[3] Alternatively, a polar moiety can be incorporated into the molecular backbone, such that a layer with buried dipole moments is created.[27] This strategy allows work function engineering without changing the chemical

character of the SAM-substrate and SAM-ambient interfaces.[3,27–29] In this way, the electrostatic and chemical properties of a SAM can be decoupled.

Of particular interest in this context are SAMs with embedded pyrimidine group, which depending on the orientation of the dipoles are able to change the work functions of Au(111) and Ag(111) substrates over a range of ~1 and ~0.85 eV, respectively.[3,27,30,31] Examples of SAMs with embedded pyrimidine group, derived from biphenyl thiol molecule, are shown in Figure 1.1a and Figure 1.1b.[2,3] Petritz *et al* used these SAMs to minimize contact resistances in p-type and n-type organic thin film transistors and distinctly improved the performance of more complex electronic circuits on flexible substrates.[2,3] Work function tuning properties of pyrimidine groups can be improved by including more than one such unit into a single molecule, with the simplest structural unit being bipyrimidine.[32–36] . Additionally, SAMs can also affect the morphology of the OSC layer, reduce the leakage current and diminish the density of the charge-trapping states. Again, embedded dipole SAMs can then be particularly useful in this regard since they allow to tune the work function and morphology of the deposited layer independently, detangling the dipole engineering and chemistry at the SAM surface.
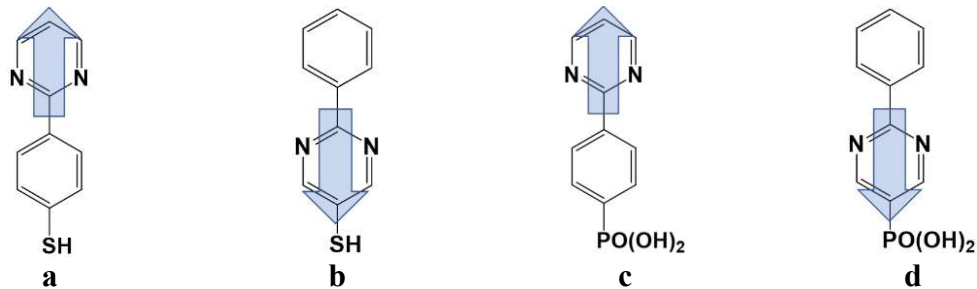
Figure 1.1: Structures of the (a) pyrimidine-phenyl-up-thiol, (b) and phenyl-pyrimidine-down-thiol, (c) pyrimidine-phenyl-up-phosphonic-acid, and (d) phenyl-pyrimidine-down-phosphonic-acid. The direction of dipole moments associated with the pyrimidine units and defined with respect to the substrate is indicated by an arrow and included into the compound name.

Based on the previous results regarding the pyrimidine-embedded SAMs on Au and Ag,[2,3,27,30,31,36–38] I started my PhD project by implementing the same concept to oxide substrates, using indium tin oxide (ITO) as representative example, which is described in subchapter 4.1.[39–49] Oxide substrates are widely used in organic electronics and organic photovoltaic devices, serving, e.g., as gate dielectrics in organic transistors as well as transparent electrodes and electron/hole transport layers in organic and perovskite solar cells and organic light-emitting devices (OLEDs).[47] These devices will strongly benefit from optimal energy-level alignment, as facilitated by suitable dipolar SAMs. Two different SAMs containing pyrimidine polar group and phosphonic acid anchoring group were used, as shown in Figure 1.1c and Figure 1.1d. The phosphonic acid anchoring group allows chemical bonding to an oxide substrate. Once SAMs were successfully assembled on ITO substrates, the samples were characterized by a variety of several complementary surface characterization techniques to study the structure and electrostatic properties of the monolayers.

A continuous adjustment of substrate work function can be achieved by using a mixture of two different polar molecules in a binary SAMs.[50–52] This strategy was implemented in this thesis by using 2 pairs of substituted/unsubstituted biphenyl thiol (BPT) SAMs, namely H-BPT combined with F-BPT (Figure 1.2a and Figure 1.2b),[53] and CH$_3$-BPT combined with CF$_3$-BPT (Figure 1.2c and Figure 1.2d).[54] Note that these SAMs only differ by the terminal atom or group, so that homogeneous mixed SAMs can be potentially formed.[23,51,55] This continuous electrostatic engineering opened an opportunity to correlate charge transport behavior of the SAM systems with their electrostatic properties, represented by the work function. Note that in the case of the single-component SAMs, halogen atom substitution has been shown to have profound influence on tunneling current density across molecular junctions,[56–59] with distinctly different result between the SAMs with aromatic and aliphatic backbone. For SAMs with aromatic backbone, F substitution of the terminal hydrogen atom causes a decrease of the tunneling rate by about an order of magnitude, similar to other halogen (F, Br, Cl, or I) .[57,58] In contrast, for SAM with aliphatic backbone, F substitution provides little difference in comparison to H-terminated SAMs, while other halogen substitution results in a progressive increase of the tunneling rate by up to three orders of magnitude and at the same time a progressive decrease of tunneling decay coefficient ß from 0.75 to 0.25 Å^{-1}.[56,60] The tunneling rate, thus, exhibits no correlation with the work function of the monolayers, varying progressively and strongly (for the work function) on going from I to F.[57] This behavior was tentatively explained by the strong confinement of the electrostatic field associated with the terminal atom and by the compensation of the Au–SAM bond dipole and the terminal group dipole in the molecular junction, affecting the energy-level alignment between the SAMs and the top electrode, provided by a tip of eutectic GaIn (EGaIn) alloy.[57] In this context, continuous variation of the work function by mixing the respective molecules in binary monolayers, following an established approach, could probably shed some light on the effect of the halogen substitution.[61,62]
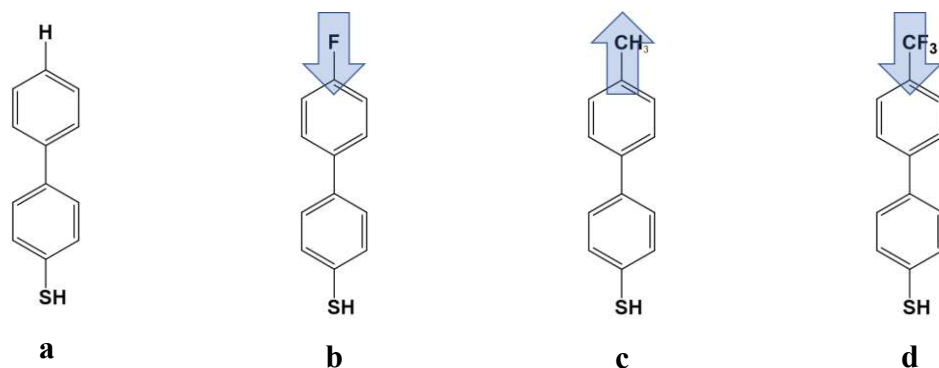
Figure 1.2: Structure and dipole moment (marked by the arrows) of the (a) H-BPT and (b) F-BPT, as well as (c) CH$_3$-BPT, and (d) CF$_3$-BPT.

The results for the binary H-BPT/F-BPT and CH3-BPT/CF3-BPT SAMs are presented in subchapters 4.2 and 4.3, underlining a strong effect of the terminal fluorine atom/atoms on the charge transport properties of the entire SAMs network. These results demonstrate the possibility to tune charge transport via single atom engineering. This idea was pursued further by exploring the charge transport properties of aromatic SAMs with ferrocene or

ruthenocene substitution, targeting specifically possible implementations of these systems as molecular diode.[63,64] Note that molecular diodes with rectification ratio (RR) varying from 10^1 to 10^5 have been successfully demonstrated using alkanethiolates SAM with 1 or 2 ferrocene substitution (Figure 1.3a).[65–81] Ruthenocene was also recently used for molecular diode with an RR of more than 1000.[82–84]

An aromatic SAM is more attractive for diode application, due to inherent higher conductivity in this type of backbone in comparison to alkane. However, recent molecular diode realizations using ferrocene-based SAMs with partially aromatic backbone (shown in Figure 1.3b) are rather discouraging, due to relatively low RR varying from 23-77.[70,85] In contrast, in my experiments, fully conjugated SAMs with ferrocene substitution (shown in Figure 1.3c) were found to exhibit consistent diode behavior with a maximal RR $\approx$ of $10^{3.3}$ at an extremely low voltage, close to zero. A very similar rectification behavior was also obtained for the SAMs with ruthenocene substitution. These novel molecular diodes are described in subchapter 4.4.
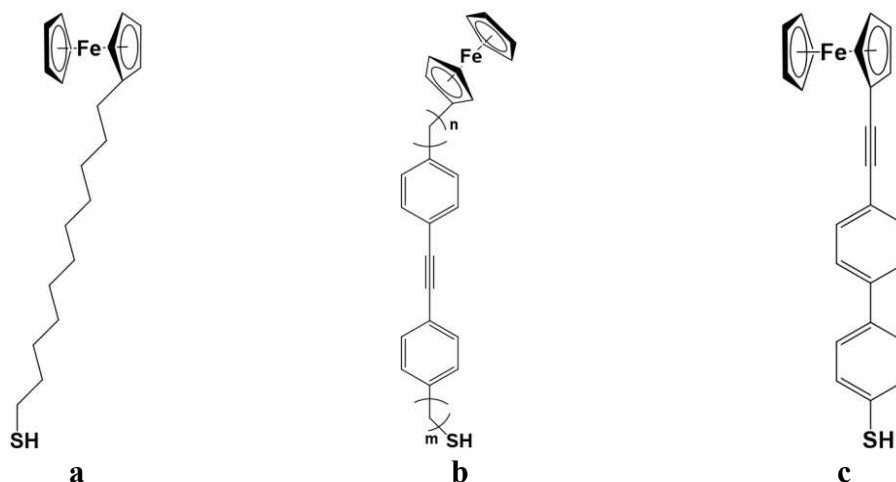
Figure 1.3: Molecular sructure of the SAMs with ferrocene substitution and (a) $(CH_2)_{11}$ alkane,[74,86–88] (b) C_n-DPA-C_m with n between 0 and 3 and m between 0 and 1,[70,85] or (c) biphebyl ethynyl backbone.[64]

The ability of SAMs to modify physical and chemical properties of surfaces and interfaces or even to redefine them completely are well known as mentioned above.[1,2,11,15,17–23,27,28,36,53,54,89–108] Apart from a specific function of a particular SAM, the knowledge of its thermal stability is important for practical purposes, for example if the preparation procedure for the SAM itself includes annealing at an elevated temperature, the assembly of a particular device requires a high temperature step, or a device could be heated during its exploitation. This issue is also important scientifically to provide insights into the energetics of the molecular films.[109] In this context, I studied two representative SAM systems with a moderate and strong bonding to the substrate, namely archetypical thiolate SAMs on Au(111) and phosphonic acid-bound SAMs on Al_2O_3, putting the emphasis on three essential questions. First, what are most important temperature-induced processes in the SAMs, defining their thermal stability? Second, what is the characteristic range of this stability, defined by maintenance of the primary identity and chemical homogeneity of the

SAMs? Third, to what extent the character and length of the molecular backbone affect the thermal stability?

As an experimental tool, high-resolution x-ray photoelectron spectroscopy was used to provide a non-local system-representative information, and allows to monitor and to understand temperature-induced processes in very detail. The results of the thermal stability experiments are presented in the subchapters 0 and 4.6, for the thiolate and phosphonic acid SAMs, respectively.

2. Basics and Background

2.1 Self-assembled Monolayers

Self-assembled monolayers are highly oriented arrangement of molecules on a substrate/surface, which form spontaneously, due to a favorable and specific interaction between substrate/surface and one end of the molecules.[110,111] SAMs formation has been achieved on a variety of substrate, for example gold,[36,53,54,98,99,102,112–118] silver,[112,115,119–121] copper,[122–124] indium tin oxide,[42,97,125–127] zinc oxide,[128–130] and diamond.[131–133] Gold is highly favored for SAM formation due to its inertness and it can be handled without exhaustive precautions.[134] Moreover most contaminants on gold surface are readily displaced during SAM formation.
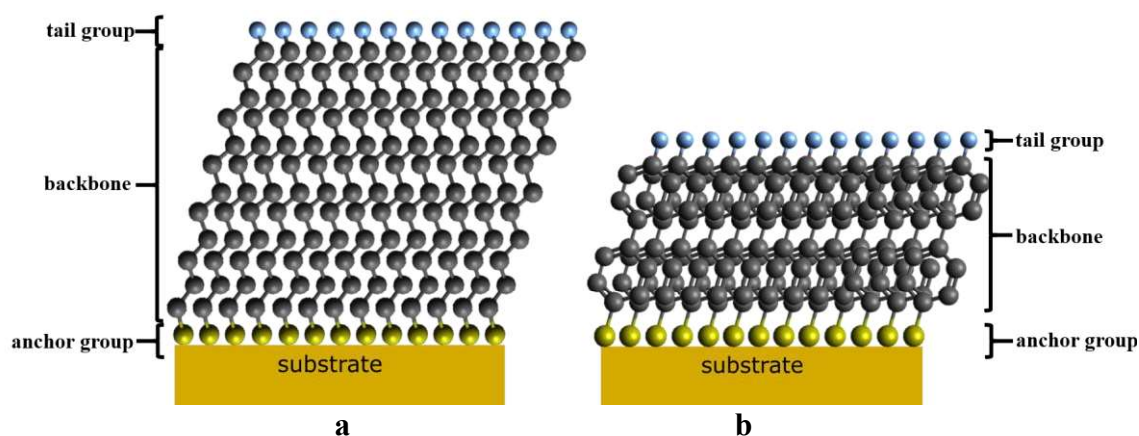
Figure 2.1: Illustration of SAM with (a)aliphatic and (b)aromatic backbone. SAM components are explained on the right side.

SAMs consist of three major parts: the anchor/head group, the backbone, and the tail group, as illustrated in Figure 2.1. SAMS anchor group is very crucial, since it binds chemically with substrate, and hence connects between substrate and SAM molecules. Thiol moiety is one of the most common example of SAMs anchor group, which generates chemical bonding with metal, like gold, silver, or copper.[135–137] SAM itself consists mostly of carbon atom, which construct SAM backbone. 2 major motives of SAM backbone are aliphatic and aromatic as illustrated in Figure 2.1a and b, respectively. The third part of SAM is tail group, which interacts with atmosphere, and therefore determines SAMs interfacial properties.[1,134,138]

SAM growth has been achieved using a variety of techniques, like from solution, gas phase, or Langmuir-Blodgettmethods.[111,134] In this thesis, only solution-based SAM growth method is used. In this method, typically freshly prepared substrates are immersed in suitable SAM precursor solutions in ethanol, tetrahydrofuran, or others. The selection of solvents depend on SAM solubility and substrate.[110] To achieve a high quality SAM

sample, normally fresh substrates are incubated in precursor solution for not less than 24 hours.
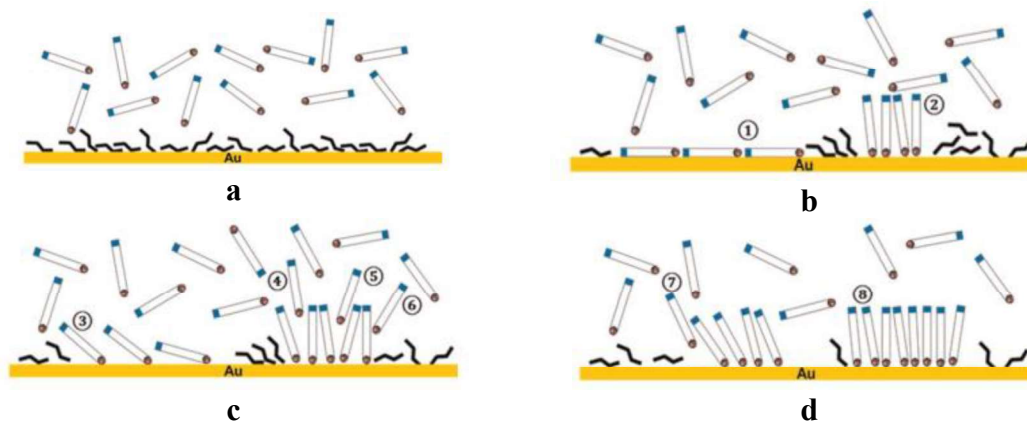
Figure 2.2: Illustration of SAM formation taken from ref [134]. (a)after gold immersion in solution, adsorbate molecules in solution approach substrate. Gold is already coated with solvent molecules. The solvent molecules surrounding adsorbate molecules are omitted for clarity. (b)adsorbate molecules displace solvent molecules to form either lying-down domains (1) or upright domains (2). (c)Additional adsorbate molecules are incorporated into the lying-down domains and initiate a transition to an upright domain (3). Alternatively, adsorbate molecules can impinge on the surface (4), within the boundaries (5), or at the boundaries (6) of upright domains and incorporate into the domains. (d)The upright domains formed from either the lying-down phase (7) or direct adsorption (8) continue to grow until maximum coverage attained.

After incubation, substrates are removed from solution and then washed intensively with ethanol or a combination of solvent to remove unbound thiol, and then immediately dried with nitrogen or argon gas. Afterward SAM can be immediately measured or stored in a sealed container with argon atmosphere.

2.2   X-Ray photoelectron spectroscopy (XPS)

XPS is a well-known technique to measure chemical composition and chemical state of a surface. This technique is based on detection of photoelectrons, which are the outcomes of an irradiation of sample of interest with X-ray photons.[139] This method is based on photoelectric phenomenon, which was found by Einstein and illustrated in Figure 2.3a. In case of interaction between atomic orbital electrons and X-ray photons, the following 3 possibilities might occur:[140]

1. Photons propagate through atom without significant interaction with nucleus and orbital electron
2. Photons are scattered by atomic orbital electron and lose a portion of its energy.
3. Photons interact with orbital electrons and exchange energy

a   **b**
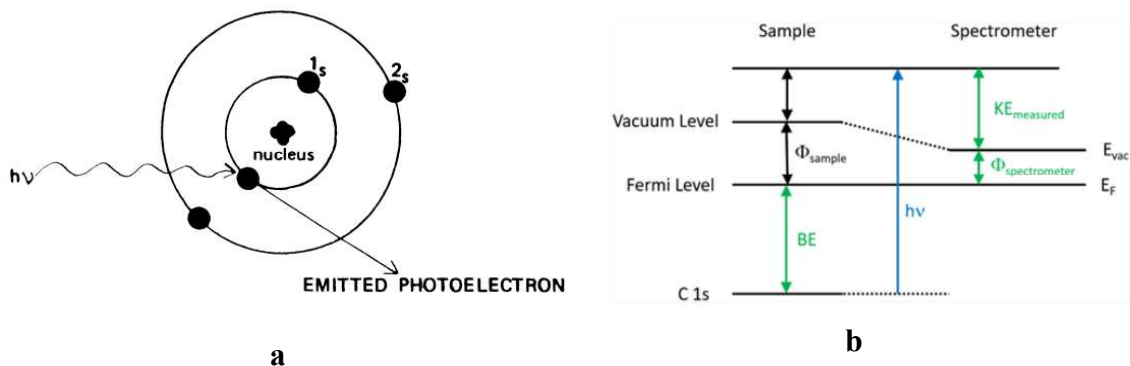
Figure 2.3: (a) Interaction between an 1s orbital electron with binding energy EB and X-ray photon with energy *hv*, taken from ref [140]. Due to this interaction, the electron is photoemitted with kinetic energy $\mathbf{EK = hv - BE}$. (b)Energy level diagram of basic XPS, taken from ref [141]. The diagram also includes X-ray photon energy (*hv*), electron binding energy (BE), kinetic energy of measured photoelectron ($KE_{measured}$), and work function of both sample(Φ_{sample}), and spectrometer($\Phi_{spectrometer}$).

The third possibility is the basic process of XPS. In case energy of X-ray photon *hv* is larger than atomic orbital binding energy *EB*, photoelectron is ejected with kinetic energy K*E*:

$$KE \cong hv - BE \qquad\qquad 2.1$$

h is Planck's constant and *v* is X-ray frequency. In an XPS measurement, photoelectron energy is measured by referring to sample Fermi energy.[141] Taking work function of spectrometer $\Phi_{spectrometer}$ into account, as illustrated in Figure 2.3b, electron binding energy can be found with the following formula:

$$BE \cong hv - KE - \Phi_{spectrometer} \qquad\qquad 2.2$$

Because photoemission process is extremely rapid (10^{-16}-10^{-14} seconds), core level electrons are assumed frozen during the process and no relaxation occurs in the sample after X-ray photon absorption. For that reason, XPS measurement is a good representation of sample in initial states before X-ray bombardment.[140]

Many chemical information of a sample can be obtained by measuring emitted photoelectron in an XPS measurement. Despite X-ray photon typically has penetration depth a few μm, most of generated photoelectrons experience many inelastic collision and lose energy before escaping from the sample to the detector.[141] Intensity of photoelectrons, which escape from a sample, is governed by the Beer's law as the following:

$$I = I_0 exp(-d\lambda) \qquad\qquad 2.3$$

The term λ is attenuation length of a photoelectron, which depends of its energy and propagation medium. \an Attenuation length describes the length scale, which photoelectrons can travel, before experiencing elastic and inelastic scattering.[141] Despite attenuation length of photoelectron depends on its kinetic energy, which vary for elements,

10 nm is typical sampling depth of XPS, since at this depth 95% of photoelectron can escape samples.[141]

Essential components for an XPS measurement are illustrated in Figure 2.4. An X-ray source needs to produce high intensity of photons with sufficient energy and narrow line width.[142] Mg Kα and Al Kα are the most commonly used X-ray sources. To separate photoelectrons according to their energies and convert them into spectrum, an energy analyzer is very important. This part determines XPS measurement sensitivity and resolution.[142] However, the current, which reach the end of analyzer, tends to be in the range 10^{-16}-10^{-14} A, which is too low to be measured with conventional techniques.[142] For this reason, electron multiplier is used before spectrum is sent to computer interface.

The counts of measured photoelectron per second (intensity) for each pixel (kinetic energy/binding energy) is plotted with respect to binding energy (BE), as shown in Figure 2.5 for the case of C16 thiol SAM on top of Au substrate. All chemical components of SAM are visible in the spectra, including carbon and thiol/sulfur. Please note, that peaks due to thiol photoelectrons are typically too weak to be visible at a wide electron binding energy range, as in Figure 2.5. However, by using a higher resolution scan photoelectron signal of thiol can be detected, as shown in Figure 2.6. For reference, XPS peak due to substrate is used. For example, in Figure 2.5 it will be gold peaks, which the most intense one is found at 84 eV for Au $4f_{7/2}$ orbital.
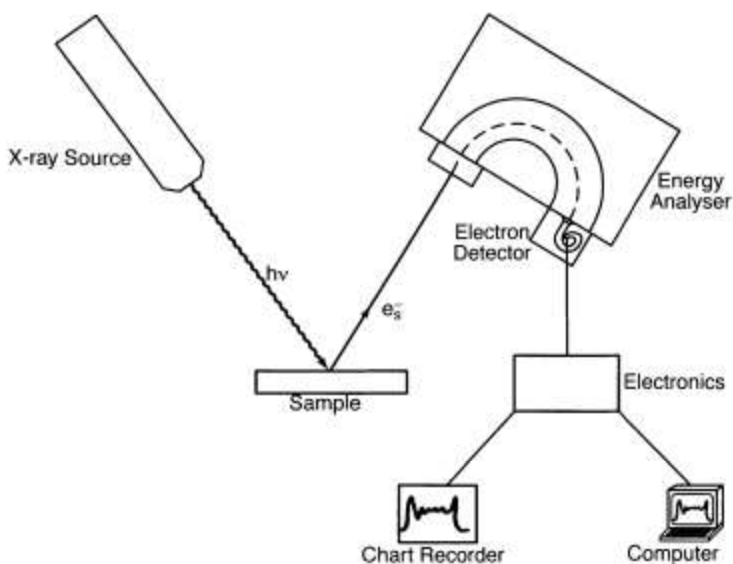
Figure 2.4: Illustration of XPS setup.[142] The incidence of X-ray photons *hv* on sample produces photoelectron emission e_s^-, which is directed by energy analyzer into electron detector to be measured. He data is delivered to chart recorder and computer through electronics.

Binding energy of core level electron is highly sensitive to chemical environment variation, oxidation state, lattice site, or others.[141–143] An example of chemical shift, detected by XPS, is shown in Figure 2.6 for C16 SAM on Au substrate. A pristine C16/Au sample appears to be bonded chemically with Au substrate, since only S2p doublet at 162 .0 eV is shown in Figure 2.6. Due to electron irradiation, this bonding transforms into physisadsorbed

thiol, since S2p doublet centered at 163.5 eV is observed. Additionally, the intensity of S2p doublet at 162.0 eV decreases after electron irradiation.[113]

XPS is also very reliable to determine atomic concentration, film thickness, and relative concentration of molecules on a surface with precision between 1 and 15%.[141] Due to attenuation length of photoelectron, XPS is only suitable to characterize the surface of a sample and it is usually assumed, that the sample is homogenous over depth and area.[141] A quantitative analysis of XPS data is usually done by first calculating XPS peaks area through fitting and background subtraction. For a subtraction of background signal, typically linear, Touggard, or Shirley background are used.[114,139,141,143–145] The shape of peaks is calculated using mixed Gaussian-Lorentzian or Voigt function.[146] After the area of XPS peaks is calculated, atomic concentration can be calculated with the following formula:[139,141,142,144]

$$C_x = \frac{\left(I_x / S_x \right)}{\sum I_i / S_i} \qquad 2.4$$

In equation 2.4, C is atomic concentration of element, I is area of an XPS peak, and S is sensitivity factor. A sensitivity factor determines the brightness of photoelectron emission of an element. Sensitivity factor also varies slightly for different XPS vendor. This parameter does not vary with different chemical environment. It is only necessary to consider sensitivity factor in comparing different concentration of different atomic species, for example C and O atoms.[141]
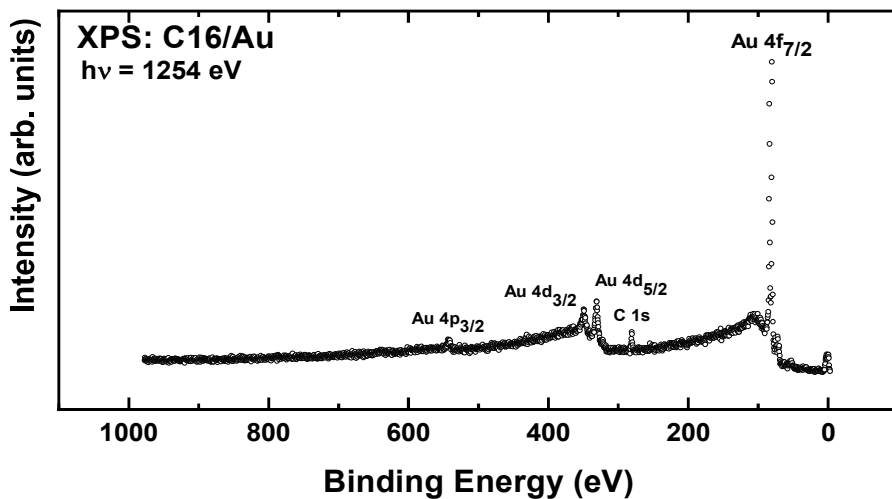
Figure 2.5: Wide scan spectrum of C16 thiol SAM on Au(111), recorded with the MAX200 XPS-setup using MgKα X-ray source. The corresponding core levels electron are depicted in the figure. All Au peaks come from the substrate, while the C 1s peak come from SAM.

XPS is commonly used to determine the thickness of an overlayer "A" d_A on top of substrate "B" using the following formula:[141,142,144,147–149]

$$I_A = I_A^{\infty}\left(1 - exp\left(-\frac{d_A}{\lambda_A(E_A)\cos\alpha}\right)\right)$$

2.5

$$I_B = I_B^{\infty}\left(exp\left(-\frac{d_A}{\lambda_A(E_B)\cos\alpha}\right)\right)$$

2.6

In equation 2.5 and 2.6, I_A and I_B are the XPS peak intensities from the overlayer A and substrate B, respectively, and I_A^{∞} and I_B^{∞} are the intensities from uncovered A and pure B. The term $\lambda_A(E_A)$ is the attenuation length of electrons traveling through A originating from overlayer A, while $\lambda_A(E_B)$ is the attenuation length of electrons traveling through A originating from substrate B. The term α is the angle of photoelectron emission in measurements with respect to normal. These calculations require measurements from pure A or B.[141] A determination of overlayer A thickness can also be done using reference sample with known thickness, for example C16 SAM on Au. The equation 2.5 and 2.6 can be rearranged as the following, in which then d_A can be calculated from a comparison of XPS peak intensities I_A/I_B:[150]

$$\frac{I_A}{I_B} = k\frac{1 - exp\left(-\frac{d_A}{\lambda_A(E_A)\cos\alpha}\right)}{exp\left(-\frac{d_A}{\lambda_A(E_B)\cos\alpha}\right)}$$

2.7
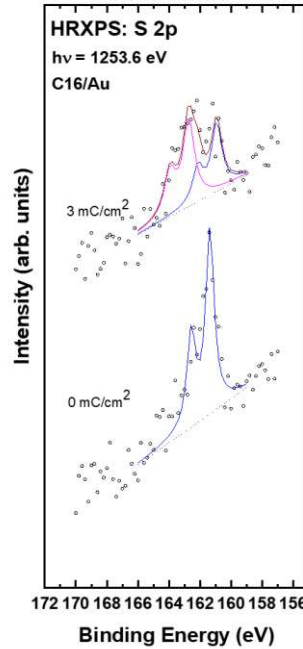
Figure 2.6: XPS spectrum of S2p orbital of C16 SAM on Au before and after electron irradiation with dose 3 mC/cm^2.

Another useful quantity, which is usually calculated from an XPS measurement, is stoichiometric composition between 2 elements, for example element C and D. Provided the attenuation length of electrons λ and cross section σ for both elements are known, the stoichiometric composition can also be found using the following formula:[151–153]

$$\frac{N_A}{N_B} = \frac{I_A}{I_B} \frac{\lambda_B}{\lambda_A} \frac{\sigma_A}{\sigma_B} \qquad\qquad 2.8$$

2.3 Ultraviolet photoelectron spectroscopy (UPS)

In XPS spectrum, spectra at binding energy lower than 30 eV, or called valence region, gives information of HOMO (Highest Occupied Molecular Orbital) energy level. Analysis of HOMO level can reveal many information regarding surface states, surface dipole, and vacuum level shift across surface/interface. While this regime is important, it is difficult to observe in XPS, due to relatively poorer photoelectric cross-section at these levels in comparison to core orbitals.[140,144,154–157] To allow a reliable observation of valence shell photoelectron, an ultraviolet source, commonly a He-1 source with energy 21.2 eV or He-2 with energy 40.8 eV, is used to allow ultraviolet photoelectron spectroscopy (UPS) measurement.[141,157,158] Due to its low energy and small line width, only valence electron shells are ionized in experiment and a high resolution measurement (< 0.1 eV) can be performed.[155] On the other hand, only the top 2-3 nm of sample is characterized by UPS, which makes the technique is even more sensitive to sample contamination.[141]
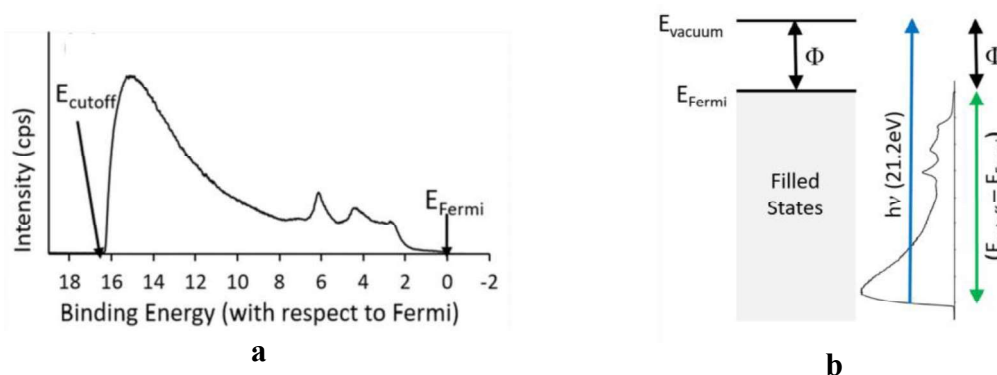
Figure 2.7: The figures are taken from ref [141]. (a) UPS spectrum of Au with the Fermi energy (E_{Fermi}) and the secondary electron cutoff (E_{cutoff}) indicated in the figure. (b) Illustration how UPS spectrum relates with density of filled states and work function (Φ).

An example of UPS spectrum is shown in Figure 2.7a for bare Au substrate. As illustrated in Figure 2.7b, UPS essentially shows electronic states below Fermi level(E_{Fermi} in Figure 2.7), including the highest occupied molecular orbital (HOMO).[141] At a certain regime (around 16 eV in Figure 2.7a), UPS intensity decreases significantly. This regime is called secondary electron cutoff (E_{cutoff}). Photoelectron energy at this regime has low kinetic energy, which corresponds to high binding energy in the spectra (around 16 eV in Figure 2.7a), and difficult to be measured by analyzer due to inelastic interactions. For this reason

in UPS experiment, samples are normally put under bias.[159,160] As illustrated in Figure 2.7b, a relation between E_{Fermi}, E_{cutoff}, and ultraviolet source excitation energy can be used to calculate sample work function (Φ) with the following formula:[141,160]

$$\Phi = hv - (E_{cutoff} - E_{Fermi}) \qquad 2.9$$

2.4 Synchrotron-based techniques

For XPS and UPS experiment, as an alternative to Mg, Al, or ultraviolet source, synchrotron radiation is a very popular option due to its high intensity, well defined polarisation, broad tunability from infrared to hard X-rays, and consequently higher photoemission cross section.[155,161] Experiments involving synchrotron radiation are performed in particle beam accelerator or synchrotron facility, such as Electron Storage Ring BESSY II in Berlin. Synchrotron radiation is produced by moving high energy charged particles (usually electrons or positrons with kinetic energy ~2-8 GeV) at a curved path, which can be achieved using strong magnetic fields, as illustrated in Figure 2.8.[159] The quality of produced radiation is defined by brilliance quantity. Brilliance is defined as the number of photons, which is emitted in one second from a source area of 1 mm^2 into a cone defined by 1 mrad^2, normalized to a spectral band width of 0.1%.[159] The advantages of synchrotron radiation in comparison to X-ray anode are generally in term of energy tunability and brilliance, despite each synchrotron facility offers different characteristic of radiation.[159]
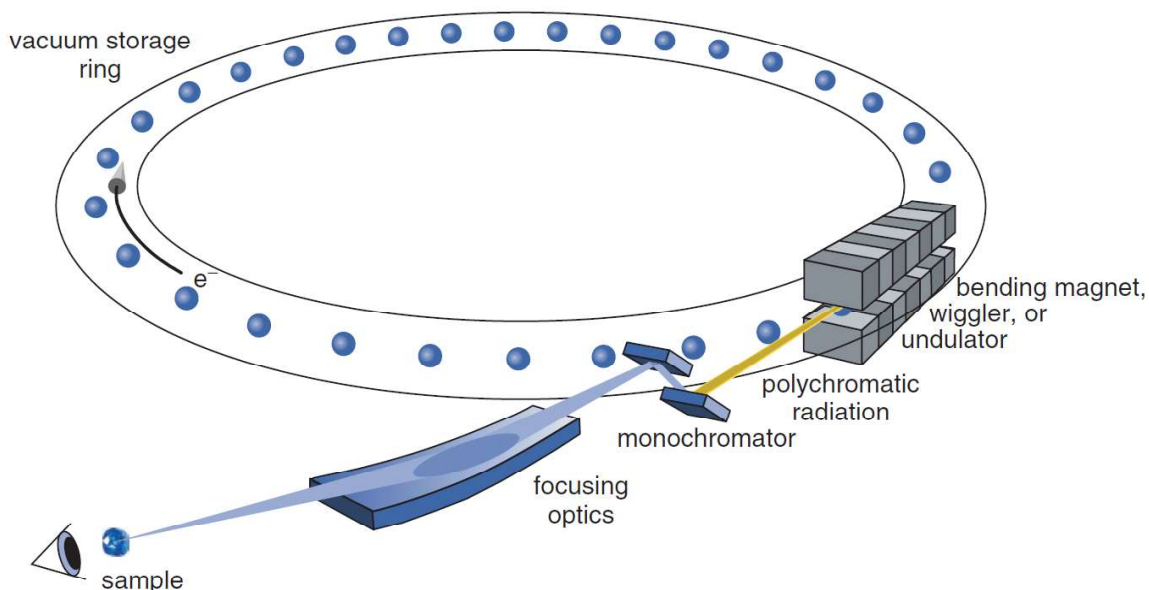

Figure 2.8: Schematic picture of radiation generation in a synchrotron, taken from *ref* [162].

By using synchrotron radiation, X-ray photoelectron spectra can be collected with higher resolution. Additionally, experiments, which require a continuous variation of excitation

energy, such as near-edge X-ray absorption fine structure (NEXAFS), can only be accomplished.[155,159,161] These methods are described in the following subchapters.

2.4.1 High resolution x-ray photoelectron spectroscopy

As previously described, synchrotron radiation offers several advantages over Mg or Al radiation in term of intensity and energy tunability. This difference is demonstrated in Figure 2.9 for measurement of S 2p XPS of C12 SAM on Au substrate. The distance between both Sulphur peaks and the intensity comparison match with the theory. However, the peaks are better distinguished in synchrotron measurement (Figure 2.9c) than lab measurement (Figure 2.9b). Aside from X-ray intensity difference between laboratory and synchrotron, S 2p photoelectron is generated at higher intensity using X-ray energy 350 eV than 1254 eV, because x-ray cross section at this energy is higher, hence allowing a measurement with better resolution. In general, high resolution XPS (HRXPS) setup in a synchrotron offers more ability to distinguish different chemical species, in comparison to laboratory XPS.
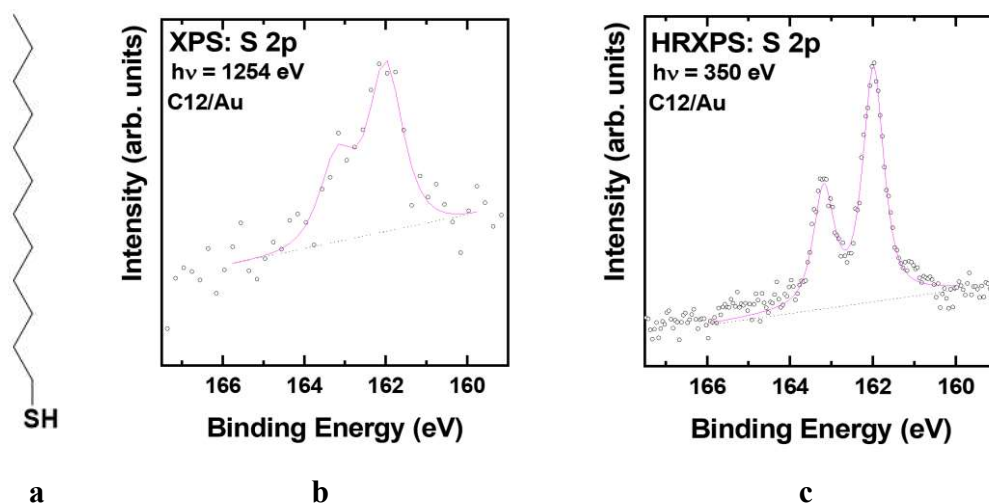
Figure 2.9: (a) Illustration of C12 SAM with thiol termination (b)S 2p XP spectra of C12 SAM on Au substrate, taken from laboratory XPS setup using Mg Kα source with energy 1254 eV (c) XP spectra of the same sample with Figure 2.9b, taken from XPS setup in Bessy using synchrotron X-ray with energy 350 eV.

2.4.2 Near edge x-ray absorption fine structure spectroscopy

Aside from photoelectron emission, absorption of X-ray photon can also be used for surface characterisation. This technique is often called near-edge X-ray absorption fine structure (NEXAFS) spectroscopy, or X-ray absorption near edge structure (XANES). Absorption of soft X-rays excites core electrons into the vacuum level or an unoccupied

molecular orbital, if this orbital is lower or at vacuum level.[163–165] The excitation only occurs, if X-ray photons have suitable energy and the transition is electric dipole allowed. A NEXAFS spectrum reflects the dependence of the photoabsorption cross section on the photon energy for values from just below the core level ionization threshold up to around 50 eV.[166] For a simplified case of an electron at core level and the absence of any other unoccupied states, absorption of photon only occurs for photon energy above the photoionization threshold, which will excite core electrons into continuum final states.[166] Based on this argument, NEXAFS spectrum for an electron at core level should follow a step function at photon energy equals to ionization potential, as shown by dashed line in Figure 2.10.
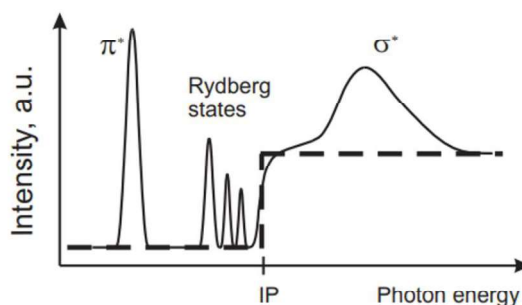
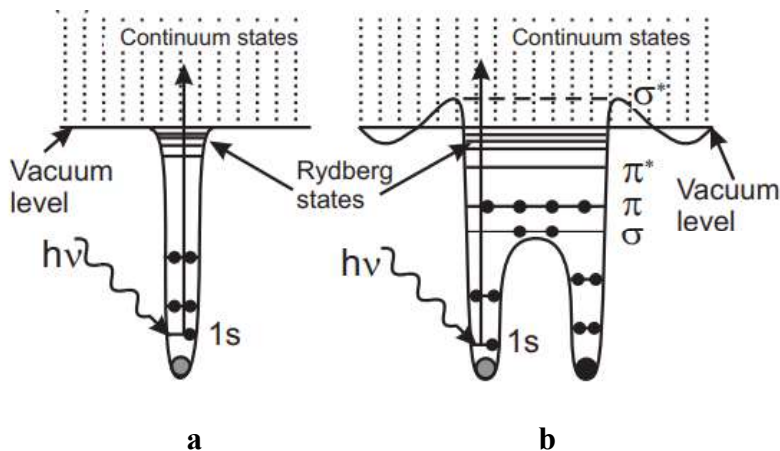**Figure 2.10:** The dashed line represents a dependence of photon absorption cross section with photon energy for the case of an electron at core level (single bound state) without any other empty electronic states. The solid line represents measured NEXAFS spectra.[166]

Figure 2.11: Schematic potential for (a) isolated atom, and (b) diatomic molecular system which show Rydberg, continuum states, and unfilled molecular orbitals, which can be found in NEXAFS spectra.[166]

However, the measured NEXAFS spectra, even for a case of single atom system, is more complicated, as shown by solid line in Figure 2.10. Due to the electrostatic potential of atom, originating from its nucleus, electronic states are found below (bound states) and above photoionization threshold (unbound states).[166] The bound states can be roughly

15

divided into valence state (π* or lowest unoccupied molecular orbital LUMO) localized in the proximity of the core and Rydberg states with binding energies, converging to the ionization threshold. The energy level illustration of single electron case is illustrated more clearly in Figure 2.11a.

For the case of diatomic molecule present molecular orbitals are shown in Figure 2.11b. Around the ionization threshold, step-like absorption edges are shown, in contrast to the single electron case in Figure 2.11s. Empty molecular orbitals are labelled as σ* and π* orbital.[166] For neutral molecules, σ*-orbitals are typically found above the vacuum level.

X-ray absorption is commonly measured indirectly as a decay of excited states.[163] Due to photoabsorption process, a photoelectron and a core hole are created. A hole is subsequently filled by another electron, which the corresponding energy excess is dissipated either radiatively by the emission of a fluorescent photon, or non-radiatively by the emission of an Auger electron. These processes, which are illustrated in Figure 2.12, can be used to determine the absorption cross section.[166] For low-Z elements (C, N, O) Auger electron yield is much higher than fluorescence yield (FY), hence an electron yield channel is better suited for low-Z molecules.[166,167] Moreover, electron detection provides a higher surface sensitivity and is preferred by the majority of published studies.[166] The reason for a higher surface sensitivity is the relatively low kinetic energy of the electrons and the corresponding mean free path in solid matter, which is typically less than 1 nm for energies between 250 eV and 600 eV. This sensitivity is be further enhanced by applying a retarding voltage to suppress lower kinetic energy electrons. Thereby, only those electrons that emerge from the outermost surface region (3 nm) are detected. For the investigation of adsorbates on surfaces, this so-called partial electron yield (PEY) detection has a better signal-to-background ratio than total electron yield (TEY) detection, where all electrons that emerge from the surface are detected.[168,169]
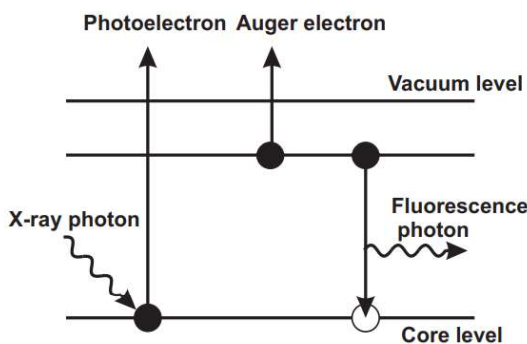
Figure 2.12: The process following X-ray absorption, including photoelectron emission, Auger electron emission, and fluorecescence.[166]

The measured width of a resonance is determined by the resolution of the instrument, the lifetime of the excited state, and the vibrational motion of the molecule.[166] A broadening due to the lifetime of a π*-resonance is generally very small, on the order of a about 100 meV for a transition between C1s and π* orbital in benzene. The final state lifetime is determined by the re-filling, or the decay of the core-hole pair, either by the excited electron falling back or by an Auger-transition. Transitions into unoccupied orbitals of σ-symmetry are considerably broader, indicating strongly reduced lifetimes for such cases. The reason

for this is a large overlap of these states with continuum states, which strongly decrease the lifetime of these states.

In comparison to XPS, NEXAFS is more sensitive toward chemical nature of intramolecular bond. The absorption spectra of organic molecule are strongly influenced by the local chemical environment and bonding structure. As an example, the difference in binding energy between carbon atoms in fully saturated hydrocarbon and aromatic compounds is only around 0.1 eV, as measured by XPS, which is often below the resolution of available electron energy analyzer.[166] In contrast, NEXAFS is also sensitive to the position of the excited state, allowing energy difference several eVs. This chemical specificity of NEXAFS is also shown in Figure 2.13 for 5 different polymers.[164]

Another advantage of NEXAFS is its ability to determine the orientation of a molecule relative to the substrate surface. Bonds and the corresponding molecular orbitals are highly directional, and therefore the transition intensities between core level and unoccupied molecular orbitals depend on the orientation of the electric field vector of incoming photon relative to the orientation of the molecule. Taking advantage of the polarization characteristics of synchrotron radiation, the orientation of a molecular orbital can be found by determining the intensity of the corresponding resonance as a function of the incidence angle of the photons, θ. The quantum mechanical description of the excitation process for a single electron in the dipole approximation leads to equation 2.10 relating the initial state Ψ_i and the final state Ψ_f to the photoabsorption cross section σ_x.[166]

$$\sigma_x \propto |< \psi_f |e \cdot p| \psi_i >|^2 \rho_f(E) \qquad 2.10$$

with e being the unit electric field vector, p the dipole transition operator, and $\rho_f(E)$ the density of final states. In the case of linearly polarized light, the expression $< \psi_f |e. p| \psi_i >$ can be simplified into $< \psi_f |p| \psi_i >$, which is known as transition dipole moment (TDM).[166] . In the case of K-edge NEXAFS, the initial state 1s-level is uniform in all directions, hence transition intensities only depend on an overlap between the photon polarization and the final state orbital.[165,170,171] The matrix element $< \psi_f |e. p| \psi_i >^2$ only depends on an overlap between the photon polarization and the final state orbital. The transition intensity becomes

$$I \propto |e < \psi_f |p| \psi_i >|^2 \propto |e \cdot O|^2 \propto cos^2 \delta \qquad 2.11$$

with δ being the angle between the electric field vector **E** and the TDM direction. From the equation 2.11, it can be understood that the intensity of a resonance is the largest when the electric field vector E lies along the direction of the final state orbital O (or the TDM direction), as illustrated in Figure 2.14. Please note that $\sigma*$-orbitals have a maximum orbital amplitude along the bond axis while $\pi*$-orbitals have maximum amplitude normal to the bond direction.[166]

In general, the TDM direction can be described through a polar angle α and an azimuthal angle φ. It means for the determination of the molecule orientation it is necessary to measure at least two series of NEXAFS spectra at two different azimuthal sample orientations. Fortunately, the azimuthal dependence is eliminated in many cases by the symmetry of the surface. The surface symmetry established several equivalent in-plane chemisorption geometries which lead to the formation of adsorbate domains.[166] Thus for

molecules adsorbed on a surface with an at least three-fold symmetry, there is an averaging over the azimuthal angle φ and the NEXAFS resonance intensities can be expressed as:

$$I \propto P\cos^2\theta \left(\cos^2\alpha + \frac{1}{2P}\tan^2\vartheta \sin^2\alpha\right) \qquad 2.12$$

where P denotes the degree of polarization of the incident X-ray light.

From the equation 2.12, it can be seen, that at the incidence angle $\theta = \tan^{-1}\sqrt{2P}$, absorption intensity does not depend on molecule orientation. Assuming that P ≈ 1, this angle θ is about 55∘ and it is known as "magic angle".[166] The absorption intensity measured at this angle is independent on molecular orientation and very useful for data analysis.

Another useful consequence of equation 2.12 is a presentation of the difference of intensities measured at normal (90˚) and gracing (20˚) incidence. Taking in to account that cos 90∘ = 0 and cos 20∘ ≈ 1, he following equation is obtained:

$$I(90^o) - I(20^o) \sim \left(\frac{3}{2}\sin^2(\alpha) - 1\right) \qquad 2.13$$

α is the angle between the electric field vector E and the TDM direction averaged over azimuthal angles φ. This difference spectra is known also as a linear dichroism and is negative for small α and positive at α ≥ 55º.[166] According to Figure 2.14, if molecule have double/triple bonds in its molecular plane, a negative dichroic signal of π∗ -resonances corresponded to a flat orientation of the molecule and positive one to upright-oriented molecules. Since σ∗ - and π∗ -orbitals are normal to each other, the dichroic signal of σ∗ - resonances has the opposite sign than for π∗ -resonances.
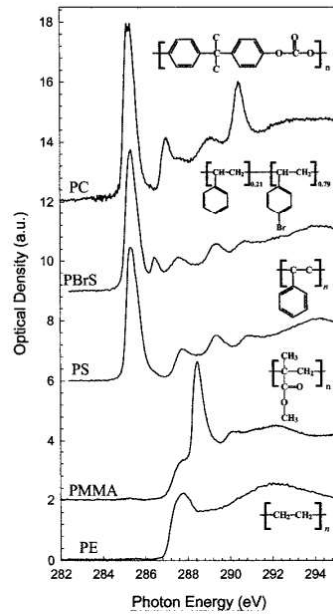
Figure 2.13: Carbon C K-edge NEXAFS spectra of several different polymers.[164]

18

Figure 2.14: Illustration of angle dependence of NEXAFS resonances for a π-bonded diatomic molecule adsorbed with its molecular axis normal to the surface. NEXAFS resonance increases with overlapping between electric filed vector of incoming X-ray excitation $\vec{E}$ with the direction of the final state orbitals $\vec{O}$. (a) The σ -resonance is maximized at grazing incidence, while (b) The π-resonance is maximized at normal incidence.[166]

It is important to note, that NEXAFS techniques probe all molecules, even those misoriented or disordered molecules that may exist at grain boundaries or at interfaces.[163] Unlike XPS, NEXAFS is not suitable for quantitative analysis, such as a direct determination of the sample stoichiometry or the relative ratio of σ- and π-bonded C atoms.[166] For that reason a combination of XPS and NEXAFS is recommended. Please note that in NEXAFS experiment, final states of molecules are neutral in excited state. Which in contrast to positive ion in XPS experiment.[165] As the consequence, binding energy of core level electrons, as measured in XPS, cannot be directly compared with photon energy of absorption peaks, as measured in NEXAFS.

2.5 Kelvin probe

Work function Φ is defined as the amount of required energy to move an electron from metal to vacuum level.[172] Work function measurement is very useful to study adsorption of molecules or to provide evidence for nanoscopic structural and chemical state on a surface.[173] The measurement is achieved by using reference electrode with known work function, or so called Kelvin probe, normally in ultra-high vacuum condition.

The schematic of Kelvin probe setup is shown in Figure 2.15. A probe (material 1) and a sample (material 2) form a parallel plate capacitor, which the distance between sample and probe is much lower than lateral dimension of capacitor plates. When both materials are in electrical contact, due to a difference in work functions, electrons will flow from material with a lower work function to the one with higher work function to establish equilibrium and Fermi alignment. This will create a bias across capacitor, referred as contact potential difference (CPD), and electric field across the system. This electric field is easily detected.[173] By applying external bias Vc until the electric field is compensated, CPD can be measured. Since the work function of reference electrode is known, the work function of sample of interest is also known.

A more recent improvement in Kelvin probe technique utilizes periodically vibrating reference electrode. Due to vibration, the distance between probe and sample and

capacitance of the system change. This variation is capacitance induces alternating current, which is formulated as the following:[172,173]

$$i(t) = CPT\omega\Delta C \cos \omega t \qquad 2.14$$

where ω is frequency of vibration and ΔC is the change in capacitance. This alternating current is easily detected. By scanning external bias Vc to nullify both electric field and alternating current, work function difference between sample and reference electrode can be found.
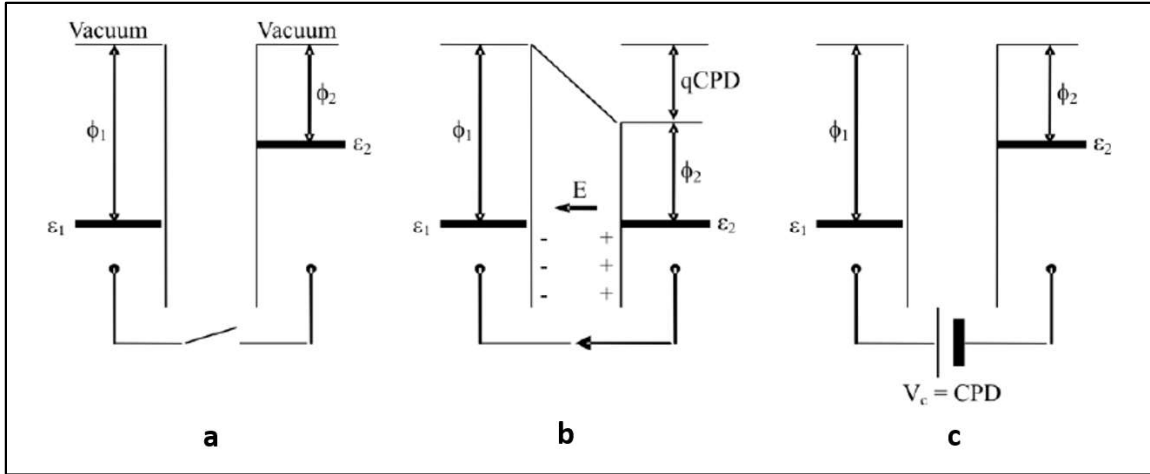
Figure 2.15: Schematic diagram of Kelvin probe physics taken from ref [173]. (a) 2 different materials 1 and 2 with each work functions ϕ1 and ϕ2, respectively, are present. (b) When material 1 is in contact with material 2, electrons flow from material 2 into 1, which aligns energy level between both materials, resulting in contact potential difference CPD. Due to the charges present in both materials, electric field E and electron charge q appear in the system. (c) Electric field is removed by applying external bias V_c, which equals to CPD.

2.6 Measurement of charge transport through SAM

Charge tunneling through SAM is usually described using Simmons model:[174]

$$J = J_o e^{-\beta d} \qquad 2.15$$

In equation 2.15, J is current density, d is molecular length, J_0 is bias-dependent pre-exponential factor, which depends on interface between SAM and Ga_2O_3/EGaIn electrode, and β is tunneling decay constant.[175] Simmons model does not consider SAM thickness variation and SAM defects, which are often found in experiments.
Reus *et al* classify defects in a SAM/Ga_2O_3/EGaIn junction into 2 classes: [175]
   1) Defects that maintain the basic of intended substrate/SAM/Ga_2O_3/EGaIn junction, while changing d, and hence can be described by equation 2.15. This type of defects

includes domain boundary, pinholes, disordered region, and physisadsorbed contaminants

2) Defects that invalidate the structure of junction. This includes a direct contact between Ga_2O_3/EGaIn and substrate and regions of EGaIn without Ga_2O.

Charge transport in the second class of defects can strongly deviate from tunneling, which is assumed in equation 2.15, and hence will give noninformative data. A reliable analysis of charge transport data, particularly using EGaIn technique, but also in other methods, needs to take the second type of defects into consideration. There are 2 different approaches, which can be used:[175]

1) To use statistical model to distinguish between informative and noninformative data

2) To assume informative data, predominate over noninformative data and use statistical analysis that is weakly influenced by a small number of extreme values.
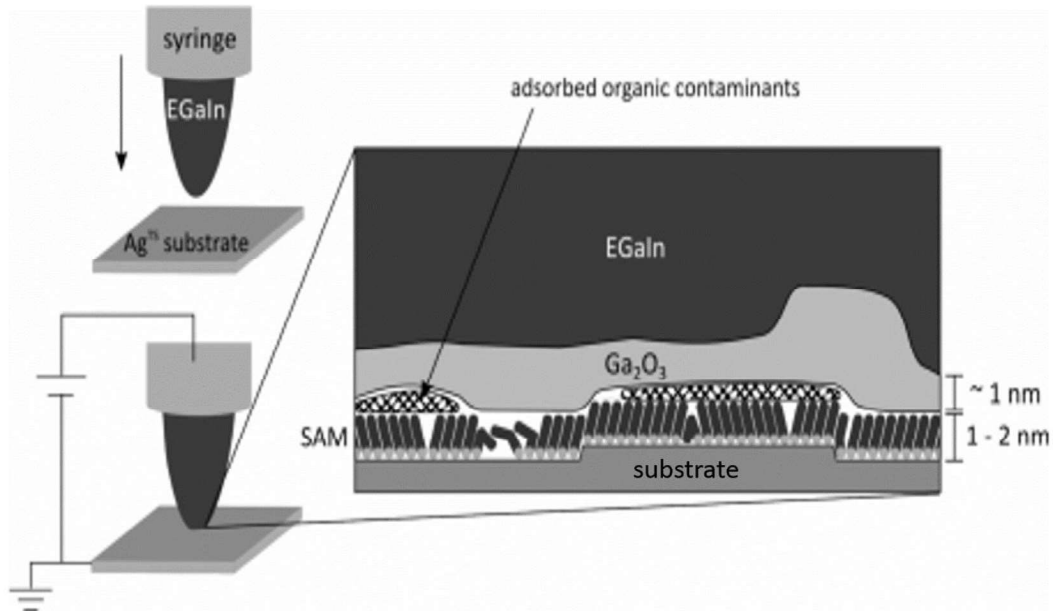
Figure 2.16: Schematic of substrate/SAM/Ga_2O_3/EGaIn junction, modified from ref [175]. A junction is formed by lowering a Ga_2O_3/EGaIn tip into contact with SAM sample. Substrate is grounded. The junction can contain defects, such as contaminants, substrate nonuniformity, Ga_2O_3/EGaIn nonuniformity, or defects in molecules. These defects can cause variation in junction thickness.

A statistical model was developed from equation 2.15 by assuming constant ß and J_0, and normally distributed d in an informative junction. Because of these assumptions, according to equation 2.15 J should follow log-normal distribution. This statistical distribution can be used to distinguish informative and noninformative data from a measurement, as shown in Figure 2.17a. While the majority of histogram in Figure 2.17a can be fitted with normal distribution equation, some deviations can be noted, which is considered noninformative and excluded from analysis. This approach is referred as Gaussian method or Gaussian

mean in this thesis.[175]. From Gaussian method, Gaussian mean (μ_G) and standard deviation (σ_G) are calculated to determine location and dispersion of log(J), respectively.[176]

a   b
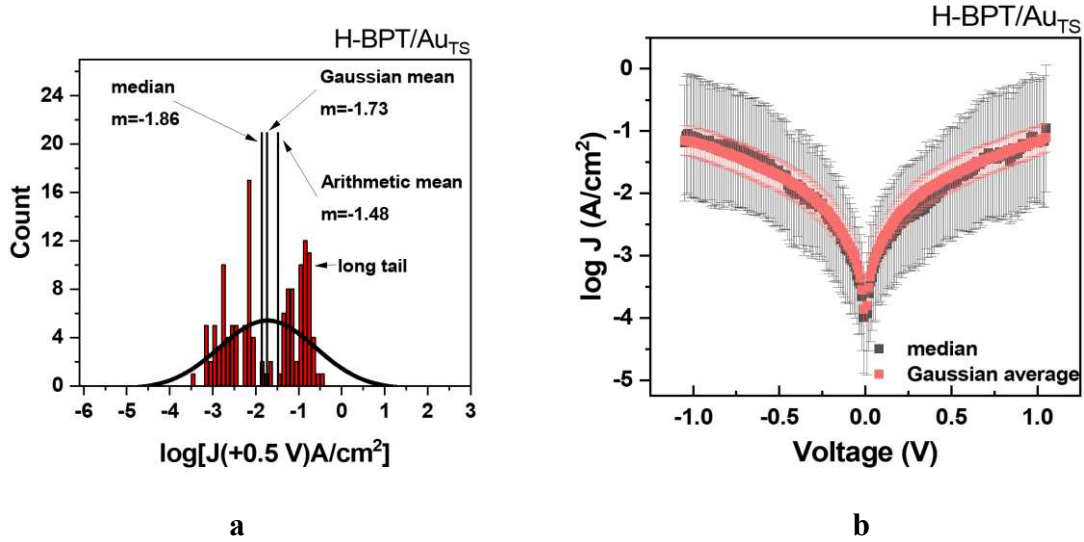
Figure 2.17: (a)Histogram of logarithmic current density at bias = +0.5 V for biphenyl thiol SAM on template-striped gold substrate. The normal distribution fitting of the histogram is shown. A long tail, defined as a group of data, which lie inside the x-range of the main peak, but with the height/intensity higher than the main peak, is found at the right side of the histogram. No outlier, defined as a group data, which lie outside the x-range of the main peak, is visible in the histogram. 3 different statistical analysis were used to estimate logarithmic current density at bias +0.5 V, which are shown in the figure. Arithmetic mean appears to be more influenced by the presence of long tail at the right side of histogram. (b) Median and Gaussian average were used to estimate the current-voltage relation of the SAM.

Table 2.1: The result of statistical analysis using Gaussian and median methods for logarithmic of current density at bias +0.5 V for SAM sample in Figure 2.17

log($|J(+0.5\ V)|$) for BPT/Au$_{TS}$	Gaussian method	Median method
Estimated location	-1.73	-1.86
Data dispersion	1.12	1.18
Confidential interval CI 95%	0.19	0.82
Confidential interval CI 99%	0.25	0.92
Confidential interval CI 99.5%	0.32	1.00

The accuracy of Gaussian analysis is in general very trustworthy.[57,95,175,177,178] However, in case equation 2.15 is considered invalid, it will consequently invalidate the whole Gaussian analysis. Another alternative statistical method is median, since it doesn't require equation 2.15 to be valid or log (J) to be normally distributed. This method assumes the majority of data to be informative and is weakly affected by outliers or long tail. The accuracy of

median for statistical analysis is illustrated in Figure 2.17a. In comparison to arithmetic mean, median is less affected by noninformative data.[175] For median method, both interquartile range (IQR) and adjusted median absolute deviation (σ_M) can be used to describe dispersion of log (J).[175]

The relation between logarithmic current density and applied bias is derived by implementing statistical analysis, either Gaussian method or median, for each applied bias. An example for H-BPT SAM on Au substrate can be found in Figure 2.17b, which the result of both Gaussian method or median are shown, and in Table 2.1, which the result of statistical analysis for log(J(+0.5 V)) is shown. According to Figure 2.17b, Gaussian method and median method agrees one another to analyze logarithmic current density-applied bias relation of H-BPT SAM on Au substrate. Please note, that data dispersions from both statistical methods are not suitable to quantify the precision of statistical analysis, since it is also affected by the number of data taken into consideration for the statistical analysis. Confidential interval (CI) quantity is more suitable to express the certainty of statistical estimation (CI).[175] Common CI in literatures include CI 95%, 99%, and 99.9 %, which have been calculated for the case of H-BPT SAM on Au at bias =0.5 V in Table 2.1.[175] These quantities tell respectively, the interval of 95%, 99%, or 99.9% of collected data surrounding estimated location. The detail of procedure to calculate confidence interval has been described elsewhere.[175,179–181]

2.7 Transition voltage spectroscopy

Transition voltage spectroscopy (TVS) was first demonstrated by Beebe *et al*.[182] In this method, I-V relation of a molecular junction is plotted as $\ln(I/V^2)$ versus I/V, as shown in Figure 2.18a. A minimum in current at certain *I/V* is found, which *V*, or called transition voltage (V_{trans}) correlates well with HOMO values from UPS measurement. By considering rectangular barrier for carriers transport, as illustrated in Figure 2.18b-Figure 2.18d, Beebe *et al* argued, that V_{trans} is a direct representation of effective barrier for charge transport.[182]. However, several theoretical investigation of TVS raise doubt of this original interpretation.[183–186]. Huisman *et al* pointed out inconsistency of rectangular barriers consideration with experiment, and showed, that TVS gives direct information of molecular level instead in the framework of coherent molecular transport model.[183] It has been pointed out, that V_{min} does not occur at the transition between direct tunnelling and FN tunnelling, but when a certain amount of the tail of the broadened resonant level comes within the bias window.[183,186,187] Regardless of disagreement in literatures regarding interpretation of TVS, it still allows a direct observation of HOMO or LUMO fingerprint in a transport experiment.
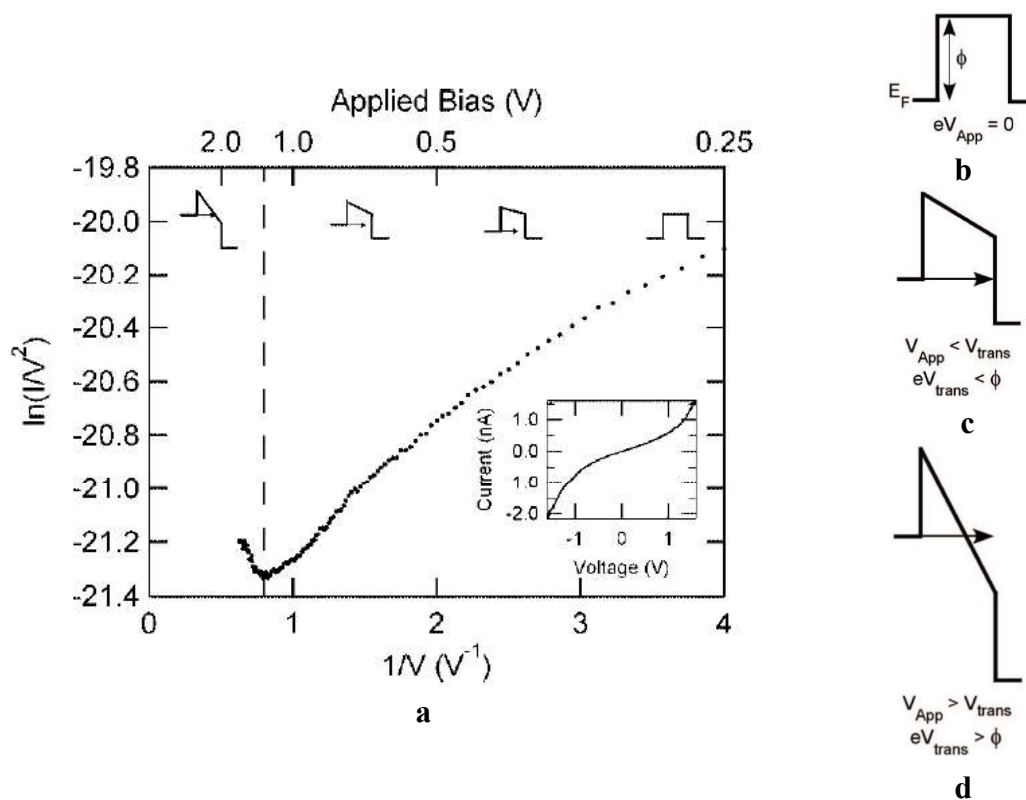
Figure 2.18: The figures are taken from ref [182]. (a)a Fowler–Nordheim (FN) plot of IV data (shown in inset). The dashed line represents required voltage to change both current dependence on applied bias (V_{App}) and carriers transport from tunneling to FN tunneling. (b) Schematic illustration of a tunneling barrier between 2 electrodes, when applied bias V_{App} is 0. The barrier height ϕ is determined by the offset between molecular orbital and fermi level, while the barrier width is determined by the length of molecule in junction.[182] (c) At low V_{App} ($V_{App} < V_{trans}$), the rectangular barrier becomes trapezoidal. Carriers transport occurs through tunneling. (d) At high V_{App} ($V_{App} > V_{trans}$), the rectangular barrier becomes triangular. Carriers transport occurs through Fowler-Nordheim (FN) tunneling.[183]

3. Methods

3.1 Materials & Preparation Procedures

3.1.1 Substrates

For most of the experiments, the SAMs were prepared on gold substrates purchased from Georg Albert PVD-Beschichtungen (Silz, Germany). These substrates were prepared by thermal evaporation of 30 nm of gold (99.99% purity) onto polished single-crystal silicon (100) wafers (Silicon Sense) that had been precoated with a 9 nm titanium adhesion layer. The films were polycrystalline, with predominant (111) orientation of individual crystallites and an RMS roughness value of 0.8 nm (5 ×5 μm^2 scan area).

The ITO coated glass slides with surface resistivity of 8-12 Ω/sq were purchased from Sigma-Aldrich (product number 703192). The RMS roughness of these substrates, measured over the 10 μm × 10 μm scan area, was estimated at 1.4-1.65 nm.[97] The measurements were performed with a Solver NEXT atomic force microscope (NT-MDT) in the tapping mode. Note, however, that there can be certain batch-to batch variations in the properties of commercial ITO, even when acquired from the same vendor.[43] A significant effect on the parameters and quality of the SAMs should not, however, be expected, since the basic surface chemistry is unchanged.

Figure 3.1: Scheme of Al$_2$O$_3$ substrate, which were used to prepare some SAM samples in this thesis.

The Al$_2$O$_3$ substrates were prepared by deposition of a thin Al$_2$O$_3$ layer on top of a boron-doped, double side polished 6 inches silicon wafer (625 μm thickness, (100) orientation, 0.001−0.005 Ω cm resistivity, prime grade). Native silicon oxide was removed directly prior to deposition by a dip in diluted, aqueous hydrofluoric acid (1 v%, DI water) for 1 minute at room temperature. The Al$_2$O$_3$ layer was deposited using Savannah S300 setup (Cambrigde Nanotech ALD) by cycling TMA/water. The thickness of this layer was estimated at 2−3 nm by spectroscopic ellipsometry; it is presumably separated by a "mixed" AlSiO$_x$ interlayer from the silicon substrate (Figure 3.1). The wafer was diced into 8 × 8 mm coupons, which were cleaned by RF-O$_2$-plasma treatment (p < 0.3 mbar, 150 W, 1 min) directly before SAM deposition.

3.1.2 SAM precursors, substrate cleaning, and SAM Preparation

The SAM precursors were either purchased from Sigma Aldrich or custom-synthesized by our partner groups, according to the literature recipes. All relevant precursors and description of solution preparation can be found in section 4.1.1, 4.2.1, 4.3.1, 4.4.1, and 4.5.1 and 4.6.1. Other chemical and solvents were purchased from Sigma Aldrich and used as received.

The Au substrates were cleaned by ultraviolet light for 30 minutes and subsequently ultrasonicated in ethanol for 10 minutes. Afterwards, Au substrates were washed with ethanol and blown dry with argon, before immersed in SAM precursor solution for 24 hours. After 24 hours, samples were cleaned to remove physisadsorbed thiol by first ultrasonication in SAM precursor solution for 10 minutes. Subsequently, samples were washed with pure ethanol, if respective SAM precursor solution was made with ethanol, then blown dry with argon flow before stored in sealed container with inert gas. In case precursor solution was made with solvents other than ethanol, samples were washed 2 times after ultrasonication, first with pure solvent, which was used to make respective precursor SAM solution, and then with ethanol.

ITO substrates were cleaned by first ultrasonic treatment in ethanol for 3-5 minutes, then ultraviolet light cleaning for 15 minutes, followed by a second ultrasonic treatment in ethanol for 3-5 minutes, before samples were immersed in precursor solution. After immersion, samples were annealed for 2 hours at 200ºC in atmosphere, before intensively washed with ethanol. Finally, samples were stored in sealed container in inert gas.

3.2 Characterization & Analysis

3.2.1 XPS & HRXPS

XPS measurements were performed at 2 different places. The laboratory XPS measurements were performed in Physikalisch-Chemisches Institut, Universität Heidelberg. This setup uses MAX200 (Leybold-Heraeus) spectrometer equipped with a non-monochromatized Mg Kα X-ray source (200 W) and a hemispherical analyzer. This XPS setup uses normal emission geometry. The recorded spectra were normalized by spectrometer transmission. The binding energy (BE) scale was referenced to the Au $4f_{7/2}$ emission at 84.0 eV.[188]

 The synchrotron-based high resolution XPS (HRXPS) measurements were carried out at the HE-SGM beamline (bending magnet) of the synchrotron storage ring BESSY II in Berlin using a custom-designed experimental station.[166] Synchrotron light served as the primary X-ray source. The spectra were measured with a Scienta R3000 electron energy analyzer in normal emission geometry. The photon energy (EP) was set to either 350, 580, or 750 eV, depending on the acquisition range. The energy resolution was ~0.3, ~0.6 eV, and ~0.8 eV at a PEs of 350, 580, and 750 eV, respectively. The binding energy (BE) scale was referenced to the substrate, either In 3d5/2peak at 444.3 eV for ITO substrate,[188–190] Au $4f_{7/2}$ at 84.0 eV for gold substrate,[188] or Al 2p at 74.0 eV for Al_2O_3 substrate.[188] Some of the spectra were fitted by symmetric Voigt functions and either a linear or Shirley

background, as far as this was necessary for the numerical evaluation of the XPS data. To fit the S $2p_{3/2,1/2}$ and P $2p_{3/2,1/2}$ doublets, 2 such peaks were used with standard parameter.[188] The XPS data were used for the evaluation of the effective thickness and packing density of the monolayers on the basis of the C 1s/ Au $4f_{7/2}$ and S $2p_{3/2, 1/2}$/Au $4f_{7/2}$ intensity ratios, respectively.[149,191] The standard, exponential attenuation of the photoemission signal was assumed[148] and the literature values for the attenuation lengths of the photoelectrons in densely packed SAMs were taken.[150] The spectrometer-specific constants were determined using a reference C16 SAM on Au(111), with a well-defined thickness (18.9 Å)[192] and packing density (4.63×10^{14} molecules per cm^2).[192]

3.2.2 NEXAFS spectroscopy

The NEXAFS measurements were conducted the same beamline as the HRXPS ones. The spectra were measured at the carbon and nitrogen K-edges, corresponding to the excitation of the C 1s and N 1s core-level electrons into the unoccupied molecular states. The spectra were collected in the partial electron yield (PEY) acquisition mode with retarding voltages of −150 V (C K-edge) and −300 V (N K-edge). The polarization factor of the synchrotron light was estimated at ~90% (linear polarization). The incidence angle of the light was varied in steps between the normal and grazing geometry, set to 90, 55, 30 (C K-edge only), and 20° with respect to the sample surface, to monitor the linear dichroism effects associated with molecular orientation and orientational order in the SAMs.[171] The energy resolution was~0.3 eV at the C K-edge and~0.45 eV at the N K-edge. The photon energy scale was referenced to the pronounced π* resonance of highly oriented pyrolytic graphite at 285.38 eV.[193]

3.2.3 Kelvin Probe Measurements

Work function measurements were carried out using a UHV Kelvin Probe 2001 system (KP technology Ltd., UK). The pressure in the UHV chamber was ~10^{-8} mbar. The work function values were referenced to that of a C16 SAM on Au(111), viz. 4.3 eV.[29] The latter value was additionally verified by comparison to the work function (WF) of freshly sputtered gold at 5.2 eV.[25]

3.2.4 UPS

The UV light (He I radiation; 21.22 eV) was provided by a UVS 40A3 source (Prevac, Poland), and the spectra were recorded with an EA 15 analyzer (Prevac, Poland) in normal emission geometry. The pass energy was set at 10 eV; the samples were biased by ca. 27 eV to record the secondary electron cutoff providing information about the WF of the samples.

3.2.5 Electrical Conductance Measurements
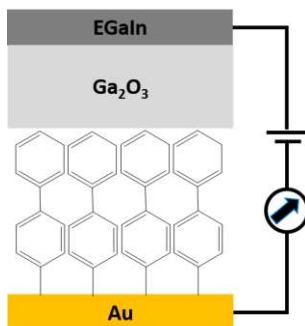
Figure 3.2: Illustration of electrical conductance measurement of SAM sample with eutectic gallium indium setup.

Charge tunneling rate measurements were performed with a custom-made two-terminal molecular junction setup, based on the Keithley 2635A source meter.[194] The reliability of the setup has been confirmed by previous experiments.[2,53,195] The gold substrate and a sharp tip of eutectic GaIn (EGaIn), covered by a ultrathin GaO_x film (ca. 0.7 nm thick),[175,196] served as the bottom and top electrodes, respectively (see a schematic drawing in Figure 3.2). Tunneling junctions were formed by contacting grounded SAM/Au samples with the EGaIn tips and applying a potential. The formation of EGaIn tip is shown in detail in Figure 3.3. The voltage was varied either between −0.5 V and +0.5 V or between −1.0 V and +1.0 V in 0.01 V steps. At least 20-25 I–V curves, measured at several different places and for several different samples, were recorded for each sample type, with a yield of reliable data of 55-95%. Average values of the current density were calculated with standard statistical analysis relying on either Gaussian mean and standard deviation or median with the adjusted interquartile range for expressing the dispersion of the samples.[175] Both procedures resulted in nearly identical values of the current density. In case, more than 70 I-V curves are collected per sample, confidential interval (CI) 95% is used to express samples dispersion.[175] Similar analysis was also performed for the transition voltage, on the basis of the I–V curves represented as Fowler–Nordheim plots.
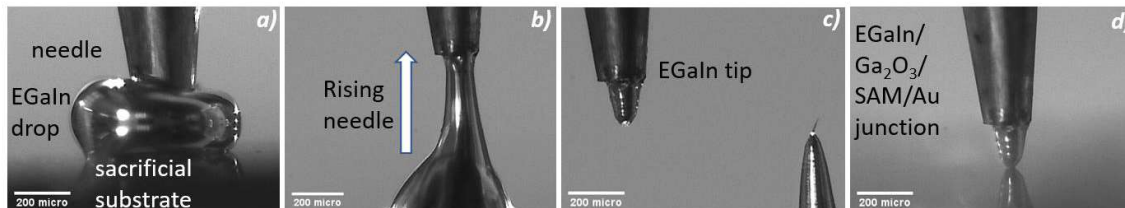
Figure 3.3: EGaIn junction is formed as the following (a) Microneedle is contacted with EGaIn droplet on a sacrificial substrate. (b) The microneedle is lifted by a manipulator, which stretches EGaIn droplet, by making it narrower in the middle part. (c) EGaIn tip is formed by lifting the microneedle further and breaking the EGaIn droplet. (d) The EGaIn tip is contacted with SAM sample of interest to measure current-voltage relation.

3.2.6 Thermal stability measurements

The experiments were performed at the HE SGM beamline (bending magnet) of the synchrotron storage ring BESSY II in Berlin, Germany, using a custom-designed experimental station.[166] The samples were mounted on the commercial sample holders with e-beam heating (Prevac, Poland). The temperature of the samples was measured by a Ni-CrNi thermoelement fixed at the sample surface by a metal stripe and controlled by the HEAT-2 unit (Prevac, Poland). The samples were mounted on the commercial sample holders with e-beam heating (Prevac, Poland). The temperature of the samples was measured by a Ni-CrNi thermoelement fixed at the sample surface by a metal stripe and controlled by the HEAT-2 unit (Prevac, Poland).

The temperature was varied with certain step size, starting from the room one (ca. 300 K). The heating rate did not exceed 1 K/sec and was even further reduced (manually) to the extent necessary upon the approaching the specific annealing temperature, to avoid its exceedance by more than 0.2-0.3° during the temperature adjustment. The samples were kept at this temperature for 2-5 minutes. Afterwards, the heating was switched off and the samples were cooled down.

The temperature-induced degradation of the SAMs was monitored by HRXPS, which was also used to characterize the sample in their pristine state (i.e., at room temperature). The experiments were conducted under UHV conditions, with a base pressure of $\sim 5 \times 10^{-10}$ mbar, which became worse to some extent as far as the samples were kept at high temperatures. The spectra acquisition was carried out in normal emission geometry with a Scienta R3000 electron energy analyzer.

.

4. Results & Discussion

4.1 Electrostatic Engineering of ITO

The concept of embedding dipolar groups into the molecular backbone of the SAM-forming molecules has been successfully demonstrated for a variety of SAMs taking gold and silver substrate.[2,3,27–29,197] The concept was adapted for the oxide substrates, taking as such in this subchapter substrate indium tin oxide (ITO) - a frequently used and application-relevant test material, prone to SAM engineering.[39–49]
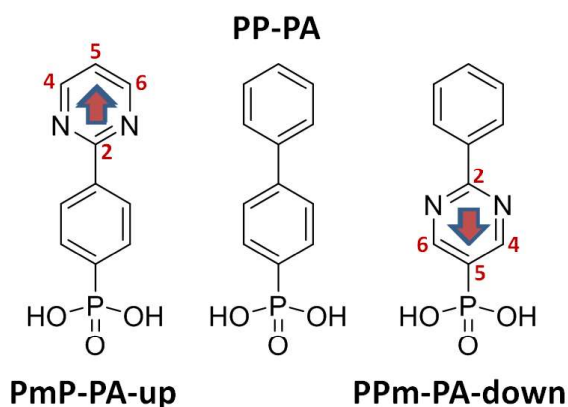
Figure 4.1: Molecular structures of SAM-forming molecules with their acronyms (P = phenyl, Pm = pyrimidyl, PA - phosphonic acid, and up/down - direction of the dipole moment (red arrows) with respect to the anchoring group and, consequently, to the substrate). The molecules were synthesized by the group of Prof. Terfort.[97]

The SAM-forming molecules selected for the present study are shown in Figure 4.1, along with their acronyms. Apart from the phosphonic acid (PA) anchoring group, their structure intentionally mimics the analogous molecules with a thiol anchor, viz. PmP-SH-up, PP-SH, and PPm-SH-down, which were optimized to achieve a high conductance while allowing work function adjustment of gold (5.2-5.3 eV) to 4.07±0.1 eV, 4.46±0.1 eV, and 4.83±0.1 eV, respectively, with a work function difference of 0.8-0.9 eV between the "up" and "down" engineered substrate.[2,3,25,198]

The PA anchoring group (Figure 4.1) was selected because of its binding capability for a broad variety of oxide substrates, such as Al_2O_3, ITO, ZnO, glass, etc.[39,199,200] The robust and reliable character of PA SAMs is generally accepted, along with the relatively simple fabrication as compared to alternative anchoring groups (trichlorosilanes, carboxilic acids, etc.), suitable to oxide substrates.[19,47,199,201,202]

4.1.1 SAM Preparation

The ITO substrates were purchased from Sigma-Aldrich. The SAM precursors were synthesized by our partners. Before the SAM preparation the substrates were cleaned using standard cleaning procedure for ITO substrate, as described in subchapter 3.1.2. The SAMs were prepared by immersion of the substrates into 1 mM solution of the SAM-forming molecules in ethanol for 24-72 h at room temperature. Only minor dependence of the SAM properties on the immersion time, within the above range, was observed, but, for the PmP-PA-up monolayers, slightly lower values of the work function were recorded at a prolonged immersion. Consequently, the results presented here correspond to 24 h immersion for the PPm-PA-down and PP-PA SAMs and to 48 h immersion for the PmP-PA-up monolayer. After the immersion, the samples were dried with Ar and annealed at 200 °C for 2 h under ambient conditions, which is a standard post-treatment step promoting conversion of the surface-adsorbed phosphonic acid to surface-bound phosphonate,[47] while the annealing temperature was selected based on literature data[203–205]. Finally, the samples were washed again with ethanol to remove physisadsorbed residues and dried with Ar.
Note that even though the post-annealing temperature is relatively high, it is well below the thermal stability limit for PA SAMs, which is 350-440°C for ITO, ca. 300°C for ZnO, and 500-600°C for alumina.[109,200,202] The reliability of the post-annealing procedure with respect to the integrity of the molecules was evidenced by the entire bulk of the experimental data for the fabricated SAMs, as described below. Note also that several series of the samples were prepared for the different experiments, some of which were repeated several times. The results were generally well reproducible.

4.1.2 XPS

In 3d, P 2p, C 1s, N 1s and O 1s XP spectra of the PmP-PA-up, PPm-PA-down, and PP-PA SAMs are shown in Figure 4.2. The total intensities of the In 3d (Figure 4.2a), P 2p (Figure 4.2b) and C 1s (Figure 4.2c) signals for the "up" and "down" SAMs are close to each other but are either higher (In 3d) or lower (P 2p and C 1s) than those for the PP-PA monolayer (the intensities were calculated within the spectra fitting procedure).Such intensity relations suggest similar packing densities of the "up" and "down" SAMs and a somewhat higher packing density for the PP-PA monolayer.
The In 3d spectra of all SAMs in Figure 4.2a exhibit an In $3d_{5/2,3/2}$ doublet, comprised of the symmetric In $3d_{5/2}$ and In $3d_{3/2}$ peaks, splitted by ~7.5 eV, in good agreement with the literature data (7.54 eV).[188] These peaks correspond to the bulk ITO. Neither side lines nor high BE shoulders, observed sometimes for ITO samples,[206,207] are perceptible.
The P 2p spectra of all SAMs in Figure 4.2b exhibit an asymmetric peak, which can be precisely reproduced by a single P $2p_{3/2,1/2}$ doublets at BE of 132.8-132.9 eV (P $2p_{3/2}$), with a standard branching of 2:1 (P $2p_{3/2}$: P $2p_{3/2}$), a spin-orbit splitting of ca. 0.9 eV,[208,209] and both components merged together. This feature corresponds to the PA groups bound to the substrate,[39,48,209] most likely in the bidentate adsorption mode.[209] The absence of other doublets as well as the similarity of the BE positions and the entire peak shapes for all three monolayers suggest a similar bonding configuration for all molecules in the films, underlining their SAM character.
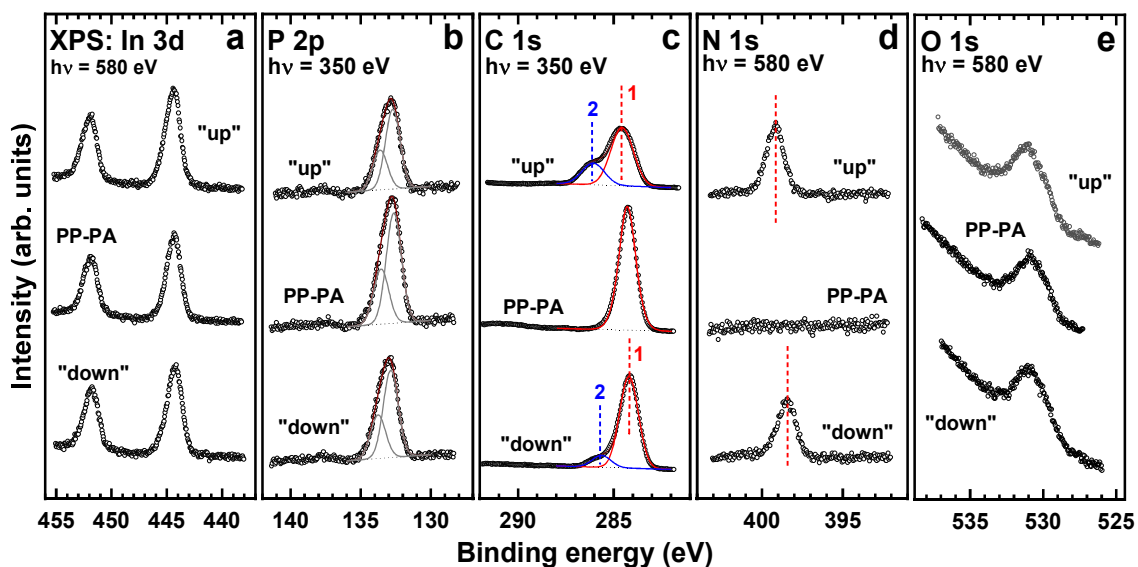
Figure 4.2: (a) In 3d, (b) P 2p, (c) C 1s, (d) N 1s, and (e) O 1s XP spectra of the PmP-PA-up ("up"), PPm-PA-down ("down"), and PP-PA SAMs on ITO. The spectra were acquired at photon energies of 350 eV (b, c) and 580 eV (a, d, e). The P 2p spectra are decomposed by the individual P $2p_{3/2}$ and P $2p_{1/2}$ components (see text for details). The C 1s spectra of the "up" and "down" SAMs can be both reproduced as a combination of two peaks (marked as 1 and 2), with the BE positions traced by the vertical red and blue dashed lines, but such a decomposition can only be considered as formal, since these spectra result from a complex combination of the chemical and electrostatic effects (see text for details). The positions of the N 1s peaks are also marked by the vertical red dashed lines.

The C 1s spectrum of the PP-PA SAM in the Figure 4.2c represents, as expected,[210] a single peak at a BE of 284.2 eV, corresponding to the biphenyl backbone. The BE position of this peak is nearly identical to that of the well-defined biphenylthiolate SAM on Au(111).[3,210] The spectra of the "up" and "down" SAMs, containing the pyrimidine unit (see Figure 4.1) are, as expected[211], more complex, representing merged contributions of phenyl (a single peak; see the spectrum of the PP-PA SAM) and pyrimidine (a combination of three peaks with a larger spectral weight at the low BE side).[211] However, what is even more important, these spectra are distinctly different from one another, in spite of the identical chemical compositions of the SAM-forming molecules (see Figure 4.1). Such a difference, observed also for the analogous "up" and "down" thiolate SAMs on Au(111) (PmP-S-up and PPm-S-down; □SH transforms to thiolate upon the adsorption),[3] can only be explained by collective electrostatic effects provided by the dipolar pyrimidine groups. Arranged in a parallel fashion within the SAM, these dipoles create a potential discontinuity inside the monolayer, electrostatically shifting the core level energies in the regions above the dipoles relative to those below the discontinuity (upwards for "up" and downwards for "down").[27,30] Consequently, in accordance with the direction of the embedded dipole, the contributions associated with the top ring either shift to higher energies ("up"), resulting in an entire two-peak-like structure with characteristic BEs of 284.6 eV (1) and 286.1 eV (2), or to lower BE ("down"), merging to a single peak at 284.15 eV (1) with a small shoulder at 285.7 eV (2). Specifically, within simplified assignments, for the "up" SAM, peak 1

stems from the C atoms in the phenyl ring and C5 atom in the pyrimidine ring while peak 2 is associated with the C2, C4, and C6 atoms in the pyrimidine ring.[3] Analogously, for the "down" SAM, peak 1 stems from the C atoms in the phenyl ring while the shoulder 2 is associated with the carbon atoms in the pyrimidine ring, with major contribution provided by C2 (see Figure 4.1 for the assignments of the carbon atoms).[3] The relative contributions of individual atoms are weighted by attenuation of the respective photoelectron signals, in accordance with their locations with respect to the SAM-ambient interface.

The N 1s spectrum of the reference PP-PA monolayer doesn't exhibit any signal, in accordance with the molecular composition (see Figure 4.1). In contrast, the spectra of the "up" and "down" SAMs in Figure 4.2d show a clear signal, viz. a single peak assigned to the nitrogen atoms in the pyrimidine rings of PmP-PA-up and PPm-PA-down (see Figure 4.1). The occurrence of a single peak only suggests a nearly identical chemical state for all pyrimidine moieties in the particular monolayer, once more underlining homogeneous and well-defined character of the PmP-PA-up of PPm-PA-down SAMs. Significantly, the BE position of the N 1s peak for the "up" SAMs, 399.15 eV, is noticeably higher than that for the "down" SAM, 398.45 eV, mimicking the behavior of the C 1s spectra. In the similar fashion as in the C 1s case, this shift correlates with the direction of the embedded dipole and arises from a discontinuity of the electrostatic potential inside the monolayer.

Apart from the peak position, the N 1s spectra were used for numerical evaluation of the packing density of the SAMs, using a well-defined PPmP-S-down monolayer on Au(111) with a packing density of 4.3×10^{14} molecules/cm^2 as a reference (the PPm part of PPmP-S-down is identical to the backbone of PPm-PA-down).[27] Accordingly, with a correction for the different attenuation of the N 1s signal for "up" and "down" positions of the nitrogen atoms, the packing density of the PmP-PA-up and PPm-PA-down SAMs could be estimated at 4.6×10^{14} and 4.3×10^{14} molecules/cm^2, respectively, with an accuracy of ±5-6%. These values are very close to the packing densities of the analogous SAMs with the thiolate anchoring group on Au(111), viz. 4.5×10^{14} molecules/cm.[23] Note that the packing density values refer to the surface plane and don't take into account the surface roughness.

The O 1s spectra of all SAMs in Figure 4.2e exhibit similar spectral shape, indicating a similar binding motif, most likely in bidentate manner.[47] The observed peaks are slightly asymmetric and are comprised of contributions from both the ITO substrate and the ITO-SAM interface. One can decompose these spectra in individual contributions,[40,47,49,209,212] which, however, in our opinion, can hardly be performed in a non-equivocal fashion without reliable reference data or dedicated theoretical simulations. Consequently, I refrain from this procedure, mentioning just that there is no signal at 533.7 eV, characteristic of unreacted PA groups.[49]

Summarizing, the XPS data suggest the formation of well-defined PmP-PA-up, PP-PA, and PPm-PA-down SAMs exhibiting similar anchoring chemistry, high packing densities, and pronounced electrostatic effects, associated with the embedded dipolar pyrimidine groups, forming a 2D array of the oriented dipoles within the monolayers.


4.1.3 NEXAFS Spectroscopy

The carbon and nitrogen K-edge NEXAFS spectra of the PmPPA-up, PPm-PA-down, and PP-PA SAMs are compiled in Figure 4.3 and Figure 4.4, respectively. Two kinds of spectra are presented, viz. those acquired at an X-ray incidence angle of 55° and those

corresponding to the difference between the spectra collected under the normal (90°) and grazing (20°) incidence geometry. The choice of these particular spectra is intentional. The 55° spectra are nearly exclusively representative of the electronic structure of the SAMs in question and are hardly affected by orientational effects.[171] In a complementary fashion, the difference spectra are primarily representative of the molecular orientation. The presence of difference peaks at the positions of characteristic absorption resonances reveals orientational order in the system in question.
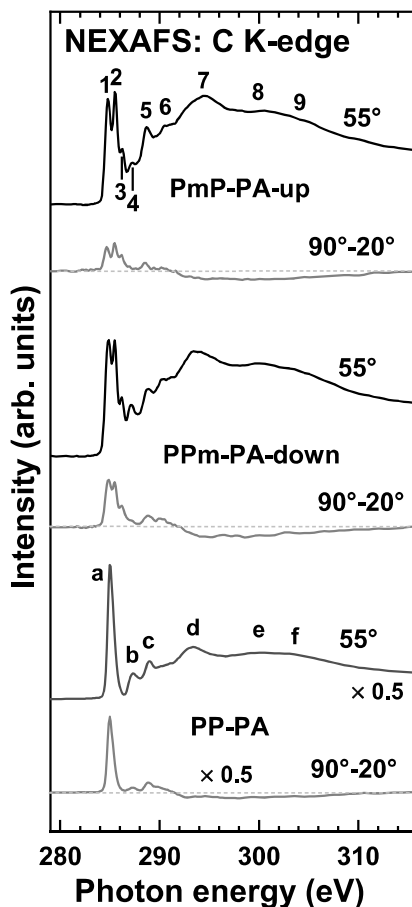
Figure 4.3: C K-edge NEXAFS spectra of the PmP-PA-up, PPm-PA-down, and PP-PA SAMs on ITO acquired at an X-ray incidence angle of 55° (black lines), along with the respective difference between the spectra collected under the normal (90°) and grazing (20°) incidence geometry (gray lines). Individual absorption resonances are marked by numbers and letters (see text for the assignments). The horizontal dashed lines correspond to zero.

Let us first consider the 55° spectra, starting with the C K-edge ones. The spectrum of the PP-PA SAM in Figure 4.3 exhibits a typical resonance pattern of phenyl groups,[171,213] observed also for oligophenyl monolayers, including those with a biphenyl backbone.[214–216] The spectrum is dominated by the strong π_1* resonance at ~285.0 eV (a), accompanied by C–H* resonance at ~287.2 eV (b), π_2* resonance at ~288.9 eV (c), and several broader $\sigma*$-type resonances at 293.5 eV (σ_1*; d), 300.2 eV (σ_2*; e), and ~304 eV (f).[171,213,217]
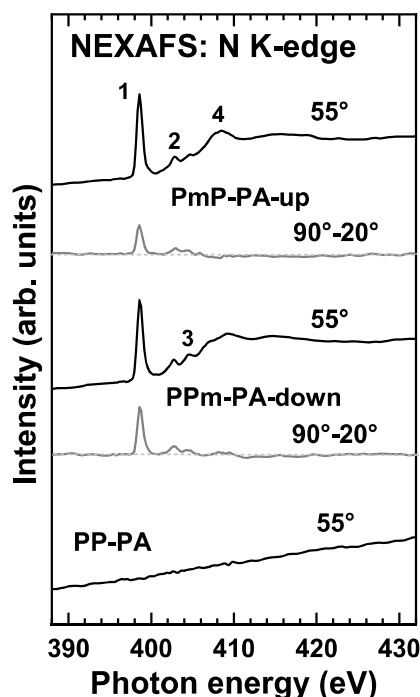
Figure 4.4: N K-edge NEXAFS spectra of the PmP-PA-up, PPm-PA-down, and PP-PA SAMs on ITO acquired at an X-ray incidence angle of 55° (black lines), along with the respective difference between the spectra collected under the normal (90°) and grazing (20°) incidence geometry (gray lines). Individual absorption resonances are marked by numbers (see text for the assignments). The horizontal dashed lines correspond to zero.

In contrast to the C K-edge spectra, the N K-edge ones originate exclusively from the pyrimidine moieties. Indeed, the 55° spectrum in Figure 4.4 exhibits a typical pattern of pyrimidine,[211,218,219]viz. a strong π_1*-resonance at 398.55 eV (**1**); a π_2*-resonance at 402.8 eV (**2**); a resonance at ~404.5 eV (**3**) alternatively assigned to a Rydberg orbital,[218] admixture of the valence and Rydberg-type transitions,[220] or double excitations,[211,219] and a resonance at ~408.3 eV (**4**) assigned to excitations to the σ* orbitals,[211,219] once more underlining the chemical identity of the monolayers. In contrast, the N K-edge spectrum of the PP-PA SAM doesn't exhibit any features, as is expected since this monolayer doesn't contain nitrogen. In addition, this spectrum represents an evidence that the ITO substrates did not contain any nitrogen contamination.

The 55° spectra of the "up" and "down" SAMs in Figure 4.3 should represent, within the generally accepted building block model,[171] a superposition of the contributions linked to the molecular building blocks, viz. phenyl and pyrimidine. The contribution of phenyl is adequately reproduced by the spectrum of the PP-PA SAM. The contribution of pyrimidine should, according to the literature data[211,218] be comprised of a rather complex and comparably intense π*-type feature at 285-286.5 eV and a variety of much weaker resonances at higher excitation energies. In its turn, the π*-type feature is comprised of three resonances, at 284.8-285.0 eV (comparably weak), ~285.4 eV (strong), and 285.9-286.2 eV (moderately weak), associated with the specific carbon atoms within the pyrimidine ring, viz. C5, C4/C6, and C2, respectively (see Figure 4.1). Such a three-resonance-structure is indeed observed in the 55° spectra of the "up" and "down" SAMs in

Figure 4.3, with individual resonances at 284.8 eV (**1**), 285.5 eV (**2**), and 286.2 eV (**3**). The resonance **1** is additionally "amplified" by merging with the resonance a of the phenyl ring and the entire π*-resonance pattern is modulated by the different attenuation of the PEY signal for the different carbon atoms within the molecular backbone.[221] Consequently, the merged resonance **1+a** is comparably stronger for the "down" SAM, where the contribution of the phenyl ring, located at the SAM-ambient interface, is stronger than in the "up" case. As to the further resonances in the spectra of the "up" and "down" SAMs, they represent a superposition of the resonances of phenyl and pyrimidine rings, with **4** being presumably identical to **b**, **5** being identical to **c**, etc.

Interestingly, the "fine structure" of the joint π*-resonance (**1-3**) is pronounced much better in the given case than for the analogous SAMs on Au(111),[3] which can be tentatively explained by the coupling of the excited states with a pool of conductance electrons in the metal substrate, resulting in a broadening of the resonances and, consequently, in the smearing of the observed "fine structure". The extent of this coupling can vary with the separation of a particular atom from the substrate, modifying the intensities of the resonances, which, probably, can explain the differences in the exact shape of the joint π*-type feature (**1-3**) for the pyrimidine SAMs on ITO (this work) and Au.[3] In addition, the influence of the matrix effects, associated with the exact packing structure of the SAMs, which can be different for Au and ITO, cannot be completely excluded.

Table 4.1. Average tilt angles of the π* orbitals in the PmP-PA-up, PPm-PA-down, and PP-PA SAMs calculated on the basis of the C K-edge and N K-edge NEXAFS data. The accuracy of the values is ±3°.

Monolayer	Tilt angle (α) from the C K-edge data	Tilt angle (α) from the N K-edge data	Average value
PmP-PA-up	60°	60°	60°
PPm-PA-down	62°	63.5°	62.5°
PP-PA	65°	-	-

The 90°-20° difference spectra at both C and N K-edge exhibit pronounced peaks at the positions of the characteristic resonances. These peaks are positive for the π* resonances and negative for the σ* ones, suggesting, in view of the orientation of the respective molecular orbitals (perpendicular and parallel to the molecular backbone for the π* and σ* states, respectively), an upright molecular orientation in all SAMs studied. Apart from this qualitative finding, numerical evaluation of the entire sets of the NEXAFS spectra was performed, based on the standard theoretical framework.[171]

Within the evaluation procedure the intensity of a particular absorption resonance is plotted as a function of the X-ray incidence angle and fitted by the suitable theoretical curve with the tilt angle of the respective molecular orbital relative to the surface normal, α, as the parameter. In the present case, the π* resonances were selected (**1-2**; joint intensity), as representative of the vector-type π* orbitals and most pronounced ones in the spectra. The

derived values of the average tilt angles for the respective π^* orbitals are compiled in Table 4.1. Significantly, for the "up" and "down" SAMs, the C K-edge and N K-edge derived values are quite close to each other, suggesting that the phenyl and pyrimidine rings are only slightly twisted with respect to one another or even lie in the same plane, as can be expected for densely packed molecular assemblies. Such a behavior agrees also with the crystallographic data for the analogous compounds with the thiol anchoring group, where, for the respective 3D crystals, planar molecular conformation was recorded.[3]
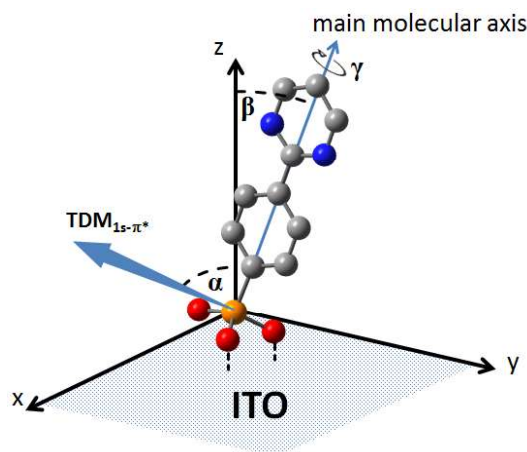
Figure 4.5: Schematic illustration of PmP-PA-up in a coordinate system along with β(tilt angle of the main molecular axis with respect to the surface normal, represented by the z-axis), γ (molecular twist angle), and α (tilt angle of the π^* orbitals with respect to the surface normal). The phenyl and pyrimidine rings are considered to be coplanar. The π^* orbitals of these rings are perpendicular to the backbone plane; the respective transition dipole moment, $TDM_{1s-\pi^*}$, is shown as a blue arrow.

Based on the derived tilt angles of the π^* orbitals (α), average molecular tilt angles (i.e., deviation of the main molecular axis with respect to the surface normal,), β, can be calculated using a relation, $\cos \alpha = \sin \beta \times \cos \gamma$, where γ is so-called twist angle describing rotation of the molecular backbone around the molecular axis with respect to the tilt plane (see Figure 4.5).[222] It is defined such that it is zero when the tilt occurs perpendicular to the backbone plane. The latter angle cannot be determined from the NEXAFS data (except for a specially derivatized molecules).[223] Thus, it is usually derived from bulk structures, IR data, or from simulations,[3,27,224] which all is regretfully not available in the present case. Assuming the twist angle equal to zero and plane molecular confirmation,[225] I get the average molecular tilt angle of ~30° for the "up" and "down" SAMs and ~25° for the PP-PA monolayer. A more realistic value for the twist angle is that for the bulk biphenyl (32°),[226–228] correlating coarsely with the values obtained for oligophenyl-like SAMs by IR spectroscopy[27] and NEXAFS spectroscopy.[223] Within this assumption I get the average molecular tilt angle of 33-36° for the "up" and "down" SAMs and ~30° for the PP-PA monolayer. These angles are more realistic than for γ = 0 but should, nevertheless, be considered as coarse estimates only since the real values of the molecular twist can differ to some extent and be somewhat different for the different SAMs. The latter can in

particular be the reason that the α value for "up" SAM is slightly smaller than that for the "down" monolayer, in spite of the denser molecular packing.

Summarizing, the NEXAFS spectra correlate precisely with the identities of the SAM forming molecules and don't show any unexpected features, which implies a chemically well-defined and contamination-free character of the monolayers in question. The molecules in these monolayers have an upright orientation, typical of well-defined SAMs.

4.1.4 Work Function

The presence of the pronounced electrostatic effects in the C 1s XP spectra of the "up" and "down" SAMs (see Section 4.1.2) suggests their expected dipolar character, which should also be reflected in the work function behavior. This is indeed the case, as demonstrated in Figure 4.6, where the work function values for these SAMs as well as for the PP-PA monolayer are shown.

The value for the PP-PA SAM with the non-polar biphenyl backbone, viz. 4.4 eV, is nearly identical to the literature values for PA monolayer with phenyl backbone on the same substrate, viz. 4.51 eV[42] and 4.42 eV[44] ; such values are also typical for non-polar alkyl PA SAMs on ITO (4.5-4.6 eV).[44,47]

Note that the work function values for the pretreated ITO substrate was 4.68 eV and for the UHV-sputtered and in situ measured ITO substrate ~4.2 eV. The true reference value lies presumably somewhere between, since the pretreated substrate was contaminated to some extent (which could not be completely avoided) while the sputtered substrate is clean but probably modified by sputtering. It is also not clear to what extent the process of self-cleaning upon the SAM formation, typical, e.g., for thiolate SAMs on Au(111),[23] occurs for the PA monolayers on ITO.
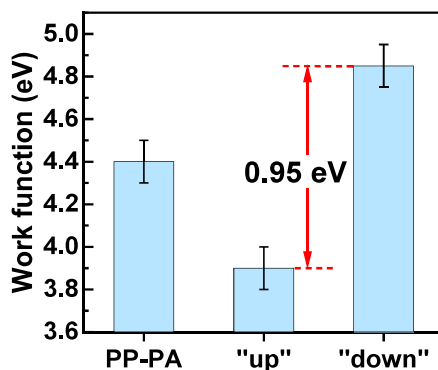
Figure 4.6: Work function values for the PmP-PA-up ("up"), PPm-PA-down ("down"), and PP-PA SAMs on ITO. The work function difference between the PPm-PA-down and PmP-PA-up case is additionally highlighted.

Anyway, since all SAMs of the present study are bound to the substrate in a similar fashion (see Section 4.1.2), the PP-PA monolayer with the non-polar biphenyl backbone represents a suitable reference for the PmP-PA-up and PPm-PA-down SAMs with the polar PmP and PPm backbones. The dipole moment of the PmP moiety could be estimated at 1.44 -1.74 D, with the exact value depending on the specific calculation methodology.[3] The projection

of this dipole moment onto the surface normal is directed either to or from the substrate for the PmP-PA-down and PPm-PA-up SAMs, respectively, shifting the work function. Indeed, as shown in Figure 4.6, the work function of the "up" monolayer is ~3.9 eV while the work function of the "down" SAM is ~4.85 eV, which correspond to the −0.5 eV and +0.45 eV shifts with respect to the reference value (~4.4 eV; PP-PA), respectively. The larger shift for the "up" SAM is presumably related to the somewhat higher packing density (see Section 4.1.2), since the inclination of the SAM-forming molecules is similar for the "up" and "down" monolayers (see Section 4.1.3).

The above changes in the work function as compared to the PP-PA case, $\Delta\Phi$, can be compared to a coarse theoretical estimate according to the formula: [48]

$$\Delta\Phi = \rho_{SAM} \cdot \mu_{Pm} \cdot \cos{(\beta)} / \varepsilon_{SAM} \, \varepsilon_0 \qquad\qquad 4.1$$

where ρ_{SAM} is the packing density of the SAMs (from the XPS data; see Section 4.1.2); μ_{Pm} the dipole moment of the pyrimidine moiety, set to 1.59 D (the average of the 1.44 - 1.74 D range); β is the molecular tilt (from the NEXAFS data, within a reasonable assumption for the twist angle; see Section 4.1.3); ε_{SAM} the dielectric constant of the SAM, set to 3.9,[3,229] and ε_0 the vacuum permittivity. Accordingly, the expected values of $\Delta\Phi$ for the "up" and "down" SAMs were estimated at −0.56 eV and +0.52 eV, respectively, in reasonable agreement with the measured work function values. A small overestimate is presumably related to the ultimate value for the molecular tilt assumed by us (see Section 4.1.3) and the ambiguity in the exact values of the other parameters. Overall, the work function values of the PmP-PA-up, PP-PA, and PPm-PA-down SAMs cover the 3.9 - 4.85 eV range, corresponding to the work function variation within the 0.95 eV range at the chemically neutral and persistent composition of the SAM-ambient interface. Note that apart from the single-component SAMs, mixed "up"/"down" monolayers can be prepared, e.g. by co-adsorption of the both components, similar to the thiolate case on gold and silver substrates,[30,31,230] which will allow continuous tuning of the work function between the ultimate values of 3.9 and 4.85 eV. In addition, the value of 3.9 eV for the "up" SAM is of importance on its own, since, according to the most recent review[47] and our own literature survey, PA compounds, being quite successful in increasing the work function of ITO, have not yet been very successful in lowering its work function except for just few recent publications. In particular, just very recently, a value of 3.7 eV has been reported for a dimethylamine-terminated SAM.[48] Our value is higher by 0.2 eV but still low enough, while the SAM-ambient interface is less hydrophilic and more robust.

4.1.5 Conclusions

The formation of SAMs with PA anchoring group on ITO substrate was reported. The backbones of these molecules, PmP-PA-up and PPm-PA-down, are comprised of phenyl and pyrimidine rings, with the latter moiety oriented such that its dipole moment is directed either to or away from the anchoring group. For the reference, nonpolar biphenyl−PA monolayer was also formed on ITO substrates. According to the detailed spectroscopic analysis, these SAMs are characterized by a uniform molecular configuration and dense

molecular packing, with the packing density in the $(4.3-4.6) \times 10^{14}$ molecules/ cm^2 range. The molecules in the SAMs are bound to the substrate over the PA group and oriented upright, even though with a noticeable inclination, represented by an average tilt angle of $\sim 30°$ with respect to the surface normal.

Most importantly, the pyrimidine-containing SAMs exhibit pronounced electrostatic effects, reflected by the shifts of the characteristic peaks in the C 1s XP spectra and by the work function values of the SAM-modified ITO substrate. Depending on the upward or downward orientation of the pyrimidine ring within the molecular backbone, the work function is shifted by −0.5 and +0.45 eV with respect to the nonpolar PP- PA SAM. Accordingly, the work function of ITO can be varied in the 3.9−4.85 eV range without modifying the SAM− ambient interface. Consequently, the presented SAMs can serve as a valuable model system to monitor dipole engineering effects in a variety of device assembles, decoupling these effects from the surface chemistry, potentially affecting the morphology of the adjacent, deposited layer (organic semiconductor, etc.). A further important point is the comparably low work function value for the PmP-PA-up SAM, 3.9 eV, which extends a rather limited variety of PA-anchored compounds capable of lowering the work function of ITO and can, thus, be useful for a variety of applications. Note that even a smaller work function value can probably be achieved with a distributed up dipole, comprised of two pyrimidine groups.[36]

Finally, the observation of electrostatic effects in photo- emission for dipolar SAMs on oxide substrates, in addition to metal substrates as demonstrated in the previous works,[3,27,29] underlines the general character of these effects and establishes XPS as a useful tool to monitor these effects and SAM morphology[30] for different types of substrate materials.

4.2 Electrostatic effects in charge transport by the example of H-BPT and F-BPT

In the present study a binary system is addressed, build by biphenylthiolates (BPT) and BPT with fluorine substitution. The respective molecules, abbreviated as H-BTP and F-BPT, are shown in Figure 4.7a. They differ only by the terminal atom, either H or F, and, otherwise, have the identical biphenyl backbones and thiol anchoring groups, suitable to the coinage metal and some semiconductor substrates, including gold support chosen for the present study.[23] It can then be consequently expected that the identity of the tail group will be of minor importance for the molecular assembly and homogeneously mixed SAMs will be formed.[51,55] A further argument for intermolecular mixture is the dipole moment of the electronegative fluorine atom in F-BPT. The neighboring dipoles will tend to repel each other, providing additional drive for dispersion of F-BPT in the H−BPT matrix.
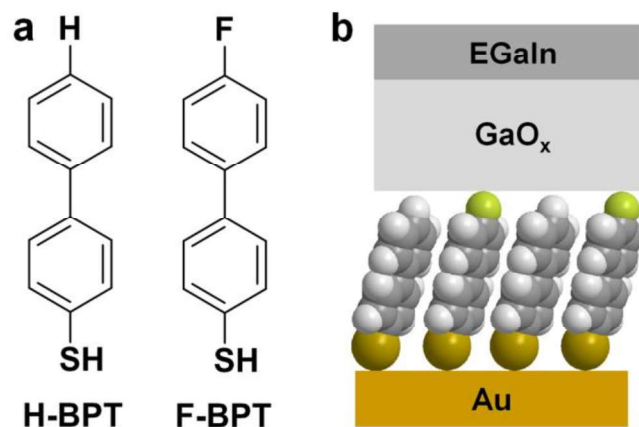
Figure 4.7. (a) SAM-forming molecules used in this project along with their acronyms. Note that H-BTP is usually abbreviated as BPT[51,231] but I prefer to use H-BTP in the present case, to underline the difference to F-BTP. H-BPT molecules were purchased commercially, while F-BPT molecules were provided by Prof. A. Ulman. (b) Two-terminal junction containing a binary H-BTP/F-BPT monolayer.

Beyond the expected homogeneous surface character, my interest in the H-BTP/F-BPT system is twofold. The first issue is the electrostatic properties of the H-BTP/F-BPT SAMs which can be reflected in both the work function behavior and X-ray photoemission. The electrostatic properties of binary monolayers represent an important issue[232–234] which, recently, became a subject of particular interest in context of electrostatic interfacial engineering and organic electronics.[28,30,31,230,231] The second, rather controversial issue, is the effect of halogen substitution on the electric transport properties of SAMs, described frequently as tunneling rate, in view of the dominant transport mechanism.[59] In the case of aliphatic backbone, halogen substitution of the terminal hydrogen atom (F, Br, Cl, or I) results in a progressive increase of the tunneling rate by up to three orders of magnitude, with only exception being F, providing no increase at all.[60] In contrast, in the case of aromatic backbone, halogen substitution of the terminal hydrogen atom (F, Br, Cl, or I) causes a decrease of the tunneling rate by about an order of magnitude, with the extent of this effect being independent of the identity of the halogen atom.[57,58] The tunneling rate, thus, exhibits no correlation with the work function and polarizability of the monolayers, varying progressively and strongly (for the work function) at going from I to F.[57] This behavior was tentatively explained by the strong confinement of the electrostatic field associated with the terminal halogen atom and by the compensation of the Au-SAM bond dipole and the terminal group dipole in the molecular junction.[57] In this context, the tunneling rate across the binary SAMs, comprised by a mixture of non-substituted and fluorine-substituted conjugated molecules can be of particular interest, shedding probably some light on the effect of the halogen substitution. In the present study, the respective measurements were performed with a two-terminal molecular junction which is schematically shown in Figure 4.7b.

The biphenylthiol-based SAMs were selected for the experiments since they can be reliably fabricated in high quality[51,57,214,231,235] and since the respective results can be directly compared with those for the analogous, halogen-substituted single-component monolayers, studied recently in context of the tunneling rate.[57]

4.2.1 SAM Preparation

H-BPT was purchased from Sigma-Aldrich and used as received. The F-BPT precursors were synthesized by our partners.[235] The single-component H-BPT and F-BPT SAMs were formed using standard procedure. The concentrations of H-BPT and F-BPT were 1 mM and 10 μM, respectively, to achieve a high quality, according to the literature recipes[51,231] and our preliminary experiments. The binary SAMs were prepared by coadsorption of both precursors; with their relative portions in solution (ethanol) being varied as 1:3, 1:1 and 3:1 and the joint concentration set at either 20 or 40 μM.

4.2.2 XPS
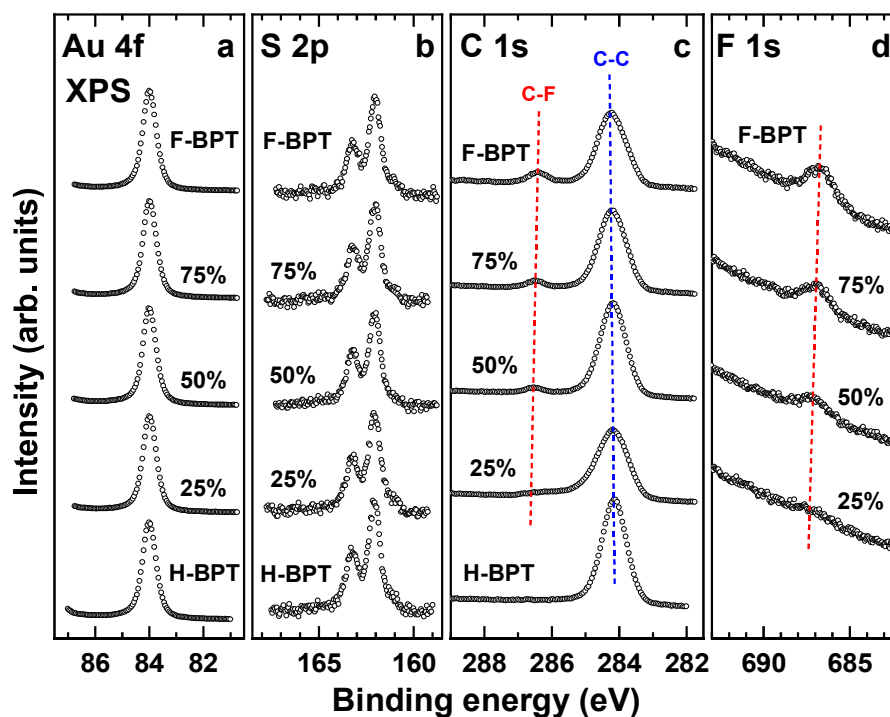
Figure 4.8. (a) Au $4f_{7/2}$, (b) C 1s, (c) S 2p, and (d) F 1s XP spectra of the single-component and mixed H-BPT and F-BPT SAMs. The spectra were acquired at photon energies of 350 eV (a- c) and 750 eV (d). The spectra of the mixed SAMs are marked with the portions of F-BPT in the solutions from which these SAMs were formed. Individual peaks in the C 1s spectra are marked; the positions of these and F 1s peaks are traced by inclined red and blue dashed lines (see text for details).

The Au $4f_{7/2}$, C 1s, S 2p, and F 1s XP spectra of the single-component and mixed H-BPT and F-BPT SAMs are presented in Figure 4.8. The Au $4f_{7/2}$ spectra in Figure 4.8a exhibits similar intensity over the entire series, along with the analogous laboratory XP spectra and the synchrotron-based XP spectra acquired at the primary photon energies of 580 eV and 750 eV (not shown). This suggests a similar effective thickness for all SAMs studied, which was additionally supported by a quantitative evaluation of this parameter (see below).

The S 2p spectra of all monolayers in Figure 4.8b exhibit a single doublet at ~162.0 eV (S $2p_{3/2}$), representative of the thiolate species bound to noble metal substrates,[210] underlying the SAM character of both single-component and binary films. The position of this doublet does not vary over the series, suggesting, in accordance with the literature,[51] that the electronegative substitution at the 4'-position does not affect the electronic state of the thiolate group. The intensity of this doublet is similar for all SAMs studied, suggesting, in accordance with the Au 4f data (see above), a similar molecular packing density over the series, which was verified by the quantitative evaluation of this parameter (see below).

The C 1s spectrum of the H-BPT SAM in Figure 4.8c exhibits a single, nearly symmetric peak at ~284.2 eV, associated with the biphenyl backbone.[51,214,231] The analogous spectrum of the F-BPT SAM shows a similar, slightly asymmetric peak at ~284.15 eV (C□C), accompanied by a low intensity peak at 286.4 eV (C-F). These features stem from the aromatic backbone and the carbon atom bound to fluorine, respectively. The spectra of the mixed films exhibit a continuous variation at going from the H-BPT to F-BPT case, with appearance and progressive increase in the intensity of the C-F peak and a change in the shape of the C□C peak. The positions of the peaks vary in the systematic way as well but the respective variation is quite small, as illustrated in Figure 4.9a and Figure 4.9b.
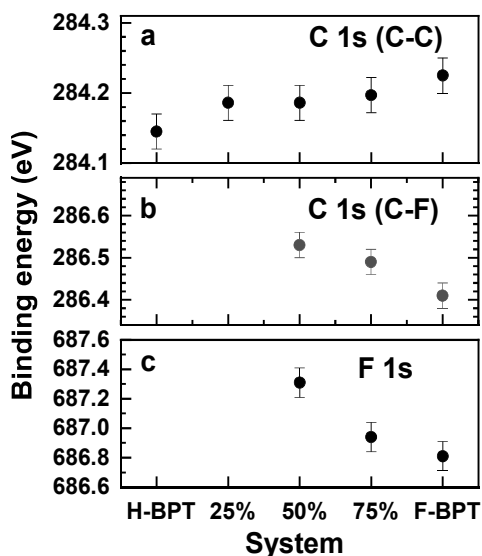
Figure 4.9. The BE positions of the (a) C-C and (b) C-F peaks in the C 1s XP spectra of the single-component and binary H-BPT and F-BPT SAMs as well as BE positions of the (c) F 1s peak in the spectra of these monolayers. The binary SAMs are labeled by the portions of F-BPT in the solutions from which they were formed.

The F 1s spectrum of the F-BPT SAM in Figure 4.8d exhibits a single peak at 686.8 eV corresponding to the terminal fluorine atom. This peak is also perceptible in the spectra of the binary films, exhibiting, as expected, a progressive decrease in intensity with decreasing content of F-BPT. This decrease is accompanied by continuous variation of the BE position of the peak, as illustrated in Figure 4.9c.

Along with the above analysis of the XP spectra, their quantitative evaluation in context of the effective thickness and packing density was performed. The derived values are compiled in Table 4.2. Accordingly, the effective thickness varied from 11.5±0.2 Å to 9.8□0.2 Å at going from the H-BPT to F-BPT SAM, with the H-BPT value correlating well with the literature data (11.7-12.1 Å)[51,57,214,231] and the F-BPT value being somewhat lower (11.9-12.1 Å).[51,57] The packing density varied from 4.6×10^{14} molecules/cm^2 to $4.1\square10^{14}$ molecules/cm^2 at going from the H-BPT to F-BPT SAM, with the H-BPT value correlating well with the literature data ($\sim4.6\times10^{14}$)[3,57] and the F-BPT value for being somewhat lower (4.57×10^{14}).[57] But, in any case, both single-component and binary H-BPT and F-BPT SAMs were densely packed and well-defined. It should also be noted that the O 1s spectra of all SAMs did not exhibit any perceptible signal, once again underlining the quality and well-defined character of the monolayers.

Table 4.2. Parameters of the single component and binary H-BPT and F-BPT SAMs derived from the XPS and NEXAFS data: effective thickness, packing density (±5%), average tilt angle of the π* orbitals, and average molecular tilt angle. The mixed SAMs are listed according to the portions of F-BPT in the solutions from which they were formed.

Monolayer	Effective thickness (Å)	Packing density molecules/cm^2	Tilt angle of the π* orbitals (°)	Molecular tilt angle (°)
H-BPT	11.5 ±0.2	4.6×10^{14}	82 ±3°	10 ±3°
25%	11.2 ±0.2	4.4×10^{14}	80.5 ±3°	11 ±3°
50%	10.2 ±0.2	4.4×10^{14}	77.5 ±3°	15 ±3°
75%	10.2 ±0.2	4.3×10^{14}	72.5 ±3°	21 ±3°
F-BPT	9.8 ±0.2	4.1×10^{14}	68.5 ±3°	25.5 ±3°

4.2.3 NEXAFS Spectroscopy

Representative C K-edge NEXAFS data for the single-component and mixed H-BPT and F-BPT SAMs are compiled in Figure 4.10. The spectra in Figure 4.10a corresponds to the so-called magic angle of X-ray incidence (55°) and are exclusively representative of the electronic structure of the monolayers.[171] Complementary, the difference spectra in Figure 4.10b represent fingerprints of orientational order in the systems, emphasized by the presence of peaks at the positions of the characteristic absorption resonances.[171]

The 55° spectrum of the H-BPT SAM in Figure 4.10a exhibits the characteristic absorption structure of oligophenyl-based monolayers including the strong π$_1$* resonance at ~285.0

eV (1), a R*/C-S* resonance at ~287.0 eV (2), π_2* resonance at ~288.8 eV (4), and several broader σ* resonances (5-7) at higher excitation energies.[171,213,214,217] The 55° spectrum of the F-BPT SAMs mimics generally the above resonance structure, except for the splitting of the π_1* resonance into the π_{1b}* (1a) and π_{1b}* (1b) features, driven by the electronegative 4'-substituent.[51] The dominant $_{1a}$* resonance at ~285.15 eV is slightly shifted with respect to the π_1* one, while the comparably weak π_{1b}* resonance at ~287.2 eV overlaps with the R*/C-S* feature. The 55° spectra of the mixed SAMs are similar to those of the H-BPT and F-BPT monolayers, exhibiting a continuous but hardly perceptible variation with the relative composition.
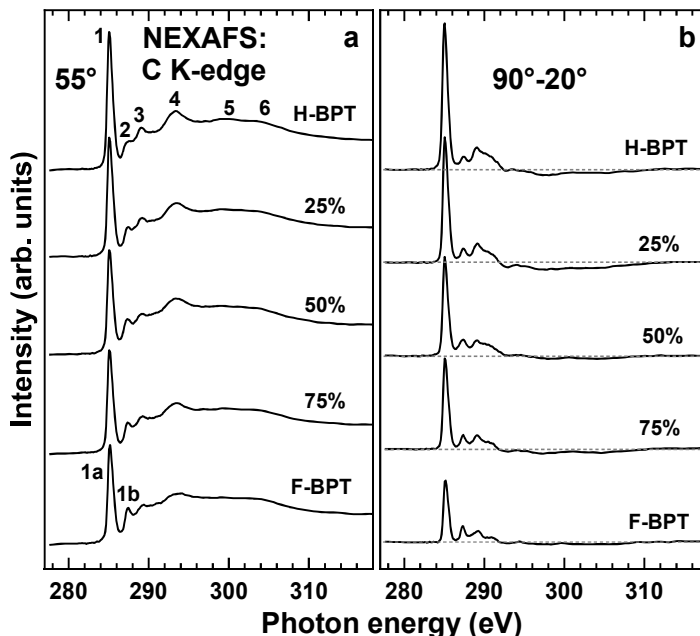

Figure 4.10. C K-edge NEXAFS spectra of the single-component and mixed H-BPT and F-BPT SAMs: (a) the spectra acquired at an X-ray incidence angle of 55°; (b) the difference between the spectra collected under the normal (90°) and grazing (20°) incidence geometry. The spectra of the mixed SAMs are marked by the portions of F-BPT in the solutions from which they were formed. Individual absorption resonances are marked by numbers and letters (see text for the assignments). The horizontal gray dashed lines in the panel b correspond to zero.

The difference spectra of both single-component and binary SAMs in Figure 4.10b exhibit pronounced positive peaks at the positions of the π* resonances and negative peaks at the positions of the σ* resonances. In view of the orientation of the respective transition dipole moments, viz. perpendicular and parallel to the ring plane, respectively, this behavior suggests the expected upright molecular orientation with respect to the substrate over the entire series. The evaluation of the entire sets of the NEXAFS spectra within the standard formalism for a vector-like orbital[171,215] (the π_1*/π_{1a}* one in our case) resulted in the average tilt angles of these orbitals with respect to the surface normal compiled in Table 4.2. Accordingly, the average tilt angle varied gradually from 82.5° to 68.5° at going from the H-BPT to F-BPT SAM.

Based on the average tilt angles of the π_1^*/π_{1a}^* orbitals, α, average molecular tilt angles with respect to the surface normal, ß, can be calculated using $\cos \alpha = \sin ß \times \cos \gamma$, where γ is the molecular twist angle describing rotation of the molecular backbone around the molecular axis with respect to the tilt plane.[222] It is defined such that it is zero when the tilt occurs perpendicular to the backbone plane. The latter angle cannot be determined from the NEXAFS data (except for a specially derivatized molecules)[223] and is usually derived from bulk structures, IR data, or from simulations. In the present case, I will rely on the value for the bulk biphenyl (32°),[226–228] following the approach of refs [51,214,215]. The resulted average molecular tilt angles (with respect to the surface normal) for the single-component and binary SAMs are compiled in Table 4.2. The value for the H-BPT SAM is noticeably smaller than the literature ones (~23°)[51,214] while the value for F-BPT monolayer is close to the literature value (21.3°).[51] Note, however, that the real twist angle in the SAMs can differ from that of the bulk biphenyl and, additionally, depend on the SAM composition, so that the average molecular tilt angles in Table 4.2 should only be considered as tentative values.

4.2.4 UPS
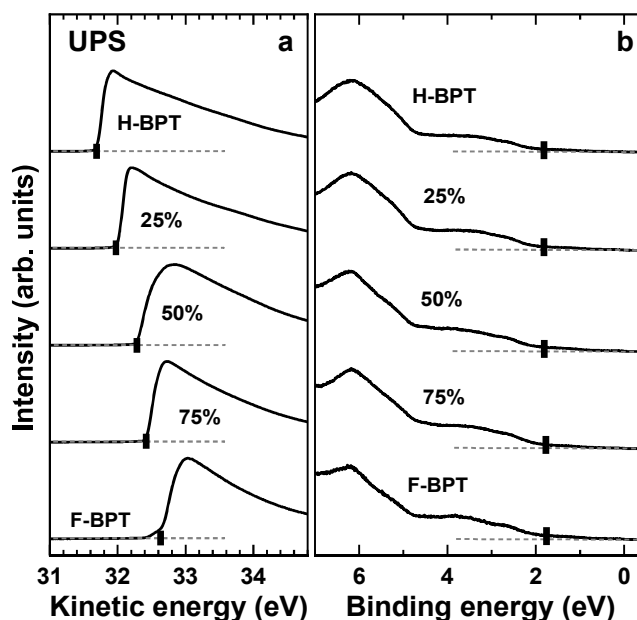
Figure 4.11. UP spectra of the single-component and mixed H-BPT and F-BPT SAMs in the secondary (a) electron cutoff and (b) valence band ranges. The spectra of the mixed SAMs are marked with the portions of F-BPT in the solutions from which they were formed. The positions of the secondary electron cutoff and the onsets of HOMO (ΔE_{HOMO}) are marked by vertical black solid lines in panel a and b, respectively. The horizontal gray dashed lines correspond to the zero level of the signal.

UP spectra of the single-component and mixed H-BPT and F-BPT SAMs in the secondary electron cutoff and valence band ranges are shown in Figure 4.11a and Figure 4.11b, respectively. The valence band spectra in Figure 4.11b is, above all, of importance in context of the energy offset of the highly occupied molecular orbital (HOMO) with respect

to the Fermi level (E_F), $\Box E_{HOMO}$. In the molecular junction experiments, this offset defines the barrier height for the charge transfer from the bottom gold electrode into the SAM.[57] In agreement with the literature data,[57] the data in Figure 4.11b suggest that the single-component H-BPT and F-BPT SAMs are characterized by similar ΔE_{HOMO}, which seems to be the case for the binary films as well.

In contrast, again in full agreement with the literature data,[57] the positions of the secondary electron cutoff in the single-componen H-BPT and F-BPT SAMs are distinctly different. The respective values, defining the work function of the SAM-modified substrate, are depicted in Figure 4.12a. These values agree well with the literature ones, viz. 4.15-4.35 eV for the H-BPT SAM and 5.2 eV for the F-BPT monolayer.[3,57] As to the binary SAMs, the position of the secondary electron cuttof (Figure 4.11a) and, consequently, the values of the work function (Figure 4.12a) are intermediate with respect to those of the single-component monolayers, showing a gradual variation with the relative SAM composition.
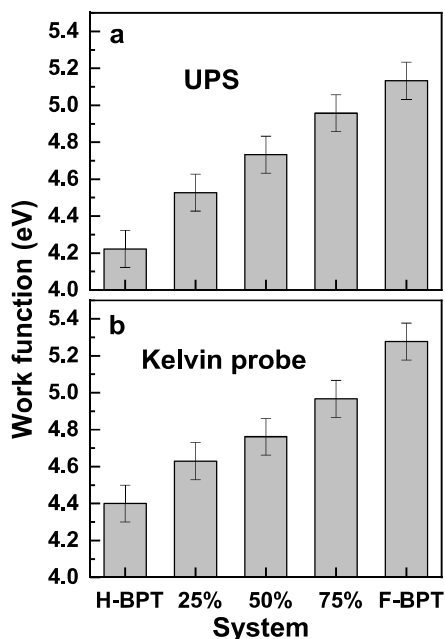

Figure 4.12. Work function values for the single-component and binary H-BPT and F-BPT SAMs derived from the (a) UPS and (b) Kelvin probe (b) data. The binary SAMs are labeled by the portions of F-BPT in the solutions from which they were formed.

4.2.5 Kelvin Probe

The work function values for the single-component and binary H-BPT and F-BPT SAMs derived from the Kelvin probe data are presented in Figure 4.12b. Whereas the absolute values of the work function differ to some extent from the UPS-derived ones (by 0.1-0.2 eV), the general behavior over the series is well reproduced. The work function is the lowest in the case of the single-component H-BPT SAM, increasing gradually upon the

admixture of F-BPT (binary monolayers) and achieving finally the maximum value for the single-component F-BPT SAM.

4.2.6 Tunnelling Rate across the Molecular Framework
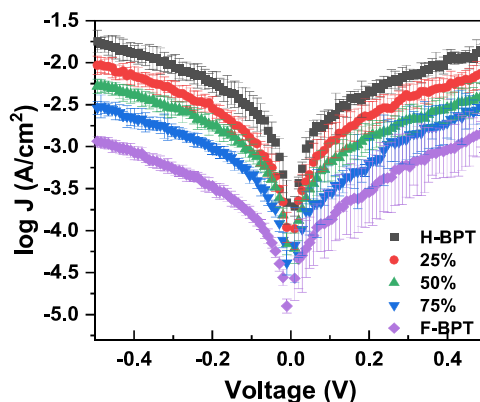
Figure 4.13. Semilogarithmic current-density versus voltage (bias) plots for the Au/SAM//EGaIn junctions with the single-component and binary H-BPT and F-BPT SAMs. The legend is given in the plot; the mixed SAMs are labeled by the portions of F-BPT in the solutions from which they were formed.

The log J vs. V plots for the Au/SAM//EGaIn junction with the single-component and binary H-BPT and F-BPT SAMs are presented in Figure 4.13. "/" indicates the SAM-substrate interface with a covalent-like coupling provided by the thiolate anchor (see section 3.1), while "//" represents the "weak coupling" interface between the SAMs and the top EGaIn electrode, covered by an ultrathin GaO_x film (see Figure 4.7b). The corresponding histograms for log |J| at representative bias -0.5 V and +0.5 V can be found in Figure A.1 in the supplementary data section. The plots for the single-component films agree well with the literature data[57] exhibiting noticeably higher current density values for the H-BPT SAM than for the F-BPT monolayer for the entire range of the voltage variation. Significantly, the observed difference (by about an order of magnitude) and even the absolute values of the current density correlate well the literature ones,[57] which, on the one hand, underlines the reliability of the presented experimental data, acquired with the distinctly different setup (see section 3.2.5) and, on the other hand, evidences the reliability of the effect of the halogen substitution in general, observed not only for the biphenyl-based SAMs but for the monolayers with a shorter aromatic backbone as well.[58]

Significantly, the log J vs. V plots for the junctions containing the binary SAMs are located between those for the single-component monolayers, with the values varying gradually with the SAM composition at every particular bias. This behavior is additionally emphasized by Figure 4.14 where the values of log|J| at the selected positive (Figure 4.14a) and negative (Figure 4.14b) bias values are presented. Accordingly, the log|J|values for the binary SAMs vary in a close-to-linear fashion between those for the single-component monolayers. Note that the difference between the log|J| values corresponding to the positive

and negative bias values is small but perceptible, so that I presented these values separately in Figure 4.14a and Figure 4.14b.
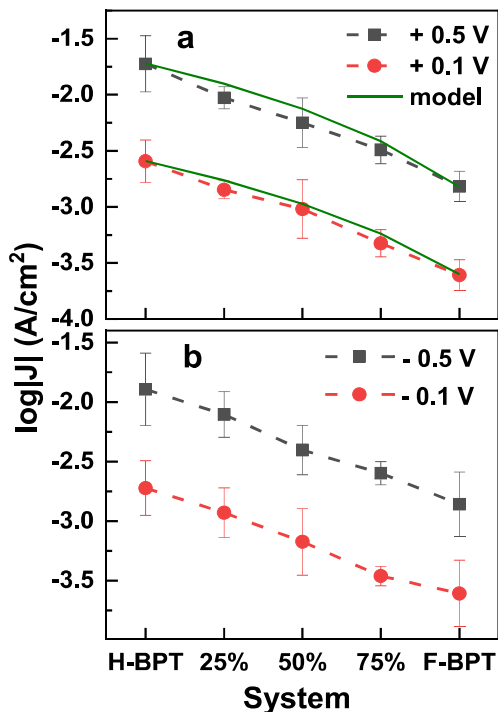

Figure 4.14. Values of log|J| at selected (a) positive and (b) negative bias values for the Au/SAM//EGaIn junctions with the single-component and binary H-BPT and F-BPT SAMs. The legend is given in the plots; the mixed SAMs are labeled by the portions of F-BPT in the solutions from which they were formed. In panel (a) the results of the model calculations for the charge transport mediated by superposition of independent molecular wires are presented (solid green lines); see section 4.3 for details.

4.2.7 Discussion

SAM Composition. The composition of the binary SAMs was determined on the basis of both laboratory and synchrotron-based XPS data and the work function data, taking the values for the single-component monolayers as the references. In the case of the XPS data, I mostly relied on the F 1s intensity and, in the case of synchrotron, could also use the intensity of the C☐F peak in the C 1s spectra (see Figure 4.8c). In the case of the work function, I considered its values as a fingerprint of the composition. The resulting relation between the relative composition of the binary SAMs and the portion of F-BPT in the solutions is presented in Figure 4.15. Accordingly, the composition of the SAMs nearly mimicked that in the solution, even though certain deviations are observed. Note that the data represent several different series of the samples, so that the reproducibility of the relative SAM composition was good enough.

Generally, deviations of the composition of binary SAM from that in solution are well possible, especially in case of preferential adsorption of one of the components[236] or

minimization of dipole-dipole interaction between the SAM constituents.[30,50,236] In the present case, the structures of H-BPT and F-BPT are identical, except for the terminal atom (see Figure 4.7a), so that no preferable adsorption of one of these molecules can be expected. Also, the dipole moment associated with the electronegative terminal fluorine atom of F-BPT is most likely of no importance for the SAM composition since its contribution is presumably small as compared to the other structure-building interactions, mediated by the thiolate-gold bonds and biphenyl backbones. Similar situation occurs, e.g., for the binary mid-ester substituted alkanethiolate SAMs (opposite orientations of the dipole moments for the SAM constituents),[230] in contrast to the analogous binary pyrimidine-substituted aromatic monolayers, where the contribution of the dipole-dipole interaction is of larger importance, favoring the 50%:50% composition.[30] In the present case, the presence of the electronegative terminal fluorine atom of F-BPT represents rather a positive factor in context of the quality of the mixed SAMs, promoting a maximal separation of the F-BPT molecules in the SAM matrix and, consequently, favoring molecular intermixing and preventing phase separation. Note that, according to the XPS and NEXAFS spectroscopy data, the parameters of the binary SAMs, such as the effective thickness, packing density, and molecular inclination, varied to some extent over the series (see Table 4.2) but this variation was rather small.
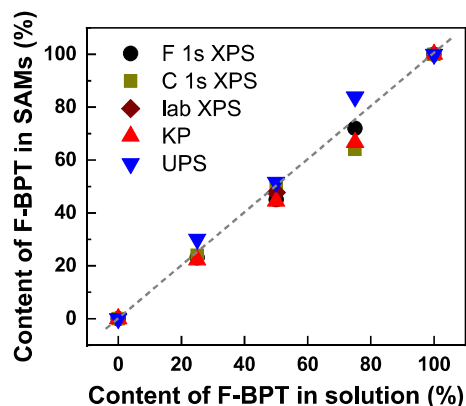
Figure 4.15. The portions of F-BPT in the single-component and binary H-BPT and F-BPT SAMs vs. the portions of F-BPT in the solutions from which these SAMs were formed. The legend is given in the plots (see text for details). The gray dashed line represents a linear dependence with a slope of 1, as a guide for the eyes.

Electrostatic Properties. The most pronounced electrostatic effect is the variation of the work function of the substrate upon the SAM formation. Whereas the work function of the clean Au(111) substrate is about 5.2-5.3 eV,[25,198] it decreases to ~4.3 eV upon the formation of the non-polar H-BPT SAM (see Figure 4.12). The reason for this behavior is the Au□SAM bond dipole, directed upwards from the substrate and associated with a charge redistribution at the substrate-SAM interface.[22,237] In the case of the F-BPT monolayer, similar to other fluorinated SAMs,[24,238] there is an additional dipole, associated with the terminal, electronegative fluorine atom and directed to the substrate. The resulting work function is ~5.2 eV, differing by 0.9-1.0 eV from that of the H-BPT SAM. The work function of the binary monolayers can be precisely tuned within this range by varying their

relative composition (see Figure 4.12), which can be potentially of interest for applications requiring precise adjustment of the work function.

Along with the work function, electrostatic effects can also be expected in photoemission.[3,30,239] This is indeed the case, as illustrated by Figure 4.9, but the extent of these effects is quite small, especially in relation to the biphenyl backbone. The binding energy of the C 1s (C☐C) peak varies by just ~0.1 eV over the series (Figure 4.9a), mediated by the charge transfer from the terminal fluorine atom[51] or/and by the respective dipole. In contrast, the binding energy of the C 1s (C☐F) peak varies by ~0.15 eV and that of F 1s peak by ~0.6 eV upon just 50% admixture of H-BPT into F-BPT matrix (Figure 4.9b and Figure 4.9c). Interestingly, the above binding energy shift of the F 1s peak correlates well with the respective work function change, viz. 0.4-0.5 eV (see Figure 4.12). This is understandable since both these effects have the same origin, viz. the presence of the dipolar "sheet" at the SAM-ambient interface. This two-dimensional "sheet" is strongly confined at the interface[68] providing maximal effect onto the "inner" fluorine atoms and successively lesser effect onto the adjacent carbon atom and the entire biphenyl backbone. The different directions of the work function and binding energy changes upon variation of the SAM composition are also typical for binary monolayers and were observed in other systems in which the electrostatic potential was varied.[31]

Charge Tunneling Rates. The charge tunneling rates across the molecular framework in the Au/SAM/EGaIn junctions represent the most interesting and controversial issue of the present study. The results for the single-component H-BPT and F-BPT SAMs agree well with the literature data,[57,58] suggesting much higher tunneling rate in the H-BPT case. Moreover, referring to the biphenyl-based SAMs only, not only qualitative but also quantitative agreement with the literature data[57] is achieved. The new element are the data for the binary SAMs, with the current density values turned out to vary gradually with the relative SAM composition between those for the single-component monolayers (see Figure 4.13 and Figure 4.14). On the one hand, this observation means that the tunneling rate can be precisely tuned by mixing the non-substituted and halogen-substituted aromatic molecules in the binary SAMs, which most likely can be extended to other types of SAM-forming molecules. On the other hand, this observation can probably shed some light on the reasons behind the behavior of the halogen-substituted SAMs in context of the charge tunneling rate. The tunneling rate across halogenated aromatic monolayer junctions are noticeably lower than in the non-substituted case (H-BPT here) but is independent of the identity of the halogen atom, such as F, Cl, Br, or I.[57,58] The tunneling rate has, thus, correlation, neither with the polarizability of the SAMs, nor with the dielectric constant ☐$_r$ varying from 2.3 (F-BPT) to 3.2 (I-BPT), nor with the respective work function varied from ~5.2 eV (F-BPT) to ~4.5 eV (I-BPT), nor with the van der Waals radius of halogen varied from 1.47 Å (F) to 1.98 Å (I).[57] The only relevant parameter which hardly changes over the F, Cl, Br, or I series and for the H-BPT SAM as well is the position of the HOMO with respect to the Fermi energy, defining the injection barrier for the charge transfer from the substrate[57]. The respective molecular orbital in all X-BPT SAMs (X = H, F, Cl, Br, and I) is delocalized along the entire molecular backbone, including the anchoring group and the terminal atom, representing, thus, an efficient pathway for the tunneling.[57] This probably explains the constancy of the tunneling rates for X = F, Cl, Br, and I but does not accounts for the difference of these rates from that for the H-BPT SAM. The latter could be, however, explained by a theoretic model suggesting the appearance of a significant

compensation dipole, induced along the backbone of H-BPT to equalize the binding dipole upon the contact to the top electrode.[574] In contrast, such an induced dipole is small for a halogen substitution since the binding dipole is initially compensated by the interfacial one, associated with the halogen substitution. This results in the different injection barriers for the SAM//EGaIn interface in the H-BPT and X-BPT (X = halogen) cases and, consequently, in the different tunneling rates.[57] Whereas this explanation can only be considered as a tentative one, the importance of the aromatic backbone is undisputed since the analogous halogenated aliphatic monomolecular junctions exhibit a distinctly different behavior, with no difference between the H and F substitutions and four orders of magnitude difference between the F and I substitutions.[60]

The results of the present study also suggest the nearly identical offsets in energy of the HOMO to E_F for the H-BPT and F-BPT SAMs, which also turned out to be the case for the binary monolayers. Thus, there is no correlation between the respective unchanging injection barrier and the tunneling rate, varying by about order of magnitude over the series. This variation is accompanied by the variation of the work function (see Figure 4.12) and $\square_r$ (from 2.5 for the H-BPT SAM to 2.3 for the F-BPT monolayer)[34] but this correlation is most likely just a coincidental one, in view of the literature data for the X-BPT SAMs (X = H, F, Cl, Br, and I) discussed above.

An important question to answer is whether the charge transport in the binary X-BPT/F-BPT SAMs is predominantly mediated by the SAM as a whole, relying on build-in fields, or by individual molecules within the SAM, acting as independent molecular wires. In the former case, taking into account the conclusions of ref [57] (see above) and relevant considerations of ref [240], one can assume that the dipole induced upon contact of a top electrode depends on the composition of the binary SAMs, changing accordingly the tunneling conditions and, consequently, the tunneling rate across the monolayers. One can then likely expect a nearly linear variation of the transfer with the nearly same efficiency (tunneling rate) as in the respective single-component films and that these molecules mediate the charge transfer in parallel fashion. The system can then be modeled as an array of independent molecular wires connected to the bottom and top electrodes in parallel and having the resistances attenuation factor with the film composition and, consequently, analogous variation of the log$\square$J$\square$ for the series, which is close to the behavior observed for the binary SAMs of this study, as shown in Figure 4.14. In the case of tunneling mediated by superposition of independent molecular wires, one can assume that both H-BPT and F-BPT species participate in the charge differing by an order of magnitude, mimicking those in the single-component H-BPT and F-BPT SAMs. The resulting curves, normalized to the positive bias log$\square$J$\square$ values for the single-component monolayers, are shown in Figure 4.14a. These curves are distinctly non-linear in the given semilogarithmic plot, whereas the experimental points exhibit a close-to-linear trend as seen in Figure 4.14. Consequently, the observed behavior of the tunneling rate can be rather ascribed to collective effect of the F-BPT and H-BPT molecules in the binary SAMs, following the mechanism suggested in ref [57] (see above).

At the same time, the model involving a superposition of independent molecular wires cannot be completely excluded since the respective curves lie within the error bars of the experimental points, even though exhibiting a distinct non-linear character. It is also possible that the charge transfer efficiency of the H-BPT and F-BPT "wires" in the binary SAMs will be different from that in the single-component films. In particular, the

difference in the dimensions of the terminal fluorine and hydrogen atoms, viz. 1.1 Å and 1.47 Å, respectively, can hinder to some extent the efficient coupling of the H-BPT molecules, "buried" between the F-BPT ones in the binary SAMs, to the EGaIn electrode. Finally, a certain intermolecular "cross-talk" upon the charge transport is possible as well, as was demonstrated for strongly interacting molecular assembles.[241,242]

4.2.8 Conclusions

In the present work we have studied the structure, composition, electrostatic properties, and charge tunneling rates in molecular junctions for a series of single-component and binary SAMs composed of H-BPT and F-BPT on Au(111) substrates. Both single-component and binary SAMs were found to be well-defined and densely packed, with all molecules bound to the substrate by the thiolate anchor and having an upright orientation with respect to the substrate. The exact structural parameters varied to some extent over the series but this variation was systematic and comparatively small. The relative composition of the binary SAMs was found to be very close to the relative contents of both molecules in the solutions from which these SAMs were formed. In view of the nearly identical molecular structure, differing by the terminal atom only, a homogeneous mixture of SAM-forming molecules in the binary monolayers was assumed, in contrast to the generally possible phase separation.

The mixing of H-BPT and F-BPT in the binary SAMs allows the work function of the functionalized substrate to be varied in a gradual and controlled fashion between the ultimate values for the single-component films, viz. ~4.3 eV and ~5.2 eV, respectively. The extent of the electrostatic effects in photoemission was rather small, affecting predominantly the apparent binding energy of the terminal fluorine atoms and, to an even lesser extent, the binding energy of the adjacent carbon atoms. The reason for this behavior is the strong spatial confinement of the step in the electrostatic potential associated with the terminal fluorine atoms.

The charge tunneling rate across the molecular framework was found to be noticeably (by about an order of magnitude) higher for the H-BPT SAM than for the F-BPT monolayer, in qualitative and quantitative agreement with the literature data. Significantly, the tunneling rates for the mixed SAM turned out to be intermediate to those of the single-component monolayers, varying in a gradual fashion with the relative SAM composition between the respective ultimate values. This means that the tunneling rate in a molecular junction can be generally controlled by mixing molecules with different charge transfer abilities in a binary SAM. The analysis of the experimental data for the systems of the present study and available literature data for the SAMs with different halogen substitutions led us to the conclusions that the charge transport in the binary SAMs is most likely mediated by the SAM as a whole, defined by the composition-dependent dipole induced upon contact of the SAM to a top electrode. Nevertheless, the scenario of charge transfer mediated by super- position of independent molecular wires cannot be completely excluded in view of the complexity of the systems and a variety of the factors affecting their behavior.

4.3 Electrostatic effects in charge transport by the example of CH$_3$-BPT and CF$_3$-BPT
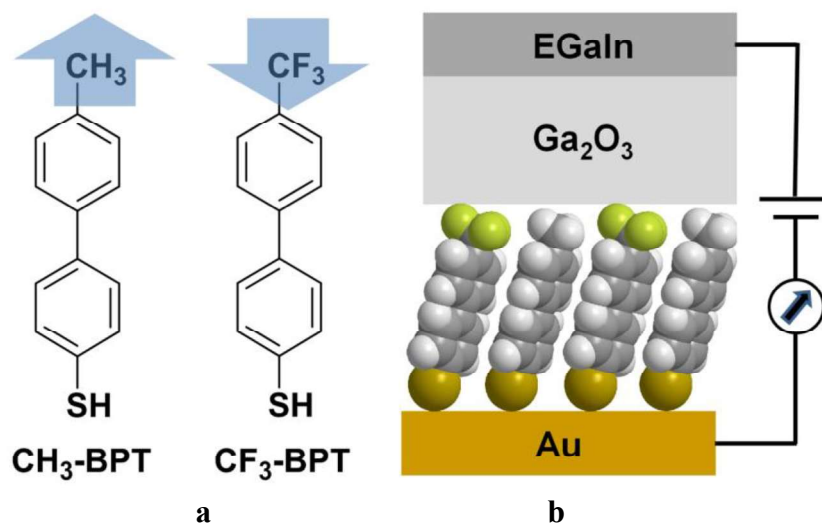
Figure 4.16: (a)SAM-forming molecules used in this study along with their acronyms (at the left). The molecules were synthesized by the group of Prof. Terfort.[54] (b) A schematic of a two-terminal junction, with the bottom Au electrode (substrate) and top EGaIn electrode, containing a binary CH$_3$-BPT/CF$_3$-BPT monolayer, Au/SAM//Ga$_2$O$_3$/EGaIn (at the right). Note that "/" indicates either the SAM-substrate interface (covalent bonding) or the interface between Ga$_2$O$_3$ and EGaIn, while "//" indicates a non-covalent contact between the tail groups of the SAMs and Ga$_2$O$_3$. The directions of the dipole moments, associated with the tail groups of CH$_3$-BPT and CF$_3$-BPT, are shown by the blue arrows.

The substantial difference between the tunnelling rate for the non-substituted and halogen-substituted aromatic SAMs led to the idea that this parameter can be tuned by mixing the respective molecules in binary monolayers, which was indeed demonstrated by the example of the C$_6$H$_5$-C$_6$H$_4$-SH (H-BPT) and F-C$_6$H$_4$-C$_6$H$_4$-SH (F-BPT) films in the previous section.[53] The analysis of this variation supported the ideas about collective electrostatic effects in halogen-substituted SAMs in their relation to the tunnelling rate,[57] even though non-equivocal conclusions could not be derived.[53]

In this context, I decided to look at a related system, viz. the single-component and binary SAM of methyl- (CH$_3$-BPT) and trifluoromethyl-substituted biphenylthiols (CF$_3$-BPT) on Au(111) (Figure 4.16a). Note that, generally, mixed SAMs of CH$_3$- and CF$_3$-terminated thiols represent a useful and widely used model system, e.g., for continuous WF variation, adjustment of the frictional properties,[55] etc. The single-component and binary CH$_3$-BTP/CF$_3$-BPT SAM were studied as well, e.g., to find a correlation between the composition of the binary SAMs and the parameters of the preparation procedure, such as the dielectric constant of solvent, to monitor band shifts in infrared spectra, etc.[50,243] In the present work, we put the emphasis on the charge tunnelling rate in these films measured with the established EGaIn setup (Figure 4.16b), monitoring at the same time another important parameter - the transition voltage, V_T.[244] This parameter is believed to represent an approximate measure of the tunneling barrier height, providing the difference between

the energy of the accessible frontier orbital of a molecule and the Fermi level of the electrode in an assembled junction.[244–246] Even though the precise physical meaning of V_T is still under debate,[37,183,187,247,248] the possibility to gain such information is quite useful, since there are no alternative ways to look inside the tunneling junction, except of theoretical simulations, suffering frequently from a variety of approximations.

4.3.1 SAM Preparation

The binary SAMs were prepared by coadsorption of CH$_3$-BPT and CF$_3$-BPT, with their relative portions in solution (ethanol) being varied as 1:3, 1:1 and 3:1 and the joint concentration set at 1 mM. The CH3-BPT and CF3-BPT precursors were synthesized by our partners.[235] For the different experiments several sets of the samples were prepared, with good reproducibility and consistency of the results. The quality and composition of the SAMs were verified by XPS, synchrotron-based XPS, infrared spectroscopy (IR), NEXAFS spectroscopy, and STM.

4.3.2 XPS

The quality and composition of the SAMs were verified by XPS. Representative C 1s and F 1s XP spectra of the single-component and mixed CH$_3$-BPT and CF$_3$-BPT SAMs are compiled in Figure 4.17; respective Au 4f$_{7/2}$ and S 2p spectra can be found in the supplementary data section (Figure A.2a and Figure A.**2**b). The C 1s spectrum of the single-component CH$_3$-BPT SAM in Figure 4.17a exhibits a single peak at ~284.1 eV (and a small shoulder at ~285 eV) representing a joint contribution of the biphenyl backbone and the terminal methyl group.[249] The analogous spectrum of the single-component CF$_3$-BPT SAM is dominated by the intense peak at ~284.3 eV, stemming from the biphenyl backbone (C☐C), and a low intensity peak at ~292.0 eV, associated with the terminal trifluoromethyl group (☐CF$_3$).[250] The spectra of the binary SAMs exhibit these two peaks as well, but the intensity of the ☐CF$_3$ feature decreases progressively with decreasing portions of CF$_3$-BPT in the solutions from which the SAMs were formed. The F 1s XP spectra in Figure 4.17b exhibits similar behavior. They show only one peak at 687.3 - 687.7 eV, which, as expected, has a maximum intensity for the single-component CF$_3$-BPT SAM and lower intensities for the binary SAMs, correlating with the portions of CF$_3$-BPT in the solutions from which these monolayers were formed.

The intensities of the C 1s (-CF$_3$) and F 1s peaks represent a measure of the relative CF$_3$-BPT content in the binary SAMs, as far as they are normalized to the values for the single-component CF$_3$-BPT monolayer. The respective data, including also the F 1s intensities measured with the laboratory XPS setup, are presented in Figure 4.18. Accordingly, the relative compositions of the binary SAMs mimic coarsely those of the solutions from which these SAMs were formed, but a certain scattering of the values and a slight deviation from the strictly linear, one-to-one relation could not be completely avoided. In particular, on the average, the CF$_3$-BPT content in the 25% samples was slightly underestimated based on the solution composition and, for the 75% samples, slightly overestimated. Such an S-

shape behavior can be a consequence of a slight preference of the 50%-50% composition, allowing to minimize the dipole-dipole interactions between the -CH$_3$ and -CF$_3$ substituted molecules within the SAMs.[31] Apart from the composition issue, the molecular mixture of both components can be assumed for the binary CF$_3$-BPT/CH$_3$-BPT monolayers as opposed to phase segregation.[55] First, a molecular mixture of both components is favorable in context of the dipole-dipole interaction at the SAM-ambient interface. Second, such a mixture is favorable in view of the steric considerations, since it allows for a dense molecular packing, evidenced for all the SAMs in the present study (see below), by dispersing the bulkier CF$_3$-BPT moieties in the CH$_3$-BPT "matrix". In addition to the intrinsic rigidity of the CF$_3$-BPT and CH$_3$-BPT molecules, excluding generally possible conformational defects, the molecular mixture character of the binary CF$_3$-BPT/CH$_3$-BPT SAMs allows to avoid specific complications related to surface morphology and interfacial defects.[251]
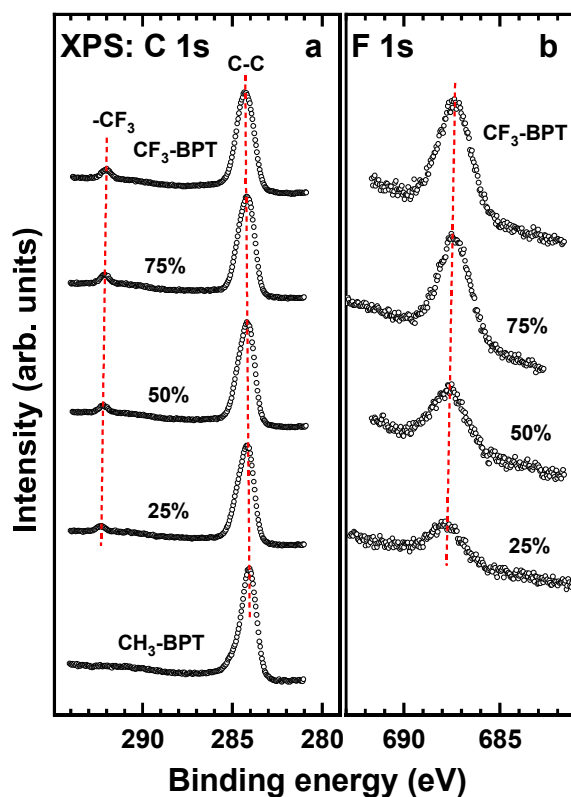
Figure 4.17: C 1s (a) and F 1s (b) XP spectra of the single-component and mixed CH$_3$-BPT and CF$_3$-BPT SAMs. The spectra were acquired at the synchrotron, at photon energies of 350 eV (a) and 750 eV (b). The spectra of the binary SAMs are marked with the portions of CF$_3$-BPT in the solutions from which these SAMs were formed. Individual peaks in the C 1s spectra are marked (see text for details). Red dashed lines trace the binding energy positions of the characteristic peaks.

Information about the molecular packing is provided by the C 1s, Au 4f, and S 2p XP data (Figure 4.17a, and Figure A.2 in the Appendix A). These data allowed to calculate the effective thickness and packing density of the SAMs, on the basis of the C 1s/Au 4f and S

2p (thiolate)/Au 4f intensity ratios, respectively, using the standard approach,[149,191] the literature values for the attenuation lengths,[150] and C16/Au as the reference.[252] The effective thicknesses were estimated at 13.9-14.5 Å - characteristic of substituted biphenyl SAMs[52] and varying only slightly over the series. The packing densities were estimated at $(4.0\text{-}4.2) \square 10^{14}$ molecules/cm^2, varying, once again, only slightly over the series. These values are smaller than those for alkanethiolates on Au(111) (4.63×10^{14})[252] but correspond to a dense molecular packing (see also STM data in the Appendix B). Note that the S 2p spectra of some monolayers do not only exhibit the spectral signature of thiolate, at ~162.0 eV for S $2p_{3/2}$, characteristic of fully homogeneous, thiolate-anchored SAMs,[62] but also a certain signal of unbound sulfur (thiol), at 163.5-163.6 eV for S $2p_{3/2}$.[210] If we suggest that this signal stems exclusively from the physisadsorbed molecules, "caught" at the SAM-ambient interface, their relative amount is quite small since the respective signal, opposite to that of thiolate, is not attenuated and, therefore, strongly exaggerated as compared to the signal of thiolate.[253]
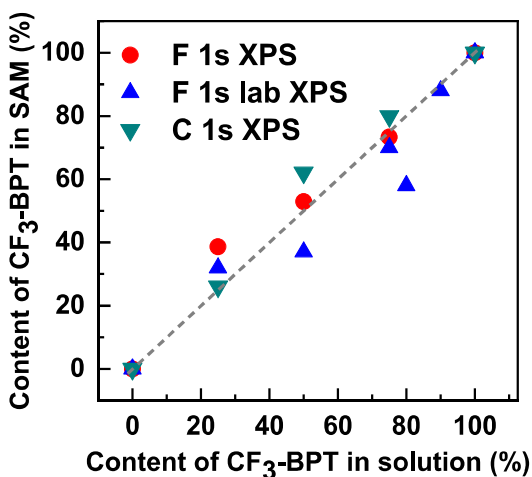
Figure 4.18: The portions of CF$_3$-BPT in the CF$_3$-BPT/CH$_3$-BPT SAMs vs. the portions of CF$_3$-BPT in the solutions from which these SAMs were formed. The values were derived from the XPS/NEXAFS data (see text for details); legend is given in the plot. The gray dashed line represents the ideal relation - a linear dependence with a slope of 1, as a guide for the eyes.

Note that the statement regarding the dense molecular packing in the CF$_3$-BPT/CH$_3$-BPT SAMs was fully supported by the STM data (see the Appendix B; Figure B.1-Figure B.3), which also provided information regarding the exact molecular packing, with the average values of the packing density close to those derived from the XPS data.

4.3.3 NEXAFS spectroscopy
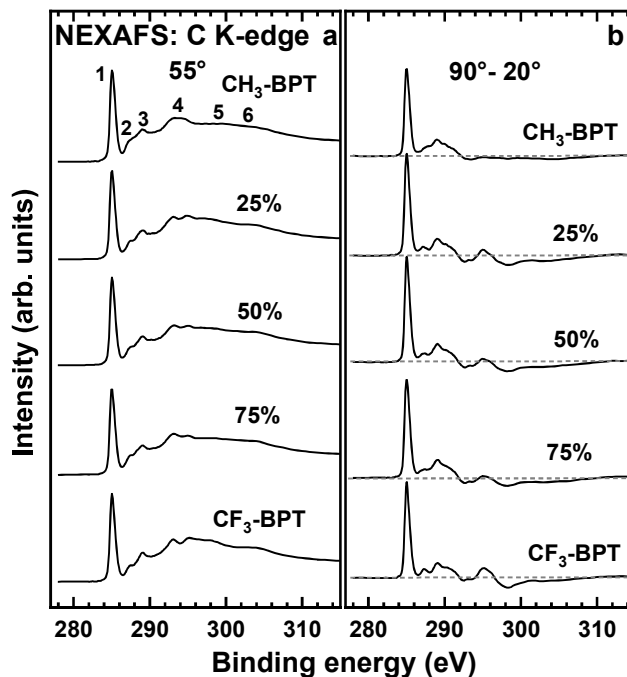
Figure 4.19: C K-edge NEXAFS spectra of the single-component and binary CH_3-BPT/CF_3-BPT SAMs: (a) the spectra acquired at an X-ray incidence angle of 55°; (b) the difference between the spectra collected under normal (90°) and grazing (20°) incidence geometry. The spectra of the binary SAMs are marked by the portions of CF_3-BPT in the solutions from which they were formed. Individual absorption resonances are marked by numbers (see text for details). The horizontal gray dashed lines in panel b correspond to zero.

Complementary information on the quality of the SAMs is provided by NEXAFS spectroscopy. The respective data are presented in Figure 4.19. The spectra in Figure 4.19a, acquired at the so-called magic angle of X-ray incidence (~55°), are exclusively representative of the electronic structure of the SAMs (unoccupied molecular orbitals), opposite to molecular orientation.[171] The spectra of both single-component and binary SAMs exhibit a characteristic resonance pattern of phenyl,[171,213,217] typical of SAMs with biphenyl backbone as well.[214,215,253] This pattern includes the dominant π_1^* resonance at ~285.0 eV (1), a R*/C-S* resonance at ~287.0 eV (2), π_2^* resonance at ~288.8 eV (3), and several σ^* resonances (**4-6**) at higher excitation energies. The spectrum of the single-component CF_3-BPT SAM exhibits an additional resonance structure at 294.0 - 296.0 eV (7), characteristic of the −CF_3 group,[254] perceptible also in the spectra of the binary monolayers.

The difference NEXAFS spectra in Figure 4.19b are characteristic of molecular orientation and orientational order in the SAMs, emphasized by the peaks at the positions of the specific absorption resonances.[171] These peaks are quite distinct in all spectra of the CH_3-BPT/CF_3-BPT SAMs being, at the same time, positive for the π^*-like resonances and

negative for the σ*-like ones. In view of the orientation of these orbitals with respect to the molecular backbone (perpendicular and within, respectively), such a dichroism implies an upright molecular orientation, as expected for SAMs. Numerical evaluation of the NEXAFS spectra within the standard theoretical framework,[171] specifically adapted to SAMs,[214,215] gives the average tilt angle of the π_1^* orbitals at 76-80°, varying slightly and non-systematically across the series. Considering possible twist of the molecules upon their tilt,[223] and taken the value of the twist angle from the bulk biphenyl data (32°),[71-73] the average molecular tilt angle in the single-component and binary CH_3-BPT/CF_3-BPT SAMs could be estimated at 12-17°. Similar to the bulk biphenyl,[226–228] a nearly planar molecular conformation can be assumed, since the dihedral rotation, typical of the molecular state of this molecule, is (nearly) lifted in densely packed molecular assemblies, including SAMs.[225] This is certainly applicable to the densely packed SAM of the present study, with the packing density varying only slightly over the series (see above).

Summarizing, the XPS data demonstrate that the single-component and binary CH_3-BPT/CF_3-BPT SAMs are predominantly comprised of the molecules bound to the substrate over the thiolate anchor. The spectroscopic and microscopic data consistently show that these SAMs exhibit a high packing density and a high degree of the orientational order, with the molecules tilted just slightly with respect to the surface normal. The compositions of the binary SAMs mimic those of the solutions from which they were prepared, even though a certain scattering and slight deviations from the one-to-one relation were recorded. No hints for phase separation could be found, supporting the concept of a truly homogeneous molecular mixture.


4.3.4 UPS and Kelvin probe

Valence structure and electrostatic properties of the SAMs were monitored by UPS and Kelvin Probe measurements. The UP spectra of the SAMs are presented in Figure 4.20, in the secondary electron cutoff (SECO) (Figure 4.20a) and valence band (Figure 4.20b) ranges, respectively. The valence band spectra exhibit a continuous evolution at going from CF_3-BPT to CH_3-BPT but the onset of the HOMO-derived state with respect to the Fermi level of the Au substrate exhibits only minor changes across the series. The position of this state agrees well with the calculations of the projected density of states (PDOS) in the given type of monomolecular films.[52] Significantly, according to the data in Figure 4.20b, this electronic state, crucially relevant in context of charge transport,[31] is nearly isoenergetic for all SAMs of the present study. Moreover, similar to the H-BPT/F-BPT case,[57] one can assume that the respective molecular orbital (HOMO) is delocalized along the entire molecular backbone, allowing efficient tunneling of the charge carriers. Also the energy barrier, associated with the tunneling into this orbital at the Au/SAM interface, is presumably the same for the CF_3-BPT and CH_3-BPT SAMs.[52]
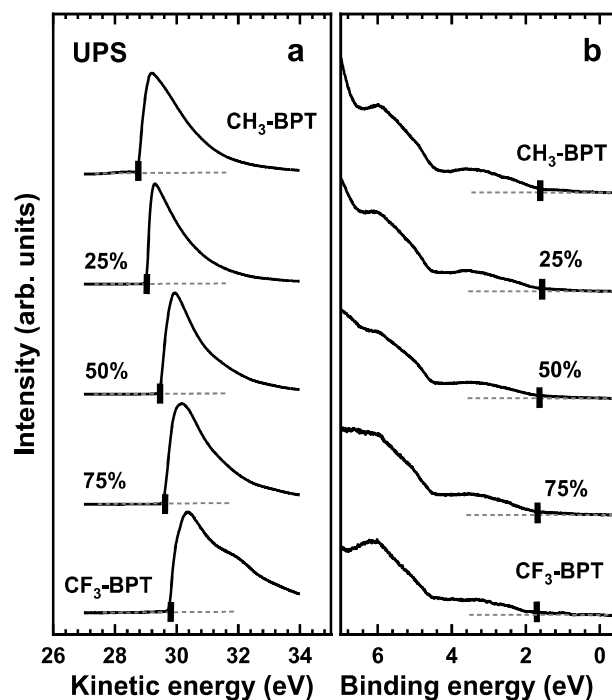
Figure 4.20: UP spectra of the single-component and binary CH$_3$-BPT/CF$_3$-BPT SAMs in the secondary electron cutoff (a) and valence band (b) ranges. The spectra of the binary SAMs are marked with the portions of CF$_3$-BPT in the solutions from which they were formed. The positions of SEGO and the onsets of HOMO are marked by vertical black solid lines in panels a and b, respectively. The horizontal gray dashed lines correspond to the zero level of the signal.

The SECO spectra in Figure 4.20a exhibit a continuous change in the position of SECO for the different SAMs, emphasizing a WF variation. The respective WF values are presented in Figure 4.21, along with the analogous values derived from the Kelvin probe (KP) experiments. The UPS- and KP-derived values in Figure 4.21a and Figure 4.21b, respectively, agree well with each other and show that the WF of the SAMs increases continuously from ~4.45 eV to ~5.5 eV at going from the CH$_3$-BPT monolayer to the CF$_3$-BPT one, over the entire composition range of the binary films. This behavior reflects a variation of the electrostatic potential at the SAM-ambient interface resulting from collective effects of the –CH$_3$ and –CF$_3$ tail groups. Due to the 2D arrangements of the molecules in the SAMs, the respective potential step is spatially confined in the region of the interface.[22,237,239]

Note that the same electrostatic effects are responsible for the shifts in the positions of the characteristic peaks in the XP spectra, presented in Figure 4.17. The exact information on these shifts is provided in the Appendix A(Figure A.3). A detailed discussion of this phenomenon can be found in ref [53].
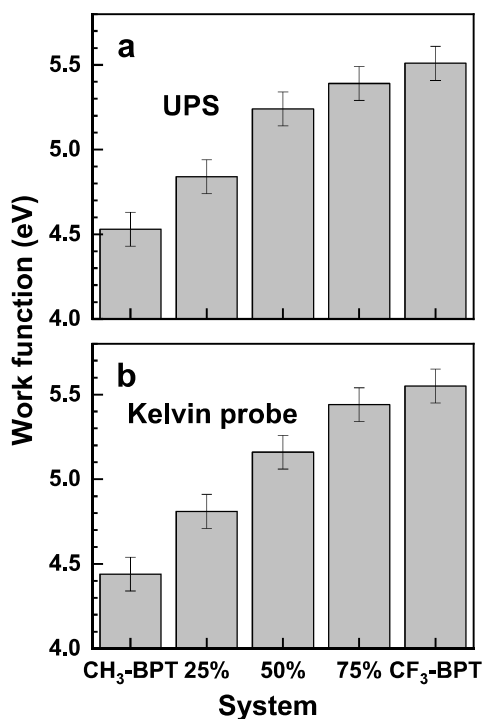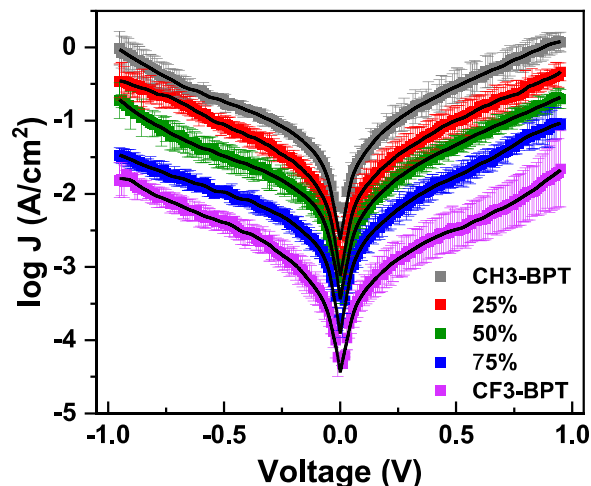
Figure 4.21. Work function values for the single-component and binary CH₃-BPT/CF₃-BPT SAMs derived from the UPS (a) and KP (b) data. The binary SAMs are labeled by the portions of CF₃-BPT in the solutions from which they were formed.

4.3.5 Charge Transport Properties of the SAMs

Semilogarithmic current-density versus voltage (bias) plots for the Au/SAM//Ga$_2$O$_3$/EGaIn junctions with the single-component and binary CH$_3$-BPT/CF$_3$-BPT monolayers are presented in Figure 4.22 for the bias range from -1.0 V to $+1.0$ V. The values of $\log\left|J\right|$ at selected positive and negative bias values are presented in Figure 4.22a and Figure 4.22b, respectively, while the respective $\log\left|J\right|$ histograms can be found in the Appendix A (Figure A.4).

According to the data, the tunneling rate across the single-component CH$_3$-BPT SAM is by 1.5-2 orders of magnitude higher than that in the CF$_3$-BPT case. The behavior of these SAMs is thus similar to that of the H-BPT and F-BPT monolayers (section 4.2),[53,57], but the extent of difference between the SAMs without and with terminal fluorine atom/atoms is even larger, with only an order of magnitude difference in the H-BPT/F-BPT case.[53,57] Interestingly, as follows from comparison in the Figure 4.14 and Figure 4.23, the absolute values of the current density for the CF$_3$-BPT and F-BPT SAMs are close to each other, whereas those for the CH$_3$-BPT monolayer are much higher than those for the H-BPT case (by an order of magnitude). The values of the current density exhibit, thus, no correlation, with the values of the molecular dipole, represented by the WF, since the difference between the WFs of the CH$_3$-BPT and H-BPT (~4.3 eV)[53] SAMs is even less than that between the WFs of the CF$_3$-BPT and F-BPT (~5.2 eV)[53] monolayers (~0.2 and ~0.3 eV, respectively).

Figure 4.22. Semilogarithmic current-density versus voltage (bias) plots for the Au/SAM//Ga$_2$O$_3$/EGaIn junctions with the single-component and binary CH$_3$-BPT/CF$_3$-BPT SAMs. The legend is given in the plot; the behavior (average values) is highlighted by thin black lines; the data for the binary SAMs are labeled by the portions of CF$_3$-BPT in the solutions from which they were formed. The error bars represent the standard deviations.

The tunneling rate across the binary CH$_3$-BPT/CF$_3$-BPT SAMs varies continuously between the values for the single-component SAMs (Figure 4.22 and Figure 4.23), exhibiting a close-to- linear dependence on the SAM composition in semilogarithmic representation (Figure 4.23). For most of the curves in Figure 4.23, this dependence has, however, a weakly pronounced S-shape character, which, most likely, is a consequence of a slight underestimation of the CF$_3$-BPT portion in the 25% samples and its slight overestimation in the 75% samples. A slight shift of the 25% and 75% points to the left and right, respectively, will nearly eliminate the S-shape.

Apart from the direct information regarding the charge tunneling rate, I-V curves allow determining the transition voltage, which is considered as an important parameter in context of charge transfer (see section 2.7).[244–246] For this purpose, these curves should be measured over a broader bias range and represented as a Fowler–Nordheim plot, $\ln(I/V^2)$ versus $1/V$[183,255]. The latter plots for the CH$_3$-BPT/CF$_3$-BPT SAMs are presented in supplementary data section (Figure A.5). The transition voltages corresponding to either positive or negative bias, V_T^+ and V_T^-, respectively, could be extracted from the minima of these plots. The respective values are presented in Figure 4.24. Whereas the absolute values of V_T^+ (Figure 4.24a) and V_T^- (Figure 4.24b) for any particular sample are very close to each other, they change slightly over the series between the ultimate values for the single-component films, viz. 0.64 ± 0.08 eV and 0.57 ± 0.05 eV for the CH$_3$-BPT and CF$_3$-BPT SAMs, respectively (a difference of ~0.07 eV). Similar to the log$|$J$|$ values (Figure 4.23), the variation of V_T^+ and $|V_T^-|$ occurs in a nearly linear fashion, with slight S-shape modulation.
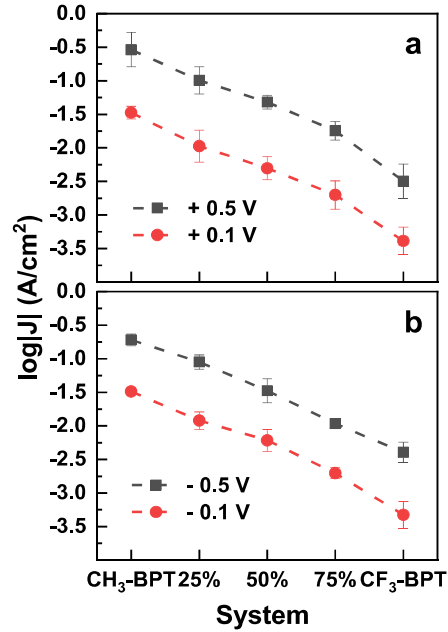
Figure 4.23. $\log|J|$ at selected positive (a) and negative (b) bias values for the Au/SAM//Ga$_2$O$_3$/EGaIn junctions containing the single-component and binary CH$_3$-BPT/CF$_3$-BPT SAMs. The legend is given in the plots; the data for the binary SAMs are labeled by the portions of CF$_3$-BPT in the solutions from which they were formed. The error bars represent the standard deviations.
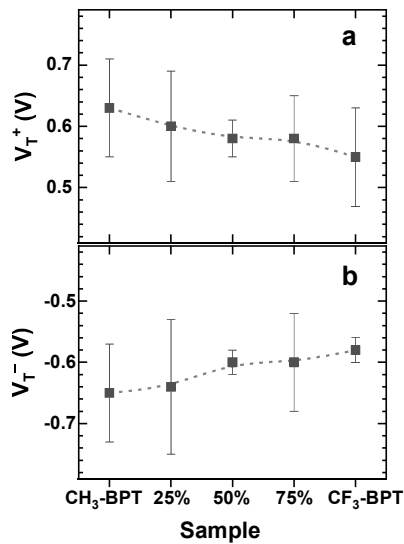
Figure 4.24: Transition voltage at the positive (a) and negative (b) bias for the single-component and binary CH$_3$-BPT/CF$_3$-BPT SAMs embedded into Au/SAM//Ga$_2$O$_3$/EGaIn junctions. The data for the binary SAMs are labeled by the portions of CF$_3$-BPT in the solutions from which they were formed.

63

Another parameter, which can be derived from the I-V curves acquired over an extended bias range, is the rectification ratio, RR. This ratio is generally defined as an average over the $\left| J(+V) \right|$ / $\left| J(-V) \right|$ values for a particular sample and is usually reported for V = 1.0 V.[67,256] Consequently, we calculated RR in the similar fashion and compiled the values in Table 4.3. Accordingly, the rectification ratio for all CH$_3$-BPT/CF$_3$-BPT SAMs, except for the 75% monolayer, is very close to 1.0, so that nearly no rectification takes place, showing also no dependence on the molecular dipole. The r^+ value for the 75% sample is also not particular high and can be probably considered as just a slight outlier.

Table 4.3. Rectification ratio for the single-component and binary CH$_3$-BPT/CF$_3$-BPT SAMs at V = 1.0 V. The mixed SAMs are labeled by the portions of CF$_3$-BPT in the solutions from which they were formed.

Monolayer	CH$_3$-BPT	25%	50%	75%	CF$_3$-BPT
RR	1.2 ± 0.74	1.3 ± 0.81	1.1 ± 0.67	2.7 ± 0.78	1.4 ± 1.88

4.3.6 Discussion

As mentioned in section 4.3.1-4.3.3, the identity, composition, and orientational order of the single-component and binary CH$_3$-BPT/CF$_3$-BPT SAMs have been verified by the spectroscopic tools, demonstrating, in particular, the thiolate-mediated anchoring to the substrate, high packing density, and a high degree of the orientational order, typical of well-defined thiolate SAMs. The high packing density suggests a nearly planar molecular conformation in all the SAMs studied, so that this parameter, generally affecting the charge transport properties of monomolecular films,[257,258] was defined and did not vary over the series. Also, the other parameters of the SAMs, mentioned above, vary only slightly over the series, so that this series is well suitable to monitor the effect of the composition on the charge transport properties. The composition of the binary SAMs could be varied in a reliable fashion. Generally, it mimicked that of the solution from which a particular binary SAM was prepared, even though a certain scattering and slight deviations from the one-to-one relation were recorded.

In accordance with the SAM composition, the WF of the binary SAMs changes continuously between the ultimate values for the single-component CH$_3$-BPT and CF$_3$-BPT monolayers, viz. ~4.45 eV and ~5.5 eV, respectively. At the same time, the HOMO-derived state, which is assumed to be crucially relevant in context of charge transport,[57] was found to be nearly isoenergetic for all SAMs. Analogously to the H-BPT/F-BPT case,[57] one can assume that the respective molecular orbital is delocalized along the entire molecular backbone, allowing efficient tunneling of the charge carriers, with the energy barrier at the Au/SAM interface being similar for all the SAMs studied.[52]

In spite of the above similarities, the charge tunneling rate across the single-component CH$_3$-BPT SAM was found to be higher by 1.5-2 orders of magnitude than that in the CF$_3$-BPT case, mimicking qualitatively the behavior of the H-BPT/F-BPT system and establishing, thus, the generality of the observed effects. The most likely reasons for this

effects are (i) the difference in the PDOS in the region of the terminal tail groups[52,259] and (ii) the appearance of an internal electrostatic field within the SAMs, emerging upon their contact to the top electrode.[57,240]

The difference in the PDOS in the region of the terminal tail groups between the CH_3-BPT and CF_3-BPT SAMs follows from the DFT calculations for the model Au/SAM//Au junctions.[52,259] Accordingly, the PDOS in proximity of the Fermi energy for the $−CH_3$ termination is noticeably larger than that for the $−CF_3$ tail group. As a consequence of this difference, the tunneling current for the CH_3-BPT monolayer was found to be noticeably higher (by a factor of ~5) than that in the CF_3-BPT case.[52] Note that a similar behavior was also calculated for the aliphatic SAMs with the $−CH_3$ and $−CF_3$ termination,[52] in good agreement with the experiment.[260]

As to internal electrostatic field, termed also as built-in field, it represents the only means to achieve thermodynamic equilibrium in a two-terminal molecular junction, leading to a renormalization of the relative energy level alignments for individual elements within the molecular backbone as well as to changes in the positions of these energy levels with respect to the joint Fermi level.[240] The exact profile of the internal field depends on the character of the molecules and the characteristics of both electrodes. In the present case we deal with an asymmetric junction, characterized by WF of ~5.3 eV and ~4.3 eV for the bottom (Au) and top (EGaIn) electrodes, respectively,[177] and a covalent and non-covalent coupling of the SAM-forming molecules to these electrodes.

One way to understand the character of the built-in field is to consider the compensation of different dipoles within the junction, which include the binding dipole at the Au/SAM interface and the "C-X" dipole at the SAM-ambient interface, associated with the dipolar tail groups.[57] Whereas the binding dipoles are nearly identical for CH_3-BPT and CF_3-BPT SAMs,[52,259] the "C-X" contributions are noticeably different in view of much stronger and opposite directed dipole of the $−CF_3$ "sheet" compared to the $−CH_3$ one. Thus, the dipoles induced upon the contact to the top electrode will be distinctly different for these monolayers, affecting the exact profile of the internal electrostatic field and, consequently, the charge transport rate in the junction.[57]

Another way to look at the situation is to take into account that the WF of the EGaIn electrode (~4.3 eV) is close to that of the CH_3-BPT SAM (see Figure 4.21), which likely results in a limited disturbance of the molecular energy landscape upon the contact to the top electrode. The situation is, however, different for the CF_3-BPT monolayer, which has a much higher WF (see Figure 4.21), stemming from a strongly confined dipolar $−CF_3$ "sheet" at the SAM-ambient interface. The contact of this sheet to the top electrode will thus result in a strong, pushback-like effect, causing a significant disturbance of the electronic density, which, in its turn, affects the tunneling rate across the junction.

Interestingly, as soon as the equilibrium in the junction is established, the contact resistance at the SAM//Ga_2O_3 interface is most likely invariant to the character of the tail group, similar to the H-BPT/F-BPT system.[31] Presumably, this is also true for the tunneling barrier at this interface as far as one can rely on the transition voltage as a fingerprint of this barrier.[37,255,261] Indeed, both V_T^+ and $\left|V_T^-\right|$ of the CH_3-BPT and CF_3-BPT SAMs differ by just 0.07-0.08 eV, with a slightly higher value for the former system (Figure 4.24).

The absence of correlation between the molecular dipole and transition voltage is a specific feature of the CH_3-BPT/CF_3-BPT systems, differing distinctly from the aromatic SAMs with a dipolar group embedded into the molecular backbone which are, thus, decoupled

from the top electrode.[262] For the latter monolayers, a clear correlation between the molecular dipole and transition voltage, varying by ~0.4 eV upon a WF variation of ~1 eV, was observed, while the charge tunneling rate values were mostly unaffected by the dipole. As shown here, the situation is exactly opposite for the SAMs with a dipolar tail group, with hardly varying transition voltage but strongly varying tunneling rate. This comparison underlines the importance of the dipolar group position on the performance of molecular systems in context of molecular electronics, as, e.g., was recently demonstrated for dipole-induced rectification in aliphatic SAMs.[256] Note that according to a recent report[263] interface dipoles associated with the terminal group can affect the coupling between the molecular film and the top electrode. Our data do not support this statement but cannot exclude such a behavior completely, to a certain extent.

Apart from the behavior of the single-component SAMs, that of the mixed monolayers is of primary interest as well. As follows from the data (Figure 4.22), the tunneling rate across the binary CH_3-BPT/CF_3-BPT SAMs varies gradually with their composition, between the ultimate values for the single-component monolayers. Specifically, the $\log|J|$ values at a particular bias exhibit nearly linear variation as functions of the film composition (Figure 4.23). This behavior is similar to that of the H-BPT/F-BPT system (Figure 4.14 in the section 4.2) and can be interpreted as characteristic of collective response of the entire SAMs, opposite to charge transport mediated by superposition of individual molecular wires connected to the bottom and top electrodes in a parallel fashion.[32] Following the tentative explanation for the behavior of the single-component SAMs, we propose that the varying tunneling rate in the binary CH_3-BPT/CF_3-BPT SAMs stems from the progressively varying PDOS in combination with a progressively varying built-in field causing a redistribution of the charge density and energy level alignments within the molecular junction. The extent of this redistribution should depend on the electrostatic properties of the tail group/top electrode interface (varying with the SAM composition), affecting progressively the tunneling rate.

The exact character of the internal field, triggered by the contact to the top electrode, should depend on the identity of the molecular backbone and be different for aliphatic and aromatic chains, which differ significantly in their ability to screen intermolecular electrostatic fields. Generally, the appearance of the internal field is accompanied by emergence of a polarization field across the monolayer, due to the dielectric screening mediating by the polarizable molecules.[16] The resulting field, responsible for the charge redistribution and the level alignment in the junction will then strongly depend on the molecular polarizability.

A further difference between the aromatic and aliphatic systems is the different positioning of the frontier molecular orbitals, with much smaller HOMO-LUMO gap and a special importance of HOMO for the charge transport in the former case. The above differences affect in particular the interpretation of the transition voltage, which may be dominated by the energy difference between the WF of the bottom electrode (Au) and the bands of the top electrode (Ga_2O_3) for aliphatic SAMs but be representative of the difference between the Fermi level of the junction and frontier molecular orbital, responsible for the charge transport, for aromatic monolayers.[261] For the halogen-substituted SAMs considered in this and previous work,[53,57,58,60] these differences explain probably the distinctly different charge tunneling rate behavior of the aliphatic[60] and aromatic[53,57,58] monolayers. In this context, theoretical simulations could be extremely useful. Such simulations, specifically

addressing the effect of the top electrode on the energy landscape in a molecular junction, are meanwhile available, dealing however mostly with symmetric electrodes.[57,240,264] An extension of these simulations to asymmetric electrode junctions, especially Au/SAM//Ga$_2$O$_3$/EGaIn and Ag/SAM//Ga$_2$O$_3$/EGaIn is highly desirable.[72]

4.3.7 Conclusions

Charge tunnelling rate across the single-component and binary CH$_3$-BPT and CF$_3$-BPT SAMs on Au(111) was studied by assembling two-terminal Au/SAM//Ga2O3/EGaIn junctions. The quality, basic parameters, and composition of these SAMs were monitored by a combination of several complementary spectroscopic and microscopic techniques. In accordance with the composition and the dipole moments of the SAM-forming molecules, the work function of the SAMs could be gradually tuned between ∼4.45 eV (CH$_3$-BPT) and ∼5.5 eV (CF$_3$-BPT).

The tunnelling rate across the single-component CH$_3$-BPT SAM was found to be higher by 1.5−2 orders of magnitude compared to the CF$_3$-BPT monolayer, while the tunnelling rate across the binary SAMs, representing most likely the molecular mixtures of both the components, varied progressively with their composition, between the values for the single- component monolayers. This behavior mimicked that of the analogous H-BPT/F-BPT films, suggesting a general character of the observed effects, which can be used for fine-tuning of the molecular conductance, underlying the importance of mixed molecular electronics.[61] At the same time, the energy position of the frontier molecular orbital responsible for the charge transport in the SAMs, derived from the UPS data, and the energy offset between this orbital and the Fermi level of the assembled junction, given tentatively by the transition voltage, were either nearly unchanged or varied only slightly with the SAM composition, providing, thus, no explanation for the observed charge tunnelling rate behavior.

This behavior was tentatively explained by the difference in the PDOS for the SAMs with the different terminations and by the appearance of a built-in field within the SAM matrix, emerging upon contact of the SAMs to the top, EGaIn electrode. This field leads to a renormalization of the relative energy-level alignments for individual elements within the molecular backbone as well to changes in the positions of these energy levels with respect to the joint Fermi level of the assembled junction.

The observed absence of correlation between the transition voltage and the dipole moment of the SAM-forming molecules suggests, in view of the relevant literature data, that the position of a dipolar group within the molecular backbone represents an important factor for the performance of the respective system in the context of molecular electronics.

4.4 Metallocene-Based Molecular Junctions

The continuous demand for a miniaturization of electronic devices calls for new approaches for their design and fabrication. A promising strategy in this context is provided by molecular electronics, employing individual molecules and their assemblies as

functional units of circuitry, which perform specific electronic and sensing functions.[62,265–267] Molecular rectifiers represent an important element for such a strategy, being potentially capable to become an alternative to current Si-based devices, carrying out a variety of functions in electronic circuits, such as signal processing, logical operations, and data storage. Generally, the design of molecular rectifier requires some sort of asymmetry in the junction, realized either by distinctly different couplings of the molecule or molecular film to the two connecting electrodes and/or by an asymmetric molecular structure. A promising strategy for realizing such a situation is based on combining ferrocenyl (Fc) with aliphatic or hybrid aliphatic-aromatic backbones, resulting a family of molecular rectifies with high rectification ratios (RRs). The first example of a ferrocene-based rectifier relied on self-assembled monolayers (SAMs) of 11-(ferrocenyl)-1-undecanethiol on Ag, embedded into a two-terminal junction with a eutectic GaIn (EGaIn) tip as top electrode. This allowed RRs of 90-180,[74] with the rectification explained by negative biases modifying the electronic level alignment such that beyond a certain voltage the highest occupied molecular orbital (HOMO) on the ferrocenyl enters into the conduction window. As a consequence, one observes distinctly higher currents for applied negative compared to positive bias voltages.[67,74] Further studies revealed a strong dependence of the rectification behavior on the substrate type,[66,69,268] on the character of the top electrode,[86] on the structure of the molecular backbone,[85,268] on the exact position of Fc in this backbone,[69] on the orientation of Fc,[268] and on the SAM quality.[70] Further improvements could be realized by enhancing the molecular asymmetry when combining two Fc units.[66,80] For a Fc-based SAM on Ag at 1 eV bias in these studies a RR of 1.1×10^3 was recorded,[80] which is comparable to the best molecular rectifiers relying on different designs and functional groups.[269,270] Even RRs exceeding 10^5 were reported for Fc-based monolayers on Pt, but these extremely high values were observed only at a comparably high bias voltage of 3V.[66] In contrast, the junctions comprising ferrocenyl-decorated molecules on Au yielded noticeably lower RRs, varying between 0.5 and 89 for a bias voltage of 1 eV, with the exact value depending on the details of the molecular structure and the quality of the SAM. This was explained by variations of the orientation of the terminal Fc moiety relative to the top EGaIn electrode as a function of the length of the aliphatic linker and by leakage currents flowing across defective parts in the monolayers.[70,268]

The above results were obtained for SAMs consisting of molecules in which the Fc's were either combined with an aliphatic backbone or in which the aromatic part of the backbone was decoupled from the Fc by an aliphatic linker.[70,85] Notably, fully conjugated backbones directly linked to ferrocenes to the best of our knowledge have not yet been studied as molecular rectifiers. This is changed in the present study, where we investigate transport through monolayers of a family of metallocenyl-substituted biphenyl and fluorene ethynyl thiols (Figure 4.25a). In the past, such monolayers have been studied in the context of self-assembly and electrochemical properties,[63,64,271] but, to the best of our knowledge, their charge transport properties are unknown. In view of the extensive literature on ferrocenyl-containing junctions, we focused on Fc-based SAMs, but also studied analogous ruthenocenyl- (Ru) based systems, as also ruthenium complexes have been reported to have promising molecular rectification properties.[82,272]

4.4.1 SAM Preparation

The SAMs were formed by immersion of the substrates into 1 mM solutions of the SAM precursors in DMF for 24 h, under ambient conditions and at room temperature, following the established procedures.[63,64,271] The SAM precursors were synthesized by our partners.[63,64,271] After immersion, the samples were ultrasonicated in DMF (to remove possible physisorbed material), rinsed with DMF first and then with ethanol, and afterward blown dry with a stream of nitrogen or Ar. Multiple sets of the samples were prepared for the repeated measurements (for the sake of statistic) and different experiments, with good reproducibility and consistency of the results. The reference BPT SAM was prepared according to the literature procedure, using the immersion procedure with ethanol as the solvent.[53]

4.4.2 Charge Transport Properties of the SAMs
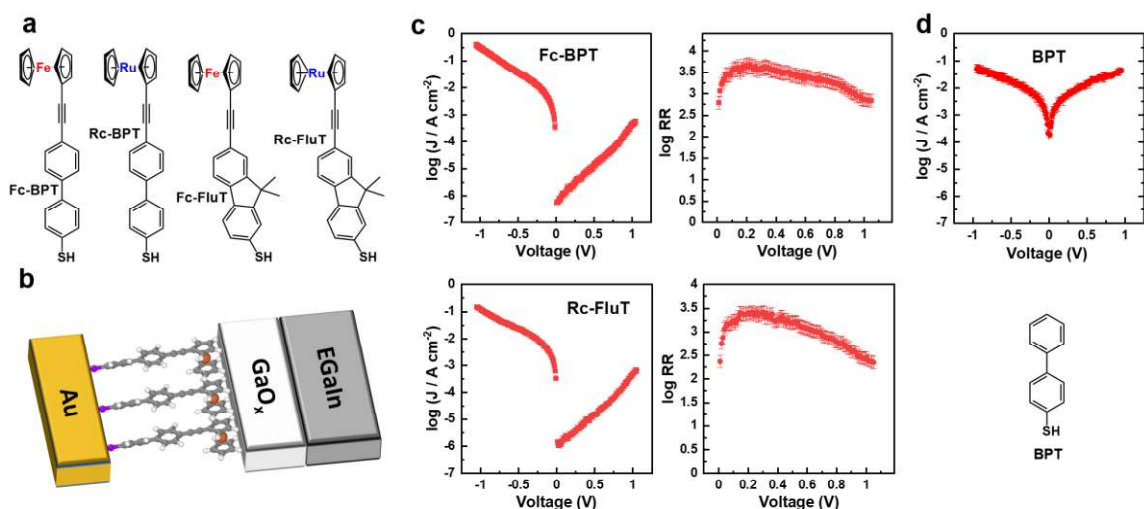
Figure 4.25: SAM-forming molecules, illustration of the junctions, and their electrical characteristics. (a) SAM-forming molecules used in this study along with their acronyms. The molecules were synthesized by the group of Prof. Lang.[63,271] (b) Illustration of the Au/SAM//Ga$_2$O$_3$/EGaIn junctions with the bottom Au electrode and top EGaIn electrode, with ′/′ corresponding to thiolate-Au bond and the interface between Ga$_2$O$_3$ and EGaIn and ′//′ indicating noncovalent contact between the Fc/Rc group of the SAM and the top electrode. (c) Semilogarithmic current density versus voltage (bias) plots and the corresponding RR versus voltage (bias) plots for the Au/SAM//Ga$_2$O$_3$/EGaIn junctions featuring the Fc-BPT and Rc-FluT SAMs. (d) Semilogarithmic current density versus voltage (bias) plot for the reference Au/BPT//Ga$_2$O$_3$/EGaIn junction and molecular structure of BPT. For measuring the current density vs. voltage plots, either positive or negative bias sweeps were repeatedly applied and the final characteristics are the outcomes of a statistical analysis of a large number of scans.

For the following investigations, the molecules were assembled as SAMs on Au(111) substrates, which also served as bottom electrodes. The top electrodes were formed by EGaIn tips, stabilized by a ~0.7 nm thick Ga_2O_3 overlayer[273] (Figure 4.25b). The bias was varied from 0 to either −1 V or to +1 V. The $\log|J|$ vs V plots for the Fc-BPT and Rc-FluT SAMs are shown in Figure 4.25c, together with the calculated rectification ratios defined as RR = $|J(–V)|$ / $|J(+V)|$; the analogous data for the Rc-BPT and Fc-FluT monolayers are shown in the supplementary data section (Figure A.6) and reveal a virtually identical behavior of these SAMs. At this stage it is important to stress that the values in the plots represent statistical averages over a large number of scans after the exclusion of curves showing a strongly deviated behavior (see Figure A.7, Figure A.8, and Table A.1-Table A.4 in the supplementary information section), which is the standard way to measure and to process I-V data for molecular junctions. As a consequence, the displayed averages represent the situation of a junction that has been repeatedly subjected to positive (or negative) voltages of up to 1V (−1V), an aspect that will become relevant later, when discussing the conductivity switching.

For all studied SAMs, the $\log|J|$ vs V plots show significantly higher current density values at negative than at positive bias, with a ′discontinuity′ at 0 V. The respective log RR values vary from ~2.3 at 0.05 V to a maximum value of ~3.3 at a bias of 0.2-0.25 V. The observation that the exceptional behavior regarding both J and RR values is essentially the same for all studied SAMs can be tentatively rationalized by the similar structures of the SAM-forming molecules (Figure 4.25a) and similar charge transport properties of biphenyl and fluorene backbones.[257]

To ensure that the observed behavior stems from the presence of the Fc and Rc units, the charge transport characteristics of the Fc/Ru-substituted SAMs are directly compared to that of a biphenylthiolate (BPT) monolayer (Figure 4.25d), as the non-substituted analogue of the Fc-BPT and Rc-BPT SAMs. As expected,[57] the BPT SAM does not exhibit a noticeable rectification or any discontinuities of the $\log|J|$ vs V curves around zero bias ((see also Figure A.9 in the supplementary data section). Interestingly, the absolute values of $\log|J|$ for the Au/Fc-BPT//Ga_2O_3/EGaIn and Au/BPT//Ga_2O_3/EGaIn junctions in the negative bias range are very close to each other, which means that the Fc-ethynyl moieties in the Fc-BPT SAM are nearly "transparent" to the carriers at the given conditions. In particular, the curves for the Fc-BPT and BPT monolayers have nearly identical shapes between 0 and −0.5 V, a value corresponding to transition voltage of the Fc-BPT SAM, indicative of a change in the charge transport regime (see Figure A.10 and Table A.5 in the supplementary data section). For higher negative biases, the curve for the Fc-BPT case increases more steeply with progressing bias, resulting in even higher $\log|J|$ values compared to the BPT case. In line with the rectification effects discussed above, for positive biases, the $\log|J|$ values for the Fc-BPT SAM are noticeably lower than those of the reference BPT monolayer.

A further in-depth analysis reveals that the low $\log|J|$ values at positive biases for the Fc and Rc containing SAMs represent the averages over a large number of scans (see above), but do not reflect the initial states of the junctions. This is illustrated in Figure 4.26a for the example of a series of subsequent J vs V scans for an Fc-FluT SAM, which is characteristic for the entire series of molecules (see Figure A.11 in the supplementary data section). At very low biases, the first scan starts with the same $\log|J|$ values as for very low negative biases but, with increasing positive bias, the current first saturates and then

even decreases. The second scan starts from much lower J values than the first one even for low biases and is already rather similar to the averaged $\log|J|$ vs V curve for the Fc-BPT SAM in Figure 4.25c. The current values then drop even further for successive scans until they fully stabilize after 6-7 scans.
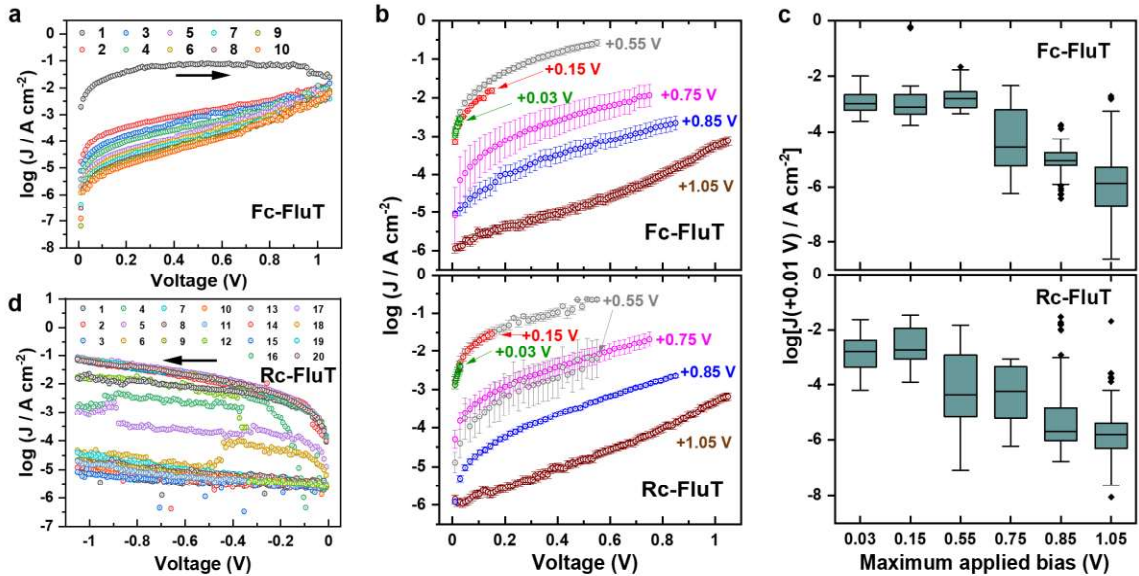
Figure 4.26: Dynamic effects in the junctions. (a) Semilogarithmic current density versus voltage (bias) plots for the Au/Fc-FluT//Ga$_2$O$_3$/EGaIn junction. Ten successive individual scans with the bias variation from 0 to +1 V (marked by the arrow) are shown. (b) Semilogarithmic current density versus voltage (bias) plots for the Au/Fc-FluT//Ga$_2$O$_3$/EGaIn and Au/Rc-FluT//Ga$_2$O$_3$/EGaIn junctions. For each curve (representing an average over a large number of scans) the bias was varied from +0.01 to the value indicated in the plot. (c) $\log_{10}|J|$ at V = +0.01 V measured at the bias variation from +0.01 V to the maximum value shown at the x-axis for the Au/Fc-FluT//Ga$_2$O$_3$/EGaIn and Au/Rc-FluT//Ga$_2$O$_3$/EGaIn junctions. The horizontal lines within the dark cyan boxes represent the medians of the distributions; the boxes denote interquartile ranges (IQRs); the error bars correspond to the values furthest from the boxes, up to a distance of 1.5 times the IRQ; and the points lying beyond these intervals are considered as outliers. d. Semilogarithmic current density versus voltage (bias) plots for the Au/Rc-FluT//Ga$_2$O$_3$/EGaIn junction. Twenty successive individual scans with the bias variation from 0 to −1.05 V are shown. The sample was in the low conductance state before the scanning.

To understand, which positive bias is necessary to trigger the switching, we varied the bias only within a limited range and monitored the J vs. V behavior. This bias range was then increased in several steps. The respective data for the Fc-FluT and Rc-FluT SAMs are presented in Figure 4.26b and Figure 4.26c, c, also Figure A.12 and Figure A.13 in the supplementary data section. According to these data, the bias variation up to +0.55 V for the Fc-FluT SAM and up to a slightly lower value for the Rc-FluT monolayer does not result in any bias-mediated switching of the electrical conductance (in the Rc-FluT case, some of the +0.55 V curves show the original behavior while the other show lower current values). In contrast, an increase of the bias beyond these ranges leads to a decrease of the

current values in the averaged characteristics. This decrease occurs in a successive fashion: the higher the maximum applied bias, the lower the current values become, until final values, similar to those in Figure 4.25c and Figure A.6 in the supplementary data section are reached for the +0.01 V to +1.05 V scans.

To check whether the bias-induced switching is the consequence of some irreversible degradation of the SAMs, we studied to what extent the low conductance state can be converted back to the initial high conductance state by (several successive) scans at negative bias. The respective data for the Rc-FluT SAM (as a representative example for the entire series) are presented in Figure 4.26d. For these experiments, the sample was first brought into the low conductance state by scanning at the positive bias. Then it was scanned at negative bias from 0 to −1.05 V, with the data for successive individual scans displayed in the plot. The current remained low during the first few scans (i.e., initially the SAM was in a low-conductivity state also for negative biases with currents at least roughly similar to the positive bias case). Upon further scanning the bias, the current sometimes changed in a step-like fashion. After approximately ten subsequent scans at negative bias, the high conductance state was, however, restored nearly completely. In contrast, when no scanning in the negative bias range was performed, the SAMs remained in the low-conductance state, as verified by measurements on the same Au/Rc-FluT//Ga$_2$O$_3$/EGaIn junction (see Figure A.14 in the supplementary data section).

4.4.3 Discussion

The data in Figure 4.26c and Figure 4.26d are relevant, as they show that the asymmetry of the curves in Figure 4.25c and the reported rectification ratio is not due to an intrinsic current-anisotropy of the switched SAM. Figure 4.25c rather shows the characteristics of the junction for stable positive and stable negative bias operation, i.e., it is representative of the two (meta)stable states that occur in the junction for the considered bias ranges. In that sense, the bias-triggered rectification observed here differs fundamentally from the behavior reported for the analogous aliphatic and hybrid Fc-substituted monolayers, where the observed rectification is not associated with any type of switching such that fixed current values for specific biases are obtained.[66,67,69,74,80,85,86,268] Moreover, in contrast to the data in Figure 4.25c, the traditional Fc-substituted monolayer junctions do not display any discontinuity in the semi-logarithmic I-V plot at zero bias. The observation of such a discontinuity in the present junctions shows that the switching-induced rectification is apparently operative at already very small biases.

This leaves the question which mechanisms causes the peculiar behavior of the SAMs studied here. One conceivable explanation would be some bias-induced modifications of the SAM structures, like, for example, a change in the molecular arrangements and tilt angles. This, however, appears rather unlikely, considering that the measured parameters of the present SAMs are typical of densely packed molecular assemblies. This has been reported in previous spectroscopic and electrochemical studies[63,271,274] and is additionally verified here by cyclic voltammetry (not shown) and work function measurements (see Figure A.15 and Table A.6 in the supplementary data section). In particular, the packing density of the SAMs, calculated on the basis of the CV data, is estimated at 3.4-4.0 × 10^{14} molecules/cm^2, with the lower values for the bulkier fluorene backbone. The molecular tilt

angle, reported previously for the Fc-BPT and Rc-BPT SAMs,[63,274] is ca 35-37°, which gives a similar orientation of the Fc/Rc moieties with respect to the top EGaIn electrode as in the Fc-substituted AT SAMs on Au and Ag.[268] Again, the dense packing does not leave much space for massive, bias-induced molecular rearrangements and the rigidity of the molecular backbones prevents a bias-induced changes of the conformation of the individual molecules. Moreover, such reorientation effects would typically not result in changes of the current density exceeding an order of magnitude, as shown by a dedicated study of odd-even effects in molecular diodes.[268] Finally, the electronic properties of the as prepared SAMs are inconspicuous: the position of HOMO, calculated on the basis of the CV data, varies only slightly from system to system between −5.21 and −5.29 V, which is very close to the analogous parameter of ferrocene (−5.0 eV).[67,74,86] Also the work function of the SAMs is determined to be 4.4 eV, which is identical to that of BPT/Au (4.4 eV as well), emphasizing a non-polar character of the Fc and Rc moieties.

These data prompt us to suggest an alternative scenario as the most likely explanation for the unusual charge transport behavior of the Fc/Rc-substituted biphenyl/fluorene ethynyl thiol SAMs of the present study: considering the well-known redox character of metallocenyls, we speculate that at least part of the molecules in the SAMs are quasi-irreversibly oxidized as a consequence of applying a large enough positive bias. A metastable cation state would be stabilized by the coupling to the conjugated BPT/Flu backbones via the ethenyl linker. The ionization potential of Fc-BPT is further reduced by dielectric screening within the SAM and by the metal electrodes. Counter-charges, e.g., trapped in the GaO$_x$ or as mirror charges in the electrodes further reduce the energetic cost of cation formation and considering that the ionization of part of the metallocenyls would also be favored by entropy, a (meta)stable situation with some of the metallocenes ionized does not appear entirely unlikely.

This raises the question, how cation formation would diminish charge transport, eventually causing the low-conductivity state. One aspect worthwhile considering is, how cation formation impacts the nature of the frontier orbitals. Of particular relevance in this context is the highest occupied molecular orbital (the HOMO), which for thiol-bonded SAMs is typically responsible for charge transport.[67] In the neutral state, simulations by our partners show that the HOMO is fully delocalized between the conjugated backbone and the ferrocenyl. This situation changes fundamentally when the molecule becomes positively charged, as shown in Figure 4.27a for Fc-BPT: the HOMOs of both spin channels become largely localized on the biphenyl part of the molecule (see Figure 4.27a and Figure B.4 in the Supplementary Data by Our Partners section). For the lowest unoccupied orbital (LUMO) a similar situation is observed, with the main difference that in the cation the LUMO becomes largely localized on the ferrocenyl (see Figure B.4 in the Supplementary Data by Our Partners section). The localization of the frontier orbitals in the cation is consistent with the localization of the excess charge, which for the cation is primarily found on the ferrocenyl, as confirmed in Figure 4.27b.

Such a charging-induced localization of the frontier orbitals (partly) interrupts the transport channel through the SAM between the two electrodes, but to be fully effective, the localization (and, thus, cation formation) would have to affect the majority of the molecules in the junction. But even if this was not the case, the existence of a positive space charge layer within the junction would give rise to the formation of a sizable potential barrier for holes passing the junction. In this context it is worthwhile noting that the holes are expected

to remain the dominant charge carriers even in the switched junction, considering that thiolate SAMs typically are in a Fermi/HOMO-level pinning situation (as can be inferred from the data shown in refs [275,276] and as has been explicitly discussed, for example, by Rodriguez-Gonzalez et al.[277]). The height of the electrostatic barrier should be sizable also for moderate ionization rates. For a semi-quantitative estimate, a simple electrostatic model was developed by our partner, as described in detail in the Figure 4.27c. The ionization of 11% of the metallocenyls results in an inter-ion distance that becomes similar to the length of the molecules. This somewhat reduces the barrier in certain regions, as illustrated in Figure 4.27c. But even then, the estimated minimum barrier for the junction remains higher than 1.2 eV. The actual height of that minimum barrier, of course, depends on the choice of the various parameters of the simple electrostatic model, but these considerations suggest that, if a fraction of the metallocenyls remained in a (meta)stable cationic state, this would pose a sizable obstruction to hole transport through the junction.
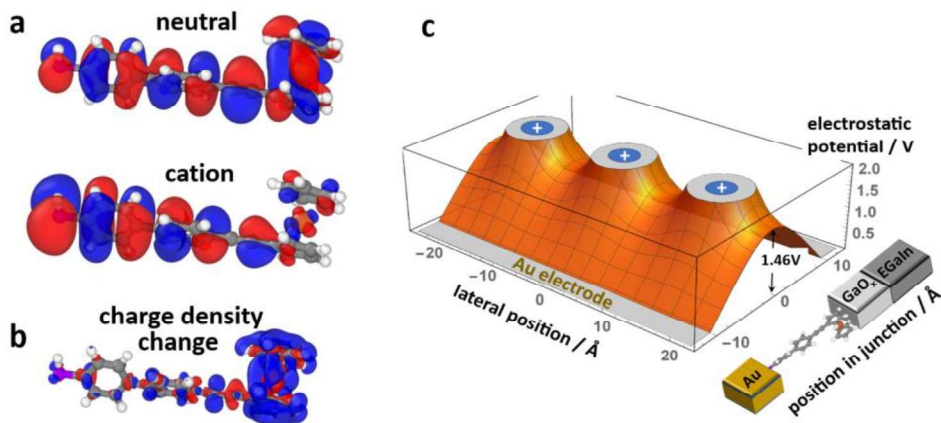
Figure 4.27: DFT calculation impact of cation formation in Fc-BPT and electrostatic potential distribution for ionized metallocenyls in the SAM, performed by our partner. (a) Shapes of the HOMO orbitals in the neutral and cation states; isovalue 0.009. (b) Isodensity plot of the change in charge density between the cation and the neutral molecule (in the neutral equilibrium geometry). Blue (red) regions correspond to electron removal (addition). (c) Potential barrier due to the ionization of a fraction of the metallocenyl units assuming a square arrangement of the charges with a distance of 15Å between the point charges (i.e., assuming an ionization of every third molecule in x- and y-directions and yielding an overall ionization rate of 11%). The plane of ionized molecules is separated from the electrodes by two dielectric layers (the conjugated backbone and the GaO_x), whose dielectric constant is assumed to be 2. The displayed cross-section is chosen such that it cuts through one of the lines of charges in x-direction to best illustrate the situation. The minimum potential barrier in that plane amounts to 1.46 V, while the overall minimum barrier amounts to 1.23 V and is located in the center of the square found by four neighboring point charges. The potential has been calculated from point charge arrays including mirror charge effects to second order.

4.4.4 Conclusions

We have experimentally studied charge transport properties of a series of fully conjugated metallocenyl (Fc and Rc) substituted biphenyl- and fluorenethiols, assembling the molecules on Au(111) and placing the respective monolayers within the Au/SAM//Ga$_2$O$_3$/EGaIn junctions. In contrast to the previous reports on Fc-substituted aliphatic and hybrid SAMs, the systems described in the present study exhibit two distinctly different conduction states, such that current densities similar to those measured for related aromatic thiolate-SAMs (in particular biphenylthiolate) are observed when applying negative biases. The situation changes fundamentally for positive biases, for which the observed current densities are by orders of magnitude smaller. This results in a rectification ratio of 10$^{3.5}$ at a bias voltage of ~0.25 V and of 10$^{2.5}$ at bias voltages close to 0 V. Especially at low biases these parameters are superior to most molecular rectifiers reported so far, making the present systems interesting for various applications. Interestingly, the appearance of the low-conductivity state is triggered by sufficiently high positive bias voltages. This switching of the junction can be reversed through a negative bias.

The observed behavior is tentatively explained by the switching a fraction of the SAM-forming molecules into a (meta)stable cation state, triggered by the sufficiently high positive bias. This hypothesis is indirectly supported by DFT simulations performed for the individual molecules. The simulations also suggest that the frontier electronic states in the ionized molecules become spatially localized, which might be one of the reasons for the massively decreased conductivity in the switched SAM. Another, potentially even dominating effect is that ionized molecules within the junction with charges primarily localized on the metallocenyls would give rise to a significant potential barrier for hole transport. In the future, such a mechanism could be specifically targeted in advanced, custom-designed systems, in this way opening new perspectives for molecular electronics.

4.5 Thermal Stability of Alkanethiolates and Aromatic Thiolate SAM on Au(111)

Thermal stability of functional SAMs is an important issue for SAMs application in modern nanotechnology.[11,23,89–94,103,109,117,192,278] In this section, thermal stability of the most basic thiolate SAMs on Au(111) was addressed using synchrotron-based HRXPS, as described in detail in section 3.2.6. The SAMs in consideration include two non-substituted aliphatic systems and two non-substituted aromatic systems with different lengths of the molecular backbone (Figure 4.28). Note that according to the literature data, with most of the reports dealing with alkanethiolates (AT) SAMs on Au(111), the thermal stability of these systems is predominantly limited by the energetics of the thiolate-gold bond,[231] which is generally considered as a weak covalent bond.[279,280] As shown by X-ray diffraction studies,[192] the typical c(4 × 2) lattice of alkanethiols is persistent until 363-373 K, with either melting or formation of incommensurate phase at higher temperatures. The latter processes are accompanied by molecular desorption and decomposition.[278,281] Other reports give

however a much higher temperature, such as 423 K, for noticeable temperature-induced changes.[282] The stability of aromatic thiolate SAMs as well as hybrid aliphatic-aromatic monolayers is supposed to be higher than that of AT SAMs,[192,282] but some of the reported values, such as a characteristic degradation temperature of 453 K for terphenyl-based SAMs on Au(111),[282] seems to be overestimated to some extent.
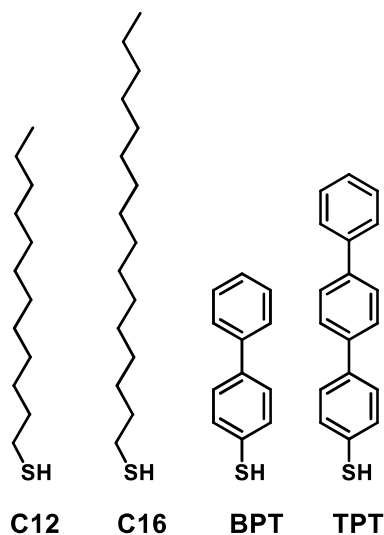
Figure 4.28: SAM-forming molecules used in the present study along with the respective acronyms. TPT molecules were synthesized by the group of Prof. Terfort, while other 3 molecules were purchased commercially.

4.5.1 SAM Preparation

The SAMs were assembled by immersing freshly fabricated substrates into solutions of the precursors (Figure 4.28) in either ethanol (C12, C16, BPT; 1 mmol) or dimethylformamide (TPT; 0.5 mmol) at room temperature and under ambient conditions. After immersion (24 h), the samples were carefully rinsed with pure solvent and blown dry with argon. Afterward, the samples were placed in containers filled with argon for their transportation to the synchrotron.

4.5.2 HRXPS analysis

The derived intensities of the characteristic XPS peaks and doublets were used for the evaluation of the effective thickness of the monolayers and density of the specific sulfur-derived species located at the SAM-substrate interface. The effective thickness was calculated from the Au 4f intensity, on the basis of the equation 2.6, as the following

$$I_{Au4f} = I_{0-Au4f} \times exp\left(-\frac{d_{SAM}}{\lambda_{Au4f}}\right) \qquad\qquad 4.2$$

where I_{Au4f} and I_{0-Au4f} are the intensities of the Au 4f signal for the SAM-covered and blank substrate, respectively, d_{SAM} is the SAM thickness, and λ_{A4f} is the attenuation length corresponding to the kinetic energy of the Au 4f photoelectrons (~260 eV), *viz.* ~10.5 Å.[150] The value of I_{0-Au4f} was not directly measured but determined using the well-known thickness of the pristine C12, C16, BPT, and TPT SAMs, *viz.* 15.0 Å, 18.9 Å, 11.5 Å, and 15.2 Å, respectively.[214,231,283] The resulting equation was

$$d_{SAM} = d_{SAM-pr} - \lambda_{Au4f-pr} \times ln\left(\frac{I_{Au4f}}{I_{Au4f-pr}}\right) \qquad\qquad 4.3$$

where d_{SAM-pr} and $I_{Au4f-pr}$ are the thickness of the given pristine SAM (at RT) and the intensity of the Au 4f signal for this sample, respectively.

Alternatively, as an additional proof, the effective thickness of the SAMs could also be evaluated from the intensity of the C 1s signal, on the basis of the equation 2.5), as the following:

$$I_{C1s} = I_{0-C1s} \times \left[1 - exp\left(\frac{d_c}{\lambda_{C1s}}\right)\right] \qquad\qquad 4.4$$

where I_{C1s} and I_{0-C1s} are the intensities of the C1s signal for the real and very thick SAMs, respectively, d_C is the thickness of the hydrocarbon overlayer, and λ_{C1s} is the attenuation length corresponding to the kinetic energy of the C 1s photoelectrons (60-65 eV), *viz.* ~6.3 Å.[150] The value of I_{0-C1s} was not directly measured but determined using the well-known thickness of the pristine SAMs corrected for the effective thickness of the S–Au interface, d_S, *viz.* ~2.4 Å.[284,285] The resulting equation was

$$d_{SAM} = -\lambda_{C1s} \times ln\left\{1 - \left[1 - exp\left(-\frac{d_{C-pr}}{\lambda_{C1s}}\right)\right] \times \frac{I_{C1s}}{I_{C1s-pr}}\right\} + d_s \qquad 4.5$$

where d_{C-pr} and I_{C1s-pr} are the thickness of the hydrocarbon overlayer for the given pristine SAM (at RT) and the intensity of the C 1s signal for this sample, respectively.

The density of the specific sulfur-derived species located at the SAM-substrate interface, n_S, was calculated from the intensity of the species-specific S 2p doublets, I_{S2p}, on the basis of the equation[148,149]

$$I_{S2p} = A \times exp\left(-\frac{d_c}{\lambda_{S2p}}\right) \qquad\qquad 4.6$$

where A is a general factor and λ_{S2p} is the attenuation length corresponding to the kinetic energy of the S 2p photoelectrons (~183 eV), *viz.* ~8.6 Å.[150] The value of A was not directly measured but determined using the well-known packing density of the thiolate species in the pristine C12, C16, BPT, and TPT SAMs, n_{S-pr}, estimated at ~4.6 × 10^{14} molecules/cm^2.[109,286,287] The resulting equation was

$$n_S = I_{S2p} / I_{S2p-pr} \times n_{S-pr} \times exp\left[-(d_{C-pr} - d_C)/\lambda_{S2p}\right) \qquad\qquad 4.7$$

where I_{S2p-pr} is the intensity of the thiolate-specific S 2p doublet for the given pristine SAM (at RT).

4.5.3 Alkanethiolates SAMs

The Au $4f_{7/2}$, C 1s, and S 2p XP spectra of the C16 SAM successively annealed at temperatures of 300-413 K are presented in Figure 4.29a, Figure 4.29b, and Figure 4.29c, respectively. Intensities of the characteristic signals, derived from the spectra, are shown in Figure 4.30. The analogous data set for the C12 SAM is presented in Figure A.16 and Figure A.17 in the supplementary data section.

The C 1s and S 2p spectra of the pristine C12 and C16 monolayers (302 K) exhibit the characteristic peak at either ~284.75 eV (C12) or ~284.85 eV (C16) assigned to the alkyl backbone[283] and S 2p doublet at 162.0 eV (S $2p_{3/2}$), representative of the thiolate anchoring groups bound to gold.[210] No other features are observed, underlying the chemically homogeneous and contamination-free character of the samples.

According to the data in Figure 4.29 and the intensity values in Figure 4.30, the character of the Au 4f, C 1s, and S 2p spectra do not change noticeably up to 373 K, accompanied by only slight variation in the intensity of the characteristic peaks and doublets. The intensity of the Au 4f signal increases to some extent, while the intensity of the C 1s signal decreases slightly, manifesting, most likely, a slowly progressing molecular desorption, likely from the defect sites and the edges of individual domains. The intensity of the S 2p thiolate signal in the S 2p spectra increases slightly reflecting a smaller attenuation by the somewhat thinner hydrocarbon overlayer (the assembly of the molecular chains represents an overlayer with respect to the thiolate and atomically adsorbed sulfur species located at the substrate-SAM interface). The spectra, however, change drastically at 383 K, with some of the changes being traceable already at 373 K. These changes include a step-like increase in the intensity of the Au 4f signal and a radical change in the character of the C 1s and S 2p spectra. The C 1s spectra exhibit a noticeable downward shift of the photoemission peak, which becomes slightly asymmetric, representing most likely two different adsorption modes (see section 4.5.5 below), and considerably lower in intensity. A similar, drastic decrease in intensity occurs also for the thiolate signal in the S 2p spectra, accompanied by the emergence of two new doublets at ~161.1 eV (S $2p_{3/2}$) and 163.4 eV (S $2p_{3/2}$) assigned to atomically adsorbed sulfur and disulfide/weakly bound/unbound sulfur, respectively.[210,281] The first of these doublets, perceptible already at 373 K, becomes the dominant feature, whereas the second is comparably weak, representing less than 10% of the entire S 2p signal.

Note that the assignment of the ~161.1 eV doublet relies primarily on the literature data for the strongly annealed (490 K) AT SAMs on Au(111): whereas the C 1s signal disappeared completely, the S 2p signal was still well perceptible, at ~161.1 eV (S $2p_{3/2}$).[281] Since sulfur was the only chemical element present on the Au(111) surface, the assignment of the respective signal to atomically adsorbed sulfur bound to Au seems to be unequivocal. In addition, the binding energy of 161.1 eV manifests a noticeably stronger involvement of sulfur into the bonding with gold, correlating well with the atomically adsorbed sulfur

model. Alternative assignments, which can be found in literature, such as differently bound and laying-down molecules,[70,288–290] appear less realistic to us.
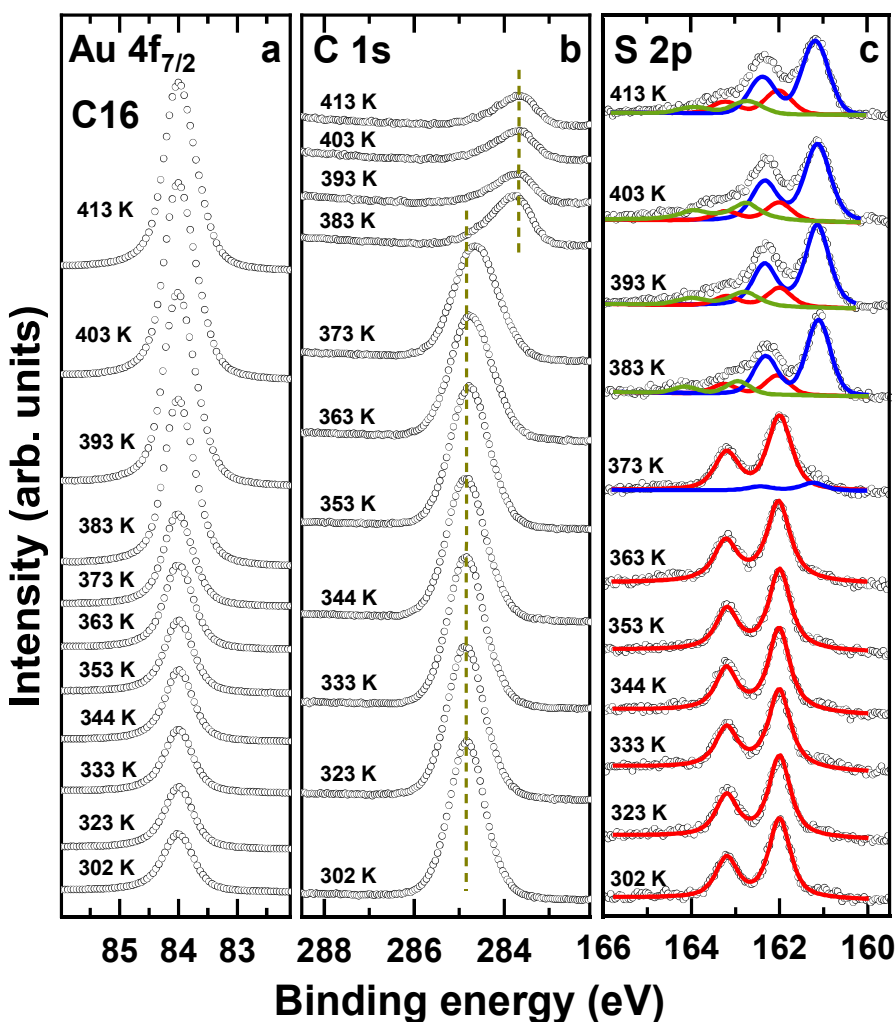
Figure 4.29: The Au 4f$_{7/2}$ (a), C 1s (b), and S 2p (c) XP spectra of the C16 SAM successively annealed in UHV at temperatures of 300-413 K as marked (open circles). The positions of the C 1s peak before and after the temperature-induced shift are traced by vertical dashed lines in (b). Individual components of the S 2p spectra, corresponding to the thiolate anchoring groups, atomically adsorbed sulfur, and disulfide/weakly bound/unbound sulfur are shown in (c) by the red, blue, and green solid lines, respectively.

The further changes of the Au 4f, C 1s, and S 2p spectra, occurring at the higher temperatures are only marginal as compared to the spectra at 383 K, with probably the major effect involving the asymmetry and intensity of the C 1s peak, which becomes symmetric and even lower in intensity (~20% of the original value) starting from 393 K. Above this temperature, the character of the spectra and the intensities of individual peaks and doublets do not change much, reflecting the stabilization of the system in a new state, distinctly different from the pristine one.

The behaviour of the C12 SAM at the temperature variation is similar to that of the C16 monolayer, with the persistence of the characteristic spectra shape up to 373 K and their drastic change at the higher temperatures (see Figure A.16 and Figure A.17 in the supplementary data section). The only difference is somewhat less abrupt character of this change, reflecting by the smaller intensity decrease in the C 1s spectrum at going from 373 K to 383 K and the smaller intensity of the atomically adsorbed sulphur feature in the S 2p spectrum at 383 K. A further temperature increase, to 393 K and higher, results, however, in the S 2p spectra, which are very similar to those of C16/Au.
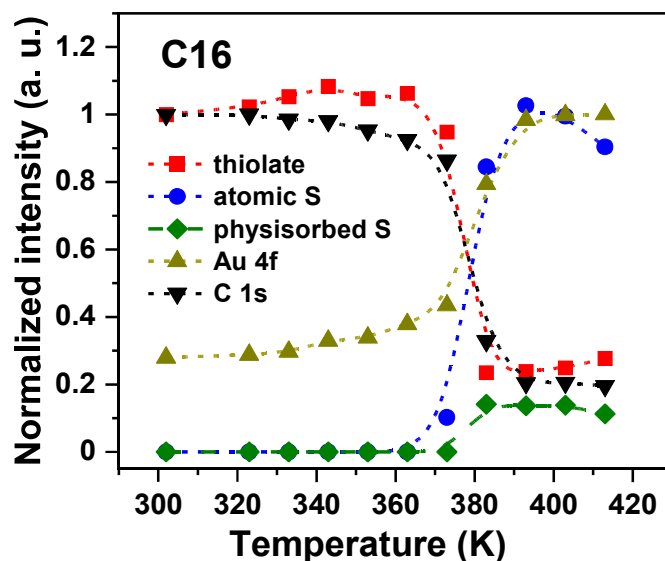
Figure 4.30: The normalized intensities of the characteristic photoemission peaks and doublets in the XP spectra of the C16 SAM as functions of the annealing temperature. The legend is given in the panel. The C 1s intensity is normalized to the value at 302 K, the S 2p intensities – to the intensity of the thiolate signal at 302 K, and the Au $4f_{7/2}$ intensity – to the value at 413 K.

Note that the observed evolution of the XP spectra for the C12 and C16 SAMs agrees well with the literature data for 1-decanethiol (C10) SAM on Au(111) single crystal – to the best of our knowledge, the only synchrotron-based HRXRS study of the thermal stability of AT SAMs reported so far.[281] This study, presenting results for few temperatures only, reports very similar changes of the spectra, which start at ~380 K and involve strong decrease in intensity and downward shift of the C 1s peak as well as strong decrease in intensity of the thiolate doublet and the emergence of the atomically adsorbed sulphur doublet. Qualitatively similar spectra evolution could also be observed in an XPS study of 1-octadecanethiolate (C18) SAM on evaporated Au(111),[278] even though the spectra measured with a laboratory setup do not allow to monitor temperature-induced changes with the same precision as those measured with a high resolution at a synchrotron.

4.5.4 Aromatic Thiolate SAMs

The Au $4f_{7/2}$, C 1s, and S 2p XP spectra of the TPT SAM successively annealed at temperatures of 300-433 K are presented in Figure 4.31a, Figure 4.31b, and Figure 4.31c, respectively. Intensities of the characteristic signals, derived from the spectra, are shown in Figure 4.32. The analogous data set for the BPT SAM is presented in Figure A.18 and Figure A.19 in the supplementary data section.
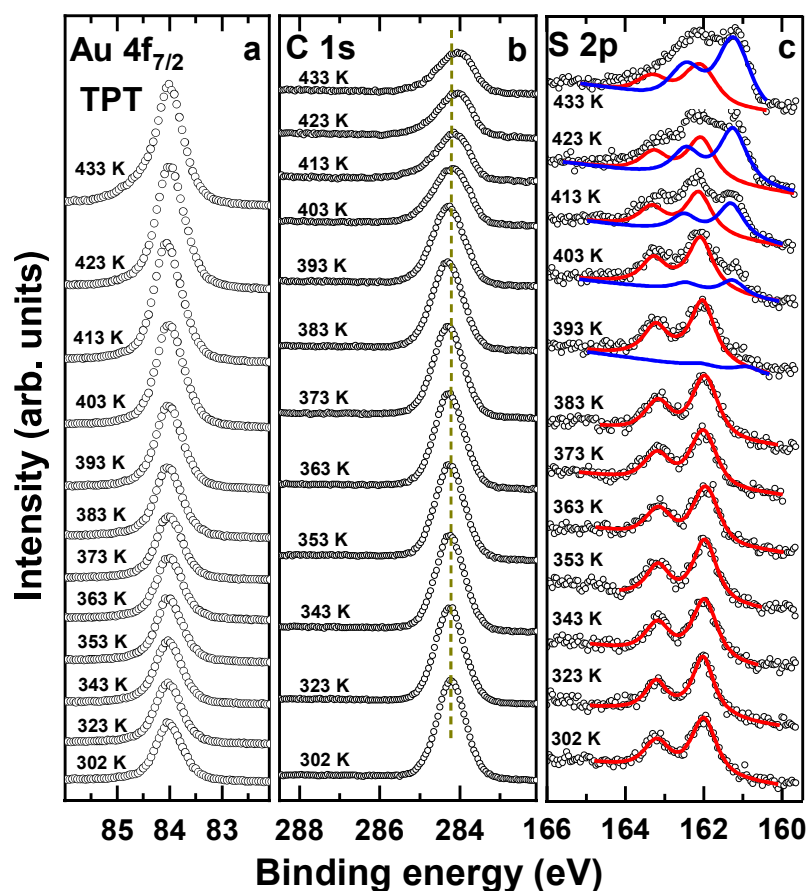
Figure 4.31: The Au $4f_{7/2}$ (a), C 1s (b), and S 2p (c) XP spectra of the TPT SAM successively annealed in UHV at temperatures of 300-433 K as marked (open circles). The position of the C 1s peak for the pristine TPT monolayer is traced by the vertical dark yellow dashed line in (b); it changes slightly at 423-433 K. Individual components of the S 2p spectra, corresponding to the thiolate anchoring groups and atomically adsorbed sulfur are shown in (c) by the solid red and blue lines, respectively.

The C 1s and S 2p spectra of the pristine TPT and BPT films (302 K) exhibit the characteristic peak at ~284.2 eV (TPT) or ~284.1 eV (BPT) assigned to the oligophenyl backbone[214,231] and S $2p_{3/2}$ doublet at 162.0 eV (S $2p_{3/2}$) assigned to the thiolate anchoring groups bound to gold.[210] No other features are observed, apart from a very small trace of atomically adsorbed sulphur in the S 2p spectrum of the BPT SAM. Apart from this minor contamination, the BPT and TPT samples are contamination-free and chemically homogeneous.

According to the data in Figure 4.31, the character of the Au 4f, and C 1s, and S 2p spectra do not change noticeably up to 383 K, accompanied by only slight variation in the intensity of the characteristic peaks and doublets. The intensity of the Au 4f signal increases to some extent (see also Figure 4.32), while the intensity of the C 1s signal decreases slightly, manifesting, most likely, a slowly progressing molecular desorption from defect sites and domain borders. The intensity of the S 2p thiolate signal in the S 2p spectra is nearly constant, exhibiting only a very slight increase. Noticeable changes start first at 393 K, manifested by a pronounced intensity change of the Au 4f and C 1s signals and the appearance of the initially very weak signal of the atomically adsorbed sulfur in the S 2p spectra. These changes evolve even stronger at the higher temperatures with a further pronounced increase in the intensity of the Au 4f signal and decrease in the intensity of the C 1s signal occurring up to 403-413 K and levelling off at the higher temperatures. The C 1s peak shifts to the lower binding energy (~284.0 eV) but this shift is much less pronounced than that for the aliphatic SAMs (see Figure 4.29) since the energy of the C 1s peak in the pristine TPT SAM (RT) is comparably low (~284.2 eV; see above). The most essential variation is however exhibited by the S 2p spectra, which change their character completely at the temperature increase from 393 K to 433 K. The contribution of the atomically adsorbed sulfur, which is hardly perceptible at 393 K, increases in intensity and becomes the dominant feature, whereas the contribution of thiolate becomes progressively smaller.
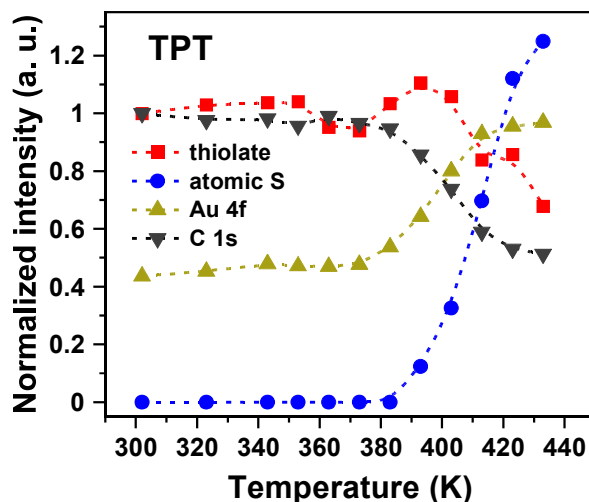
Figure 4.32: The normalized intensities of the characteristic photoemission peaks and doublets in the XP spectra of the TPT SAM as functions of the annealing temperature. The C 1s intensity is normalized to the value at 302 K, the S 2p intensities – to the intensity of the thiolate signal at 302 K, and the Au $4f_{7/2}$ intensity – to the value at 413 K.

The behaviour of the BPT SAM at the temperature variation is similar to that of the TPT monolayer, with the persistence of the characteristic spectra shape up to 383-393 K and their pronounced change at the higher temperatures (see Figure A.18 and Figure A.19 in the supplementary data section).

4.5.5 Discussion
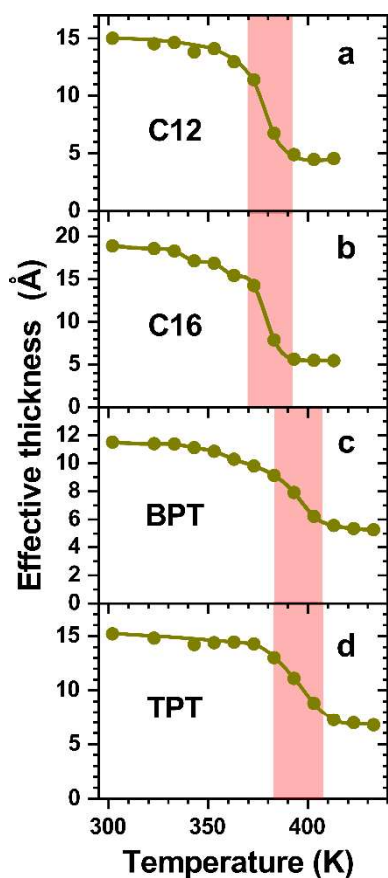
Figure 4.33: Effective thicknesses of the C12 (a), C16 (b), BPT (c), and TPT (d) SAMs (filled dark yellow circles) as functions of temperature. The values were calculated on the basis of the Au 4f intensities, according to equation 4.3. The solid lines trace the observed behavior. The temperature ranges corresponding to pronounced changes in the SAM composition are highlighted.

The spectra of the SAMs presented in Figure 4.29 and Figure 4.31 as well as in the supplementary data section (Figure A.16 and Figure A.18) give a good insight into the temperature-mediated processes, which include molecular adsorption, molecular fragmentation, and chemical transformations in the films. Additional information is provided by the intensity plots in Figure 4.30 and Figure 4.32 as well as in Figure A.17 and Figure A.19. However, whereas these intensities represent useful fingerprints of the temperature-induced processes, they do not adequately reflect quantitative changes in the SAM thickness and composition, because of the attenuation effects in photoemission, which have specific extents for individual species.[150] These effects can, however, be corrected for, as discussed in detail in section 4.5.2.

As the first quantitative parameter, the effective thickness of the SAMs was evaluated on the basis of the Au 4f and C 1s intensities, in accordance with equations 4.3 and 4.5, respectively. The results are presented in Figure 4.33 and Figure A.20. The values

calculated by the different methods correlate well with each other, which verifies their reliability. According to these values, the aliphatic SAMs are less stable than the aromatic ones, with the noticeable and comparably stronger thickness reduction starting at ~373 K and finishing at ~393 K. In the aromatic monolayers, the analogous process starts first at 383-393 K and is less extensive and slower progressing (in relation to the temperature increase). There is hardly any dependence on the chain length, with the very similar curves for the C12 and C16 SAMs and qualitatively similar curves for BPT and TPT.
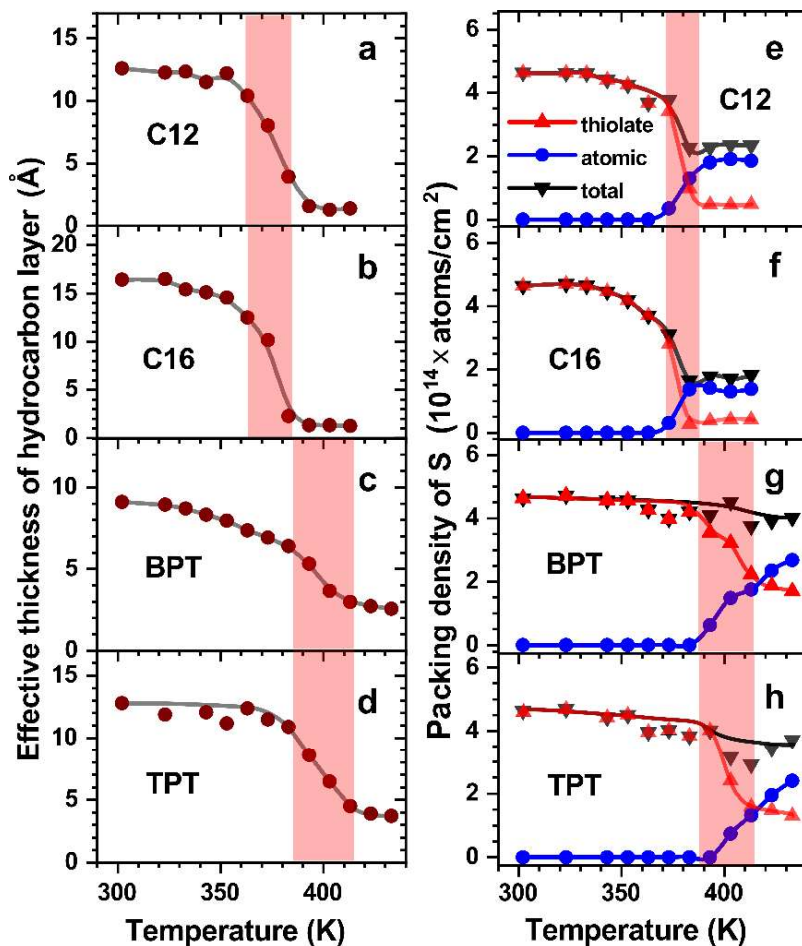
Figure 4.34: Effective thicknesses of the hydrocarbon part in the C12 (a), C16 (b), BPT (c), and TPT (d) SAMs (filled dark yellow circles) as well as packing densities of the sulfur species in these SAMs (e, f, g, and h, respectively) as functions of temperature. The legend for (e-h) is given in panel (e). The solid lines trace the observed behavior. The temperature ranges corresponding to the pronounced changes in the SAM composition are highlighted.

Further information can be obtained by quantitative monitoring of the SAM composition. For this purpose, we calculated the effective thickness of the hydrocarbon part of the SAMs by equation 4.5 (with a correction for d_S) and the densities of the thiolate and atomically adsorbed sulfur at the SAM-substrate interface by equation 4.7. The respective data are shown in Figure 4.34. The effective thickness of the hydrocarbon part (Figure 4.34a-d) represents a measure of the carbon content while the sum of the thiolate and atomically adsorbed sulfur densities represents coarsely the total sulfur content. As seen in the spectra

of the SAMs (Figure 4.29 and Figure 4.31 as well as Figure A.16 and Figure A.18, some of the samples exhibit a signature of physisorbed/unbound/disulfide sulfur at the elevated temperatures. The intensity of the respective signal is however comparably low and the location of the respective species in the residual films is not defined in contrast to the thiolate and atomically adsorbed sulfur moieties, which are located at the SAM-substrate interface. Consequently, the signal of physisorbed/unbound/disulfide sulfur can experience a distinctly different attenuation or no attenuation at all (if these species are located at the film-ambient interface), so that one cannot handle it in the same way as the signals of thiolate and atomically adsorbed sulfur. In view of this limitation, we only took into accounts the latter signals at the calculation of the total packing density of the sulfur species, shown in Figure 4.34e-h.

The effective thicknesses of the hydrocarbon part, d_C, in Figure 4.34a-d mimic the analogous curves for the effective thicknesses of the SAMs (Figure 4.33 and Figure A.20), apart from the contribution related to d_S. The difference in the onsets of the noticeable thickness reduction for the aliphatic and aromatic SAMs is well pronounced. The difference in the carbon content of the residual films is even more drastic than the analogous difference in d_{SAM}. In contrast to the very low values of d_C observed for the AT SAMs at 393-313 K (~10% of the initial value), such values for the aromatic SAMs are still high enough at 413-433 K (30-35% of the initial value). This suggests a nearly complete desorption of the aliphatic chains (as a part of the molecules or their fragment) and their fragments in the former case, in contrast to a noticeable amount of the residual material in the latter case.

The behavior of d_C correlates nicely with that of the sulfur species, with the different onsets for the noticeable changes in their composition for the aliphatic and aromatic SAMs, as shown in Figure 4.34e-h. Starting from 373 K in the C12/C16 case and from 383-393 K in the BPT/TPT case, the density of the thiolate species, $n_{thiolate}$, decreases significantly, accompanied by the emergence and density increase of atomically adsorbed sulfur, n_{AS}, and, to a noticeably lesser extent, by the emergence of physisorbed/unbound/disulfide sulfur (see Figure 4.29 and Figure 4.31 as well as Figure A.16 and Figure A.18. The reduction of $n_{thiolate}$ is noticeably stronger for the C12/C16 case, accompanied by just a moderate increase of n_{AS} and a noticeable reduction of the total amount of sulfur, with all these processes levelling off at 383-393 K. In contrast, the total density of sulfur, n_T, changes only slightly (if at all) in the BPT/TPT case, accompanied by progressing changes in $n_{thiolate}$ and n_{AS} occurring in a nearly symmetrical way.

Rationalizing the above tendencies and the evolution of the XP spectra, specific scenarios of the temperature-induced processes in aliphatic and aromatic thiolate SAMs on Au(111), represented here by the C12, C16, BPT, and TPT monolayers, can be derived, illustrated in Figure 4.35. In the C12/C16 case, the SAMs retain their identity up to ~373 K, even though with a slight reduction of the molecular density. At the higher temperature, pronounced molecular desorption takes place, as follows from the strong simultaneous decrease of d_C and $n_{thiolate}$. This process is accompanied by molecular decomposition, mediated by the cleavage of C−S bond and resulting in the desorption of the alkyl chains and emergence of atomically adsorbed sulfur. Thus, the latter bond, complementary to the thiolate-substrate one (Au−S), represents so-called "weak link" for the temperature-induced SAM degradation. Such a weak link, defined predominantly by the molecular structure and the character of the substrate, has been reported for a variety of different

SAMs, playing leading role in the thermal stability of these systems.[109,291,292] After the extensive desorption, occurring in the 373-383 K range, the residual films stabilizes at the higher temperature. Most likely, they represent a combination of the lying-down molecules, as also proposed in literature,[252] and atomically adsorbed sulfur. The transformation from the upright orientation of the backbones, decoupled electronically from the substrate, to the lying-down geometry is manifested by the pronounced downward shift of the C 1s peak (see Figure 4.29 and Figure A.16). This shift can be rationalized as a consequence of efficient electronic coupling of the backbone to the substrate for the lying-down phase, resulting in particular in much more efficient screening of the photoemission hole by the conduction electrons in the substrate. Note, however, that the lying-down phase has also a limited thermal stability, since the carbon signal disappears at the sufficiently high temperatures (490 K) and only the signal of atomically adsorbed sulfur can be recorded.[281] Note also that whereas d_C correlates nicely with $n_{thiolate}$ at 393-413 K, being both comparably small with respect to the values at RT (~10% for both d_C and $n_{thiolate}$), n_{AT} is noticeably larger (30-40% of the initial value). Consequently, the respective species cannot be related to the residual aliphatic chains (the laying-down phase), which is one more evidence for their assignment to atomically adsorbed sulfur.

The BPT and TPT SAMs retain their identity up to 383-393 K, even though with some reduction of the molecular density (more pronounced in the BPT case). At 393-413 K, pronounced loss of hydrocarbon material takes place, accompanied by the transformation of thiolate into atomically adsorbed sulfur, with n_{total} decreasing only slightly. A suitable scenario corresponding to this behavior is the cleavage of S−C bonds, followed by desorption of either biphenyl (BPT) or terphenyl (TPT) moieties. In contrast to the C12/C16 case, such a cleavage seems to be the dominant temperature-induced degradation process for the BPT and TPT monolayers, with S−C bond representing the "weakest link" in these films. At the same time, the values of d_C and $n_{thiolate}$ at 413-433 K correlate nicely with one another if compared with the values at RT (~35% for both d_C and $n_{thiolate}$), so that the residual films represent most likely a superposition of the intact molecules and atomically adsorbed sulfur. The residual intact molecules can have both laying-down and standing-up geometry, arranging both in ordered and disordered patches. Note that in the case of BPT, the area per molecule of the standing-up phase (21.6 Å^2)[252] corresponds to ca. 27% of that for the laying-down structure (57.7 Å^2),[286] which is not far away from the residual molecular density in the strongly annealed BPT SAMs (~35%). Consequently, the laying-down phase is most likely the dominant one in the BPT case and is presumably available in the residual TPT films as well (with a larger area per molecule), coexisting with the standing-up phase, comprised, most likely, by the strongly inclined molecules. Note that polymorphism is typical of aromatic thiolate SAMs, even at RT,[287,293] so that a superposition of different structural phases can be expected at the elevated temperatures as well.
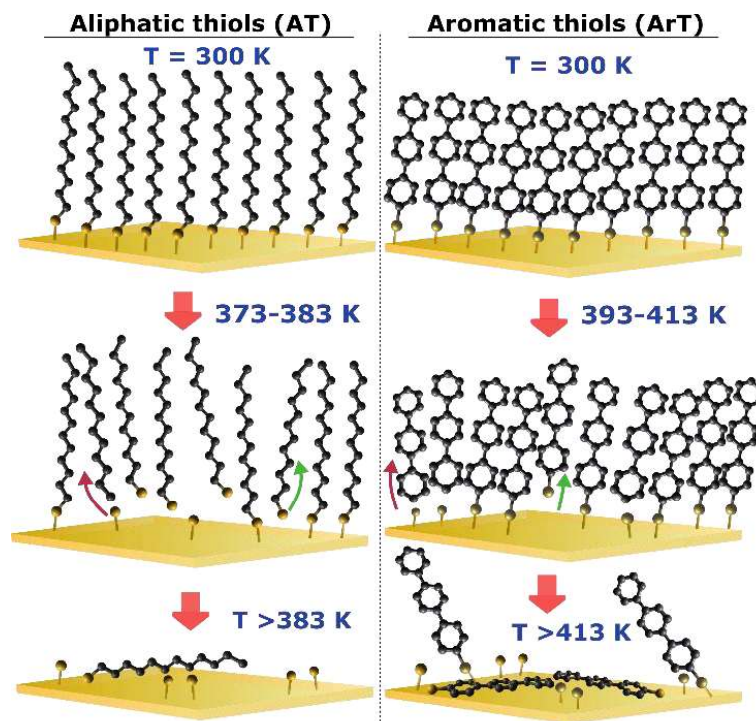
Figure 4.35: Schematic illustration of the temperature-induced modification of the AT and ArT SAMs; hydrogen atoms and the minor physisorbed/unbound/disulfide sulfur species are not shown for the sake of clarity. The molecular desorption event, dominating in the AT case, is marked by green arrows, whereas the C-S bond scission events, dominating in the ArT case, are marked by the dark red arrows.

The comparably higher thermal stability of aromatic thiolate (ArT) SAMs agrees qualitatively with the literature data.[252] The character of the molecular backbone is obviously of importance, defining,[291] along with the redistribution of the electron density within the substrate–S–C joint, the strength of S–C bond. Note that, generally, the bonding of the molecules to the substrate over S–Au bond results in a withdrawing of the electron density from the adjacent S–C bond, resulting in its weakening. A further relevant aspect is the intermolecular interaction, which is supposed to be stronger in the ArT case as compared to AT SAMs.[294] In addition to the van-der-Waals interaction, typical of AT species, molecules in the ArT monolayers feature π-σ interaction, characteristic of the proposed herring-bone packing motif in these films.[295]

An interesting aspect is the identity of the moieties emerging after the cleavage of S–C bonds, which are most likely primary carbocations and/or radicals. In the AT case, these species can subsequently undergo a rearrangement by migration of the beta-hydrogen to the electron deficient alpha carbon.[296] The result is an energetically stable tertiary carbocation, which is encountered frequently during organic electrophilic rearrangements. In sharp contrast, aryl carbocations (ArT radical/cations in our case) are believed to be energetically higher owing to both repulsive orbital interactions and geometry factors.[296] The electronegative sp^2 orbitals on β-C destabilize the positively charged ArT cation center and stereochemical distortion of the phenyl ring cannot be disregarded. Consequently, the situation in the ArT SAMs is more complicated and probably deems further investigation.

87

Few words should also be said about the disulfide/weakly bound/unbound sulfur species appearing upon the pronounced molecular desorption and decomposition in most of the SAMs studied (Figure 4.29 and Figure 4.31 as well as Figure A.16 and Figure A.18.). The respective minor species represent most likely disulfides or alkylsulfides caught in the residual matrix. An alternative assignment would be dialkylsulfide, appearing as a result of chemical reaction between the released alkyl-S⁻ and biphenyl-S⁻ species and molecular backbones.[297]

Note that this is of importance that the doublet at 163.4 eV is not perceptible at temperatures below 383 K (C12/Au and C16/Au) and even 413 K (BPT/Au), since, along with the signature of the specific sulfur-derived species, this feature represents a fingerprint of X-ray induced damage in the monolayers.[210,297] Consequently, such a damage did not take place at the low and moderate temperatures and had only a small extent (if at all) at the temperatures corresponding to the SAM desorption and decomposition. We have taken special care to avoid X-ray damage effects, which indeed can be a problem for XPS and HRXPS studies of thiolate SAMs, specially at an elevated temperature.[298,299] It should also be emphasized that the doublet at 161.1 eV (S $2p_{3/2}$) – the major emerging spectroscopic feature at the elevated temperatures – has no relation to the X-ray damage effects[210] and is therefore exclusively representative of the temperature-induced effects.

4.5.6 Conclusions

Thermal stability of AT and ArT SAMs on Au(111) was studied by synchrotron-based HRXPS, taking the C12, C16, BPT, and TPT monolayers as representative test systems. As the substrates we used evaporated, grain-structured Au(111), which does not have the structural perfection of a single crystal but is a typical support for applications, possessing in this regard larger practical relevance. The samples were kept at an elevated temperature for a fixed time (2 min), with the temperature varying in excess of that required for SAM degradation. It was found that AT SAMs maintain their identity and character up to a temperature of ~373 K, followed by extensive molecular desorption and decomposition, mediated by the cleavage of S−Au and C−S bonds and occurring in the 373−383 K range. The residual films represent a superposition of the laying-down phase and atomically adsorbed sulphur. The ArT SAMs turned out to be somewhat more stable, retaining their identity and character up to a temperature of ~383−393 K, followed by the extensive loss of material, mediated mostly by the cleavage of C−S bonds and occurring in the 383−403 K range. The residual films, characterized by ca. 35% of the initial packing density, represent most likely a superposition of several structural phases (both laying-down and standing-up) and atomically adsorbed sulphur. A noticeable dependence of the above behavior on the length of the molecular backbone was not observed, even though certain differences between C12/Au and C16/Au as well as between BPT/Au and TPT/Au could be recorded.

Both for AT and ArT SAMs, the C−S bond represents the weak or even weakest link in context of the thermal stability, once more underlining the importance of this concept for functional SAMs and stressing the fact that the temperature-induced degradation of SAMs is not only mediated by molecular desorption. Along with the bond to the substrate (Au−S), this link governs the stability of the entire system, which can only perform its specific

function in the defined temperature range. As far as a higher temperature is required, SAMs with higher thermal stability can be used, such as those of N-heterocyclic carbenes in the case of Au(111).[300,301]

Whereas the experiments were performed in UHV, their results should also be relevant for other environments, such as under ambient conditions or in solution, even though certain differences can take place. The same is true for differently fabricated gold substrates, since surface perfection and morphology can influence the packing density and structural organization of the SAMs[23,117] thus, affect their thermal stability to some extent.

4.6 Thermal Stability of Phosphonic Acid SAMs on Alumina Substrates
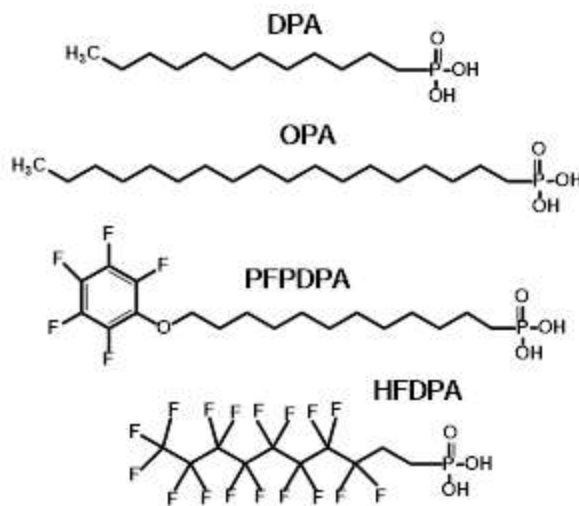
Figure 4.36: The SAM forming molecules of the present study along with the respective acronyms. DPA – dodecyl-PA; OPA – octadecyl-PA; PFPDPA - 12 pentafluorophenoxydodecyl-PA; and HFDPA - (3,3,4,4,5,5,6,6,7,7,8,8,9,9,10,10,11,11,12,1,2,12-heneicosafluorododecyl)-PA. These molecules were purchased from Merck.

In this section, thermal stability of SAMs with phosphonic acid (PA) anchoring group, covalently bound on Al_2O_3 substrates is considered.[47,202,302] These films rely on the formation of the quite robust P−O−substrate linkage as a result of the condensation reaction between the hydroxyl groups of the anchoring moiety and the substrate.[303] The exact binding scheme is still under discussion, with different studies giving a preference to the bidentate or tridentate modes or their mixture, with dependence on the size of the SAM forming molecules and specific type of the substrate.[47,303–306] But the robust character of PA SAMs is generally accepted along with the relative easiness of their fabrication as compared to alternative anchoring groups (trichlorosilanes, etc.) suitable to oxide substrate. Consequently, PA SAMs are broadly used for different applications, such as optimization

of the buffer layers in organic photovoltaics,[108] photocurrent generation,[307] modification of transparent conductive electrodes in optoelectronic devices,[19,201,308] engineering of gate dielectric in organic transistors,[92,309,310][7,39,40] and even as active layer in these devices.[1141] In view of the robustness of PA SAMs, the thermal stability and temperature-induced effects of few typical PA SAMs (Figure 4.36) were investigated. The selected SAMs feature non-substituted alkyl chain, substituted alkyl chain, and partly fluorinated alkyl chain as the molecular backbone. The length of the non-substituted alkyl chain was varied to monitor a possible correlation of this parameter with the thermal stability. The terminal substitution with pentafluorophenoxy and partial fluorination of the backbone were intentionally used, mimicking the standard ways to engineer wetting properties and work function of surfaces and interfaces.[19–21,47,311]

Note that, for the best of our knowledge, the literature on the thermal stability of PA SAMs is quite scarce. A representative example is the study of OPA formation and thermal stability on an aluminum substrate.[302] Applying water contact-angle goniometry and time-of-flight secondary ion mass-spectroscopy (TOF-SIMS), the authors of this study showed that the parameters of OPA SAMs are maintained upon its annealing under air up to 200°C, even though a small portion of the alkyl chains inside the molecules were oxidized at this temperature. Interestingly, the oxidation of the alkyl chains turned out to be the dominant degradation mechanism upon annealing to higher temperatures - in contrast to possible break-up of the covalent bond between the anchoring group and the substrate or between the anchoring group and molecular backbone. Further, Kanta et. al. examined the influence of heat treatment in air on the stability of OPA SAMs on titania under ambient conditions. This publication deduced the breakage of the aliphatic chain at temperatures of 350°C, leaving the phosphorus anchoring group attached to the surface up to temperature of over 800°C.[31243] However, this research was also performed at ambient conditions. The only study dealing with an oxygen-free heating of PA monolayers, is the work by Bhairamadgi et al. (to the best of our knowledge), who monitored thermal stability of OPA SAMs on porous aluminium oxide by in situ XPS using the C 1s and Al 2p peaks as fingerprints.[202] These SAMs were found to be stable up to ~500 °C, in contrast to several other monolayers using different anchoring chemistry and showing much lower thermal stability.[202] The signal of the anchoring group was however not monitored, which made it difficult to deduce specific degradation pathways.

In this context, we monitor in the present work the behavior of both the molecular backbone and the anchoring group upon annealing of the PA SAMs under oxygen-free, ultra-high vacuum (UHV) conditions. As a major experimental tool synchrotron-based HRXPS was used, which is an established technique in material science and physical chemistry in general as well as a useful probe for molecular films and SAMs in particular.[148,210] The temperature-induced changes were monitored in situ, upon SAM annealing in the same UHV chamber.

4.6.1 SAM sample in the study

N-dodecylphosphonic acid (DPA), n-octadecylphosphonic acid (OPA), 12-pentafluorophenoxydodecylphosphonic acid (PFPDPA), and 1H,1H,2H,2H-

perfluorododecylphosphonic acid (PFDPA) were prepared by Merck on thin Al_2O_3 layer on top of a boron doped, double side polished 6'' silicon wafer (625 μm thickness, (100) orientation, $0.001 - 0.005$ Ω cm resistivity, prime grade), as illustrated in Figure 3.1.

4.6.2 HRXPS experiment and analysis

Thermal stability of the phosphonic acid-based SAMs was addressed using synchrotron-based HRXPS, as described in detail in section 3.2.6.[46] The temperature was varied with 50 K step size, starting from the room one (ca. 300 K). Considering the oxide character of the substrates, charging was possible in principle. It was however not distinctly observed (since the oxide films were relatively thin) but cannot be excluded completely in some of the spectra.

The samples turned out to be extremely sensitive to X-ray induced damage, with the extent and rate that are significantly higher than those for the analogous thiolate-based SAMs on Au(111).[210] To minimize this damage and to avoid an interference of the respective effects with the temperature-induced degradation, we kept the spectra acquisition time as short as possible and varied the spot position on the samples, checking the homogeneity of the SAM over the probed area in advance. The "frequency" of the spot variation steps was adapted and optimized during the measurements. Some of the experiments were repeated because of too strong effect of the X-ray damage but in few cases we let the results as is, as far as the temperature effects were clear enough.

When necessary, the spectra were fitted by symmetric Voigt functions and either a linear or Shirley-type background. The effective thicknesses of the SAMs was evaluated using the standard procedure,[148] on the basis of the Al 2p signal from the substrate, which was attenuated by the SAM according the equation 2.6

$$I_{SAM} = I_0 \times exp\left(-\frac{d_{SAM}}{\lambda_{Al2p}}\right) \qquad\qquad 4.8$$

where I_{SAM} and I_0 are the intensities of the Al 2p signal for the SAM-covered and blank substrate, respectively, d_{SAM} the SAM thickness, and λ_{Al2p} the attenuation length for the given kinetic energy of the photoelectrons. Accordingly, the thickness of a SAM is given by the expression

$$d_{SAM} = \lambda_{Al2p} \times \ln\left(\frac{I_0}{I_{SAM}}\right) \qquad\qquad 4.9$$

The literature data for λ_{Al2p} were used, relying on the measurements of alkanethiolate SAMs, viz. 10.9 and 16.0 Å for kinetic energies of 271 and 501 eV, respectively (corresponding to PEs of 350 eV and 580 eV, respectively).[150]

In contrast to the effective thicknesses, only relative values of the packing density could be estimated coarsely, on the basis of the P2p/Al2p intensity ratio. Note, however, that the kinetic energies of the respective photoelectrons are somewhat different (222 eV and 271

eV, respectively, for a PE of 350 eV), resulting in the different λ values (9.6 and 10.9 Å, respectively) and, consequently, in the different, film-thickness-depending attenuation. Consequently, the relative values of the packing densities should be taken with a grain of salt.

4.6.3 Pristine SAMs

The C 1s, Al 2p, and P 2p HRXPS spectra of the pristine (T = 300 K) PA SAMs are presented in Figure 4.37, along with the C 1s and Al 2p spectra of the blank substrate. The O 1s and F 1s spectra were acquired as well and will be discussed later.
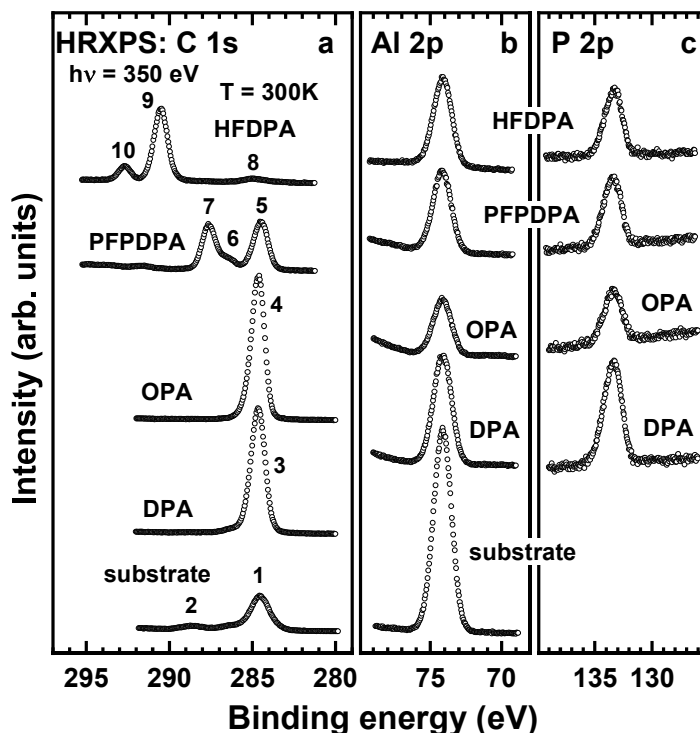
Figure 4.37: The C 1s (a), Al 2p (b), and P 2p (c) HRXPS spectra of the DPA, OPA, PFPDPA, and HFSPA SAMs as well as C 1s (a) and Al 2p (b) spectra of the blank substrate (reference) acquired at T = 300 K. Some characteristic peaks are marked by numbers (see text for details).

The C 1s spectra of the PA SAMs in Figure 4.37 are specific for the respective precursors and characteristic of high-quality monolayers. This correlates with a noticeable decrease in the intensity of the substrate signal, as demonstrated in Figure 4.37b by the example of the Al 2p spectra, and with the appearance of the characteristic P 2p signal of the anchoring group at 133.3 eV, as demonstrated in Figure 4.37c. The presence of only one P 2p feature suggests that all PA groups of the adsorbed molecules are in the same chemical state, providing the anchoring of the molecules to the substrate and corresponding, thus, to the well-defined SAMs. This feature, which is a P $2p_{3/2,1/2}$ doublet in reality, appears as a somewhat asymmetric peak (in agreement with the branching ratio)[148] but the components,

92

separated by ~1 eV (spin-orbit splitting),[188] could not be resolved, which is most likely related to a certain inhomogeneity of the bonding configuration and geometries for the anchoring groups. In contrast, the spin-orbit splitting of the Al 2p feature is much smaller[188] and this doublet appears as a nearly symmetric peak.

The C 1s spectrum of the substrate exhibits a typical signature of contamination, viz. a broad peak at 284.8 eV (**1**; C–C and C–H) and a weak feature at 288.5 eV (**2**; COOH and C=O). Both these peaks became not perceptible upon the assembly of the SAMs. The spectra of the DPA and OPA SAM exhibit a single, comparably narrow peak at 286.6 eV (**3** and **4**), which is assigned to the alkyl backbone.[210] The intensity of this peak is higher for the OPA SAM than for the DPA film, in accordance with the molecular composition. The C 1s spectrum of the PFPDPA SAM exhibits three peaks at 284.5 eV (**5**), 286.4 eV (**6**) and 287.5 eV (**7**), assigned to the alkyl linker, the carbon atom adjacent to O, and the carbon atom in the fluorinated ring adjacent to fluorine, respectively.[191] The C 1s spectrum of the HFDPA SAM exhibits three peaks at 284.9 eV(**8**), 290.5 eV (**9**), and 292.7 eV (**10**), assigned to the short alkyl linker, fluorinated alkyl chain ($-CF_2-$), and the terminal $-CF_3$ moiety, respectively.[313]

The Al 2p and P 2p intensities varied upon the series (Figure 4.37b and Figure 4.37c). Based on these values the effective thicknesses and relative packing densities of the PA SAMs were estimated (see section 4.6.2 for details). The results are compiled in Table 4.4. Note that the effective thicknesses represent the lowest estimates, since the blank substrate was contaminated to some extent (see Figure 4.37a) and the respective intensity, used for the thickness evaluation (see Eq 4.9), and was therefore somewhat lower than for the entirely clean support. All the derived values are comparable to the molecular lengths, evidencing once more a monomolecular assembly. As for the relative packing density, it is the highest for the OPA SAM, which is understandable in view of the long and compact molecular backbone, promoting efficient self-assembly. The values for the shorter alkyl backbone (DPA) and its substitution (PFPDPA) are somewhat lower, which is understandable. The value for the partially fluorinated backbone is the lowest, in agreement with the comparably large atomic radius of fluorine and helical conformation of the fluorinated alkyl chain.[313,314]

Table 4.4: Effective thickness and relative packing density with respect to OPA SAMs as well as the length of the SAM building molecules. The effective thickness values represent the lowest estimates (see text for details); the relative packing density values are course estimates only (see section 2). The error of the values is ±5%.

Parameter /SAM	DPA	OPA	PFPDPA	HFDPA
molecular length, Å	18.3	26.0	25.1	17.4
effective thickness (lowest estimate), Å	9.0	14.7	11.5	10
relative packing density	0.68	1	0.71	0.54

The O 1s spectra of all PA SAMs (partly shown below) exhibit an asymmetric peak at 531.8 eV assigned to the substrate (Al_2O_3).[315] The intensity of this peak varies from SAM to SAM, depending on the coverage and thickness. For the PFPDPA SAM this feature overlap with an additional symmetric peak at 533.7 eV, assigned - in accordance with the molecular composition (Figure 4.36) - to the oxygen atom linking the alkyl chain to the fluorinated phenyl ring (see subchapter 4.6.6).

The F 1s spectra of the PFPDPA and HFDPA monolayers (shown below) exhibit a pronounced single peak at 687.9-688.1 eV, assigned - in accordance with the molecular compositions (Figure 4.36) - to the fluorine atoms in the respective SAM building molecules (see subchapter 4.6.6 and 4.6.7).

Generally, the characterization of the PA SAMs at room temperature, in their pristine state, suggests their identity and well-defined character, qualifying them, thus, as representative model systems for the thermal stability experiments.

4.6.4 Temperature effect: DPA
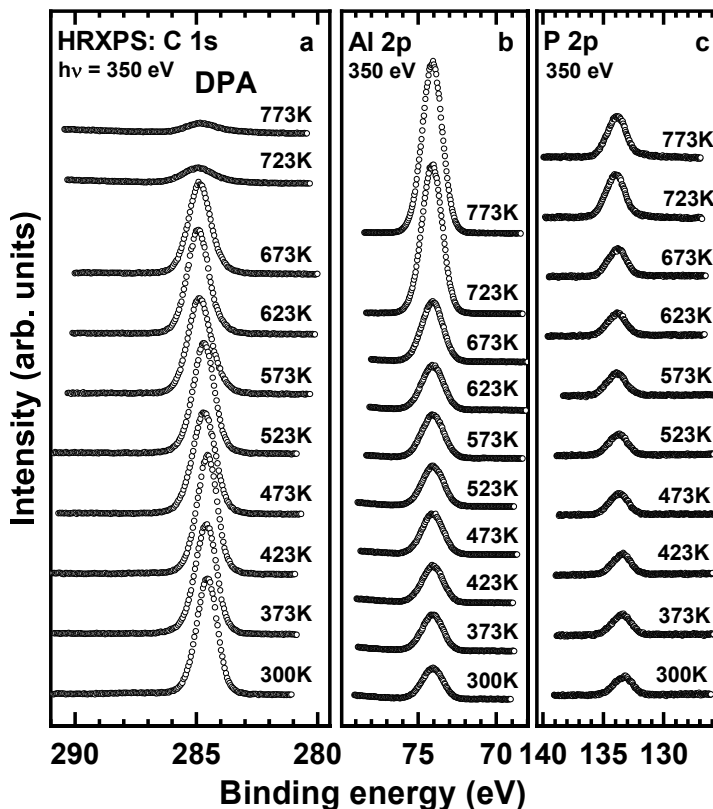
Figure 4.38: The C 1s (a), Al 2p (b), and P 2p (c) HRXPS spectra of the DPA SAM successively annealed in UHV at temperatures of 300-773 K. The spectra were acquired at a PE of 350 eV.

94

The C 1s, Al 2p, and P 2p spectra of the DPA SAM successively annealed in UHV at temperatures of 300-773 K are presented in Figure 4.38; the temperature dependence of the intensities of the characteristic photoemission peaks is compiled in Figure 4.39. The intensity of the characteristic C 1s peak in Figure 4.38a exhibits only slight decrease upon the annealing up to 673 K, followed by the abrupt decrease at the higher temperatures. The intensity of the substrate signal exhibits a reverse behavior, with the slightly increasing values up to 673 K and abrupt increase at the higher temperatures. The above behavior suggests a thermal stability of the DPA SAM up to 623 K, start of its degradation at 673 K, and extensive molecular decomposition with the desorption of the released fragments at the higher temperatures. Interestingly, the intensity of the PA group signal in Figure 4.38c does not behave as the C 1s signal but rather as the substrate intensity, exhibiting an only slight increase up to 623 K, large increase at 673 K, and an abrupt increase at the higher temperatures. This means that the vast majority of the PA moieties remain on the surface upon the temperature-induced desorption of the alkyl backbones and their fragments.

Considering the data in Figure 4.38 and Figure 4.39, one can conclude that the most likely temperature-affected weak link in the DPA case is the bond between the PA group and the molecular backbone. Consequently, the backbones represent the major released fragments.
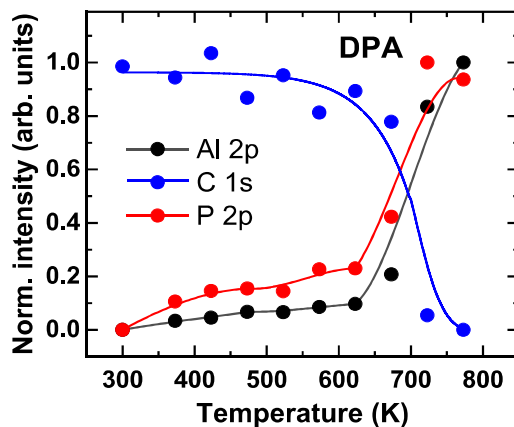
Figure 4.39: The normalized intensities of the characteristic photoemission peaks in the HRXPS spectra of the DPA SAM as functions of annealing temperature. The C 1s intensity is normalized to the value at 300 K; the Al 2p and P 2p intensities - to the values at 723 or 773 K. The solid curves are guides for the eyes.

4.6.5 Temperature effect: OPA
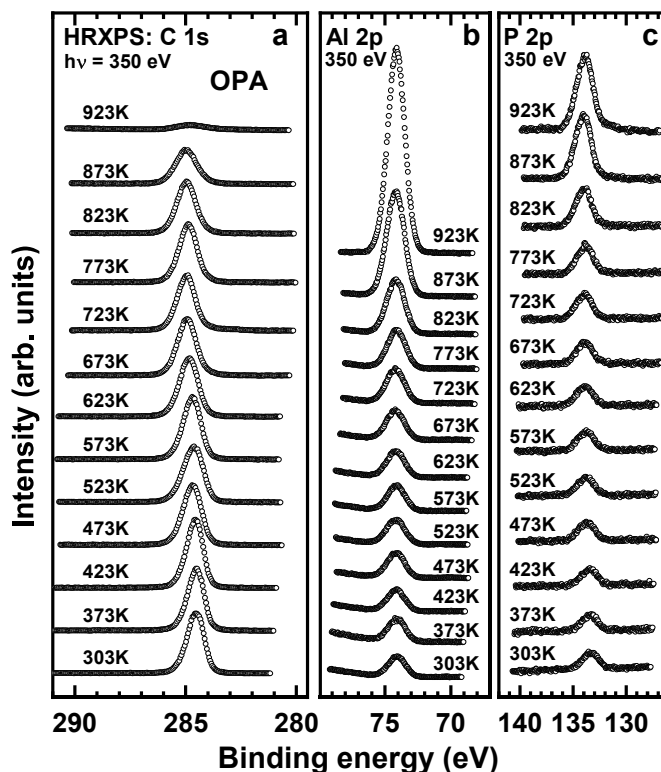
Figure 4.40: The C 1s (a), Al 2p (b), and P 2p (c) HRXPS spectra of the OPA SAM successively annealed in UHV at temperatures of 300-923 K. The spectra were acquired at a PE of 350 eV.
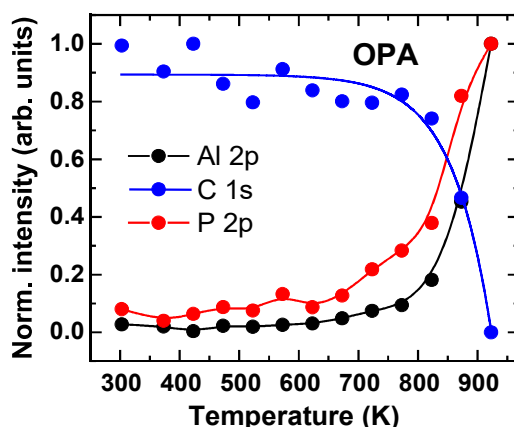
Figure 4.41: The normalized intensities of the characteristic photoemission peaks in the HRXPS spectra of the OPA SAM as functions of annealing temperature. The C 1s intensity is normalized to the value at 300 K; the Al 2p and P 2p intensities – to the values at 923 K. The solid curves are guides for the eyes.

The C 1s, Al 2p, and P 2p spectra of the DPA SAM successively annealed in UHV at temperatures of 300-923 K are presented in Figure 4.40; the intensity's temperature dependence of the characteristic photoemission peaks is compiled in Figure 4.41. Generally, the behavior of the spectra in Figure 4.40 mimics that in Figure 4.38, which is understandable because of the similarity of the chemical structures of DPA and OPA, with the only difference being the length of the molecular backbone. The latter parameter seems, however, to be of importance (as can be expected) since, according to the data in Figure 4.40 and Figure 4.41, the OPA SAM has a higher temperature stability than the DPA monolayer. Indeed, the intensities of the characteristic peaks in Figure 4.40 vary only slightly upon annealing up to 773 K and only start changing upon the heating to the higher temperatures, with a drop in the C 1s intensity accompanied by a simultaneous rise of the Al 2p and P 2p intensities (see Figure 4.41). Similar to the DPA case, this behavior is characteristic of the temperature-induced break-up of the bond between the PA groups and the alkyl backbone with subsequent desorption of the released fragments.

4.6.6 Temperature effect:PFPDPA
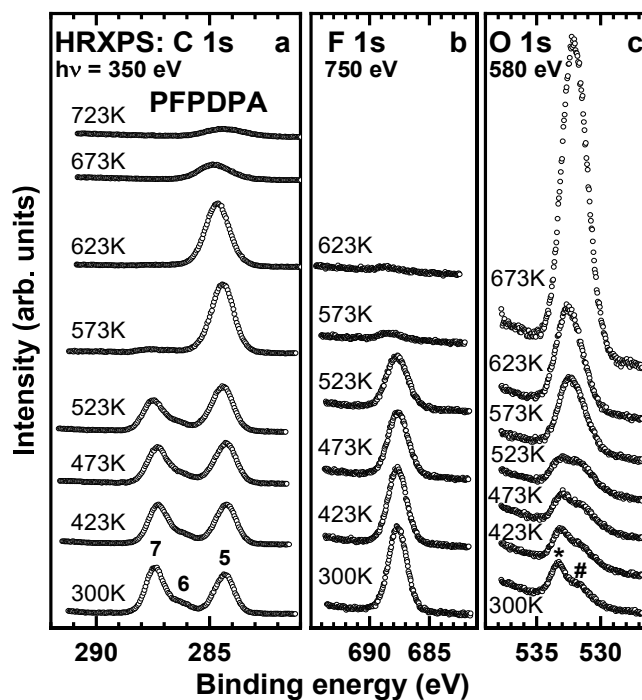
Figure 4.42: The C 1s (a), F 1s (b), and O 1s (c) HRXPS spectra of the PFPDPA SAM successively annealed in UHV at temperatures of 300-723 K. The spectra were acquired at Pes of 350 eV (C 1s), 750 eV (F 1s), and 580 eV (O 1s). The peaks in the C 1s and O 1s spectra are marked by numbers and signs (see Figure 4.37 and text for details).

The C 1s, F 1s, and O 1s spectra of the PFPDPA SAM successively annealed in UHV at temperatures of 300-723 K are presented in Figure 4.42; the intensity's temperature dependence of the characteristic photoemission peaks is compiled in Figure 4.43, including the data for the Al 2p and P 2p spectra (not shown), which, in the terms of the spectral shape, are similar to the DPA/OPA case.

The F 1s spectrum of the pristine SAM (T = 300 K) in Figure 4.42b exhibits a single peak at 687.9 eV, which can be assigned to the fluorine atoms in the fluorinated phenyl ring. The O 1s spectrum of the pristine SAM (T = 300 K) in Figure 4.42c exhibits a superposition of two peaks, viz. an asymmetric peak at 531.8 eV (#) and a symmetric peak at 533.7 eV (*). As mentioned in section 4.6.3, the former feature was observed in the O 1s spectra of all PA SAMs and is characteristic of the signal from the substrate (Al_2O_3); it becomes the only feature at T ≥ 573K. The latter peak was only recorded in the spectra of the PFPDPA SAM and is therefore specific for this particular monolayer. In accordance with the molecular composition, it is assigned to the oxygen atom linking the alkyl chain to the fluorinated phenyl ring.
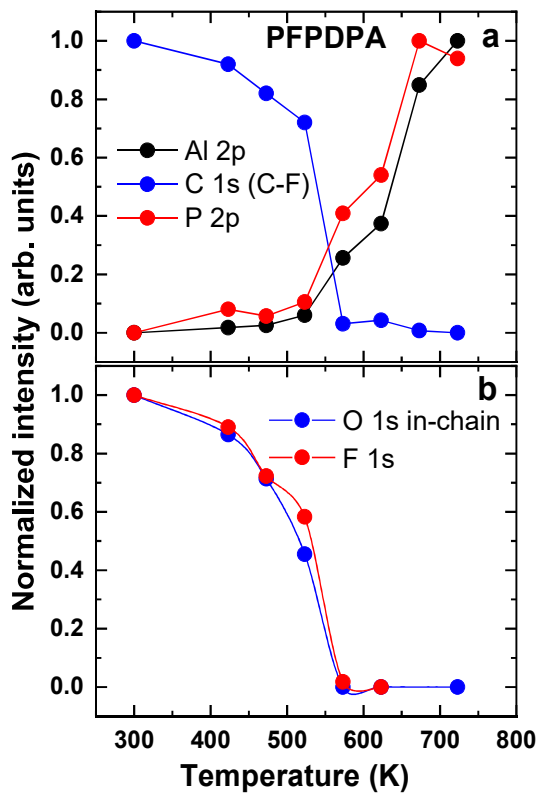
Figure 4.43: The normalized intensities of the characteristic photoemission peaks in the HRXPS spectra of the PFPDPA SAM as functions of annealing temperature: (a) Al 2p, C 1s (C-F), and P 2p for a PE of 350 eV; (b) O 1s (in-chain) and F 1s. The C 1s, O 1s, and F 1s intensities are normalized to the value at 300 K; the Al 2p and P 2p intensities – to the values at 673 or 723 K. The solid curves are guides for the eyes.

The C 1s spectra in Figure 4.42a exhibit a slight decrease in the intensity of peak **7**, assigned to the carbon atoms bound to fluorine in the fluorinated ring (see section 4.6.3), up to T =

473 K, followed by a further decrease at T = 523 K, and nearly complete intensity drop at the higher temperatures. The above behavior is exactly mimicked by the F 1s peak and the O 1s peak of the in-chain oxygen (**2**). This is additionally verified in Figure 4.43, where the intensities of the above peaks are shown as functions of the temperature.

Such a correlation of the C 1s (C–F), F 1s, and O 1s (in-chain) intensities suggests a temperature-induced break-up of the bond between the linking oxygen atom and the alkyl chain, with the subsequent desorption of the released fragments. This is accompanied by the significant increase in the intensity of peak **5**, assigned to the alkyl chain (see Figure 4.42a). Such a strong increase can be surprising but one has to consider that the C 1s signal is in the nearly saturation regime. Indeed, the intensity of this signal, I_{C1s}, is given by the equation 4.4[148] Considering that λ_{C1s} is quite small at the given kinetic energy of the photoelectrons (4-6 Å),[150] the C 1s intensity does not entirely reflect the amount of carbon. Consequently, a removal of the topmost part of the SAM (including the fluorine atoms as well) results in the increase of intensity from the bottom part, without much in the total C 1s intensity.

At the temperatures above 523 K, residual part of the PFPDPA SAM mimics the DPA monolayer (see subchapter 4.6.4) and exhibits a similar behavior upon the further heating. The intensity of the respective peak 5 remains nearly constant at 573 K and 623 K, and then decreased abruptly upon the heating up to 673 K. This decrease is accompanied by a strong increase of the signal from the substrate, as demonstrated by the O 1s spectra in Figure 4.42c (peak **1**) and the intensity of the Al 2p signal in Figure 4.43a.

Similar to the DPA/OPA case, the signal of the PA group (P 2p) shows the inverse behavior as compared to the C 1s one, mimicking almost exactly the substrate signal (Al 2p). Consequently, once again, the bond between the PA group and the alkyl chain serves as a temperature-sensitive weak link, with the subsequent desorption of the released fragments.

4.6.7 Temperature effect: HFDPA

The C 1s, F 1s, and O 1s spectra of the HFDPA SAM successively annealed in UHV at temperatures of 300-623 K are presented in Figure 4.44; the temperature dependence of the intensities of the characteristic photoemission peaks is compiled in Figure 4.45, including the data for the Al 2p and P 2p spectra at a PE of 350 eV (not shown), which, in the terms of the spectral shape, are similar to the DPA/OPA case. The latter data should however be taken with a grain of salt since the 350 eV data suffer to some extent from the X-ray induced damage and the 750 eV data, with a more frequent variation of the measurement spot, are more reliable in the case of the HFDPA SAM.

The F 1s spectrum of the pristine HFDPA SAM (T = 300 K) in Figure 4.44b exhibits a single peak at 688.1 eV, which can be assigned to the fluorine atoms in the fluorinated alkyl chain. The Al 2p spectra in Figure 4.44c, acquired at a PE of 750 eV, are analogous to the same spectra acquired at a PE of 350 eV, and only differ by a lower energy resolution and a lesser attenuation of the photoemission signal.
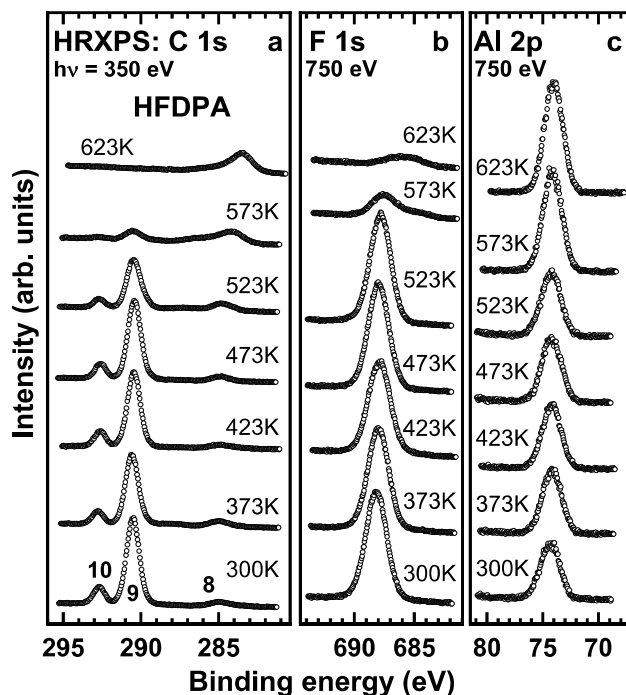
Figure 4.44: The C 1s (a), F 1s (b), and Al 2p (c) HRXPS spectra of the HFDPA SAM successively annealed in UHV at temperatures of 300-623 K. The spectra were acquired at Pes of 350 eV (C 1s) and 750 eV (F 1s and Al 2p). The peaks in the C 1s spectra are marked by numbers (see Figure 4.37 and text for details).
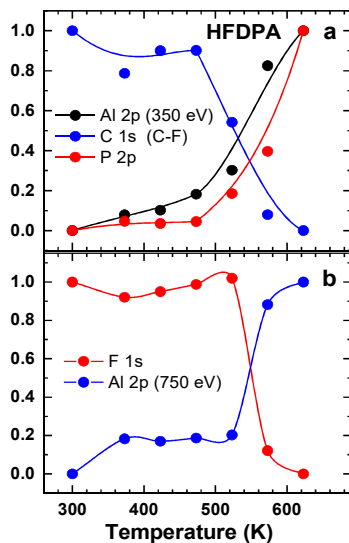
Figure 4.45: The normalized intensities of the characteristic photoemission peaks in the HRXPS spectra of the HFDPA SAM as functions of annealing temperature: (a) Al 2p, C 1s (C-F), and P 2p for a PE of 350 eV; (b) Al 2p (a PE of 750 eV) and F 1s. The C 1s, O 1s, and F 1s intensities are normalized to the value at 300 K; the Al 2p and P 2p intensities – to the values at 673 or 723 K. The solid curves are guides for the eyes.

The C 1s spectra in Figure 4.44a exhibit a slight decrease in the intensities of the peaks **9** and **10**, assigned to the carbon atoms in the fluorinated part of the backbone ($-CF_2-$ and $-CF_3$, respectively), up to T = 473 K, followed by a further decrease at T = 523 K, strong intensity drop at T = 573 K, and complete intensity drop at T = 623 K (see also Figure 4.45a). The above behavior is mimicked by the F 1s peak (Figure 4.44b and Figure 4.45b), which shows a nearly constant intensity up to T = 523 K, followed by strong intensity drop at T = 573 K and nearly complete intensity drop at T = 623 K. The intensity of the Al 2p peak in Figure 4.44c, Figure 4.45a, and Figure 4.45b show the inverse behavior upon temperature variation. Similar to the other SAMs of this study, the intensity of the PA group signal mimics that of the substrate (Figure 4.45a), which suggests that the anchoring groups of the HFDPA SAM are hardly affected by the annealing.

Interestingly, the intensity drop of the peaks **9** and **10** is accompanied by an increase in intensity of the peak 8, assigned to the very short, non-fluorinated part of the backbone. Consequently, the most likely scenario is a temperature-induced break-up of the bond between the non-fluorinated and fluorinated parts of the backbone, with the subsequent desorption of the released fragments.

4.6.8 Temporal stability
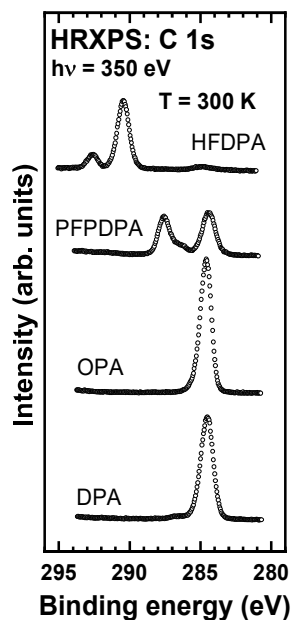
Figure 4.46: The C 1s HRXPS spectra of the DPA, OPA, PFPDPA, and HFSPA SAMs stored under ambient conditions in dark for two months.

Along with the thermal stability, the temporal stability of functional films is of importance. In this context, we monitored the quality of the PA SAMs after two months storage under ambient conditions but in dark − to exclude possible photochemistry processes. The

respective C 1s spectra – as the most representative of the SAMs – are presented in Figure 4.46. The general spectral shapes, characteristic photoemission peaks, and the intensity relations within the particular spectra and between the spectra of the individual SAMs mimics those in Figure 4.37a. Thus, it can be concluded that the PA SAMs are generally stable upon a prolonged storage under ambient conditions.

4.6.9 Discussion

The data suggest a predominant role of the molecular backbone for thermal stability of PA SAMs on oxide substrates, including alumina in particular. The "weak link" in this context is either the bond between the PA group and the backbone or a bond within the backbone. The former is most likely the case for non-substituted alkyl SAMs, such as DPA and OPA (see subchapter 14.6.4 and 4.6.5), even though a certain extent of temperature-induced bond breakage within the backbone cannot be completely excluded. The latter seems to be the case for substituted and partly fluorinated alkyl SAMs, such as PFPDPA and HFDPA. The HRXPS data for the PFPDPA monolayer (subchapter 4.6.6) suggests a temperature-induced break-up of the bond between the linking oxygen atom and the alkyl chain ("weak link"), with the subsequent desorption of the released fragments. This scenario is additionally verified by the DFT calculations.[109] The HRXPS data for the HFDPA monolayer suggests a temperature-induced break-up of the bond between the non-fluorinated and fluorinated parts of the backbone ("weak link"), with the subsequent desorption of the released fragments (subchapter 4.6.7).

The "weak links" in the PFPDPA and HFDPA SAMs, associated with the specific functional groups, are obviously more sensitive to temperature than the bond between the PA group and alkyl backbone. Indeed, the DPA and OPA SAMs remain stable up to 673 K and 773 K, respectively, whereas the PFPDPA and HFDPA monolayers are stable up to 523 K only. Also, the bond between the alkyl segment and the PA group in the residual of the latter SAMs remains preserved after the respective "weak link" bond within the molecular backbone is cleaved (subchapter 4.6.6 and 4.6.7).

Another interesting correlation between the SAM data is the two-steps character of temperature-induced decomposition of for the PFPDPA system which can be traced both in the XPS data for the SAMs (Figure 4.42).

According to the HRXPS data (subchapter 4.6.4 and 4.6.5), an analogous backbone length effect takes place in the SAMs, with a noticeably better thermal stability of the OPA monolayer as compared to the DPA films (773 K vs 673 K). On the one hand, a longer molecular backbone suggests a higher interaction energy in a 2D assembly, which is additionally "amplified" by a better orientational order. On the other hand, the length of molecular backbone can affect the exact course of degradation pathways, as observed e.g. in the case of electron irradiation induced modification of alkanethiolate SAMs on Au.[316] Whereas in the case of a long-chain SAM, the dominant, irradiation-induced processes were decomposition of the alkyl chains and capture of the released alkylsulfide moieties in the aliphatic matrix, desorption of the complete molecular species emerging after the cleavage of the thiolate-gold bond prevailed in the case of a short-chain monolayers.[316]

Finally, it is of particular importance to compare the presented data on thermal stability of the PA SAMs with the results of the previous publications. As mentioned in the introduction, Chen et. al stated that the parameters of OPA SAMs on an aluminum film are maintained upon its annealing under air up to 200°C (473 K) and claimed that no OPA molecules could stand for annealing at 300°C (573 K) and above.[302] In contrast, Kanta et. al. stated the breakage of the aliphatic chain upon heat treatment of OPA SAMs on titania in air at temperatures of 350°C (623 K)[312] and Bhairamadgi et al. found that OPA SAMs on porous aluminium oxide are stable up to ~500 °C (773 K) upon their annealing in UHV.[202] Our value for the degradation onset of the OPA monolayer on Al_2O_3, viz. 773 K (see section 4.6.5), correlates perfectly with the latter value. Note that the exact value of this onset can, to a certain extent, depend on the substrate,[202] we do not expect this effect to be strong since the bonding of PA group to any oxide substrate is strong enough and this is not the bond to the substrate but bond within the molecular backbone, which represents the "weak link".

4.6.10 Conclusions

Al_2O_3 substrate was studied in the 300−923 K range. The annealing to the elevated temperatures was performed under UHV conditions and the temperature-induced degradation was monitored in situ, by synchrotron-based HRXPS. The range of the thermal stability and the degradation pathways were found to be dependent on the chemical composition of the SAM forming molecules, with the molecular-specific "weak links". Whereas the anchoring PA groups were hardly (if at all) affected by the annealing, temperature-induced breakup of the bond between the backbone and the PA group or a specific bond within the backbone was observed. The former is the case for the nonsubstituted alkyl backbone, which is cleaved at temperatures above 673 K, with the subsequent desorption of the released fragments. The latter is the case for the substituted (pentafluorophenoxy) or partly fluorinated alkyl backbone, with the bond cleavage occurring either between the substitution and alkyl linker or between the fluorinated and nonfluorinated parts of the backbone at temperatures above 523 K. The released fragments desorb from the surface, but the alkyl linker remains unaffected until its degradation at the higher temperature.

The above results suggest a common stability of the PA SAMs at temperatures below 523 K (250 °C), which should be probably sufficient for most applications. It is however advisable not to trust this result completely but, generally, to test thermal stability of custom-designed functional PA SAM in context of possible "weak link" as far as thermal stability is important for the performance of a particular device.

5. Conclusions and Outlook

5.1 Conclusions

In this thesis, molecular structure of monomolecular films was successfully correlated with their properties, particularly electrostatic properties, charge transport properties, rectification behaviour, and thermal stability. Monomolecular films (SAMs) were characterized from different perspectives, using conventional and synchrotron-based X-ray photoelectron spectroscopy (XPS), ultraviolet photoelectron spectroscopy (UPS), near-edge x-ray absorption fine structure (NEXAFS) spectroscopy, two-terminal junction approach with top EGaIn electrode, and Kelvin Probe (KP) measurements.

The concept of SAMs with embedded dipolar group was successfully implemented to oxide substrates due to the phosphonic acid (PA) anchoring group. The backbones of these molecules, PmP-PA-up and PPm-PA-down, contain pyrimidine rings. These SAMs are oriented upright on the substrate, hence allowing dipole moment to be directed either to or away from the substrate. The SAMs exhibit pronounced electrostatic effects, reflected by the shifts of the characteristic peaks in the C 1s XP spectra and by the work function values of the SAM-modified ITO substrate in the range of 3.9 - 4.85 eV, without changing the chemical character of the SAM-ambient interface. The observation of the electrostatic effects in photoemission for dipolar SAMs on oxide substrates underlines the general character of these effects and establishes XPS as a useful tool to monitor these effects and SAM morphology for different types of substrate materials.

The Au(111) substrate work function was tuned in a gradual fashion in the thesis by binary SAMs, comprised of either H-BPT and F-BPT or CH_3-BPT and CF_3-BPT. A correlation between the electrostatic properties (work function) and charge transport across the SAMs was investigated using both binary SAMs series. The charge tunneling rate across the mixed SAMs framework turned out to be intermediate to those of the single-component monolayers, varying also in a gradual fashion with the relative SAM composition between the respective ultimate values. Our analysis suggests that, the charge transport in the binary SAMs is most likely mediated by the SAM as a whole, defined by the composition-depending dipole induced upon contact of the SAM to a top electrode. At the same time, the energy positions of the frontier molecular orbitals responsible for the charge transport in the SAMs and the energy offset between this orbital and the Fermi level of the assembled junction were either nearly unchanged or varied only slightly with the SAM composition. Additionally, custom-designed SAMs of ferrocene/ruthenocene-substituted biphenylthiolates and fluorenethiolates on Au(111) were investigated. These fully conjugated SAMs exhibited two distinctly different conduction states, with a conventional conduction observed at a negative bias and a low conduction occurring at a positive bias, leading to a rectification ratio (RR) higher than 1000 at a very low bias, close to zero volts. The observed behavior was explained by a formation of metastable cation state of the SAM-building molecules, triggered by the applied positive bias.

Finally, the issue of thermal stability of functional SAMs with thiol anchoring group on Au(111) and with PA anchoring group on Al_2O_3 substrates were addressed. This issue is of a crucial importance for applications, defining the temperature range of SAM-based

devices and framing the preparation routes involving high temperature steps. The strength of substrate-anchoring group bond and the presence of a backbone-specific "weak links" were found to be crucial in determining SAMs thermal stability and SAMs degradation pathway. For both for alkanethiol and aromatic-thiol SAMs, C–S bond represents the weak link in context of the thermal stability.

PA anchor groups on oxide substrates were found to have higher robustness and better thermal stability compared to thiol on coinage metal substrate. No thermal degradation of anchoring PA groups was observed in our experiment. The results suggest a common stability of the PA SAMs at temperatures below 523 K (250 °C), which should be sufficient for most applications.

5.2 Outlook

The concepts of SAMs with either terminal- or embedded dipolar have been shown in this thesis to be very attractive to tune substrate work function or charge transport properties. Implementations of these concepts into electronic and optoelectronic are highly promising to enhance performance of nanodevices.

SAMs with embedded dipole on Au substrate were used recently to tune the contact resistance of organic thin-film transistors over three orders of magnitude, and fabricate not only p-type, but also n-type transistors with an improved performance.[2,3] These SAMs are almost identical with the PPm-PA-down and the PmP-PA-up molecules in Figure 4.1, except for the SAMs anchoring group. By using SAMs with phosphonic acid group, similar advantages of embedded dipole SAMs can be realized on transparent substrates as well, which is crucial for optoelectronic devices,[317–322] like solar cell or LED, without modifying the growth of the active layer.

Additionally, more investigations are necessary to understand how halogen substitution in SAMs influences their charge transport properties. A single halogen atom substitution for the case of aliphatic SAMs has been shown to change the tunnelling decay coefficient β from 0.75 to 0.25 Å^{-1}.[56] The influence of halogen atom substitution for the case of SAMs with aromatic backbone SAM was discussed in this thesis in subchapter 4.2 and 4.3 in the context of electrostatic effects. However, this issue also needs to be investigated from other perspectives, for example electronic coupling between SAMs and top electrodes.

The presented results in this thesis of molecular diode based-on ferrocene- and ruthenocene-substituted fully conjugated SAMs strongly encourage more investigations of the phenomenon and device optimization. Despite a very promising RR ($\sim 10^3$), this value is still inferior to those of the commercial diodes ($\sim 10^5$-10^8).[66] The strength of chemical bond between thiol and substrate has been suggested to be highly important to optimize RR of a molecular diode,[66] hence allowing a molecular diode with RR$\sim 10^5$ by using platinum as substrate. The same concept needs to be investigated for the case of ferrocene- and ruthenocene-substituted molecules described in the present study.

Appendix A. Supplementary data
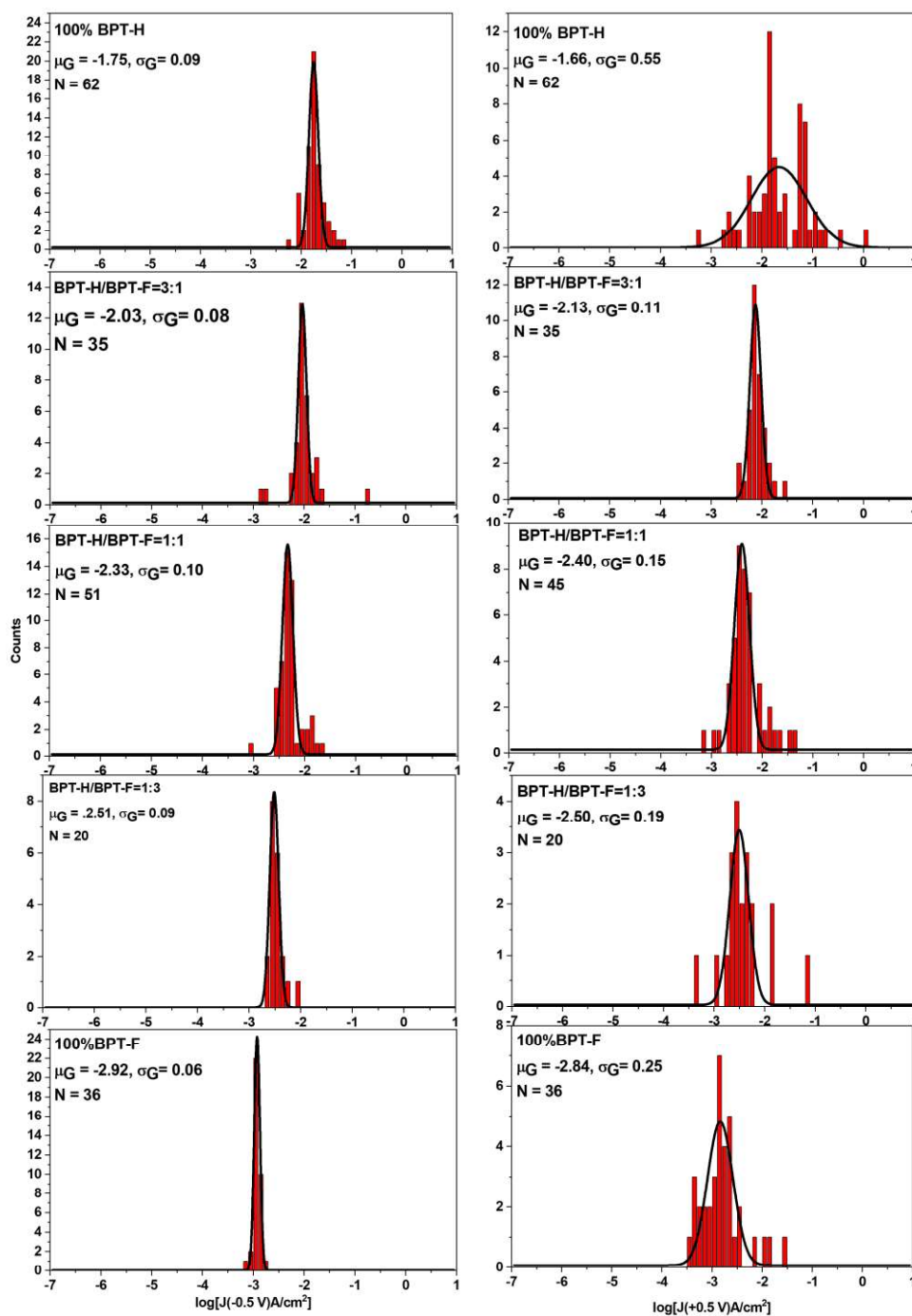
Figure A.1: Histograms of $\log|J(-0.5\,V)|$ (left column) and $\log|J(+0.5\,V)|$ (right column) for the single-component and binary H-BPT/F-BPT SAMs on Au substrate
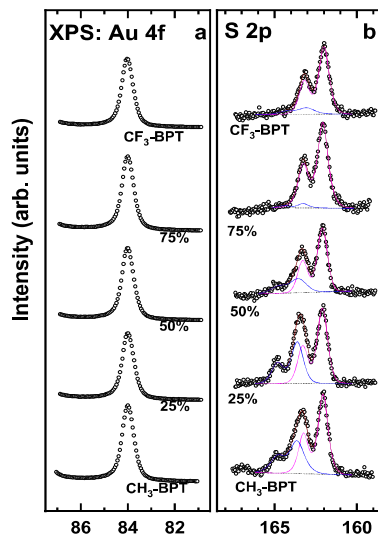
Figure A.2: Au 4f$_{7/2}$ (a) and S 2p (b) XP spectra of the single-component and mixed CH$_3$-BPT and CF$_3$-BPT SAMs. The spectra were acquired at the synchrotron, at a photon energy of 350 eV. The spectra of the binary SAMs are marked with the portions of CF$_3$-BPT in the solutions from which these SAMs were formed. The Au 4f$_{7/2}$ spectra of all SAMs exhibit similar intensities suggesting similar effective thicknesses and packing densities of the monolayers. The S 2p spectra are decomposed to individual doublet associated with the thiolate and unbound sulfur (thiol), drawn by the red and blue, respectively, whereas the sum of these two doublets is drawn by gray; the background is drawn by the black dotted lines.
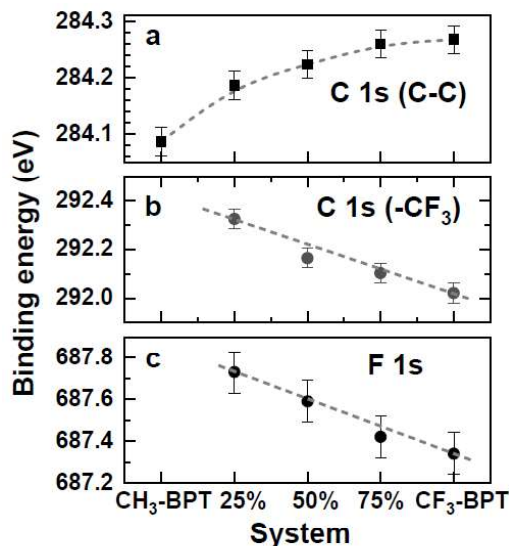
Figure A.3: The BE positions of the C-C (a) and -CF$_3$ (b) peaks in the C 1s XP spectra of the single-component and binary CH$_3$-BPT and CF$_3$-BPT SAMs as well as BE positions of the F1s peak in the spectra of these monolayers (c). The data for the binary SAMs (X-axes) is labeled by the portions of CF$_3$-BPT in the solutions from which they were formed.
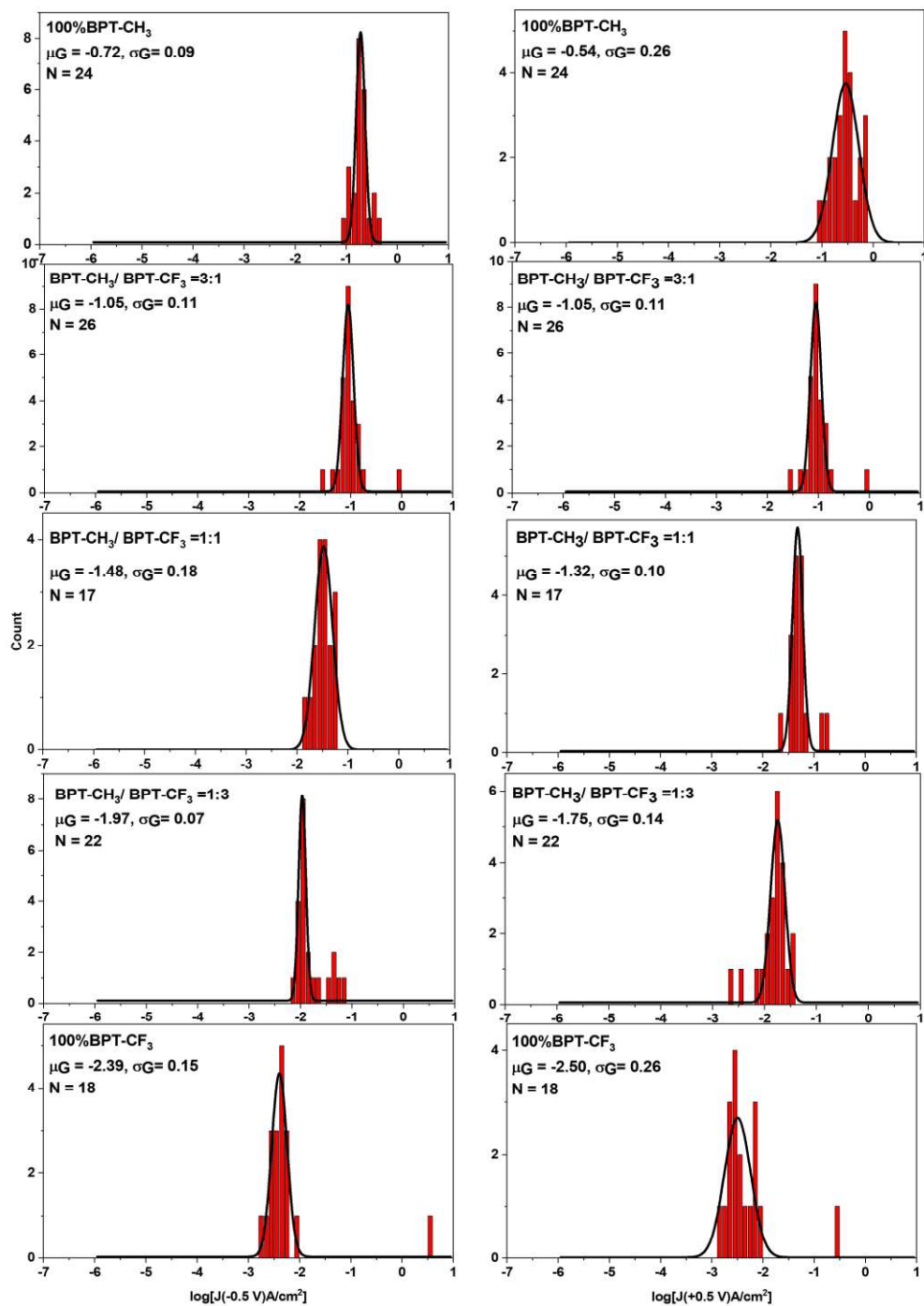
Figure A.4: Histograms of $\log|J(-0.5\,V)|$ (left column) and $\log|J(+0.5\,V)|$ (right column) for the single-component and binary CH_3-BPT/CF_3-BPT SAMs on Au substrate.
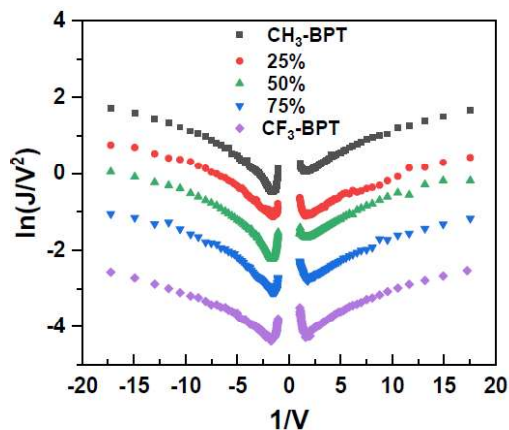
Figure A.5: Fowler-Nordheim (FN) plots for the Au/SAM//Ga_2O_3/EGaIn junctions with the single-component and binary CH_3-BPT/CF_3-BPT SAMs. The legend is given in the plot; the data for the binary SAMs are labeled by the portions of CF_3-BPT in the solutions from which they were formed.
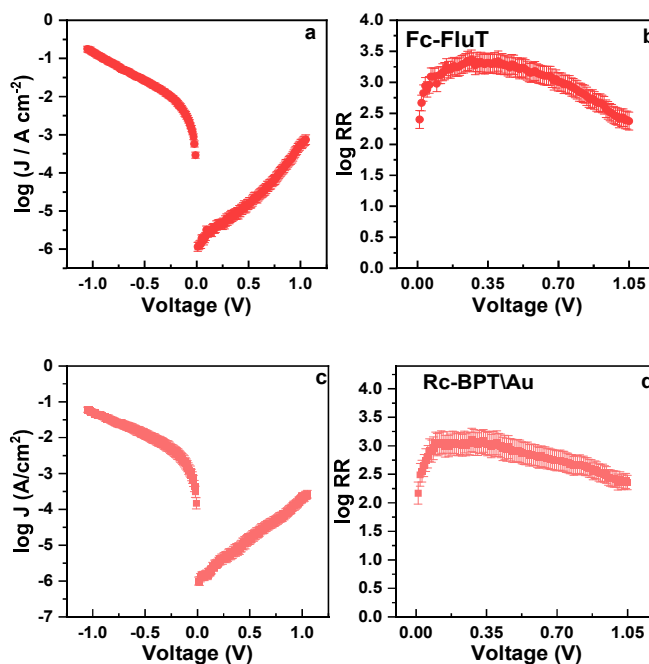
Figure A.6: Electrical characteristics of the Au/Fc-FluT//$Ga2O3$/EGaIn junction. (a) Semilogarithmic current density versus voltage (bias) plot; (b) Semilogarithmic RR versus voltage plot. Electrical characteristics of the Au/Rc-BPT//$Ga2O3$/EGaIn junction. (c) Semilogarithmic current density versus voltage (bias) plot; (d) Semilogarithmic RR versus voltage plot. Electrical characteristics of the Au/Rc-BPT//$Ga2O3$/EGaIn junction.
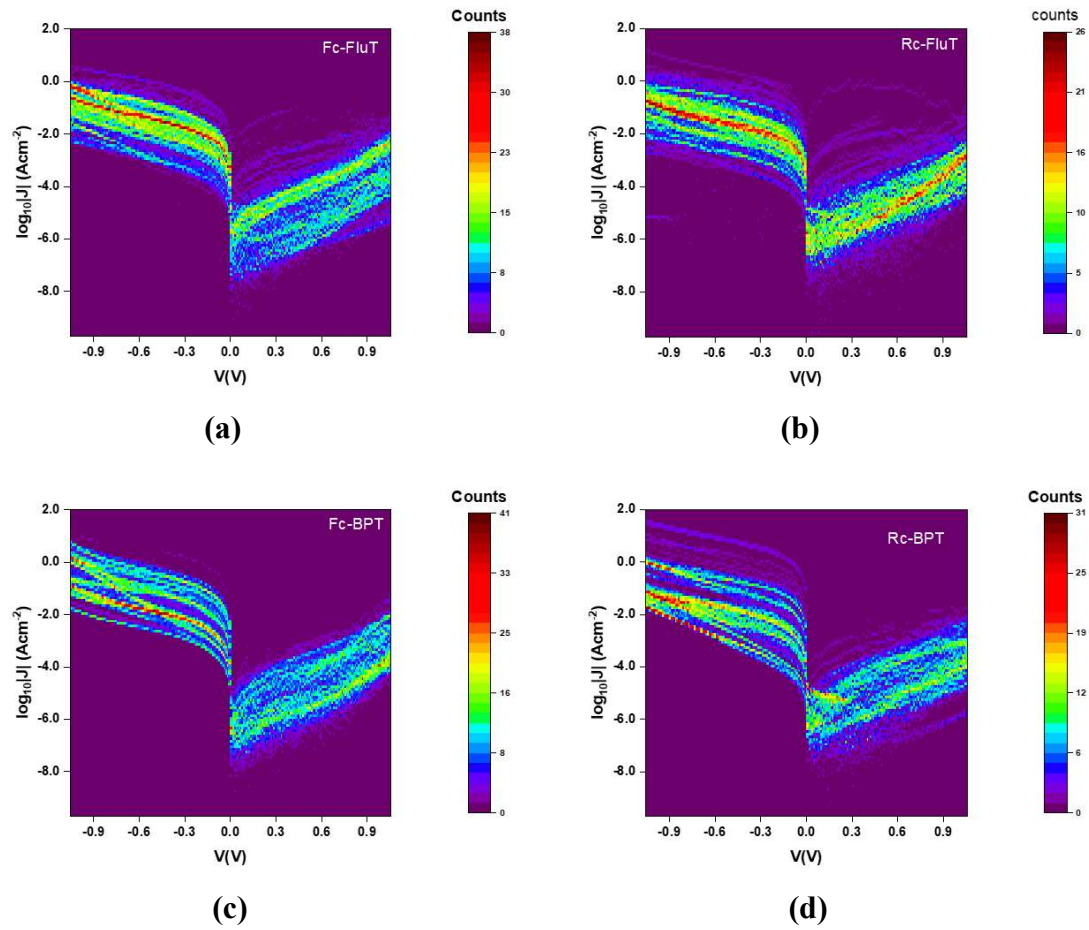
Figure A.7: Heat map of the semi-$\log_{10} |J(V)|$ curves of (a)the Au/Fc-FluT//Ga_2O_3/EGaIn junction (b)the Au/Rc-FluT//Ga_2O_3/EGaIn junction (c)the Au/Fc-BPT//Ga_2O_3/EGaIn junction (d)the Au/Rc-BPT//Ga_2O_3/EGaIn junction
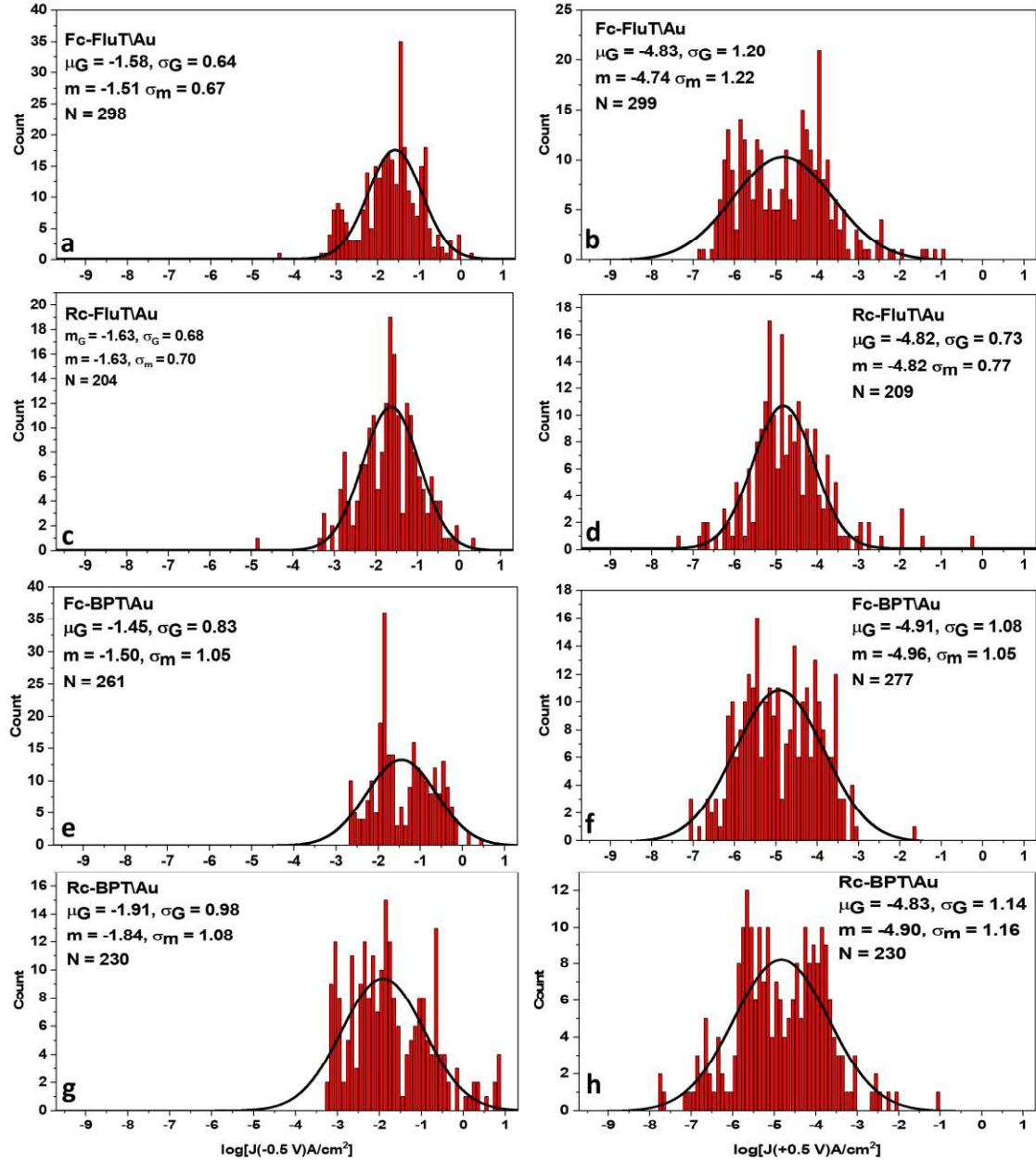
Figure A.8: Histograms of the $\log_{10}|J|$ at V = -0.5 V (left panel) and V = +0.5 V (right panel) of the (a and b)Au/Rc-FluT//Ga$_2$O$_3$/EGaIn, (c and d) Au/Fc-FluT//Ga$_2$O$_3$/EGaIn, (e and f)Au/Rc-BPT//Ga$_2$O$_3$/EGaIn, and (g and h) Au/Rc-BPT//Ga$_2$O$_3$/EGaIn A junction. The characteristic parameters are given: μ_G – Gaussian mean; σ_G – Gaussian standard deviation; m – median; σ_m - adjusted median absolute deviation; and N – number of scans.[175]

Table A.1: Summary of metallocene-based molecular junctions in the positive bias range.

SAM	Samples	Junctions	Scans	Processed	Yield
Fc-BPT	6	36	468	277	59.19%
Rc-BPT	5	17	263	164	62.36%
Fc-FluT	8	42	432	299	69.21%
Rc-FluT	6	34	324	209	62.96 %

Table A.2: Summary of metallocene-based molecular junctions in the negative bias range.

SAM	Samples	Junctions	Scans	Processed	Yield
Fc-BPT	6	25	261	261	100%
Rc-BPT	5	20	260	230	88.46%
Fc-FluT	8	29	308	298	96.75%
Rc-FluT	6	31	214	204	97.66 %

Table A.3: Statistical analysis of the $\log_{10}\left|J(+0.5\ \text{V})\right|$ data for the metallocene-based molecular junctions.

log[J(+0.5 V)A/cm^2]	μ_G	CI$_{95\%}$	median	CI$_{95\%}$
Fc-BPT	-4.91	0.13	-4.96	0.42
Rc-BPT	-4.83	0.15	-4.90	0.66
Fc-FluT	-4.83	0.14	-4.74	0.45
Rc-FluT	-4.82	0.10	-4.82	0.29

Table A.4: Statistical analysis of the $\log_{10}\left|J(-0.5\ V)\right|$ data for the metallocene-based molecular junctions.

log[J(-0.5 V)A/cm²]	μ_G	CI$_{95\%}$	median	CI$_{95\%}$
Fc-BPT	-1.45	0.10	-1.50	0.45
Rc-BPT	-1.91	0.13	-1.84	0.32
Fc-FluT	-1.58	0.07	-1.61	0.45
Rc-FluT	-1.63	0.09	-1.63	0.16
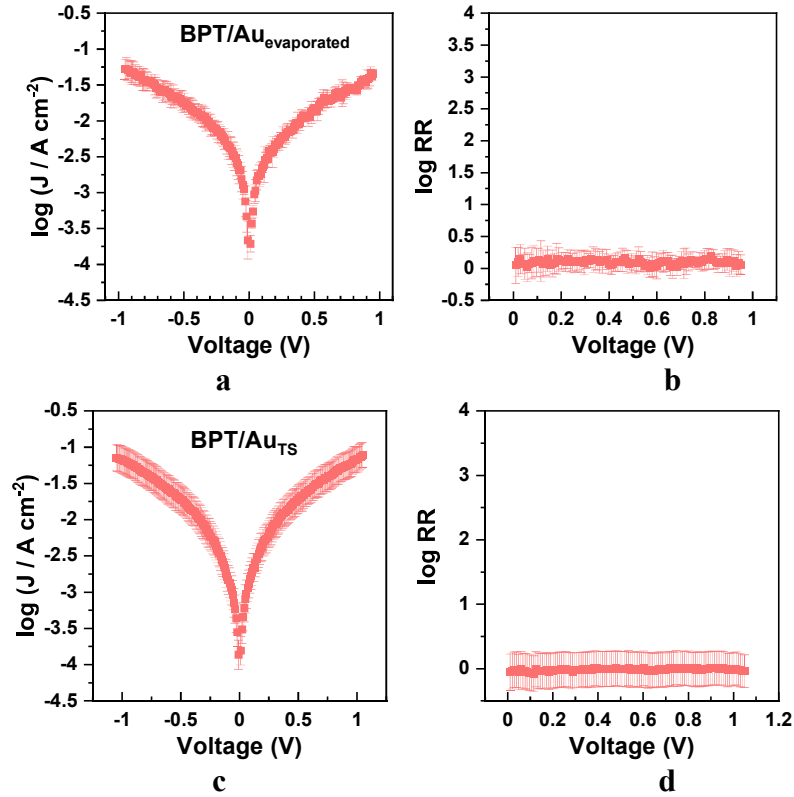
Figure A.9: Semilogarithmic current density versus voltage (bias) plot and the corresponding RR versus voltage (bias) plot for the reference Au/BPT//Ga$_2$O$_3$/EGaIn junction, featuring the (a and b) same evaporated Au substrate as in the case of the metallocene-substituted SAMs (top panels) and (c and d)the template-stripped Au substrate (bottom panels). The I-V curves for the latter, most frequently used substrate type agree well with those for the evaporated gold, verifying thus the validity of the latter substrate type for the charge transport measurements described in the present study. Apart from this comparison, the I-V curves for the Au/BPT//Ga$_2$O$_3$/EGaIn junction are nearly symmetric, as reflected by log RR close to zero (RR ≈ 1).
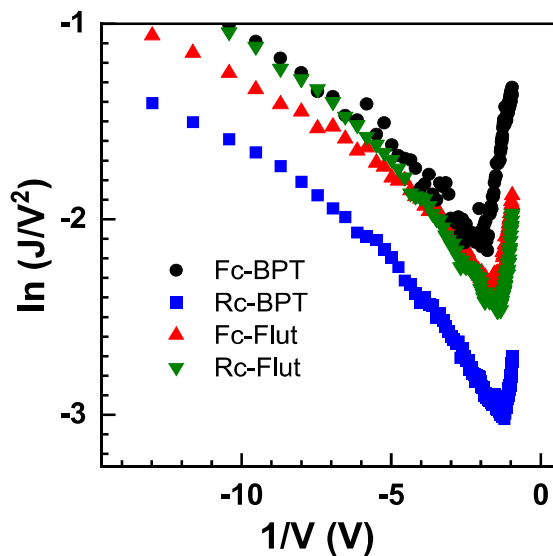
Figure A.10: Fowler-Nordheim plots for the metallocene-based molecular junctions.
The plots are processed from JV curves in Figure A.7. The minimum of the plots
corresponds to the value of the transition voltage.[183] The transition voltage is believed to
represent an approximate measure of the tunneling barrier height, providing the difference
between the energy of the accessible frontier orbital of a molecule and the Fermi level of
the electrode in an assembled junction.[244–246]

Table A.5: Transition voltage values, V_T^-, corresponding to the negative bias for the
metallocene-based molecular junctions in Figure A.10.

SAM	V_T^-
Fc-BPT	-0.57 V
Rc-BPT	-0.81 V
Fc-FluT	-0.69 V
Rc-FluT	-0.74 V

114
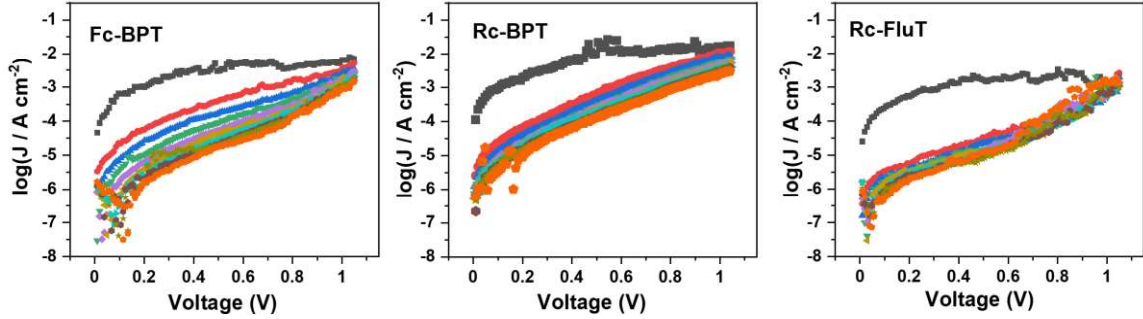
Figure A.11: Dynamics of the low-conduction state. Semilogarithmic current density versus voltage (bias) plots for the Au/SAM//Ga$_2$O$_3$/EGaIn junctions with SAM = Fc-BPT, Rc-BPT, and Rc-FluT. Ten successive individual scans with the bias variation from 0.05 to +1 V are shown; the first scan is drawn by the black signs.
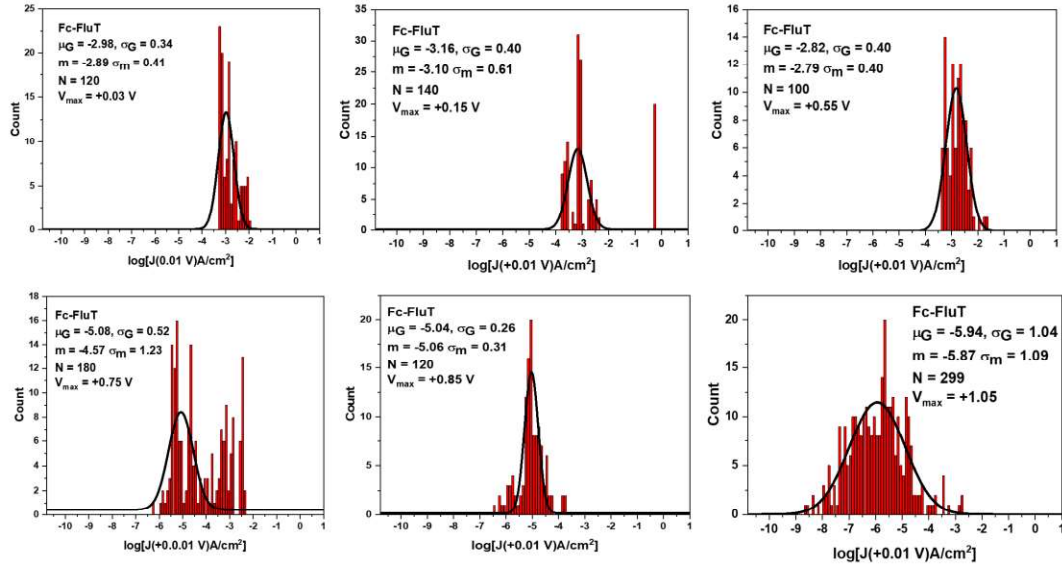
Figure A.12: Bias-mediated switching of the low conductance state in the Au/Fc-FluT//Ga$_2$O$_3$/EGaIn junction. Histograms of the $\log_{10}|J|$ at V = +0.01 V (see Figure 4.26b and Figure 4.26c) measured at the bias variation from +0.01 to the V_{max} value shown in the figure legend. The characteristic parameters are given: μ_G – Gaussian mean; σ_G – Gaussian standard deviation; m – median; σ_m - adjusted median absolute deviation; and N – number of scans.[175]
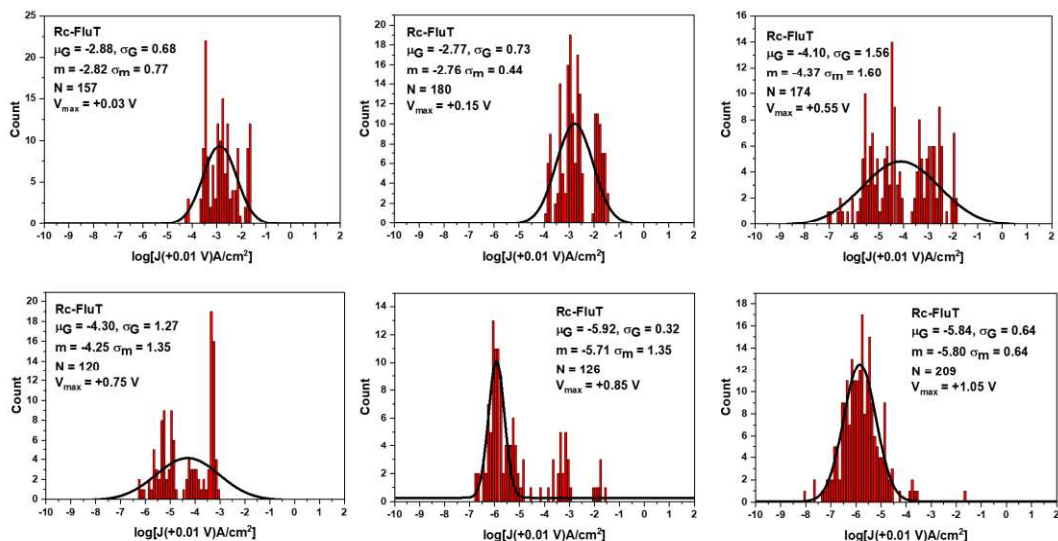
Figure A.13: Bias-mediated switching of the low conductance state in the Au/Rc-FluT//Ga₂O₃/EGaIn junction. Histograms of the $\log_{10}|J|$ at V = +0.01 V (see Figure 4.26b and Figure 4.26c) measured at the bias variation from +0.01 to the V_{max} value shown in the figure legend. The characteristic parameters are given: μ_G – Gaussian mean; σ_G – Gaussian standard deviation; m – median average; σ_m - adjusted median absolute deviation; and N – number of scans.[175]
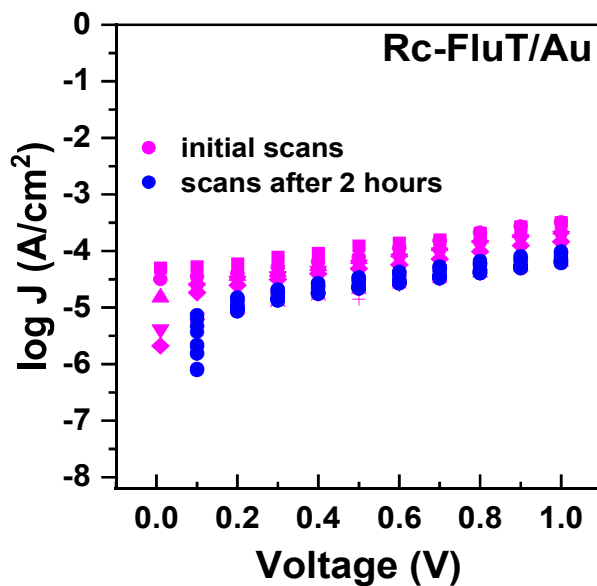
Figure A.14: Time stability of the Au/Rc-FluT//Ga₂O₃/EGaIn junctions. Representative of the entire series - semilogarithmic current density versus voltage (bias) plots for the Au/Ru-FluT//Ga₂O₃/EGaIn junction acquired with a time interval of 2 hours.
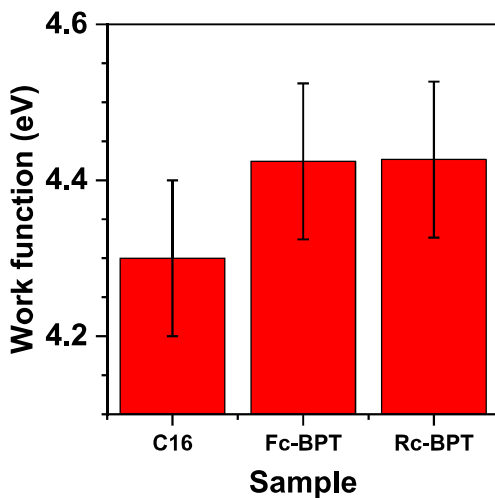
Figure A.15: Work function of the Fc-BPT and Rc-BPT SAMs. The reference value of the C16 monolayer is given for comparison.

Table A.6: Work functions of the Fc-BPT, Rc-BPT and C16 (reference) SAMs.

SAM	Work function (eV)
C16	4.3 ± 0.1
Fc-BPT	4.4 ± 0.1
Rc-BPT	4.4 ± 0.1
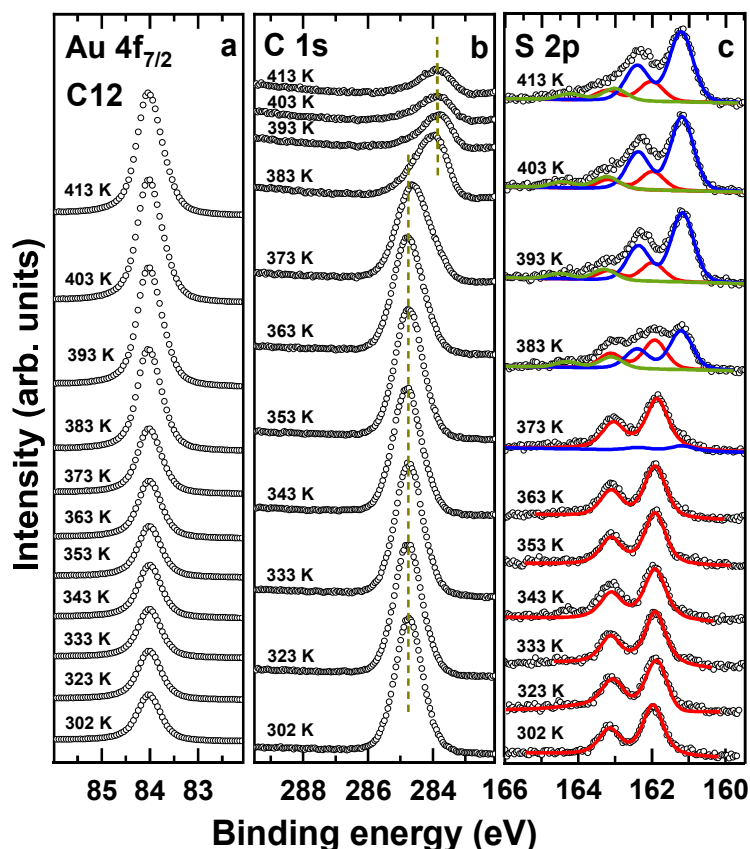
Figure A.16: The Au $4f_{7/2}$ (a), C 1s (b), and S 2p (c) XP spectra of the C12 SAM successively annealed in UHV at temperatures of 300-413 K (open circles). The temperatures are marked at the spectra. The positions of the C 1s peak before and after the temperature-induced shift are traced by vertical dashed lines in (b). Individual components of the S 2p spectra, corresponding to the thiolate anchoring groups, atomic sulfur, and disulfide/weakly bound/unbound sulfur are shown in (c) by the red, blue, and green solid lines, respectively.
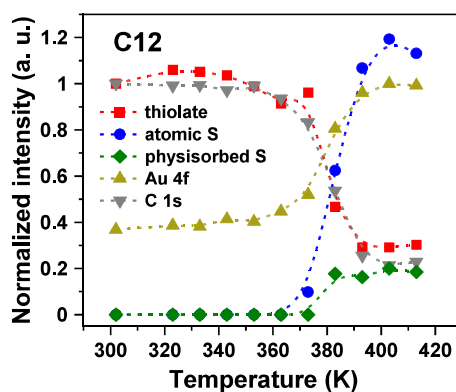
Figure A.17: The normalized intensities of the characteristic photoemission peaks and doublets in the XP spectra of the C12 SAM as functions of the annealing temperature. The legend is given in the panel. The C 1s intensity is normalized to the value at 302 K, the S 2p intensities – to the intensity of the thiolate signal at 302 K, and the Au $4f_{7/2}$ intensity – to the value at 413 K.
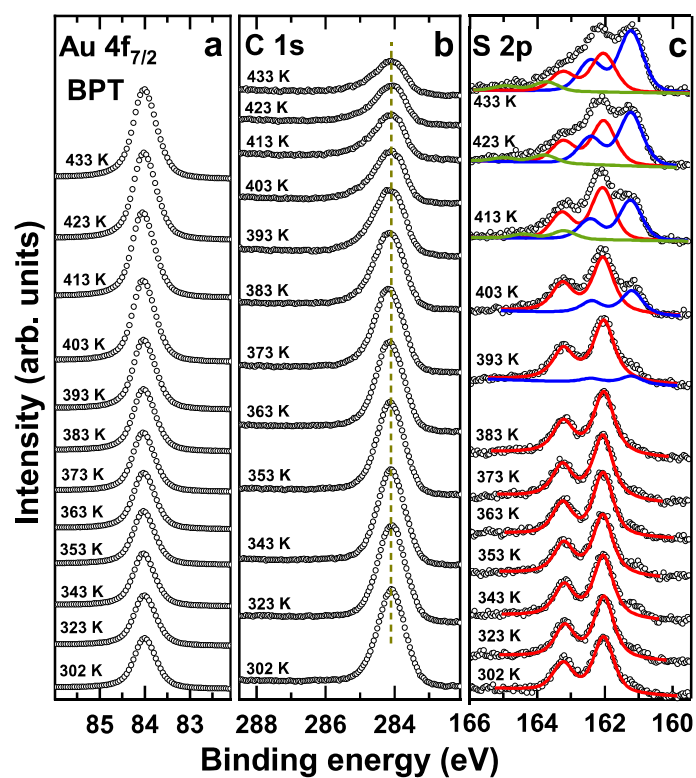
Figure A.18: The Au $4f_{7/2}$ (a), C 1s (b), and S 2p (c) XP spectra of the BPT SAM successively annealed in UHV at temperatures of 300-433 K (open circles). The temperatures are marked at the spectra. The position of the C 1s peak, which hardly changes at the temperature variation, is traced by vertical dashed line in (b). Individual components of the S 2p spectra, corresponding to the thiolate anchoring groups, atomic sulfur, and disulfide/weakly bound/unbound sulfur are shown in (c) by the red, blue, and green solid lines, respectively.
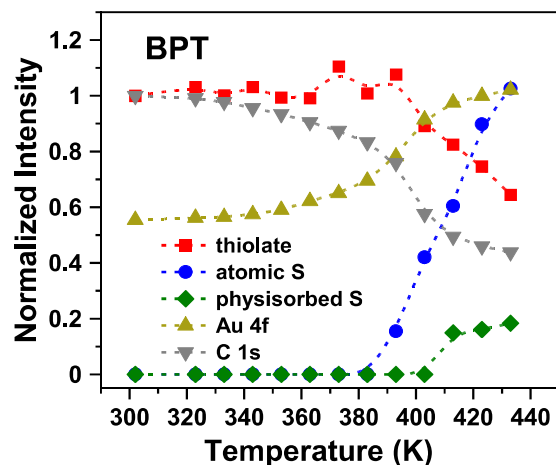
Figure A.19: The normalized intensities of the characteristic photoemission peaks and doublets in the XP spectra of the BPT SAM as functions of the annealing temperature. The legend is given in the panel. The C 1s intensity is normalized to the value at 302 K, the S 2p intensities – to the intensity of the thiolate signal at 302 K, and the Au $4f_{7/2}$ intensity – to the value at 413 K.
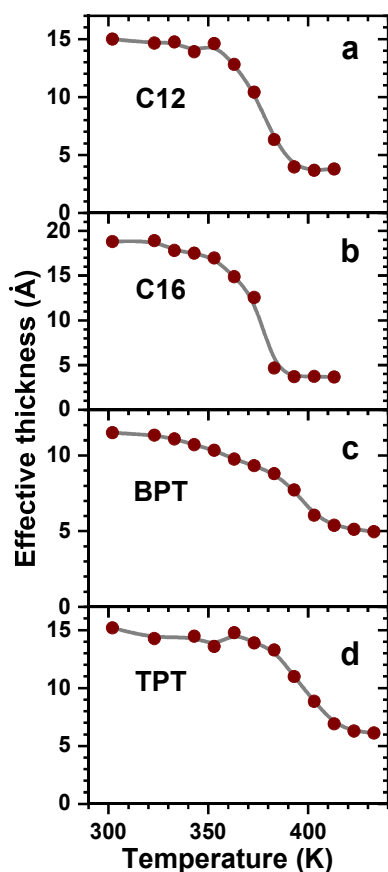
Figure A.20: Effective thicknesses of the C12 (a), C16 (b), BPT (c), and TPT (d) SAMs as functions of temperature (filled wine circles). The values were calculated on the basis of the C 1s intensities, according to equation 4.5. The gray solid lines just trace the observed behavior.

120

Appendix B. Supplementary Data by Our Partners
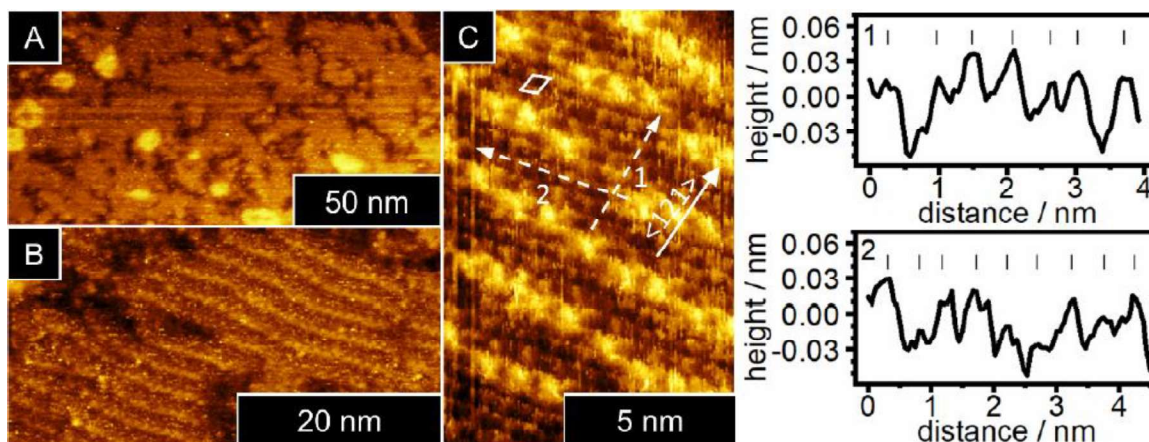
Figure B.1: STM images of a CH$_3$-BPT SAM recorded at 5 pA and 240 mV at different magnifications (A-C). The apparent height profiles at the right were recorded along the dashed arrows in panel C. The images show the densely packed structure very similar to the previously ($\sqrt{3}\times\sqrt{3}$)R30° one, with brighter molecules exhibiting another adsorption state.
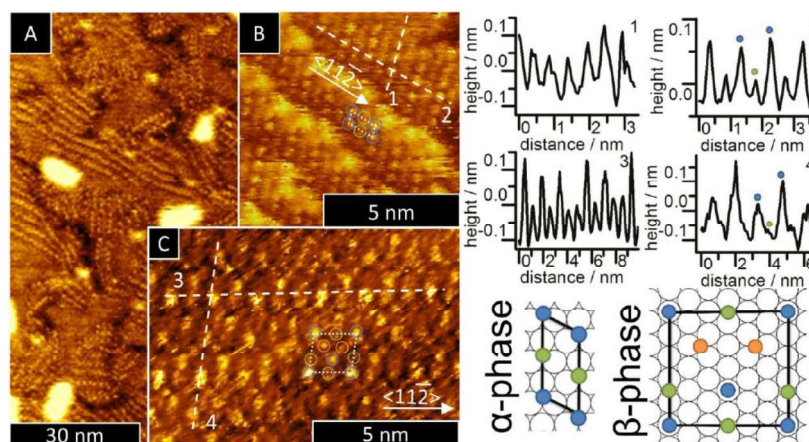
Figure B.2: STM data for the CF$_3$-BPT SAM (10 pA, 300 mV), including representative images (A-C) and the apparent height profiles along the dashed lines in the images (at the right). Structural models of the α- and ß-phases are shown at the right; blue and green circles indicate different apparent heights of molecules; orange circles indicate that molecules are disordered.
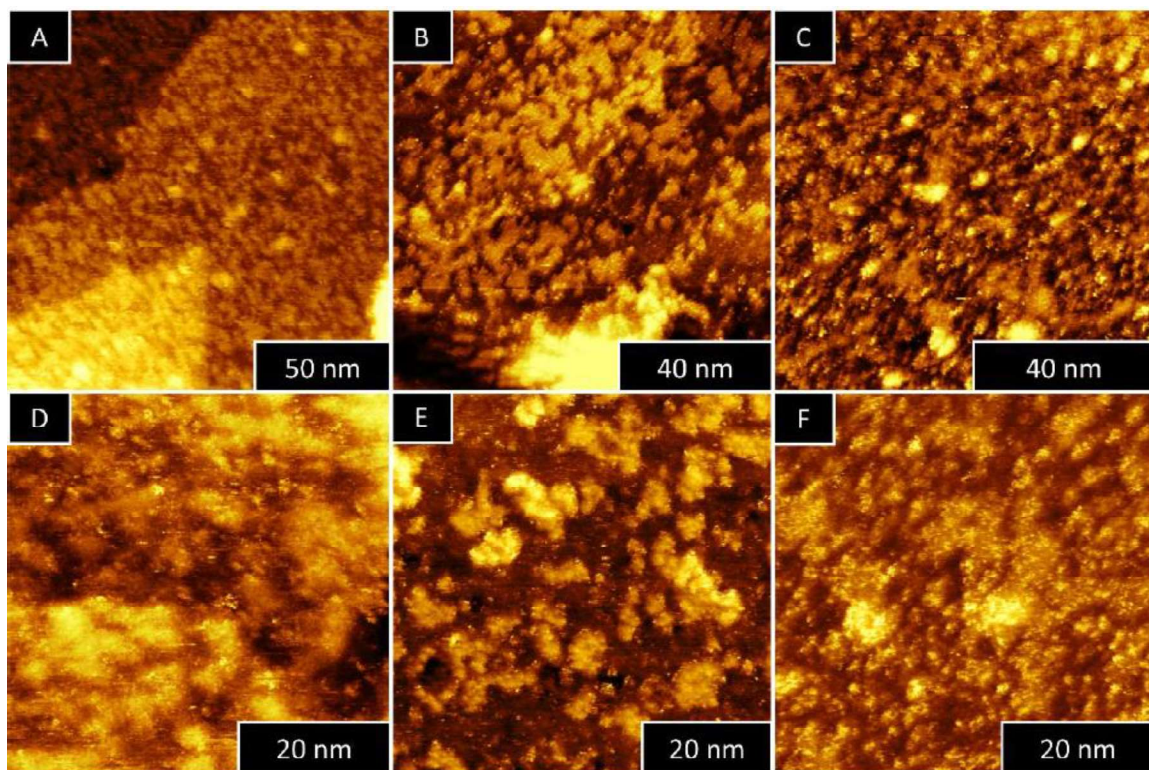
Figure B.3: STM micrographs of the binary CF$_3$-BPT/CH$_3$-BPT SAMs (all recorded at 15 pA, 100 mV). A,D (25% CF$_3$-BPT), B,E (50% CF$_3$-BPT), C,F (75% CF$_3$-BPT).

(a) neutral

HOMO-1	HOMO	LUMO
-5.72 eV	-5.50 eV	-1.54 eV

(b) cation

SOMO-1	SOMO, SUMO	SUMO+1
-9.17 eV	-7.91 eV	-6.31 eV
-7.90 eV	-6.66 eV	-5.29 eV
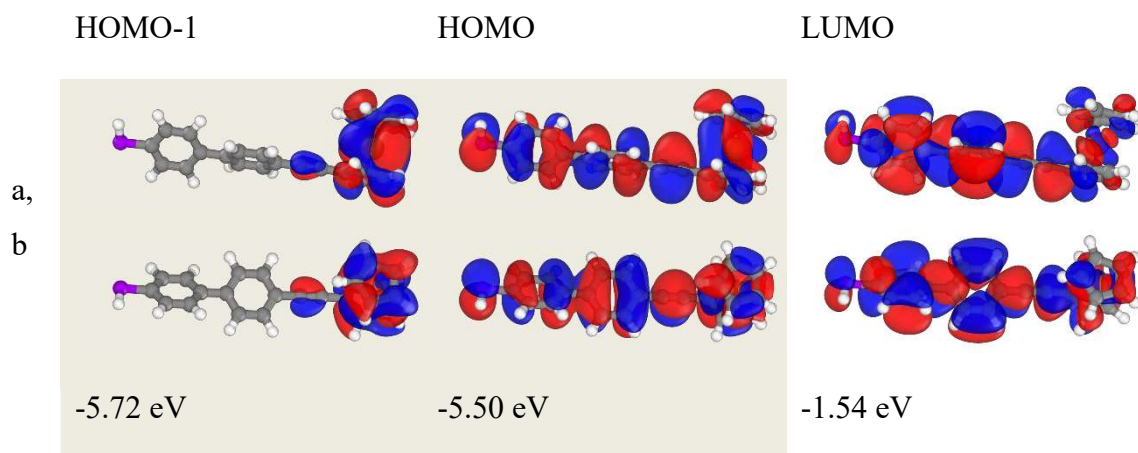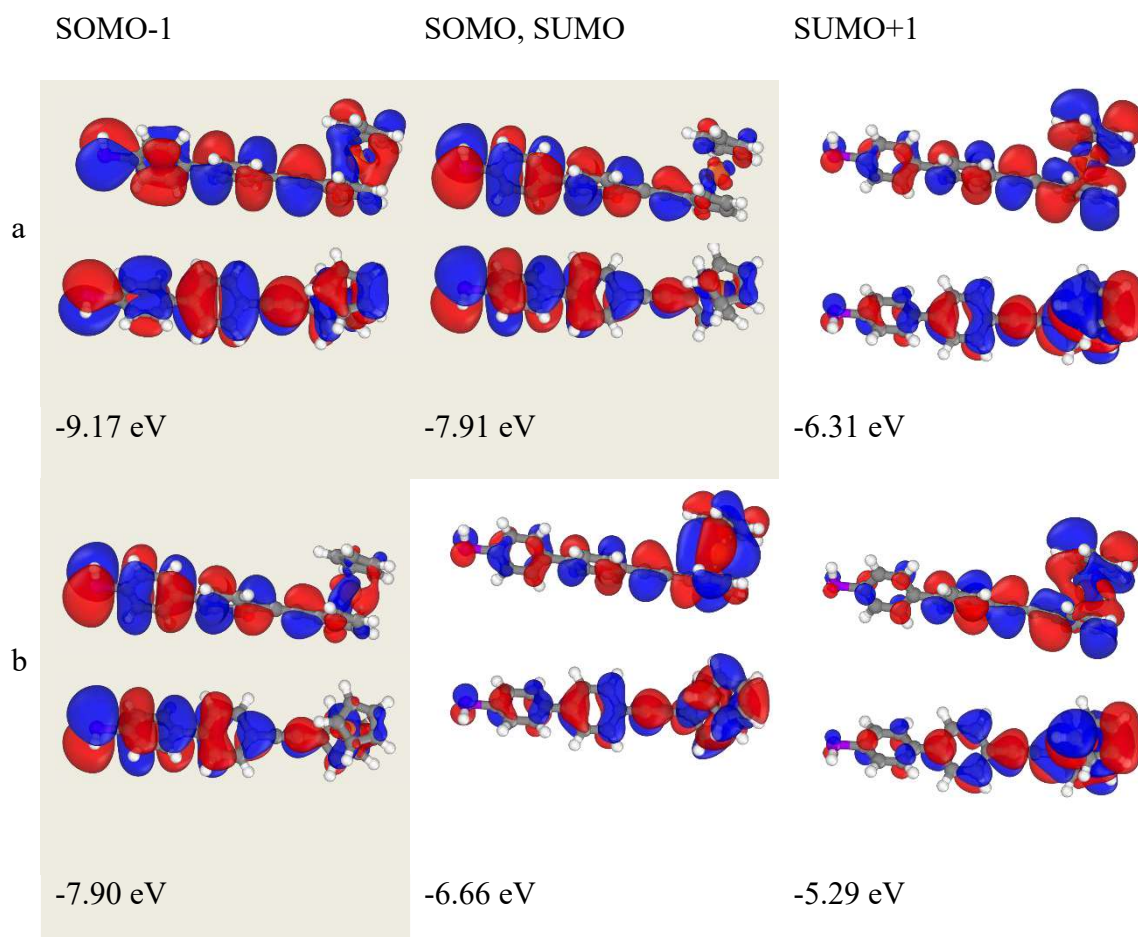
Figure B.4: Frontier orbitals: Isovalue plots of the frontier orbitals of an Fc-BPT molecule in its neutral(a) and cation state (b) calculated using the LANL2 effective core potential (ECP, see methods section). Note that for calculating the cations also the respective geometry has been optimized. The same shapes are obtained when employing the SDD ECP and when performing full potential calculations. Occupied orbitals are plotted with a

grey background. The orbital energies are noted below the isovalue plots. In passing we note that for the sake of comparison we also performed calculations employing the PBE0 functional (for the neutral molecule), which again yielded orbitals shapes like the ones shown above, with orbital energies consistently shifted to somewhat more negative energies by ~0.25 eV. For a pure GGA functional like PBE we find that the many-electron self-interaction error artificially destabilizes localized orbitals such that there the HOMO is no longer fully delocalized.

List

List of Figures

List of Tables

List of Abbreviations

SAM   self-assembled monolayer
ITO   indium tin oxide
SAMFET   self-assembled monolayer field-effect transistors
OSC   organic semiconductor

OLED	organic light-emitting diode
XPS	X-ray photoelectron spectroscopy
BE	binding energy
KE	kinetic energy
UPS	ultraviolet photoelectron spectroscopy
HOMO	highest occupied molecular orbital
LUMO	lowest unoccupied molecular orbital
HRXPS	high resolution X-ray photoelectron spectroscopy
NEXAFS	near-edge X-ray absorption fine structure
XANES	X-ray absorption near edge structure
FY	fluorescence yield
PEY	partial electron yield
TEY	total electron yield
TDM	transition dipole moment
CPD	contact potential difference
EGaIn	eutectic gallium indium
TVS	Transition voltage spectroscopy
FN	Fowler-Nordheim
EP	photon energy
CI	confidential interval
WF	work function
RT	Room temperature
TOF-SIMS	time-of-flight secondary ion mass-spectroscopy
UHV	ultra-high vacuum
RR	Rectification ratio
AT	alkanethiolate
ArT	aromatic thiolate
V_T	Transition voltage
SECO	secondary electron cutoff
DFT	density functional theory

List of Chemicals

PA	phosphonic acid
PmP-PA-up	pyrimidyl phenyl - phosphonic acid -up
PPm-PA-down	phenyl pyrimidyl - phosphonic acid -down
PP-PA	biphenyl - phosphonic acid
PmP-SH-up	pyrimidyl phenyl -thiol-up
PPm-SH-down	phenyl pyrimidyl -thiol-down
BPT	biphenyl thiol
F-BPT	fluorine-substituted-BPT
CH_3-BPT	4-methyl-4′-BPT
CF_3-BPT	4-trifluoromethyl-4′-BPT
Fc	ferrocene
DMF	Dimethylformamide

FluT	Fluorene thiol	
TPT	terphenyl thiol	
C16	1-Hexadecanthiol	
C12	1-Dodecanthiol	
n-DPA	n-dodecylphosphonic acid	
n-OPA	n-octadecylphosphonic acid	
12-PFPDPA	12-pentafluorophenoxydodecylphosphonic acid	
1H,1H,2H,2H-PFDPA	1H,1H,2H,2H-PFDPA	
Fc	ferrocene	
DMF	Dimethylformamide	

List of Symbols

I	intensity	Arbitrary units
d_{SAM}	SAM thickness	Å
λ	Attenuation length	Å
ρ	Packing density	molecules/cm^2
h	Planck's constant	4.14×10^{-15} eV/Hz
v	Photon frequency	Hz
Φ	Work function	eV
C	atomic concentration of element	
E_{Fermi}	Fermi energy	eV
E_{cutoff}	Cut-off energy	eV
ψ_{if}	Initial and final states	
α	polar angle	º
φ	azimuthal angle	º
θ	incidence angle	º
e	unit electric field vector	V/m
$\rho_f(E)$	density of final states	
P	polarization of the incident X-ray light.	
ω	frequency of vibration	Hz
ΔC	capacitance change	
J	current density	A/cm^2
α	Tilt angle	º
μ	dipole moment	Debye
ε	Dielectric constant	
α	orbitals tilt angles with respect to the surface normal	º
β	molecular tilt angles with respect to the surface normal	º
γ	molecular twist angle	º

List of Publications

Included in this thesis

1) <u>A. Asyuda</u>, X. Wan, and M. Zharnikov, Binary aromatic self-assembled monolayers: electrostatic properties and charge tunneling rates across the molecular framework. Phys. Chem. Chem. Phys. **22**, 10957-10967 (2020)
2) X. Wan, I. Lieberman, <u>A. Asyuda</u>, S. Resch, H. Seim, P. Kirsch, and M. Zharnikov, Thermal Stability of Phosphonic Acid Self-Assembled Monolayers on Alumina Substrates. J. Phys. Chem. C **124**, 4, 2531- 2542 (2020)
3) <u>A. Asyuda</u>, M. Gärtner, X. Wan, I. Burkhart, T. Saßmannshausen, A. Terfort, and M. Zharnikov, Self-Assembled Monolayers with Embedded Dipole Moments for Work Function Engineering of Oxide Substrates. J. Phys. Chem. C **124**, 16, 8775- 8785 (2020)
4) <u>A. Asyuda</u>, A. Wiesner, X. Wan, A. Terfort, and M. Zharnikov, Charge Transport Properties of Single-Component and Binary Aromatic Self-Assembled Monolayers with Methyl and Trifluoromethyl Tail Groups. J. Phys. Chem. C **124**, 45, 24837–24848 (2020)
5) <u>A. Asyuda</u>, S. Das, and M. Zharnikov, Thermal stability of alkanethiolate and aromatic thiolate self-assembled monolayers on Au(111): An X-ray Photoelectron Spectroscopy Study. J. Phys. Chem. C **125**, 39, 21754–21763 (2021)
6) <u>A. Asyuda</u>, S. Das, H. Lang, E. Zojer, and M. Zharnikov, Bias-Mediated Rectification in Metallocene-Based Molecular Junctions. In preparation

Beside this thesis

1) S. Schuster, M. Füser, <u>A. Asyuda</u>, P. Cyganik, A. Terfort, and M. Zharnikov, Photoisomerization of azobenzene-substituted alkanethiolates on Au(111) substrates in context of work function variation. Phys. Chem. Chem. Phys. **21**, 9098-9105 (2019)
2) C. Partes, E. Sauter, M. Gärtner, M. Kind, <u>A. Asyuda</u>, M. Bolte, M. Zharnikov, and A. Terfort, Reestablishing Odd–Even Effects in Anthracene-Derived Monolayers by Introduction of a Pseudo-C2v Symmetry. J. Phys. Chem. C. **123**, 33, 20362- 20372 (2019)
3) M. Schmid, X. Wan, <u>A. Asyuda</u>, and M. Zharnikov, Modification of Self-Assembled Monolayers by Electron Irradiation: The Effect of Primary Energy (10–500 eV). J. Phys. Chem. C **123**, 46, 28301- 28309 (2019)
4) M. Gärtner, E. Sauter, G. Nascimbeni, A. Wiesner, M. Kind, P. Werner, C. Schuch, T. Abu-Husein, <u>A. Asyuda</u>, J. W. Bats, M. Bolte, E. Zojer, A. Terfort, and M. Zharnikov, T. Abu-Husein, A. Asyuda, J. W. Bats, M. Bolte, E. Zojer, A. Terfort, and M. Zharnikov Self-Assembled Monolayers with Distributed Dipole. J. Phys. Chem. C **124**, 1, 504-519 (2020)
5) R.O. de la Morena, <u>A. Asyuda</u>, H. Lu, H. Aitchison, K. Turner, S. M. Francis, M. Zharnikov, and M. Buck Shape controlled assembly of carboxylic acids: formation of

a binary monolayer by intercalation into molecular nanotunnels. Phys. Chem. Chem. Phys. **22**, 4205-4215 (2020)

6) S. Soni, G.Ye, J. Zhen, Y. Zhang, <u>A. Asyuda</u>, M. Zharnikov, W. Hong, and R.C. Chiechi, Understanding the Role of Parallel Pathways via In-Situ Switching of Quantum Interference in Molecular Tunneling Junctions. Angew. Chem. Int. Ed. **59**, 14308–14312 (2020)

7) P. Werner, T. Wächter, <u>A. Asyuda</u>, A. Wiesner, M. Kind, M. Bolte, L. Weinhardt, A. Terfort, and M. Zharnikov, Electron Transfer Dynamics and Structural Effects in Benzonitrile Monolayers with Tuned Dipole Moments by Differently Positioned Fluorine Atoms. ACS Appl. Mater. Interfaces **12**, 35, 39859–39869 (2020)

8) Y. Liu, L. Ornago, M. Carlotti, Y. Ai, M.E. Abbassi, S. Soni, <u>A. Asyuda</u>, M. Zharnikov, H.S.J. van der Zant, and R.C. Chiechi, ntermolecular Effects on Tunneling through Acenes in Large-area and Single-molecule Junctions. J. Phys. Chem. C **124**, 41, 22776–22783 (2020)

9) <u>A. Asyuda</u>, R.O. de la Morena, E. Sauter, K. Turner, K. McDonald, M. Buck, and M. Zharnikov, Electron Induced Modification of Self-Assembled Monolayers of Aromatic Carboxylic Acids. J. Phys. Chem. C **124**, 45, 25107–25120 (2020)

10) V. Rohnacher, F.S. Benneckendorf, M. Münch, E. Sauter, <u>A. Asyuda</u>, M.M. Barf, J.N. Tisserant, S. Hillebrandt, F. Rominger, D. Jänsch, J. Freudenberg, W. Kowalsky, W. Jaegermann, U. Bunz, A. Pucci, M. Zharnikov, and K. Müllen, Functionalized Tetrapodal Diazatriptycenes for Electrostatic Dipole Engineering in n-Type Organic Thin Film Transistors. Adv. Mater. Technol. **6**, 202000300 (2021)

11) S. Settele, F. J. Berger, S. Lindenthal, S. Zhao, A. Ali El Yumin, N. F. Zorn, <u>A. Asyuda</u>, M. Zharnikov, A. Högele and J. Zaumseil, Synthetic control over the binding configuration of luminescent sp3- defects in single-walled carbon nanotubes. Nat. Commun. **12**, 2119 (2021)

12) E. Thauer, G. S. Zakharova, E. I. Andreikov, V. Adam, S. A. Wegener, J.- H. Nölke, L. Singer, A. Ottmann, <u>A. Asyuda</u>, M. Zharnikov, D. M. Kiselkov, Q. Zhu, I. S. Puzyrev, N. V. Podval'naya, and R. Klingeler, Novel synthesis and electrochemical investigations of ZnO/C composites for lithium-ion batteries. J. Mater. Sci. **56**, 13227–13242 (2021)

13) S. Das, <u>A. Asyuda</u>, Y. Shoji, A. Kosaka, T. Fukushima, M. and Zharnikov , Cyano-Substituted Triptycene-Based Monolayers on Au(111): Tripodal Adsorption, Dipole Engineering, and Charge Transfer. J. Phys. Chem. C **125**, 34, 18968–18978 (2021)

14) M. Werr, E. Kaifer, M. Enders, <u>A. Asyuda</u>, M. Zharnikov, and H.J. Himmel, A Copper(I) Complex with Two Unpaired Electrons, Synthesised by Oxidation of a Copper(II) Complex with Two Redox-Active Ligands. Angew. Chem. Int. Ed. **60**, 23451–23462 (2021)

References

1. Casalini, S., Bortolotti, C. A., Leonardi, F. & Biscarini, F. Self-assembled monolayers in organic electronics. *Chem. Soc. Rev.* **46**, 40–71 (2017).
2. Petritz, A. *et al.* Embedded Dipole Self-Assembled Monolayers for Contact Resistance Tuning in p-Type and n-Type Organic Thin Film Transistors and Flexible Electronic Circuits. *Adv. Funct. Mater.* **28**, 1804462 (2018).
3. Gärtner, M. *et al.* Understanding the Properties of Tailor-Made Self-Assembled Monolayers with Embedded Dipole Moments for Interface Engineering. *J. Phys. Chem. C* **122**, 28757–28774 (2018).
4. Jesper, M. *et al.* Dipolar SAMs Reduce Charge Carrier Injection Barriers in n-Channel Organic Field Effect Transistors. *Langmuir* **31**, 10303–10309 (2015).
5. Asadi, K., Gholamrezaie, F., Smits, E. C. P., Blom, P. W. M. & De Boer, B. Manipulation of charge carrier injection into organic field-effect transistors by self-assembled monolayers of alkanethiols. *J. Mater. Chem.* **17**, 1947–1953 (2007).
6. Fukuda, K. *et al.* Effects of the alkyl chain length in phosphonic acid self-assembled monolayer gate dielectrics on the performance and stability of low-voltage organic thin-film transistors. *Appl. Phys. Lett.* **95**, 20–22 (2009).
7. Bommel, S. *et al.* Unravelling the multilayer growth of the fullerene C60 in real time. *Nat. Commun.* **5**, 5388 (2014).
8. Halik, M. *et al.* Low-voltage organic transistors with an amorphous molecular gate dielectric. *Nature* **431**, 963–966 (2004).
9. Park, Y. D. *et al.* Low-voltage polymer thin-film transistors with a self-assembled monolayer as the gate dielectric. *Appl. Phys. Lett.* **87**, 1–3 (2005).
10. Mathijssen, S. G. J. *et al.* Monolayer coverage and channel length set the mobility in self-assembled monolayer field-effect transistors. *Nat. Nanotechnol.* **4**, 674–680 (2009).
11. Sizov, A. S., Agina, E. V & Ponomarenko, S. A. Self-assembled semiconducting monolayers in organic electronics. *Russ. Chem. Rev.* **87**, 1226–1264 (2018).
12. Smits, E. C. P. *et al.* Bottom-up organic integrated circuits. *Nature* **455**, 956–959 (2008).
13. Mendes, P. M. Stimuli-responsive surfaces for bio-applications. *Chem. Soc. Rev.* **37**, 2512–2529 (2008).
14. Kind, M. & Wöll, C. Organic surfaces exposed by self-assembled organothiol monolayers: Preparation, characterization, and application. *Prog. Surf. Sci.* **84**, 230–278 (2009).
15. Rosenhahn, Axel Schilp, Sören Kreuzer, Hans Jürgen Grunze, M. The role of '"inert"' surface chemistry in marine biofouling prevention. *Phys. Chem. Chem. Phys.* **12**, 4273–4274 (2010).
16. Koch, N. Energy levels at interfaces between metals and conjugated organic molecules. *J. Phys. Condens. Matter* **20**, 184008 (2008).
17. Liu, C., Xu, Y. & Noh, Y. Y. Contact engineering in organic field-effect transistors. *Mater. Today* **18**, 79–96 (2015).
18. Hamadani, B. H., Corley, D. A., Ciszek, J. W., Tour, J. M. & Natelson, D. Controlling charge injection in organic field-effect transistors using self-assembled monolayers. *Nano Lett.* **6**, 1303–1306 (2006).

19. Lange, I. *et al.* Tuning the work function of polar zinc oxide surfaces using modified phosphonic acid self-assembled monolayers. *Adv. Funct. Mater.* **24**, 7014–7024 (2014).

20. Lee, H. J., Jamison, A. C. & Lee, T. R. Surface Dipoles: A Growing Body of Evidence Supports Their Impact and Importance. *Acc. Chem. Res.* **48**, 3007–3015 (2015).

21. Borchert, J. W. *et al.* Small contact resistance and high-frequency operation of flexible low-voltage inverted coplanar organic transistors. *Nat. Commun.* **10**, 1–11 (2019).

22. Zojer, E., Taucher, T. C. & Hofmann, O. T. The Impact of Dipolar Layers on the Electronic Properties of Organic/Inorganic Hybrid Interfaces. *Adv. Mater. Interfaces* **6**, 1900581 (2019).

23. Love, J. C., Estroff, L. A., Kriebel, J. K., Nuzzo, R. G. & Whitesides, G. M. Self-Assembled Monolayers of Thiolates on Metals as a Form of Nanotechnology. *Chem. Rev.* **105**, 1103–1170 (2005).

24. Alloway, D. M. *et al.* Interface dipoles arising from self-assembled monolayers on gold: UV-photoemission studies of alkanethiols and partially fluorinated alkanethiols. *J. Phys. Chem. B* **107**, 11690–11699 (2003).

25. Ford, W. E. *et al.* Organic dipole layers for ultralow work function electrodes. *ACS Nano* **8**, 9173–9180 (2014).

26. Schmidt, C., Witt, A. & Witte, G. Tailoring the Cu(100) work function by substituted benzenethiolate self-assembled monolayers. *J. Phys. Chem. A* **115**, 7234–7241 (2011).

27. Abu-Husein, T. *et al.* The Effects of Embedded Dipoles in Aromatic Self-Assembled Monolayers. *Adv. Funct. Mater.* **25**, 3943–3957 (2015).

28. Kim, J. *et al.* Interface control in organic electronics using mixed monolayers of carboranethiol isomers. *Nano Lett.* **14**, 2946–2951 (2014).

29. Cabarcos, O. M. *et al.* Effects of Embedded Dipole Layers on Electrostatic Properties of Alkanethiolate Self-Assembled Monolayers. *J. Phys. Chem. C* **121**, 15815–15830 (2017).

30. Hehn, I. *et al.* Employing X-ray Photoelectron Spectroscopy for Determining Layer Homogeneity in Mixed Polar Self-Assembled Monolayers. *J. Phys. Chem. Lett.* **7**, 2994–3000 (2016).

31. Sauter, E., Gilbert, C. O., Morin, J. F., Terfort, A. & Zharnikov, M. Mixed Monomolecular Films with Embedded Dipolar Groups on Ag(111). *J. Phys. Chem. C* **122**, 19514–19523 (2018).

32. Morales, G. M. *et al.* Inversion of the rectifying effect in diblock molecular diodes by protonation. *J. Am. Chem. Soc.* **127**, 10456–10457 (2005).

33. Lee, Y., Carsten, B. & Yu, L. Understanding the anchoring group effect of molecular diodes on rectification. *Langmuir* **25**, 1495–1499 (2009).

34. Díez-Pérez, I. *et al.* Rectification and stability of a single molecular diode with controlled orientation. *Nat. Chem.* **1**, 635–641 (2009).

35. Egger, David A. Ferdinand, Rissner Rangger, Gerold M. Hofmann, Oliver T. Wittwer, Lukas Heimel, Georg Zojer, E. Self-assembled monolayers of polar molecules on Au(111) surfaces: distributing the dipoles. *Phys. Chem. Chem. Phys.* **12**, 4291–4294 (2010).

36. Gärtner, M. *et al.* Self-Assembled Monolayers with Distributed Dipole Moments Originating from Bipyrimidine Units. *J. Phys. Chem. C* **124**, 504–519 (2020).

37. Kovalchuk, A. *et al.* Transition voltages respond to synthetic reorientation of embedded dipoles in self-assembled monolayers. *Chem. Sci.* **7**, 781–787 (2016).

38. Sauter, E., Yildirim, C., Terfort, A. & Zharnikov, M. Adjustment of the Work Function of Pyridine and Pyrimidine Substituted Aromatic Self-Assembled Monolayers by Electron Irradiation. *J. Phys. Chem. C* **121**, 12834–12841 (2017).

39. Paniagua, S. A. *et al.* Phosphonic acid modification of indium-tin oxide electrodes: Combined XPS/UPS/ contact angle studies. *J. Phys. Chem. C* **112**, 7809–7817 (2008).

40. Paramonov, P. B. *et al.* Theoretical characterization of the indium tin oxide surface and of its binding sites for adsorption of phosphonic acid monolayers. *Chem. Mater.* **20**, 5131–5133 (2008).

41. An, D., Liu, H., Wang, S. & Li, X. Modification of ITO anodes with self-assembled monolayers for enhancing hole injection in OLEDs. *Appl. Phys. Lett.* **114**, 153301 (2019).

42. Bardecker, J. A. *et al.* Self-assembled electroactive phosphonic acids on ITO: Maximizing hole-injection in polymer light-emitting diodes. *Adv. Funct. Mater.* **18**, 3964–3971 (2008).

43. Hotchkiss, P. J. *et al.* Modification of the surface properties of indium tin oxide with benzylphosphonic acids: A joint experimental and theoretical study. *Adv. Mater.* **21**, 4496–4501 (2009).

44. Lacher, S., Matsuo, Y. & Nakamura, E. Molecular and supramolecular control of the work function of an inorganic electrode with self-assembled monolayer of umbrella-shaped fullerene derivatives. *J. Am. Chem. Soc.* **133**, 16997–17004 (2011).

45. Jo, K., Yu, H. Z. & Yang, H. Formation kinetics and stability of phosphonate self-assembled monolayers on indium-tin oxide. *Electrochim. Acta* **56**, 4828–4833 (2011).

46. Koldemir, U. *et al.* Molecular design for tuning work functions of transparent conducting electrodes. *J. Phys. Chem. Lett.* **6**, 2269–2276 (2015).

47. Paniagua, S. A. *et al.* Phosphonic Acids for Interfacial Engineering of Transparent Conductive Oxides. *Chem. Rev.* **116**, 7117–7158 (2016).

48. Benneckendorf, F. S. *et al.* Structure-Property Relationship of Phenylene-Based Self-Assembled Monolayers for Record Low Work Function of Indium Tin Oxide. *J. Phys. Chem. Lett.* **9**, 3731–3737 (2018).

49. Timpel, M. *et al.* Electrode Work Function Engineering with Phosphonic Acid Monolayers and Molecular Acceptors: Charge Redistribution Mechanisms. *Adv. Funct. Mater.* **28**, 1–12 (2018).

50. Kang, J. F., Liao, S., Jordan, R. & Ulman, A. Mixed self-assembled monolayers of rigid biphenyl thiols: Impact of solvent and dipole moment. *J. Am. Chem. Soc.* **120**, 9662–9667 (1998).

51. Shaporenko, A., CHeister, K., Ulman, A., Grunze, M. & Zharnikov, M. The Effect of Halogen Substitution in Self-Assembled Monolayers of 4-Mercaptobiphenyls on Noble Metal Substrates. *J. Phys. Chem. B* **109**, 4096–4103 (2005).

52. Sun, Q. & Selloni, A. Interface and molecular electronic structure vs tunneling characteristics of CH 3- and CF 3-terminated thiol monolayers on Au(111). *J. Phys.*

Chem. A **110**, 11396–11400 (2006).

53. Asyuda, A., Wan, X. & Zharnikov, M. Binary aromatic self-assembled monolayers: Electrostatic properties and charge tunneling rates across the molecular framework. *Phys. Chem. Chem. Phys.* **22**, 10957–10967 (2020).

54. Asyuda, A., Wiesner, A., Wan, X., Terfort, A. & Zharnikov, M. Charge Transport Properties of Single-Component and Binary Aromatic Self-Assembled Monolayers with Methyl and Trifluoromethyl Tail Groups. *J. Phys. Chem. C* **124**, 24837–24848 (2020).

55. Li, S. *et al.* Local packing environment strongly influences the frictional properties of mixed CH 3- and CF 3-terminated alkanethiol SAMs on Au(111). *Langmuir* **21**, 933–936 (2005).

56. Chen, X. *et al.* A single atom change turns insulating saturated wires into molecular conductors. *Nat. Commun.* **12**, 1–11 (2021).

57. Chen, X. *et al.* Interplay of Collective Electrostatic Effects and Level Alignment Dictates the Tunneling Rates across Halogenated Aromatic Monolayer Junctions. *J. Phys. Chem. Lett.* **10**, 4142–4147 (2019).

58. Kong, G. D., Kim, M., Jang, H. J., Liao, K. C. & Yoon, H. J. Influence of halogen substitutions on rates of charge tunneling across SAM-based large-area junctions. *Phys. Chem. Chem. Phys.* **17**, 13804–13807 (2015).

59. Adams, D. M. *et al.* Charge transfer on the nanoscale: Current status. *J. Phys. Chem. B* **107**, 6668–6697 (2003).

60. Wang, D. *et al.* Tuning the Tunneling Rate and Dielectric Response of SAM-Based Junctions via a Single Polarizable Atom. *Adv. Mater.* **27**, 6689–6695 (2015).

61. Kong, G. D. *et al.* Mixed Molecular Electronics: Tunneling Behaviors and Applications of Mixed Self-Assembled Monolayers. *Adv. Electron. Mater.* **6**, 1–19 (2020).

62. Liu, Y., Qiu, X., Soni, S. & Chiechi, R. C. Charge transport through molecular ensembles: Recent progress in molecular electronics. *Chem. Phys. Rev.* **2**, 021303 (2021).

63. Weidner, T. *et al.* Self-assembled monolayers of ruthenocene-substituted biphenyl ethynyl thiols on gold. *J. Electroanal. Chem.* **621**, 159–170 (2008).

64. Shaporenko, A., Rössler, K., Lang, H. & Zharnikov, M. Self-Assembled Monolayers of Ferrocene-Substituted Biphenyl Ethynyl Thiols on Gold. *J. Phys. Chem. B* **110**, 24621–24628 (2006).

65. Kitagawa, K., Morita, T. & Kimura, S. Molecular rectification of a helical peptide with a redox group in the metal-molecule-metal junction. *J. Phys. Chem. B* **109**, 13906–13911 (2005).

66. Chen, X. *et al.* Molecular diodes with rectification ratios exceeding 10^5 driven by electrostatic interactions. *Nat. Nanotechnol.* **12**, 797–803 (2017).

67. Nijhuis, C. A., Reus, W. F. & Whitesides, G. M. Mechanism of rectification in tunneling junctions based on molecules with asymmetric potential drops. *J. Am. Chem. Soc.* **132**, 18386–18401 (2010).

68. Melville Metzger, R. Ferrocenes as One-Electron Donors in Unimolecular Rectifiers. in *Photophysics, Photochemical and Substitution Reactions - Recent Advances* vol. i 13 (IntechOpen, 2021).

69. Yuan, L. *et al.* Controlling the direction of rectification in a molecular diode. *Nat.*

Commun. **6**, 6324 (2015).

70. Wang, L. *et al.* Unraveling the Failure Modes of Molecular Diodes: The Importance of the Monolayer Formation Protocol and Anchoring Group to Minimize Leakage Currents. *J. Phys. Chem. C* **123**, 19759–19767 (2019).

71. Souto, M. *et al.* Tuning the Rectification Ratio by Changing the Electronic Nature (Open-Shell and Closed-Shell) in Donor-Acceptor Self-Assembled Monolayers. *J. Am. Chem. Soc.* **139**, 4262–4265 (2017).

72. Duche, D. *et al.* Model of self assembled monolayer based molecular diodes made of ferrocenyl-alkanethiols. *J. Appl. Phys.* **121**, 115503 (2017).

73. Jia, C. *et al.* Redox Control of Charge Transport in Vertical Ferrocene Molecular Tunnel Junctions. *Chem* **6**, 1172–1182 (2020).

74. Nijhuis, C. A., Reus, W. F., Barber, J. R., Dickey, M. D. & Whitesides, G. M. Charge transport and rectification in arrays of SAM-based tunneling junctions. *Nano Lett.* **10**, 3611–3619 (2010).

75. Nijhuis, C. A., Reus, W. F. & Whitesides, G. M. Molecular rectification in metal-SAM-metal oxide-metal junctions. *J. Am. Chem. Soc.* **131**, 17814–17827 (2009).

76. Thompson, D. & Nijhuis, C. A. Even the Odd Numbers Help: Failure Modes of SAM-Based Tunnel Junctions Probed via Odd-Even Effects Revealed in Synchrotrons and Supercomputers. *Acc. Chem. Res.* **49**, 2061–2069 (2016).

77. Welker, M. E. Ferrocenes as building blocks in molecular rectifiers and diodes. *Molecules* **23**, 1–9 (2018).

78. Broadnax, A. D., Lamport, Z. A., Scharmann, B., Jurchescu, O. D. & Welker, M. E. Ferrocenealkylsilane molecular rectifiers. *J. Organomet. Chem.* **856**, 23–26 (2018).

79. Li, Q. *et al.* Capacitance and conductance characterization of ferrocene-containing self-assembled monolayers on silicon surfaces for memory applications. *Appl. Phys. Lett.* **81**, 1494–1496 (2002).

80. Yuan, L., Breuer, R., Jiang, L., Schmittel, M. & Nijhuis, C. A. A Molecular Diode with a Statistically Robust Rectification Ratio of Three Orders of Magnitude. *Nano Lett.* **15**, 5506–5512 (2015).

81. Song, P., Yuan, L., Roemer, M., Jiang, L. & Nijhuis, C. A. Supramolecular vs Electronic Structure: The Effect of the Tilt Angle of the Active Group in the Performance of a Molecular Diode. *J. Am. Chem. Soc.* **138**, 5769–5772 (2016).

82. Atesci, H. *et al.* Humidity-controlled rectification switching in ruthenium-complex molecular junctions. *Nat. Nanotechnol.* **13**, 117–121 (2018).

83. Frath, D., Nguyen, V. Q., Lafolet, F., Martin, P. & Lacroix, J. C. Electrografted monolayer based on a naphthalene diimide-ruthenium terpyridine complex dyad: Efficient creation of large-area molecular junctions with high current densities. *Chem. Commun.* **53**, 10997–11000 (2017).

84. Terada, K., Kobayashi, K., Hikita, J. & Haga, M. A. Electric conduction properties of self-assembled monolayer films of ru complexes with disulflde/phosphonate anchors in a Au-(molecular ensemble)-(Au nanoparticle) junction. *Chem. Lett.* **38**, 416–417 (2009).

85. Yuan, L. *et al.* Transition from direct to inverted charge transport Marcus regions in molecular junctions via molecular orbital gating. *Nat. Nanotechnol.* **13**, 322–329 (2018).

86. Jeong, H. *et al.* Redox-induced asymmetric electrical characteristics of ferrocene-

alkanethiolate molecular devices on rigid and flexible substrates. *Adv. Funct. Mater.* **24**, 2472–2480 (2014).

87. Müller-Meskamp, L. *et al.* Field-emission resonances at tip/α,ω-mercaptoalkyl ferrocene/Au interfaces studied by STM. *Small* **5**, 496–502 (2009).

88. Mentovich, E. D. *et al.* Gated-Controlled Rectification of a Self-Assembled Monolayer-Based Transistor. *J. Phys. Chem. C* **117**, 8468–8474 (2013).

89. Telegdi, J. Formation of self-assembled anticorrosion films on different metals. *Materials (Basel).* **13**, 1–25 (2020).

90. Terfort, A. & Zharnikov, M. Electron-Irradiation Promoted Exchange Reaction as a Tool for Surface Engineering and Chemical Lithography. *Adv. Mater. Interfaces* **8**, 2100148 (2021).

91. Eck, W. 3.8.10 Chemisorption of polyatomic chain-like hydrocarbons on metals and semiconductors. in *Adsorbed Layers on Surfaces* (ed. Bonzel, H. P.) 371–385 (Springer-Verlag, 2005). doi:10.1007/10932216_14.

92. Halik, M. & Hirsch, A. The potential of molecular self-assembled monolayers in organic electronic devices. *Adv. Mater.* **23**, 2689–2695 (2011).

93. Turchanin, A. & Gölzhäuser, A. Carbon Nanomembranes. *Adv. Mater.* **28**, 6075–6103 (2016).

94. Vilan, A. & Cahen, D. Chemical Modification of Semiconductor Surfaces for Molecular Electronics. *Chem. Rev.* **117**, 4624–4666 (2017).

95. Soni, S. *et al.* Understanding the Role of Parallel Pathways via In-Situ Switching of Quantum Interference in Molecular Tunneling Junctions. *Angew. Chemie - Int. Ed.* **59**, 14308–14312 (2020).

96. Rohnacher, V. *et al.* Functionalized Tetrapodal Diazatriptycenes for Electrostatic Dipole Engineering in n-Type Organic Thin Film Transistors. *Adv. Mater. Technol.* **6**, 2000300 (2021).

97. Asyuda, A. *et al.* Self-Assembled Monolayers with Embedded Dipole Moments for Work Function Engineering of Oxide Substrates. *J. Phys. Chem. C* **124**, 8775–8785 (2020).

98. Liu, Y. *et al.* Intermolecular Effects on Tunneling through Acenes in Large-Area and Single-Molecule Junctions. *J. Phys. Chem. C* **124**, 22776–22783 (2020).

99. Asyuda, A. *et al.* Electron-Induced Modification of Self-Assembled Monolayers of Aromatic Carboxylic Acids. *J. Phys. Chem. C* **124**, 25107–25120 (2020).

100. Werner, P. *et al.* Electron Transfer Dynamics and Structural Effects in Benzonitrile Monolayers with Tuned Dipole Moments by Differently Positioned Fluorine Atoms. *ACS Appl. Mater. Interfaces* **12**, 39859–39869 (2020).

101. Ortiz De La Morena, R. *et al.* Shape controlled assembly of carboxylic acids: Formation of a binary monolayer by intercalation into molecular nanotunnels. *Phys. Chem. Chem. Phys.* **22**, 4205–4215 (2020).

102. Schuster, S. *et al.* Photoisomerization of azobenzene-substituted alkanethiolates on Au(111) substrates in the context of work function variation: The effect of structure and packing density. *Phys. Chem. Chem. Phys.* **21**, 9098–9105 (2019).

103. Srisombat, L., Jamison, A. C. & Lee, T. R. Stability: A key issue for self-assembled monolayers on gold as thin-film coatings and nanoparticle protectants. *Colloids Surfaces A Physicochem. Eng. Asp.* **390**, 1–19 (2011).

104. Shaporenko, A., Adlkofer, K., Johansson, L. S. O., Tanaka, M. & Zharnikov, M.

Functionalization of GaAs surfaces with aromatic self-assembled monolayers: A synchrotron-based spectroscopic study. *Langmuir* **19**, 4992–4998 (2003).

105. Ballav, N., Thomas, H., Winkler, T., Terfort, A. & Zharnikov, M. Making protein patterns by writing in a protein-repelling matrix. *Angew. Chemie - Int. Ed.* **48**, 5833–5836 (2009).

106. Gras, S. L., Mahmud, T., Rosengarten, G., Mitchell, A. & Kalantar-Zadeh, K. Intelligent control of surface hydrophobicity. *ChemPhysChem* **8**, 2036–2050 (2007).

107. Landoulsi, J., Cooksey, K. E. & Dupres, V. Review - Interactions between diatoms and stainless steel: Focus on biofouling and biocorrosion. *Biofouling* **27**, 1105–1124 (2011).

108. Chiu, J. M. & Tai, Y. Improving the efficiency of ZnO-based organic solar cell by self-assembled monolayer assisted modulation on the properties of ZnO acceptor layer. *ACS Appl. Mater. Interfaces* **5**, 6946–6950 (2013).

109. Wan, X. *et al.* Thermal Stability of Phosphonic Acid Self-Assembled Monolayers on Alumina Substrates. *J. Phys. Chem. C* **124**, 2531–2542 (2020).

110. Singh, M., Kaur, N. & Comini, E. The role of self-assembled monolayers in electronic devices. *J. Mater. Chem. C* **8**, 3938–3955 (2020).

111. Schwartz, D. K. Mechanisms and kinetics of self-assembled monolayer formation. *Annu. Rev. Phys. Chem.* **52**, 107–137 (2001).

112. Schoenfisch, M. H. & Pemberton, J. E. Air stability of alkanethiol self-assembled monolayers on silver and gold surfaces. *J. Am. Chem. Soc.* **120**, 4502–5413 (1998).

113. Schmid, M., Wan, X., Asyuda, A. & Zharnikov, M. Modification of Self-Assembled Monolayers by Electron Irradiation: The Effect of Primary Energy (10-500 eV). *J. Phys. Chem. C* **123**, 28301–28309 (2019).

114. Konno, H. Chapter 8 - X-ray Photoelectron Spectroscopy. in *Materials Science and Engineering of Carbon* (eds. Inagaki, M. & Kang, F.) 153–171 (Butterworth-Heinemann, 2016). doi:https://doi.org/10.1016/B978-0-12-805256-3.00008-8.

115. Laibinis, P. E., Fox, M. A., Folkers, J. P. & Whitesides, G. M. Comparisons of Self-Assembled Monolayers on Silver and Gold: Mixed Monolayers Derived from $HS(CH_2)_{21}X$ and $HS(CH_2)_{10}Y$ (X, Y = CH_3, CH_2OH) Have Similar Properties. *Langmuir* **7**, 3167–3173 (1991).

116. Colangelo, E. *et al.* Characterizing self-assembled monolayers on gold nanoparticles. *Bioconjug. Chem.* **28**, 11–22 (2017).

117. Vericat, C., Vela, M. E., Benitez, G., Carro, P. & Salvarezza, R. C. Self-assembled monolayers of thiols and dithiols on gold: new challenges for a well-known system. *Chem. Soc. Rev.* **39**, 1805–1834 (2010).

118. Bhattarai, J. K., Neupane, D., Mikhaylov, V., Demchenko, A. V. & Stine, K. J. Self-Assembled Monolayers of Carbohydrate Derivatives on Gold Surfaces. in *Carbohydrate* 13 (InTech, 2017). doi:10.5772/66194.

119. Ghosh, A., Prasad, A. K. & Chuntonov, L. Two-Dimensional Infrared Spectroscopy Reveals Molecular Self-Assembly on the Surface of Silver Nanoparticles. *J. Phys. Chem. Lett.* **10**, 2481–2486 (2019).

120. Christwardana, M., Kim, D. H., Chung, Y. & Kwon, Y. A hybrid biocatalyst consisting of silver nanoparticle and naphthalenethiol self-assembled monolayer prepared for anchoring glucose oxidase and its use for an enzymatic biofuel cell. *Appl. Surf. Sci.* **429**, 180–186 (2018).

121. Wang, G., Wang, C., Yang, R., Liu, W. & Sun, S. A Sensitive and Stable Surface Plasmon Resonance Sensor Based on Monolayer Protected Silver Film. *Sensors* **17**, 2777 (2017).

122. Salcı, A. & Solmaz, R. Fabrication of rhodanine self-assembled monolayer thin films on copper: Solvent optimization and corrosion inhibition studies. *Prog. Org. Coatings* **125**, 516–524 (2018).

123. Kwok, S. C. T., Ciucci, F. & Yuen, M. M. F. Chemisorption Threshold of Thiol-based Monolayer on Copper: Effect of Electric Potential and Elevated Temperature. *Electrochim. Acta* **198**, 185–194 (2016).

124. Hu, S., Chen, Z. & Guo, X. Inhibition effect of three-dimensional (3D) nanostructures on the corrosion resistance of 1-dodecanethiol self-assembled monolayer on copper in NaCl solution. *Materials (Basel).* **11**, 1–17 (2018).

125. Zheng, H. *et al.* Self-assembled monolayer-modified ITO for efficient organic light-emitting diodes: The impact of different self-assemble monolayers on interfacial and electroluminescent properties. *Org. Electron.* **56**, 89–95 (2018).

126. Huang, F., Liu, H., Li, X. & Wang, S. Highly efficient hole injection/transport layer-free OLEDs based on self-assembled monolayer modified ITO by solution-process. *Nano Energy* **78**, 105399 (2020).

127. Khan, M. Z. H. Effect of ITO surface properties on SAM modification: A review toward biosensor application. *Cogent Eng.* **3**, 1170097 (2016).

128. Zhang, B. *et al.* Surface functionalization of zinc oxide by carboxyalkylphosphonic acid self-assembled monolayers. *Langmuir* **26**, 4514–4522 (2010).

129. Zhang, S., Zhan, L., Li, S., Li, C. Z. & Chen, H. Enhanced performance of inverted non-fullerene organic solar cells through modifying zinc oxide surface with self-assembled monolayers. *Org. Electron.* **63**, 143–148 (2018).

130. Liao, S. H., Jhuo, H. J., Cheng, Y. S., Gupta, V. & Chen, S. A. A high performance inverted organic solar cell with a low band gap small molecule (p-DTS(FBTTh2)2) using a fullerene derivative-doped zinc oxide nano-film modified with a fullerene-based self-assembled monolayer as the cathode. *J. Mater. Chem. A* **3**, 22599–22604 (2015).

131. Ohta, R., Saito, N., Inoue, Y., Sugimura, H. & Takai, O. Organosilane self-assembled monolayers directly linked to the diamond surfaces. *J. Vac. Sci. Technol. A Vacuum, Surfaces, Film.* **22**, 2005–2009 (2004).

132. Lud, S. Q. *et al.* Chemical grafting of biphenyl self-assembled monolayers on ultrananocrystalline diamond. *J. Am. Chem. Soc.* **128**, 16884–16891 (2006).

133. Choi, J., Sakurai, K. & Kato, T. Observation of self-assembled monolayers on diamond-like carbon films: Agglomeration of self-assembled FDTS molecules. *Surf. Interface Anal.* **42**, 1373–1376 (2010).

134. Park, C. S., Colorado, R., Jamison, A. C. & Lee, T. R. Thiol-Based Self-Assembled Monolayers: Formation, Organization, and the Role of Adsorbate Structure. in *Reference Module in Materials Science and Materials Engineering* 1–16 (Elsevier, 2016). doi:10.1016/B978-0-12-803581-8.03780-2.

135. Laiho, T., Leiro, J. A., Heinonen, M. H., Mattila, S. S. & Lukkari, J. Photoelectron spectroscopy study of irradiation damage and metal-sulfur bonds of thiol on silver and copper surfaces. *J. Electron Spectros. Relat. Phenomena* **142**, 105–112 (2005).

136. Kazan, R., Müller, U. & Bürgi, T. Doping of thiolate protected gold clusters through

reaction with metal surfaces. *Nanoscale* **11**, 2938–2945 (2019).

137. Malola, S., Lehtovaara, L. & Häkkinen, H. TDDFT Analysis of Optical Properties of Thiol Monolayer-Protected Gold and Intermetallic Silver–Gold Au 144 (SR) 60 and Au 84 Ag 60 (SR) 60 Clusters. *J. Phys. Chem. C* **118**, 20002–20008 (2014).

138. Ulman, A. Formation and Structure of Self-Assembled Monolayers. *Chem. Rev.* **96**, 1533–1554 (1996).

139. Baer, D. R. & Thevuthasan, S. Characterization of Thin Films and Coatings. in *Handbook of Deposition Technologies for Films and Coatings* 749–864 (Elsevier, 2010). doi:10.1016/B978-0-8155-2031-3.00016-8.

140. Andrade, J. D. X-ray Photoelectron Spectroscopy (XPS). in *Surface and Interfacial Aspects of Biomedical Polymers: Volume 1 Surface Chemistry and Physics* (ed. Andrade, J. D.) 105–195 (Springer US, 1985). doi:10.1007/978-1-4684-8610-0_5.

141. Stevie, F. A. & Donley, C. L. Introduction to x-ray photoelectron spectroscopy. *J. Vac. Sci. Technol. A* **38**, 063204 (2020).

142. Kibel, M. H. X-Ray Photoelectron Spectroscopy. in *Surface Analysis Methods in Materials Science* (eds. O'Connor, D. J., Sexton, B. A. & Smart, R. S. C.) 175–201 (Springer Berlin Heidelberg, 2003). doi:10.1007/978-3-662-05227-3_7.

143. Tougaard, S. SURFACE ANALYSIS | X-ray Photoelectron Spectroscopy. in *Reference Module in Chemistry, Molecular Sciences and Chemical Engineering* 400–409 (Elsevier, 2013). doi:10.1016/B978-0-12-409547-2.00527-8.

144. Watts, J. F. X-ray photoelectron spectroscopy. *Vacuum* **45**, 653–671 (1994).

145. Venezia, A. M. X-ray photoelectron spectroscopy (XPS) for catalysts characterization. *Catal. Today* **77**, 359–370 (2003).

146. Zharnikov, M. & Grunze, M. Modification of thiol-derived self-assembling monolayers by electron and x-ray irradiation: Scientific and lithographic aspects. *J. Vac. Sci. Technol. B Microelectron. Nanom. Struct.* **20**, 1793 (2002).

147. Bluhm, H. 4 - X-ray photoelectron spectroscopy (XPS) for in situ characterization of thin film growth. in *In Situ Characterization of Thin Film Growth* (eds. Koster, G. & Rijnders, G.) 75–98 (Woodhead Publishing, 2011). doi:https://doi.org/10.1533/9780857094957.2.75.

148. Ratner, M. Castner, D. Electron Spectroscopy for Chemical Analysis. in *Surface Analysis - The principal techniques* 43–98 (1997).

149. Thome, J., Himmelhaus, M., Zharnikov, M. & Grunze, M. Increased lateral density in alkanethiolate films on gold by mercury adsorption. *Langmuir* **14**, 7435–7449 (1998).

150. Lamont, C. L. a & Wilkes, J. Attenuation Length of Electrons in Self-Assembled Monolayers of n -Alkanethiols on Gold. *Langmuir* **15**, 2037–2042 (1999).

151. Schneider, S. Physikalische Chemie. *Angew. Chemie* **100**, 892–893 (1988).

152. Hofmann, S. *Auger- and X-Ray Photoelectron Spectroscopy in Materials Science*. vol. 49 (Springer Berlin Heidelberg, 2013).

153. van der Heide, P. *X-Ray Photoelectron Spectroscopy*. (John Wiley & Sons, Inc., 2011). doi:10.1002/9781118162897.

154. Briggs, G. Beamson, D. High Resolution XPS of Organic Polymers: The Scienta ESCA300 Database (Beamson, G.; Briggs, D.). *J. Chem. Educ.* **70**, A25 (1993).

155. Forsythe, E. W. & Gao, Y. *Interfaces in Organic Light-Emitting Devices. Handbook of Surfaces and Interfaces of Materials* vol. 1 (Academic Press, 2001).

156. Schlettwein, D. Electronic Properties of Molecular Organic Semiconductor Thin Films. in *Supramolecular Photosensitive and Electroactive Materials* 211–338 (Elsevier, 2001). doi:10.1016/B978-012513904-5/50005-3.

157. Suzuki, N. X-Ray Photoelectron Spectroscopy and its Application to Carbon. in *Carbon Alloys* 211–222 (Elsevier, 2003). doi:10.1016/B978-008044163-4/50013-9.

158. Dechun, Z. Chemical and photophysical properties of materials for OLEDs. in *Organic Light-Emitting Diodes (OLEDs)* 114–142 (Elsevier, 2013). doi:10.1533/9780857098948.1.114.

159. Strehblow, H.-H. & Lützenkirchen-Hecht, D. 2.31 - Spectroscopies, Scattering and Diffraction Techniques. in *Shreir's Corrosion* (eds. Cottis, B. et al.) 1374–1404 (Elsevier, 2010). doi:https://doi.org/10.1016/B978-044452787-5.00069-X.

160. Helander, M. G., Greiner, M. T., Wang, Z. B. & Lu, Z. H. Pitfalls in measuring work function using photoelectron spectroscopy. *Appl. Surf. Sci.* **256**, 2602–2605 (2010).

161. Lovelock, K. R. J., Villar-Garcia, I. J., Maier, F., Steinrück, H. P. & Licence, P. Photoelectron spectroscopy of ionic liquid-based interfaces. *Chem. Rev.* **110**, 5158–5190 (2010).

162. Zharnikov, M. Synchrotrongestützte Methoden in der Chemie, Physik und Biologie. (2021).

163. Rivnay, J., Mannsfeld, S. C. B., Miller, C. E., Salleo, A. & Toney, M. F. Quantitative determination of organic semiconductor microstructure from the molecular to device scale. *Chem. Rev.* **112**, 5488–5519 (2012).

164. Smith, A. P., Urquhart, S. G., Winesett, D. A., Mitchell, G. & Ade, H. Use of near edge X-ray absorption fine structure spectromicroscopy to characterize multicomponent polymeric systems. *Appl. Spectrosc.* **55**, 1676–1681 (2001).

165. Duncan, D. A. Synchrotron-based Spectroscopy In On-Surface Polymerization of Covalent Networks. in *Encyclopedia of Interfacial Chemistry* (ed. Wandelt, K.) 436–445 (Elsevier, 2018). doi:https://doi.org/10.1016/B978-0-12-409547-2.13768-0.

166. Nefedov, A. & Wöll, C. Advanced Applications of NEXAFS Spectroscopy for Functionalized Surfaces. in *Surface Science Techniques* (eds. Bracco, G. & Holst, B.) 277–303 (Springer Berlin Heidelberg, 2013). doi:10.1007/978-3-642-34243-1_10.

167. Darlatt, E. *et al.* Evidence of click and coordination reactions on a self-assembled monolayer by synchrotron radiation based XPS and NEXAFS. *J. Electron Spectros. Relat. Phenomena* **185**, 85–89 (2012).

168. Graf, N. *et al.* XPS and NEXAFS studies of aliphatic and aromatic amine species on functionalized surfaces. *Surf. Sci.* **603**, 2849–2860 (2009).

169. Chen, W. & Wee, A. T. S. Synchrotron PES and NEXAFS studies of self-assembled aromatic thiol monolayers on Au(1 1 1). *J. Electron Spectros. Relat. Phenomena* **172**, 54–63 (2009).

170. Battocchio, C. *et al.* Gold nanoparticles stabilized with aromatic thiols: Interaction at the molecule-metal interface and ligand arrangement in the molecular shell investigated by SR-XPS and NEXAFS. *J. Phys. Chem. C* **118**, 8159–8168 (2014).

171. Charbonneau, G.-P. & Delugeard, Y. Structural transition in polyphenyls. III. Crystal structure of biphenyl at 110 K. *Acta Crystallogr. Sect. B Struct. Crystallogr. Cryst. Chem.* **32**, 1420–1423 (1976).

172. Rohwerder, M. Passivity of Metals and the Kelvin Probe Technique. in *Encyclopedia of Interfacial Chemistry* (ed. Wandelt, K.) 414–422 (Elsevier, 2018). doi:10.1016/B978-0-12-409547-2.13405-5.

173. Palermo, V., Palma, M. & Samori, P. Electronic characterization of organic thin films by Kelvin probe force microscopy. *Adv. Mater.* **18**, 145–164 (2006).

174. Simmons, J. G. Generalized Formula for the Electric Tunnel Effect between Similar Electrodes Separated by a Thin Insulating Film. *J. Appl. Phys.* **34**, 1793–1803 (1963).

175. Reus, W. F. *et al.* Statistical tools for analyzing measurements of charge transport. *J. Phys. Chem. C* **116**, 6714–6733 (2012).

176. Jiang, L., Sangeeth, C. S. S., Yuan, L., Thompson, D. & Nijhuis, C. A. One-Nanometer Thin Monolayers Remove the Deleterious Effect of Substrate Defects in Molecular Tunnel Junctions. *Nano Lett.* **15**, 6643–6649 (2015).

177. Penner, P. *et al.* Charge transport through carbon nanomembranes. *J. Phys. Chem. C* **118**, 21687–21694 (2014).

178. Bowers, C. M. *et al.* Tunneling across SAMs Containing Oligophenyl Groups. *J. Phys. Chem. C* **120**, 11331–11337 (2016).

179. Casella, George Berger, R. L. *Statistical Inference*. (Thomson Learning, 2002).

180. John L. Stanford, S. B. V. *Statistical Methods for Physical Science*. (cademic Press, 1994).

181. C., E. L. & Bevington, P. R. Data Reduction and Error Analysis for the Physical Sciences. *J. Am. Stat. Assoc.* **67**, 249 (1972).

182. Beebe, J. M., Kim, B. S., Frisbei, C. D. & Kushmerick, J. G. Measuring relative barrier heights in molecular electronic junctions with transition voltage spectroscopy. *ACS Nano* **2**, 827–832 (2008).

183. Huisman, E. H., Guédon, C. M., Van Wees, B. J. & Van Der Molen, S. J. Interpretation of transition voltage spectroscopy. *Nano Lett.* **9**, 3909–3913 (2009).

184. Trouwborst, M. L. *et al.* Transition voltage spectroscopy and the nature of vacuum tunneling. *Nano Lett.* **11**, 614–617 (2011).

185. Markussen, T., Chen, J. & Thygesen, K. S. Improving transition voltage spectroscopy of molecular junctions. *Phys. Rev. B - Condens. Matter Mater. Phys.* **83**, 1–6 (2011).

186. Mirjani, F., Thijssen, J. M. & Van Der Molen, S. J. Advantages and limitations of transition voltage spectroscopy: A theoretical analysis. *Phys. Rev. B - Condens. Matter Mater. Phys.* **84**, 1–8 (2011).

187. Araidai, M. & Tsukada, M. Theoretical calculations of electron transport in molecular junctions: Inflection behavior in Fowler-Nordheim plot and its origin. *Phys. Rev. B - Condens. Matter Mater. Phys.* **81**, 1–7 (2010).

188. Moulder, J. F., Stickle, W. F., Sobol, P. E. & Bomben, K. D. *Handbook of X-ray Photoelectron Spectroscopy*. (1992).

189. Georgieva, V. *et al.* Study of quartz crystal microbalance NO2 sensor coated with sputtered indium tin oxide film. *J. Phys. Conf. Ser.* **558**, (2014).

190. Dang, M. T., Lefebvre, J. & Wuest, J. D. Recycling Indium Tin Oxide (ITO) Electrodes Used in Thin-Film Devices with Adjacent Hole-Transport Layers of Metal Oxides. *ACS Sustain. Chem. Eng.* **3**, 3373–3381 (2015).

191. Chesneau, F. *et al.* Self-assembled monolayers of perfluoroterphenyl-substituted

alkanethiols: Specific characteristics and odd-even effects. *Phys. Chem. Chem. Phys.* **12**, 12123–12137 (2010).

192. Schreiber, F. Structure and growth of self-assembling monolayers. *Prog. Surf. Sci.* **65**, 151–257 (2000).

193. Batson, P. E. Carbon 1s near-edge-absorption fine structure in graphite. *Phys. Rev. B* **48**, 2608–2610 (1993).

194. Querebillo, C. J., Terfort, A., Allara, D. L. & Zharnikov, M. Static conductance of nitrile-substituted oligophenylene and oligo(phenylene ethynylene) self-assembled monolayers studied by the mercury-drop method. *J. Phys. Chem. C* **117**, 25556–25561 (2013).

195. Yildirim, C., Sauter, E., Terfort, A. & Zharnikov, M. Effect of Electron Irradiation on Electric Transport Properties of Aromatic Self-Assembled Monolayers. *J. Phys. Chem. C* **121**, 7355–7364 (2017).

196. Chiechi, R. C., Weiss, E. A., Dickey, M. D. & Whitesides, G. M. Eutectic Gallium–Indium (EGaIn): A Moldable Liquid Metal for Electrical Characterization of Self-Assembled Monolayers. *Angew. Chemie* **120**, 148–150 (2008).

197. Bruce, R. C. *et al.* Contrasting Transport and Electrostatic Properties of Selectively Fluorinated Alkanethiol Monolayers with Embedded Dipoles. *J. Phys. Chem. C* **122**, 4881–4890 (2018).

198. Derry, G. N., Kern, M. E. & Worth, E. H. Recommended values of clean metal surface work functions. *J. Vac. Sci. Technol. A Vacuum, Surfaces, Film.* **33**, 060801 (2015).

199. Wu, Q. H. Progress in modification of indium-tin oxide/organic interfaces for organic light-emitting diodes. *Crit. Rev. Solid State Mater. Sci.* **38**, 318–352 (2013).

200. Ostapenko, A. *et al.* Etching of Crystalline ZnO Surfaces upon Phosphonic Acid Adsorption: Guidelines for the Realization of Well-Engineered Functional Self-Assembled Monolayers. *ACS Appl. Mater. Interfaces* **8**, 13472–13483 (2016).

201. Knesting, K. M., Hotchkiss, P. J., MacLeod, B. A., Marder, S. R. & Ginger, D. S. Spatially modulating interfacial properties of transparent conductive oxides: Patterning work function with phosphonic acid self-assembled monolayers. *Adv. Mater.* **24**, 642–646 (2012).

202. Bhairamadgi, N. S. *et al.* Hydrolytic and thermal stability of organic monolayers on various inorganic substrates. *Langmuir* **30**, 5829–5839 (2014).

203. Neves, B. R. A., Salmon, M. E., Russell, P. E. & Troughton, E. B. Thermal stability study of self-assembled monolayers on mica. *Langmuir* **16**, 2409–2412 (2000).

204. Perkins, C. L. Molecular anchors for self-assembled monolayers on ZnO: A direct comparison of the thiol and phosphonic acid moieties. *J. Phys. Chem. C* **113**, 18276–18286 (2009).

205. Chen, X. *et al.* Studies on the effect of solvents on self-assembled monolayers formed from organophosphonic acids on indium tin oxide. *Langmuir* **28**, 9487–9495 (2012).

206. Donley, C. *et al.* Characterization of indium-tin oxide interfaces using X-ray photoelectron spectroscopy and redox processes of a chemisorbed probe molecule: Effect of surface pretreatment conditions. *Langmuir* **18**, 450–457 (2002).

207. Khan, G. G. *et al.* Defect engineered d 0 ferromagnetism in tin-doped indium oxide nanostructures and nanocrystalline thin-films. *J. Appl. Phys.* **118**, 0–8 (2015).

208. Textor, M. *et al.* Structural chemistry of self-assembled monolayers of octadecylphosphoric acid on tantalum oxide surfaces. *Langmuir* **16**, 3257–3271 (2000).

209. Wagstaffe, M. *et al.* An experimental investigation of the adsorption of a phosphonic acid on the anatase TiO2(101) surface. *J. Phys. Chem. C* **120**, 1693–1700 (2016).

210. Zharnikov, M. High-resolution X-ray photoelectron spectroscopy in studies of self-assembled organic monolayers. *J. Electron Spectros. Relat. Phenomena* **178–179**, 380–393 (2010).

211. Bolognesi, P. *et al.* Inner shell excitation, ionization and fragmentation of pyrimidine. *J. Phys. Conf. Ser.* **212**, 0–6 (2010).

212. Szörényi, T., Laude, L. D., Bertóti, I., Kántor, Z. & Geretovszky, Z. Excimer laser processing of indium-tin-oxide films: An optical investigation. *J. Appl. Phys.* **78**, 6211–6219 (1995).

213. Horsley, J. A. *et al.* Resonances in the K shell excitation spectra of benzene and pyridine: Gas phase, solid, and chemisorbed states. *J. Chem. Phys.* **83**, 6099–6107 (1985).

214. Frey, S. *et al.* Structure of thioaromatic self-assembled monolayers on gold and silver. *Langmuir* **17**, 2408–2415 (2001).

215. Zharnikov, M., Küller, A., Shaporenko, A., Schmidt, E. & Eck, W. Aromatic self-assembled monolayers on hydrogenated silicon. *Langmuir* **19**, 4682–4687 (2003).

216. Shaporenko, A., Cyganik, P., Buck, M., Terfort, A. & Zharnikov, M. Self-assembled monolayers of aromatic selenolates on noble metal substrates. *J. Phys. Chem. B* **109**, 13630–13638 (2005).

217. Yokoyama, T., Seki, K., Morisada, I., Edamatsu, K. & Ohta, T. X-ray absorption spectra of poly-p-phenylenes and polyacenes: Localization of π orbitals. *Phys. Scr.* **41**, 189–192 (1990).

218. Lin, Y. S. *et al.* Measurement and prediction of the NEXAFS spectra of pyrimidine and purine and the dissociation following the core excitation. *Chem. Phys. Lett.* **636**, 146–153 (2015).

219. Vall-Llosera, G. *et al.* The C 1s and N 1s near edge x-ray absorption fine structure spectra of five azabenzenes in the gas phase. *J. Chem. Phys.* **128**, (2008).

220. Kolczewski, C. *et al.* Detailed study of pyridine at the C 1s and N 1s ionization thresholds: The influence of the vibrational fine structure. *J. Chem. Phys.* **115**, 6426–6437 (2001).

221. Zharnikov, M., Frey, S., Heister, K. & Grunze, M. An extension of the mean free path approach to X-ray absorption spectroscopy. *J. Electron Spectros. Relat. Phenomena* **124**, 15–24 (2002).

222. Rong, H. T. *et al.* On the importance of the headgroup substrate bond in thiol monolayers: A study of biphenyl-based thiols on gold and silver. *Langmuir* **17**, 1582–1593 (2001).

223. Ballav, N. *et al.* Direct probing molecular twist and tilt in aromatic self-assembled monolayers. *J. Am. Chem. Soc.* **129**, 15416–15417 (2007).

224. Sauter, E. *et al.* A dithiocarbamate anchoring group as a flexible platform for interface engineering. *Phys. Chem. Chem. Phys.* **21**, 22511–22525 (2019).

225. Shaporenko, A. *et al.* Self-assembled monolayers from biphenyldithiol derivatives: Optimization of the deprotection procedure and effect of the molecular

conformation. *J. Phys. Chem. B* **110**, 4307–4317 (2006).

226. Trotter, J. The crystal and molecular structure of biphenyl. *Acta Crystallogr.* **14**, 1135–1140 (1961).

227. Hargreaves, A. & Rizvi, S. H. The crystal and molecular structure of biphenyl. *Acta Crystallogr.* **15**, 365–373 (1962).

228. Charbonneau, B. Y. G. & Delugeard, Y. Structural Transition in Polyphenyls. III. Crystal Structure of Biphenyl at 110 K. *Acta Crystallogr., Sect. B Struct. Sci.* 1420–1423 (1976).

229. Levstik, A., Filipic, C. & Levstik, I. Dielectric properties of biphenyl. *J. Phys. Condens. Matter* **2**, 3031–3033 (1990).

230. Sauter, E., Gilbert, C. O., Boismenu-Lavoie, J., Morin, J. F. & Zharnikov, M. Mixed Aliphatic Self-Assembled Monolayers with Embedded Polar Group. *J. Phys. Chem. C* **121**, 23017–23024 (2017).

231. Shaporenko, A., Terfort, A., Grunze, M. & Zharnikov, M. A detailed analysis of the photoemission spectra of basic thioaromatic monolayers on noble metal substrates. *J. Electron Spectros. Relat. Phenomena* **151**, 45–51 (2006).

232. Watcharinyanon, S., Moons, E. & Johansson, L. S. O. Mixed self-assembled monolayers of ferrocene-terminated and unsubstituted alkanethiols on gold: Surface structure and work function. *J. Phys. Chem. C* **113**, 1972–1979 (2009).

233. Wu, K. Y., Yu, S. Y. & Tao, Y. T. Continuous modulation of electrode work function with mixed self-assembled monolayers and its effect in charge injection. *Langmuir* **25**, 6232–6238 (2009).

234. Venkataraman, N. V. *et al.* Spatial tuning of the metal work function by means of alkanethiol and fluorinated alkanethiol gradients. *J. Phys. Chem. C* **113**, 5620–5628 (2009).

235. Kang, J. F. *et al.* Self-assembled rigid monolayers of 4′-substituted-4-mercaptobiphenyls on gold and silver surfaces. *Langmuir* **17**, 95–106 (2001).

236. Hirsch, T. *et al.* Size-controlled electrochemical synthesis of metal nanoparticles on monomolecular templates. *Angew. Chemie - Int. Ed.* **44**, 6775–6778 (2005).

237. Heimel, G., Romaner, L., Zojer, E. & Bredas, J. L. The interface energetics of self-assembled monolayers on metals. *Acc. Chem. Res.* **41**, 721–729 (2008).

238. De Boer, B., Hadipour, A., Mandoc, M. M., Van Woudenbergh, T. & Blom, P. W. M. Tuning of metal work functions with self-assembled monolayers. *Adv. Mater.* **17**, 621–625 (2005).

239. Taucher, T. C., Hehn, I., Hofmann, O. T., Zharnikov, M. & Zojer, E. Understanding Chemical versus Electrostatic Shifts in X-ray Photoelectron Spectra of Organic Self-Assembled Monolayers. *J. Phys. Chem. C* **120**, 3428–3437 (2016).

240. Van Dyck, C. & Bergren, A. J. Large Built-In Fields Control the Electronic Properties of Nanoscale Molecular Devices with Dipolar Structures. *Adv. Electron. Mater.* **4**, 1–10 (2018).

241. Käfer, D. *et al.* Evidence for band-like transport in craphene-based organic monolayers. *Adv. Mater.* **22**, 384–388 (2010).

242. Bashir, A. *et al.* Charge carrier mobilities in organic semiconductors: Crystal engineering and the importance of molecular contacts. *Phys. Chem. Chem. Phys.* **17**, 21988–21996 (2015).

243. Kang, J. F., Ulman, A., Jordan, R. & Kurth, M. G. Optically Induced Band Shifts in

Infrared Spectra of Mixed Self-assembled Monolayers of Biphenyl Thiols. *Langmuir* **15**, 5555–5559 (1999).

244. Beebe, J. M., Kim, B., Gadzuk, J. W., Frisbie, C. D. & Kushmerick, J. G. Transition from direct tunneling to field emission in metal-molecule-metal junctions. *Phys. Rev. Lett.* **97**, 1–4 (2006).

245. Wang, G. *et al.* Investigation of the transition voltage spectra of molecular junctions considering frontier molecular orbitals and the asymmetric coupling effect. *J. Phys. Chem. C* **115**, 17979–17985 (2011).

246. Tan, A. *et al.* Length dependence of frontier orbital alignment in aromatic molecular junctions. *Appl. Phys. Lett.* **101**, (2012).

247. Sotthewes, K., Hellenthal, C., Kumar, A. & Zandvliet, H. J. W. Transition voltage spectroscopy of scanning tunneling microscopy vacuum junctions. *RSC Adv.* **4**, 32438–32442 (2014).

248. Vilan, A., Cahen, D. & Kraisler, E. Rethinking transition voltage spectroscopy within a generic taylor expansion view. *ACS Nano* **7**, 695–706 (2013).

249. Heister, K. *et al.* Odd-even effects at the S-metal interface and in the aromatic matrix of biphenyl-substituted alkanethiol self-assembled monolayers. *J. Phys. Chem. B* **105**, 6888–6894 (2001).

250. Bashir, A. *et al.* Side-Group-Induced Polymorphism in Self-Assembled Monolayers: 3,5-Bis(trifluoromethyl)benzenethiolate Films on Au(111). *ChemPhysChem* **18**, 702–714 (2017).

251. Kong, G. D. *et al.* Elucidating the Role of Molecule-Electrode Interfacial Defects in Charge Tunneling Characteristics of Large-Area Junctions. *J. Am. Chem. Soc.* **140**, 12303–12307 (2018).

252. Schreiber, F. Structure and growth of self-assembling monolayers. *Prog. Surf. Sci.* **65**, 151–257 (2000).

253. Tai, Y. *et al.* Fabrication of thiol-terminated surfaces using aromatic self-assembled monolayers. *J. Phys. Chem. B* **108**, 16806–16810 (2004).

254. Gahl, C. *et al.* Structure and excitonic coupling in self-assembled monolayers of azobenzene-functionalized alkanethiols. *J. Am. Chem. Soc.* **132**, 1831–1838 (2010).

255. Kim, B., Choi, S. H., Zhu, X. Y. & Frisbie, C. D. Molecular tunnel junctions based on π-conjugated oligoacene thiols and dithiols between Ag, Au, and Pt contacts: Effect of surface linking group and metal work function. *J. Am. Chem. Soc.* **133**, 19864–19877 (2011).

256. Baghbanzadeh, M. *et al.* Dipole-Induced Rectification Across AgTS/SAM//Ga2O3/EGaIn Junctions. *J. Am. Chem. Soc.* **141**, 8969–8980 (2019).

257. Vonlanthen, D. *et al.* Chemically controlled conductivity: torsion-angle dependence in a single-molecule biphenyldithiol junction. *Angew. Chemie - Int. Ed.* **48**, 8886–8890 (2009).

258. Mishchenko, A. *et al.* Influence of conformation on conductance of biphenyl-dithiol single-molecule contacts. *Nano Lett.* **10**, 156–163 (2010).

259. Sun, Q., Selloni, A. & Scoles, G. Electronic structure of metal/molecule/metal junctions: A density functional theory study of the influence of the molecular terminal group. *J. Phys. Chem. B* **110**, 3493–3498 (2006).

260. Pflaum, J. *et al.* Structure and electronic properties of CH3- and CF3-terminated alkanethiol monolayers on Au(1 1 1): A scanning tunneling microscopy, surface X-

ray and helium scattering study. *Surf. Sci.* **498**, 89–104 (2002).

261. Fracasso, D., Muglali, M. I., Rohwerder, M., Terfort, A. & Chiechi, R. C. Influence of an atom in EGaIn/Ga2O3 tunneling junctions comprising self-assembled monolayers. *J. Phys. Chem. C* **117**, 11367–11376 (2013).

262. Kovalchuk, A. *et al.* Dipole-induced asymmetric conduction in tunneling junctions comprising self-assembled monolayers. *RSC Adv.* **6**, 69479–69483 (2016).

263. Chen, J. *et al.* Understanding Keesom Interactions in Monolayer-Based Large-Area Tunneling Junctions. *J. Phys. Chem. Lett.* **9**, 5078–5085 (2018).

264. Wang, S., Wei, M. Z., Hu, G. C., Wang, C. K. & Zhang, G. P. Mechanisms of the odd-even effect and its reversal in rectifying performance of ferrocenyl-n-alkanethiolate molecular diodes. *Org. Electron.* **49**, 76–84 (2017).

265. Metzger, R. M. Unimolecular Electronics. *Chem. Rev.* **115**, 5056–5115 (2015).

266. Vilan, A., Aswal, D. & Cahen, D. Large-Area, Ensemble Molecular Electronics: Motivation and Challenges. *Chem. Rev.* **117**, 4248–4286 (2017).

267. Xiang, D., Wang, X., Jia, C., Lee, T. & Guo, X. Molecular-Scale Electronics: From Concept to Function. *Chem. Rev.* **116**, 4318–4440 (2016).

268. Yuan, L., Thompson, D., Cao, L., Nerngchangnong, N. & Nijhuis, C. A. One Carbon Matters: The Origin and Reversal of Odd-Even Effects in Molecular Diodes with Self-Assembled Monolayers of Ferrocenyl-Alkanethiolates. *J. Phys. Chem. C* **119**, 17910–17919 (2015).

269. Capozzi, B. *et al.* Single-molecule diodes with high rectification ratios through environmental control. *Nat. Nanotechnol.* **10**, 522–527 (2015).

270. Perrin, M. L. *et al.* A gate-tunable single-molecule diode. *Nanoscale* **8**, 8919–8923 (2016).

271. Döring, K., Ballav, N., Zharnikov, M. & Lang, H. Synthesis, Electrochemical Behavior, and Self-Assembly of Metallocene-Functionalized Thiofluorenes. *Eur. J. Inorg. Chem.* **2010**, 3952–3960 (2010).

272. Schwarz, F. *et al.* Field-induced conductance switching by charge-state alternation in organometallic single-molecule junctions. *Nat. Nanotechnol.* **11**, 170–176 (2016).

273. Cademartiri, L. *et al.* Electrical resistance of Ag TS-S(CH 2) n -1CH 3//Ga 2O 3/EGaIn tunneling junctions. *J. Phys. Chem. C* **116**, 10848–10860 (2012).

274. Rößler, K. *et al.* Synthesis, characterization and electrochemical behavior of unsymmetric transition metal-terminated biphenyl ethynyl thiols. *J. Organomet. Chem.* **692**, 1530–1545 (2007).

275. Heimel, G., Romaner, L., Zojer, E. & Bredas, J. L. Toward control of the metal-organic interfacial electronic structure in molecular electronics: A first-principles study on self-assembled monolayers of π-conjugated molecules on noble metals. *Nano Lett.* **7**, 932–940 (2007).

276. Heimel, G., Romaner, L., Bre, J. & Zojer, E. Odd - Even Effects in Self-Assembled Monolayers of ω - (Biphenyl-4-yl) alkanethiols : A First-Principles Study. 474–482 (2008).

277. Rodriguez-Gonzalez, S. *et al.* HOMO Level Pinning in Molecular Junctions: Joint Theoretical and Experimental Evidence. *J. Phys. Chem. Lett.* **9**, 2394–2403 (2018).

278. Chandekar, A., Sengupta, S. K. & Whitten, J. E. Thermal stability of thiol and silane monolayers: A comparative study. *Appl. Surf. Sci.* **256**, 2742–2749 (2010).

279. Xue, Y., Li, X., Li, H. & Zhang, W. Quantifying thiol-gold interactions towards the

efficient strength control. *Nat. Commun.* **5**, (2014).

280. Häkkinen, H. The gold-sulfur interface at the nanoscale. *Nat. Chem.* **4**, 443–455 (2012).
281. Yang, Y. W. & Fan, L. J. High resolution XPS study of decanethiol on Au(111): Single sulfur-gold bonding interaction. *Langmuir* **18**, 1157–1164 (2002).
282. Ishida, T. *et al.* Annealing effect of self-assembled monolayers generated from terphenyl derivatized thiols on Au(111). *Langmuir* **18**, 83–92 (2002).
283. Heister, K., Johansson, L. S. O., Grunze, M. & Zharnikov, M. A detailed analysis of the C 1s photoemission of n-alkanethiolate films on noble metal substrates. *Surf. Sci.* **529**, 36–46 (2003).
284. Kondoh, H. *et al.* Adsorption of Thiolates to Singly Coordinated Sites on Au(111) Evidenced by Photoelectron Diffraction. *Phys. Rev. Lett.* **90**, 4 (2003).
285. Roper, M. G. *et al.* Atop adsorption site of sulphur head groups in gold-thiolate self-assembled monolayers. *Chem. Phys. Lett.* **389**, 87–91 (2004).
286. Leung, T. Y. B., Schwartz, P., Scoles, G., Schreiber, F. & Ulman, A. Structure and growth of 4-methyl-4′-mercaptobiphenyl monolayers on Au(111): a surface diffraction study. *Surf. Sci.* **458**, 34–52 (2000).
287. Ishida, T. *et al.* Adsorption processes of self-assembled monolayers made from terphenyl thiols. *Langmuir* **17**, 7459–7463 (2001).
288. Himmelhaus, M. *et al.* Adsorption of docosanethiol from solution on polycrystalline silver surfaces: An XPS and NEXAFS study. *J. Electron Spectros. Relat. Phenomena* **92**, 139–149 (1998).
289. Ishida, T. *et al.* High-resolution X-ray photoelectron spectra of organosulfur monolayers on Au(111): S(2p) spectral dependence on molecular species. *Langmuir* **15**, 6799–6806 (1999).
290. Ishida, T. *et al.* High resolution X-ray photoelectron spectroscopy measurements of octadecanethiol self-assembled monolayers on Au(111). *Langmuir* **14**, 2092–2096 (1998).
291. Ossowski, J. *et al.* Thiolate versus Selenolate: Structure, Stability, and Charge Transfer Properties. *ACS Nano* **9**, 4508–4526 (2015).
292. Ossowski, J. *et al.* Relative Thermal Stability of Thiolate- and Selenolate-Bonded Aromatic Monolayers on the Au(111) Substrate. *J. Phys. Chem. C* **121**, 28031–28042 (2017).
293. Azzam, W. *et al.* Coexistence of different structural phases in thioaromatic monolayers on Au(111). *Langmuir* **19**, 4958–4968 (2003).
294. Hekele, J. *et al.* A fresh look at the structure of aromatic thiols on Au surfaces from theory and experiment. *J. Chem. Phys.* **155**, (2021).
295. Bashir, A. *et al.* Selenium as a key element for highly ordered aromatic self-assembled monolayers. *Angew. Chemie - Int. Ed.* **47**, 5250–5252 (2008).
296. Naredla, R. R. & Klumpp, D. A. Contemporary Carbocation Chemistry: Applications in Organic Synthesis. *Chem. Rev.* **113**, 6905–6948 (2013).
297. Heister, K., Zharnikov, M., Grunze, M., Johansson, L. S. O. & Ulman, A. Characterization of X-ray induced damage in alkanethiolate monolayers by high-resolution photoelectron spectroscopy. *Langmuir* **17**, 8–11 (2001).
298. Feulner, P. *et al.* Strong temperature dependence of irradiation effects in organic layers. *Phys. Rev. Lett.* **93**, 1–4 (2004).

299. Shaporenko, A., Zharnikov, M., Feulner, P. & Menzel, D. Quantitative analysis of temperature effects in radiation damage of thiolate-based self-assembled monolayers. *J. Phys. Condens. Matter* **18**, S1677–S1689 (2006).

300. Crudden, C. M. *et al.* Ultra stable self-assembled monolayers of N-heterocyclic carbenes on gold. *Nat. Chem.* **6**, 409–414 (2014).

301. Krzykawska, A., Wróbel, M., Kozieł, K. & Cyganik, P. N-Heterocyclic Carbenes for the Self-Assembly of Thin and Highly Insulating Monolayers with High Quality and Stability. *ACS Nano* **14**, 6043–6057 (2020).

302. Chen, D. *et al.* An extremely rapid dip-coating method for self-assembly of octadecylphosphonic acid and its thermal stability on an aluminum film. *J. Mater. Chem. C* **2**, 9941–9948 (2014).

303. Luschtinetz, R. *et al.* Adsorption of phosphonic and ethylphosphonic acid on aluminum oxide surfaces. **602**, 1347–1359 (2008).

304. R.D. Ramsier, P.N. Henriksen, A. N. G. Adsorption of phosphorus acids on alumina. *Surf. cience* **203**, 72–88 (1988).

305. Hector Jr., L. G. *et al.* Investigation of Vinyl Phosphonic Acid/Hydroxylated α–Al. *Surf. Sci.* **494**, 1–20 (2001).

306. Adolphi, B., Jähne, E., Busch, G. & Cai, X. Characterization of the adsorption of w-(thiophene-3-yl alkyl) phosphonic acid on metal oxides with AR-XPS. *Anal. Bioanal. Chem.* **379**, 646–652 (2004).

307. Aiko Sakamoto, Yutaka Matsuo, Keiko Matsuo, E. N. Efficient Bidirectional Photocurrent Generation by Self-Assembled. *Chem. Asian J.* **0033**, 1208–1212 (2009).

308. Piersimoni, F. *et al.* Charge Transfer Absorption and Emission at ZnO/Organic Interfaces. *J. Phys. Chem. Lett.* **6**, 500–504 (2015).

309. Acton, O. *et al.* Simultaneous modification of bottom-contact electrode and dielectric surfaces for organic thin-film transistors through single-component spin-cast monolayers. *Adv. Funct. Mater.* **21**, 1476–1488 (2011).

310. Liu, D. *et al.* Self-Assembled Monolayers of Cyclohexyl-Terminated Phosphonic Acids as a General Dielectric Surface for High-Performance Organic Thin-Film Transistors. *Adv. Mater.* **26**, 7190–7196 (2014).

311. Fukushima, H. *et al.* Microstructure, wettability, and thermal stability of semifluorinated self-assembled monolayers (SAMs) on gold. *J. Phys. Chem. B* **104**, 7417–7423 (2000).

312. Kanta, A., Sedev, R. & Ralston, J. The formation and stability of self-assembled monolayers of octadecylphosphonic acid on titania. **291**, 51–58 (2006).

313. Lu, H., Zeysing, D., Kind, M., Terfort, A. & Zharnikov, M. Structure of Self-Assembled Monolayers of Partially Fluorinated Alkanethiols with a Fluorocarbon Part of Variable Length on Gold Substrate. *J. Phys. Chem. C* **117**, 18967–18979 (2013).

314. Lu, H., Kind, M., Terfort, A. & Zharnikov, M. Structure of Self-Assembled Monolayers of Partially Fluorinated Alkanethiols on GaAs(001) Substrates. *J. Phys. Chem. C* **117**, 26166–26178 (2013).

315. Thissen, P. *et al.* Stability of Phosphonic Acid Self-Assembled Monolayers on Amorphous and Single-Crystalline Aluminum Oxide Surfaces in Aqueous Solution. **36**, 156–164 (2010).

316. Hamoudi, H., Chesneau, F., Patze, C. & Zharnikov, M. Chain-Length-Dependent Branching of Irradiation-Induced Processes in Alkanethiolate Self-Assembled Monolayers. 534–541 (2011).

317. Wang, Q. *et al.* Dynamically Switching the Electronic and Electrostatic Properties of Indium-Tin Oxide Electrodes with Photochromic Monolayers: Toward Photoswitchable Optoelectronic Devices. *ACS Appl. Nano Mater.* **2**, 1102–1110 (2019).

318. Ligorio, G. *et al.* Modulating the luminance of organic light-emitting diodes: Via optical stimulation of a photochromic molecular monolayer at transparent oxide electrode. *Nanoscale* **12**, 5444–5451 (2020).

319. Ligorio, G., Zorn Morales, N. & List-Kratochvil, E. J. W. Large and continuous tuning of the work function of indium tin oxide using simple mixing of self-assembled monolayers. *Appl. Phys. Lett.* **116**, 3–8 (2020).

320. Koslowski, N., Trouillet, V. & Schneider, J. J. Solution-processed amorphous yttrium aluminium oxide YAl: XOyand aluminum oxide AlxOy, and their functional dielectric properties and performance in thin-film transistors. *J. Mater. Chem. C* **8**, 8521–8530 (2020).

321. Büschges, M. I., Hoffmann, R. C., Regoutz, A., Schlueter, C. & Schneider, J. J. Atomic Layer Deposition of Ternary Indium/Tin/Aluminum Oxide Thin Films, Their Characterization and Transistor Performance under Illumination. *Chem. - A Eur. J.* **27**, 9791–9800 (2021).

322. Koslowski, N. *et al.* Synthesis, oxide formation, properties and thin film transistor properties of yttrium and aluminium oxide thin films employing a molecular-based precursor route. *RSC Adv.* **9**, 31386–31397 (2019).

Acknowledgements